INVESTIGATION OF THE CORROSION BEHAVIOUR OF BARE AND POLYPYRROLE-COATED WE43 MAGNESIUM ALLOY FOR THE DEVELOPMENT OF BIODEGRADABLE IMPLANTS

By

Mario Alberto Ascencio Pinedo

A Thesis Submitted to the Faculty of Graduate Studies and Research in Partial Fulfillment of the requirements for the Degree of Doctor of Philosophy

Department of Chemical Engineering

McGill University

Montreal, Canada

February 2016

ABSTRACT

The development of biodegradable implants for orthopaedic and cardiovascular applications has gained considerable attention as an alternative to avoid long-term complications caused by permanent implants. Magnesium is an attractive material for such applications mainly due to its biocompatibility and good mechanical properties. Mg alloys biodegrade via corrosion reaction; however, they corrode too fast in the body, leading to a premature decrease in the mechanical properties and implant failure. Current research efforts to control the corrosion rate of Mg alloys are oriented mainly in two directions: (*i*) the development of new Mg alloys with improved corrosion resistance and biocompatibility, and (*ii*) the development of protective biocompatible coatings. However, faster and more efficient development of Mg-based materials is limited by the lack of a complete understanding of the Mg alloy corrosion mechanisms in the real physiological environment and by difficulties at emulating such environment *in vitro*.

The focus of this PhD project was to investigate the short-term corrosion behaviour of bare and polypyrrole-coated WE43 Mg alloy at *in vitro* experimental conditions closer resembling those experienced in the physiological environment. This was done by performing 5-day immersion experiments in a modified simulated body fluid (m-SBF) with an ionic composition similar to that of blood plasma, at the physiological pH and average body temperature. Interfacial processes such as charge transfer, diffusion and adsorption of species were investigated by electrochemical impedance spectroscopy (EIS). The corrosion kinetics was investigated by hydrogen evolution, inductively coupled plasma optical emission spectroscopy (ICP-OES) and

EIS. The polypyrrole coating and corrosion products layer were characterized by scanning electron microscopy (SEM), energy dispersive spectroscopy (EDS), X-ray diffraction (XRD), attenuated total reflectance Fourier transform infrared spectroscopy (ATR-FTIR) and X-ray photoelectron spectroscopy (XPS).

The corrosion kinetics and mechanisms of WE43 Mg alloy in m-SBF and their time dependence were investigated. An initial decrease in the corrosion rate was related to formation of a partially protective corrosion layer, while an increase in the corrosion rate observed after 48 h was related to onset of a localized corrosion process. Four corrosion stages were proposed involving: (*i*) the formation of a partially protective corrosion layer, (*ii*) the adsorption of Mg intermediates, (*iii*) the formation of an inner protective MgO layer with increasing coverage over time, (*iv*) the rupture of the corrosion layer, and (*v*) lateral growth of stable pits. Characterization of the corrosion products layer revealed the presence of an amorphous carbonated apatite/$Mg(OH)_2$ mixed corrosion layer.

The effect of daily electrolyte renewal, as a method to better simulate physiological homeostasis, on the corrosion behaviour of WE43 Mg alloy in m-SBF was investigated. Electrolyte renewal was found to affect the corrosion mechanisms by promoting partial dissolution of the corrosion layer and by increasing mass transport through the corrosion layer, thereby delaying the increase in the MgO barrier film coverage and the occurrence of localized corrosion. No significant variation in the corrosion layer morphology and composition with respect to the results obtained without electrolyte renewal was observed.

The corrosion behaviour of polypyrrole-coated WE43 Mg alloy in m-SBF with daily electrolyte renewal was also investigated. Polypyrrole (PPy) was found to effectively contribute to a decrease in both the corrosion rate of WE43 Mg alloy and in the production of hydrogen gas during the time period investigated. A temporary increase in the corrosion resistance after electrolyte renewal was related to the increase in the concentration of dissolved CO_2 in the m-SBF. The corrosion protection of PPy was attributed to: (*i*) the PPy coating barrier properties, and (*ii*) the adsorption of dissolved CO_2 species on the PPy coating, which leads to a decrease in the PPy conductivity and to substrate/coating decoupling due to uncompensated coating positive charging and misalignment of the substrate and coating Fermi levels.

Lastly, results on the corrosion behaviour of WE43 Mg alloy in m-SBF under continuous electrolyte flow conditions are presented in the appendix of the thesis. It is shown that the presence of a continuous flow leads to a slower increase in the MgO barrier film coverage, with respect to static immersion experiments, resulting in a higher corrosion rate. These results demonstrate the importance of the experimental set-up for an accurate determination of the Mg alloys corrosion behaviour for biodegradable applications.

The present thesis contributes to (*i*) a better understanding of the corrosion mechanisms of bare and PPy-coated WE43 Mg alloy at *in vitro* conditions partially resembling the physiological environment and (*ii*) to the advancement of *in vitro* methodologies for the screening and development of new Mg alloys for biodegradable implants applications.

RÉSUMÉ

Le développement d'implants biodégradables pour des applications orthopédiques et cardiovasculaires a gagné une attention considérable en tant qu'alternative pour éviter les complications à long terme causées par des implants permanents. Le magnésium est un matériau attrayant pour de telles applications, principalement en raison de sa biocompatibilité et ses bonnes propriétés mécaniques. La dégradation des alliages de magnésium se produit via corrosion; cependant, ils se corrodent trop vite dans le corps, ce qui conduit à une diminution prématurée des propriétés mécaniques et l'échec de l'implant. Des efforts pour contrôler la vitesse de corrosion des alliages de magnésium sont orientés principalement dans deux directions: (*i*) le développement de nouveaux alliages de Mg avec une meilleure résistance à la corrosion et une meilleure biocompatibilité, et (*ii*) le développement de couches de protection biocompatibles. Toutefois, un développement plus rapide et plus efficace des matériaux à base de Mg est limité par l'absence d'une compréhension complète des mécanismes de corrosion des alliages de Mg dans le corps et par des difficultés à émuler tel environnement *in vitro*.

Le but de ce projet était d'étudier le comportement de corrosion à court terme de l'alliage de magnésium WE43 nu et avec une couche de polypyrrole, dans des conditions expérimentales *in vitro* ressemblant à celles rencontrées dans l'environnement physiologique. Ceci a été réalisé en effectuant des expériences d'immersion de 5 jours dans un fluide corporel simulé modifié (m-SBF) ayant une composition ionique analogue à celle du plasma sanguin, au pH physiologique et à la

température moyenne du corps. Les procédés d'interface tels que le transfert de charge, la diffusion et l'adsorption des espèces ont été étudiés par spectroscopie d'impédance électrochimique (EIS). La cinétique de corrosion a été étudiée par le dégagement d'hydrogène, la spectroscopie d'émission optique avec plasma à couplage inductif (ICP-OES) et EIS. La couche de polypyrrole et les produits de corrosion ont été caractérisés par la microscopie électronique à balayage (SEM), la spectroscopie à rayons X à dispersion d'énergie (EDS), la diffraction des rayons X (XRD), la spectroscopie infrarouge à transformée de Fourier avec un montage de réflexion totale atténuée (ATR-FTIR) et la spectroscopie photoélectronique à rayons X (XPS).

La cinétique et les mécanismes de corrosion de l'alliage de Mg WE43 ainsi que leur comportement en fonction du temps dans le m-SBF ont été étudiés. Une diminution initiale du taux de corrosion est liée à la formation d'une couche d'oxyde protectrice, tandis qu'une augmentation de la vitesse de corrosion observée après 48 h est liée à l'apparition d'un processus de corrosion localisée. Quatre étapes de corrosion ont été proposées impliquant : (*i*) la formation d'une couche d'oxyde protectrice, (*ii*) l'adsorption des produits de corrosion intermédiaires, (*iii*) la formation d'une couche protectrice interne d'oxyde de magnésium (MgO) avec une superficie augmentant au cours du temps, (*iv*) la rupture de la couche d'oxyde, et (*v*) la croissance latérale des piqûres de corrosion. La caractérisation de la couche d'oxyde a montré la présence d'une couche amorphe contenant une apatite carbonatée et $Mg(OH)_2$.

L'effet du renouvellement quotidien de l'électrolyte, en tant que méthode pour mieux simuler l'homéostasie physiologique, sur la corrosion de l'alliage de Mg WE43 dans le m-SBF a été étudié. Il a été observé que le renouvellement de l'électrolyte

affecte les mécanismes de corrosion en favorisant la dissolution partielle de la couche d'oxyde et en augmentant le transport de masse à travers cette couche, ce qui retarde l'augmentation de la surface recouverte par le film barrière de MgO et l'apparition de la corrosion localisée. Aucune variation significative de la morphologie et la composition de la couche d'oxyde par rapport aux résultats obtenus sans renouvellement d'électrolyte n'a été observée.

L'évolution de la corrosion de l'alliage de Mg WE43 avec une couche de polypyrrole (PPy) dans le m-SBF avec renouvellement quotidien de l'électrolyte a également été étudiée. Il a été observé que la couche de PPy contribue efficacement à la diminution de la vitesse de corrosion de l'alliage de Mg WE43 et de la production du gaz d'hydrogène au cours de la période étudiée. D'autre part, une augmentation temporaire de la résistance à la corrosion après le renouvellement de l'électrolyte a été liée à l'augmentation de la concentration de CO_2 dissous dans le m-SBF. La protection contre la corrosion par la couche de PPy a été attribuée à: (*i*) les propriétés de barrière de la couche PPy, et (*ii*) l'adsorption de molécules de CO_2 sur la couche de PPy, ce qui conduit à une diminution de la conductivité du PPy et à son découplage électrique avec le substrat. Ceci est expliqué en raison d'une charge positive non compensée dans la couche de polypyrrole et du décalage des niveaux de Fermi du substrat et du polypyrrole.

À la fin de cette thèse, des résultats sur le comportement à la corrosion de l'alliage de Mg WE43 dans le m-SBF et dans des conditions d'écoulement continu d'électrolyte sont présentés dans l'annexe. Il est démontré que la présence d'un écoulement continu conduit à une augmentation plus lente de la surface recouverte par

le film barrière de MgO, par rapport à des expériences d'immersion statique, résultant en un taux de corrosion plus élevé. Ces résultats démontrent l'importance du montage expérimentale pour une détermination précise du comportement à la corrosion des alliages de Mg pour des applications biodégradables.

Cette thèse contribue (*i*) à une meilleure compréhension des mécanismes de corrosion de l'alliage de Mg WE43 nu et avec une couche de Ppy dans des conditions expérimentales *in vitro* partiellement ressemblant l'environnement physiologique, et (*ii*) au développement des méthodes expérimentales *in vitro* pour la sélection et le développement de nouveaux alliages de Mg pour des applications biodégradables.

I dedicate this thesis to my parents Artemisa and Rodolfo, my siblings Martha, Cecilia, Miguel, Rodolfo, Susana, Laura and Victor, and my nieces Marlet, Fran and Paula, for their unconditional love and support throughout my life.

ACKNOWLEDGEMENTS

I would like to express my deepest gratitude to Prof. Sasha Omanovic for giving me the opportunity to work under his supervision and for his constant support and guidance along these years. His vast knowledge in the area of electrochemistry and corrosion and his critical thinking had a crucial impact on my learning experience and on the development and completion of this PhD project. I was inspired not only by his scientific skills but also by his human qualities, which made this research journey a very enriching experience.

I would like to sincerely thank Prof. Mihriban Pekguleryuz for her mentoring and support during these years. I was inspired by her vast knowledge in the area of materials science and metallurgy, her commitment to science and her kindness towards collaborators and students.

I would like to thank my former and current colleagues in the Electrochemistry and Corrosion Lab: Saad, Irshad, Arash, Hesam, Diana, Sajad, Mehdi, Nehar, Mark, Saloumeh, Laurent, Jacob, Hediye, Emmanuel, Abraham, Mike, Aqeel, Hawa and Remi for their support and advice, for the stimulating discussions and for all the good times we shared during the past years. My appreciation is extended to the staff members in the Chemical Engineering Department: Lou, Frank, Ranjan, Andrew, Gerald, Melanie, Lisa, Jo-Ann, Emily, Louise and Marcia for all their help and support. I would like to thank my research colleagues in the Prof. Pekguleryuz's group: Mandana, Meltem, Amir and Karan for their useful inputs and valuable comments. Special thanks go to Pierre

Vermette for his assistance in the casting of Mg alloys and his support in any other experimental work.

I would like to express my gratitude to my dear friends Che, Tania, Michael, Jean-Philippe, Laurent, Melanie, Juliette Malgrange, Diogo, Mathias, Danielle, Juliette Belle, Fernando, Yanek, Elis and specially Norma, Marx, Carlos and Eder, thank you for being my family in Montreal and for the unconditional support and motivation.

I would like to sincerely thank my friends in Mexico: Sandra, Eliu, Enrique Michel, Eduardo, Alberto, Belinda and Marco for their support and for being an inspiration to pursue my dreams and not to give up.

My deepest gratitude goes to my parents Artemisa and Rodolfo, my siblings Martha, Cecilia, Miguel, Rodolfo, Susana, Laura and Victor, and my nieces Marlet, Fran and Paula for their unconditional love and support over the years, for being my inspiration and my strength.

Lastly, I gratefully acknowledge the financial support from the Natural Science and Engineering Research Council of Canada (NSERC), the National Council of Science and Technology of Mexico (CONACYT) and MITACS.

TABLE OF CONTENTS

LIST OF FIGURES

LIST OF TABLES

Chapter 1

Introduction and Problem Statement

1.1 INTRODUCTION

Recently, the use of biodegradable materials for temporary implant applications has been suggested, the justification being twofold: 1) the short-term need of an implant to assist in the healing process of diseased or injured tissues and 2) the avoidance of potential long-term complications caused by permanent implants [1, 2]. So far, the development of biodegradable metal-based materials has focused mainly in two applications: biodegradable stents for the treatment of occlusive arterial disease [3] and biodegradable implants to assist with the repair of bone tissue [4]; however, applications in other areas such as tissue engineering [5-7] and soft tissue repair [1, 6, 8, 9] are currently being investigated (Figure 1.1).

Metallic implants are suitable for load bearing applications due to their combination of high mechanical strength and fracture toughness [10]. Currently-approved most-commonly used biomedical metals include stainless steel, titanium-nickel and cobalt-chromium alloys [2]. However, a disadvantage of these materials is the possible release of toxic metallic ions or particles through corrosion or wear processes, leading to inflammatory reactions and decreased implant biocompatibility [4]. Moreover, permanent implant materials are related to long-term complications in cardiovascular and orthopedic applications [3, 11].

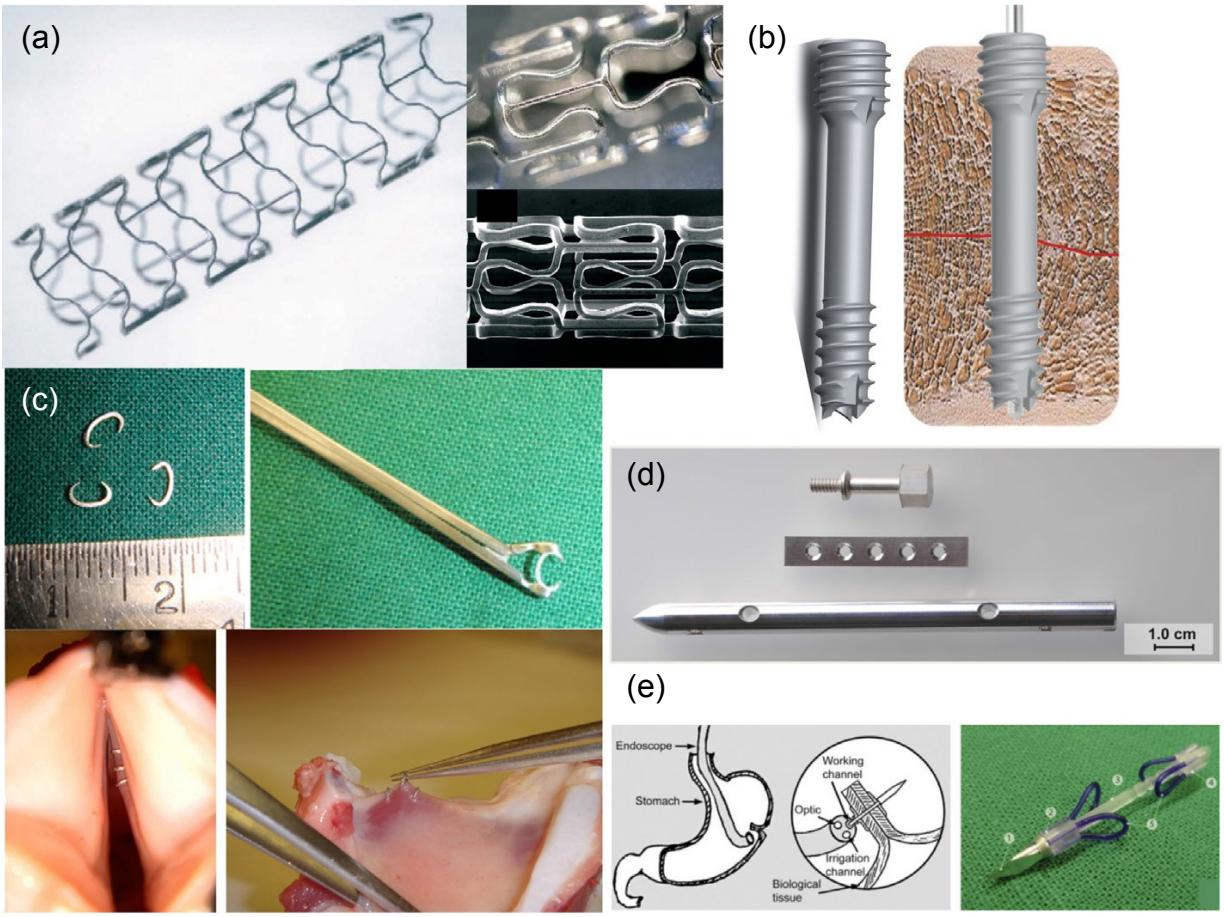

Figure 1.1: Applications of biodegradable magnesium implants: (a) cardiovascular stents, (b) screws, (c) micro-clip for laryngeal microsurgery (pure magnesium), (d) orthopedic implants, and (e) wound closing devices [19].

Cardiovascular disease remains a leading cause of death in industrialized countries [12]. Currently, the first choice treatment of occlusive arterial disease in selected groups includes the placement of a stent (Figure 1.1a) inside the narrowed or blocked artery [13]. Stents, which are small wire mesh devices, provide mechanical support to hold the artery open, allowing for blood flow and preventing further complications such as heart attack [14]. The use of stents has considerably improved the treatment of occlusive arterial disease; however, currently-used stents are

permanent implants that are frequently related to the occurrence of complications such as in-stent restenosis [15, 16]. Restenosis occurs when the treated artery becomes blocked again due to neointimal proliferation (scar tissue growth) [16]. Restenosis occurs as a biological response to injury and is considered to be part of a local and systemic inflammatory response syndrome after stent implantation [13, 16]; this condition is aggravated by the presence of enmeshed wires, which act as a chronic injury/inflammatory stimulus [3]. Additional limitations of permanent stents are long-term endothelial dysfunction, thrombogenicity, difficulties in the treatment of in-stent restenosis due to the presence of a metallic shield at the blockage site and, their inability to adapt to growth, which limit their application in pediatric patients [17].

Regarding orthopedic implants, plates, screws and pins are commonly used to fix bone fractures [4]. However, drawbacks of currently used metallic materials are their higher elastic modulus compared to that of natural bone, leading to stress shielding effects that reduce stimulation of new bone formation, eventually leading to implant loosening and, the need of a second surgery to remove the implant after the tissue has healed, thus increasing health care costs and patient morbidity [4, 11].

It is worth emphasising the *temporary need* of the implants in the previous applications. Cardiovascular stents are needed only for the time required to complete the artery healing process, usually from 6 to 12 months after stent implantation [7], while conventional bone implants are expected to maintain mechanical integrity over a time range of 12 to 16 weeks [7]. In addition, permanently-implanted stents are not suitable for still-growing children. The purpose of biodegradable implants for cardiovascular and orthopedic applications is thus, to provide mechanical support and enhance tissue

healing and regeneration while simultaneously degrading, with the implant eventually being replaced by the newly formed tissue [4, 18]. Most important, biodegradable implants are expected to improve the performance and biocompatibility of cardiovascular and orthopedic implants, avoiding the occurrence of long-term complications [19].

Polymeric and metallic materials have been investigated for the development of biodegradable implants [3, 18, 20, 21]. However, metals are preferred over polymers due to their superior mechanical properties, which make them good candidates for orthopedic and coronary stent applications, where a high strength-to-bulk ratio is required [3, 4, 10, 19]. Among metals, the feasibility of biodegradable iron and magnesium implants has been investigated [19]. *In vivo* experiments suggest that iron can be safely used as a biodegradable material [19, 22-24]; however, some limitations are its slow degradation rate and the risk of local toxicity due to high iron concentrations [1, 19, 25]. Magnesium is an attractive material for biodegradable implants mainly due to its good mechanical properties and good biocompatibility [1]. Mg is an essential element and its importance in many metabolic reactions and physiological functions has been reviewed [3, 26, 27]. Mg depletion is attributed to cardiac arrhythmias, development of atherosclerosis and increased blood pressure [27, 28] and therefore, its slow release during implant degradation can be expected rather to have beneficial effects. Moreover, Mg and its alloys have a similar Young modulus and a favorable compression and tensile strength with respect to the cortical bone, which have encouraged its use in orthopaedic applications [4, 29].

So far, the largest progress in the development of Mg alloy implants has been achieved with cardiovascular stents. The feasibility and safety of biodegradable Mg alloy implants has been demonstrated by *in vivo* experiments [30-35] and clinical trials [36-39]; however, the main limitations of Mg alloy implants remain [3, 19]

(i) their fast corrosion rate in the physiological environment, which leads to premature loss of mechanical properties and implant failure,

(ii) fast production of hydrogen gas during the degradation process leading to subcutaneous gas accumulation, which delays tissue healing, and

(iii) the potential toxicity of some of the alloying elements found in commercially available Mg alloys, whose development has been driven mainly by the needs of the transportation industry.

The corrosion of magnesium is a complex process and various corrosion mechanisms have been proposed [6, 40-42]; however, up to the present date, no agreement regarding the Mg partial corrosion reactions has been reached. The corrosion of Mg in an aqueous environment can be represented as follows [42]:

$2H_2O + 2e^- \rightarrow H_2 + 2OH^-$ (cathodic reaction) (1.1)

$2Mg \rightarrow 2Mg^+ + 2e^-$ (anodic reaction) (1.2)

$2Mg^+ + 2H_2O \rightarrow 2Mg^{2+} + 2OH^- + H_2$ (chemical reaction) (1.3)

$2Mg + 4H_2O \rightarrow 2Mg^{2+} + 4OH^- + 2H_2$ (overall reaction) (1.4)

$Mg^{2+} + 2OH^- \rightarrow Mg(OH)_2$ (product formation) (1.5)

According to the previous reactions, reduction of water (reaction 1.1) and electrochemical and chemical oxidation of Mg (reactions 1.2-1.3) lead to formation of hydrogen gas, Mg^{2+} and OH^- species. Thermodynamic data show that Mg^{2+} is the stable species up to a pH of about 10, above which the formation of a $Mg(OH)_2$ layer occurs (reaction 1.5) [42]. $Mg(OH)_2$ accumulates on the substrate surface forming a protective corrosion layer; however, Mg has a poor corrosion resistance in the presence of metallic impurities or aggressive electrolyte species such as Cl^- ions, which lead to dissolution of the magnesium hydroxide layer and formation of soluble magnesium chloride [43]:

$$Mg(OH)_2 + 2Cl^- \rightarrow Mg^{2+} + 2Cl^- + 2OH^- \quad (1.6)$$

Magnesium and its alloys can suffer different forms of corrosion such as galvanic and pitting [44]. In neutral or alkaline solutions the corrosion of Mg alloys usually takes the form of pitting [42, 44]. Microgalvanic corrosion occurs due to the presence of metallic impurities such as Ni, Fe and Cu, and second phases, which act as cathode sites [42].

The corrosion behaviour of Mg described above allows us to understand the rapid degradation of Mg alloy implants observed *in vivo*. In the physiological environment, with a pH of 6.8-7.4 and a chloride concentration of about 0.15 M, magnesium hydroxide converts into soluble magnesium chloride and Mg alloys can undergo severe pitting corrosion [19, 43]. In addition, the presence of impurities and secondary phases with low hydrogen overpotential lead to fast hydrogen production [41], thus causing considerable galvanic corrosion and subcutaneous gas accumulation [4]. Furthermore, the corrosion behaviour of Mg alloys depends on several parameters

involving the properties of the implant material (e.g., presence of impurities, alloying elements and composition, phase components and microstructure) and environmental factors (e.g., composition of corrosive medium, pH, temperature, biological components and the presence of a flow) [7, 19, 42], making difficult a complete understanding of the corrosion mechanisms *in vivo*.

Current research efforts aim at the development of methods to control the corrosion rate of Mg-based implants and to ideally, tailor the implant degradation rate to specific body applications. Most of these efforts are oriented in two directions: tailoring the composition and microstructure of Mg alloys for improved biocompatibility and targeted corrosion resistance [42] and, the development of protective coatings [45]. However, faster and more efficient development of Mg-based materials is limited by the lack of a complete understanding of the Mg alloy corrosion mechanisms in the real physiological environment and by difficulties at emulating such environment *in vitro*. The corrosion performance of prospect Mg-based materials can be evaluated by *in vivo* and/or *in vitro* experiments [19]. *In vivo* experiments are expensive, time consuming and pose some limitations for the investigation and monitoring of the implant corrosion behaviour [43] and thus, *in vitro* evaluation is usually preferred. However, it has been reported that the corrosion behaviour of Mg alloys observed *in vivo* does not always correlate to the corrosion behaviour observed in *in vitro* experiments for the same alloys [46, 47], which reveals deficiencies in the current *in vitro* methodologies for the evaluation of Mg-based biodegradable materials. Since the corrosion behaviour of Mg alloys depends on the corrosive environment, the observed lack of correlation between *in vivo* and *in vitro* experiments can be attributed to experimental difficulties at

simulating physiological conditions. For instance, the concentration of the implant degradation products, i.e., Mg^{2+} and OH^- species, is regulated *in vivo* by homeostatic processes; however, *in vitro* experiments often report a fast increase in the concentration of these species as a result of the corrosion process, leading to an increase in the electrolyte pH and thus, possibly affecting the Mg alloy corrosion mechanisms and degradation rate. Additional limitations of current *in vitro* methodologies are (i) the absence of relevant physiological ions with an effect on the corrosion behaviour, such as phosphates and carbonates [48-50]; (ii) the lack of an appropriate experimental set-up tailored to specific body applications, e.g., the presence of a flow to simulate physiological shear stress inside the arteries [51]; and (iii) the absence of important biological components in the corrosive medium, such as proteins and cells, which have been shown to influence the degradation process [52, 53]. Therefore, in order to improve the performance of biodegradable Mg-based materials it is necessary to first develop a fundamental understanding of the corrosion mechanisms at experimental conditions that closer resemble the complex nature of the *in vivo* corrosion process and corrosive media the most.

The corrosion behaviour of commercially available and novel Mg alloys has been extensively investigated for their potential use in biodegradable applications, with published studies describing the effect of several parameters on the corrosion behaviour, such as the selection of alloying elements [19, 54], alloy composition [7, 19], microstructure [55-61], electrolyte components [48, 50, 54, 62, 63] and the use of surface pretreatments and protective coatings [45, 64]. However, little information is available regarding the corrosion mechanisms of the investigated Mg alloys in simulated

body fluids [6]. Moreover, Mg and its alloys are very reactive and their corrosion behaviour changes with time, ultimately depending on the protective properties and stability of the corrosion layer formed at the corresponding experimental conditions [6]. Therefore, in order to have a better understanding of the parameters determining the corrosion behaviour of Mg alloys *in vivo*, it is necessary to first understand the time-dependence of the corrosion mechanisms and their relationship to the formation, growth and stability of the corrosion layers formed at experimental conditions simulating the physiological environment.

The aim of this PhD project is threefold:

(i) Investigate the corrosion mechanisms of WE43 Mg alloy in a modified simulated body fluid (m-SBF) for an immersion time up to five days,

(ii) Investigate the effect of electrolyte renewal, as a method to better simulate physiological homeostasis, on the corrosion behaviour of WE43 Mg alloy in m-SBF, and

(iii) Investigate the short-term (up to five days) corrosion behaviour of polypyrrole-coated WE43 Mg alloy in m-SBF with daily electrolyte renewal.

Commercially available WE43 Mg alloy (4 wt.% yttrium, 3 wt.% rare-earths, Mg balance) was selected as a model alloy in this project due to its good corrosion resistance, which led to its use in clinical trials by the company Biotronik (Germany) for the development of biodegradable cardiovascular stents [19, 36]. WE43 Mg alloy is thus an important reference often used as a control in the investigation of the corrosion behaviour of Mg-based biodegradable materials. The m-SBF was selected as corrosive

medium due to the combination of its similar ionic composition to that of blood plasma and higher stability compared to other available simulated body fluids [65]. The m-SBF is buffered with HEPES to better control changes in the electrolyte pH. HEPES is an organic buffering agent widely used in cell culture media and in the investigation of the corrosion behaviour of Mg alloys for biodegradable applications.

As it was already mentioned, a limitation of current *in vitro* methods is the accumulation of corrosion products as a result of the corrosion process, leading to a fast increase in the electrolyte pH and thus, possibly affecting the corrosion behaviour of Mg alloys. Despite the use of buffering agents to control the pH increase as a result of the corrosion process, studies often report an increase in the electrolyte pH to values above the physiological range [66-69]. To address this issue, daily electrolyte renewal was performed by some researchers to avoid the accumulation of corrosion products and control the fast increase in the electrolyte pH, thereby better simulating physiological homeostasis [70-73]. However, the effect of electrolyte renewal on the corrosion behaviour of Mg alloys has not yet been reported. Consequently, in (ii) above, the effect of daily electrolyte renewal, as a method to better simulate physiological homeostasis, on the corrosion behaviour of WE43 Mg alloy in m-SBF was investigated.

An interesting approach to control the corrosion rate of Mg alloys is by developing biocompatible protective coatings [45]. Polypyrrole (PPy) is an electrically-conductive polymer with well-known biocompatibility that offers the possibility of controlled released of a variety of drugs and enzymes, which can be incorporated in the polymer as dopant species [74]. Moreover, PPy has been extensively investigated for the corrosion protection of metals, showing a number of promising corrosion protection

mechanisms [75, 76]. Recently, the potential of PPy coatings to control the corrosion rate of biodegradable Mg implants has been demonstrated [77, 78]; however, little information has been provided on the corrosion behavior of PPy-coated Mg alloys in a simulated body fluid and on the corresponding corrosion mechanisms. Consequently, in (iii) above, PPy coatings were electrochemically synthesized on a WE43 Mg alloy substrate and the corrosion behaviour of the PPy-coated WE43 Mg alloy in m-SBF with daily electrolyte renewal was investigated.

1.2 REFERENCES

[1] M. Peuster, P. Beerbaum, F.W. Bach, H. Hauser, Are resorbable implants about to become a reality?, Cardiology in the Young, 16 (2006) 107-116.

[2] P. Schmutz, Quach-Vu Ngoc-Chang, Gerber, Isabel, Metallic Medical Implants: Electrochemical Characterization of Corrosion Products, in: Interface, 2008, pp. 35-40.

[3] P. Erne, M. Schier, T.J. Resink, The road to bioabsorbable stents: Reaching clinical reality?, CardioVascular and Interventional Radiology, 29 (2006) 11-16.

[4] M.P. Staiger, A.M. Pietak, J. Huadmai, G. Dias, Magnesium and its alloys as orthopedic biomaterials: A review, Biomaterials, 27 (2006) 1728-1734.

[5] M. Yazdimamaghani, M. Razavi, D. Vashaee, L. Tayebi, Development and degradation behavior of magnesium scaffolds coated with polycaprolactone for bone tissue engineering, Materials Letters, 132 (2014) 106-110.

[6] A. Atrens, G.-L. Song, M. Liu, Z. Shi, F. Cao, M.S. Dargusch, Review of Recent Developments in the Field of Magnesium Corrosion, Advanced Engineering Materials, 17 (2015) 400-453.

[7] N. Li, Y. Zheng, Novel Magnesium Alloys Developed for Biomedical Application: A Review, Journal of Materials Science & Technology, 29 (2013) 489-502.

[8] N. Ikeo, R. Nakamura, K. Naka, T. Hashimoto, T. Yoshida, T. Urade, K. Fukushima, H. Yabuuchi, T. Fukumoto, Y. Ku, T. Mukai, Fabrication of a magnesium alloy with excellent ductility for biodegradable clips, Acta Biomaterialia, 29 (2016) 468-476.

[9] A.C. Hänzi, A. Metlar, M. Schinhammer, H. Aguib, T.C. Lüth, J.F. Löffler, P.J. Uggowitzer, Biodegradable wound-closing devices for gastrointestinal interventions: Degradation performance of the magnesium tip, Materials Science and Engineering: C, 31 (2011) 1098-1103.

[10] G. Binyamin, B.M. Shafi, C.M. Mery, Biomaterials: A primer for surgeons, Seminars in Pediatric Surgery, 15 (2006) 276-283.

[11] J. Nagels, M. Stokdijk, P.M. Rozing, Stress shielding and bone resorption in shoulder arthroplasty, Journal of Shoulder and Elbow Surgery, 12 (2003) 35-39.

[12] D. Lloyd-Jones, R. Adams, M. Carnethon, G. De Simone, T.B. Ferguson, K. Flegal, E. Ford, K. Furie, A. Go, K. Greenlund, N. Haase, S. Hailpern, M. Ho, V. Howard, B. Kissela, S. Kittner, D. Lackland, L. Lisabeth, A. Marelli, M. McDermott, J. Meigs, D. Mozaffarian, G. Nichol, C. O'Donnell, V. Roger, W. Rosamond, R. Sacco, P. Sorlie, R. Stafford, J. Steinberger, T. Thorn, S. Wasserthiel-Smoller, N. Wong, J. Wylie-Rosett, Y. Hong, Heart disease and stroke statistics - 2009 update. A report from the American heart association statistics committee and stroke statistics subcommittee, Circulation, 119 (2009) 480-486.

[13] W.J. Gomes, E. Buffolo, Coronary Stenting and Inflammation: Implications for Further Surgical and Medical Treatment, Annals of Thoracic Surgery, 81 (2006) 1918-1925.

[14] U. Sigwart, J. Puel, V. Mirkovitch, F. Joffre, L. Kappenberger, Intravascular stents to prevent occlusion and restenosis after transluminal angioplasty, N Engl J Med, 316 (1987) 701-706.

[15] A. Colombo, M. Ferraro, A. Itoh, G. Martini, S. Blengino, L.E.O. Finci, Results of Coronary Stenting for Restenosis, Journal of the American College of Cardiology, 28 (1996) 830-836.

[16] V. Rajagopal, S.G. Rockson, Coronary restenosis: A review of mechanisms and management, American Journal of Medicine, 115 (2003) 547-553.

[17] B. Heublein, R. Rohde, V. Kaese, M. Niemeyer, W. Hartung, A. Haverich, Biocorrosion of magnesium alloys: A new principle in cardiovascular implant technology?, Heart, 89 (2003) 651-656.

[18] J. Ormiston, M. Webster, Absorbable coronary stents, Lancet, 369 (2007) 1839-1840.

[19] Y.F. Zheng, X.N. Gu, F. Witte, Biodegradable metals, Materials Science and Engineering: R: Reports, 77 (2014) 1-34.

[20] B. O'Brien, W. Carroll, The evolution of cardiovascular stent materials and surfaces in response to clinical drivers: A review, Acta Biomaterialia, 5 (2009) 945-958.

[21] S. Ramcharitar, P.W. Serruys, Fully biodegradable coronary stents: Progress to date, American Journal of Cardiovascular Drugs, 8 (2008) 305-314.

[22] M. Peuster, C. Hesse, T. Schloo, C. Fink, P. Beerbaum, C. von Schnakenburg, Long-term biocompatibility of a corrodible peripheral iron stent in the porcine descending aorta, Biomaterials, 27 (2006) 4955-4962.

[23] M. Peuster, P. Wohlsein, M. Brügmann, M. Ehlerding, K. Seidler, C. Fink, H. Brauer, A. Fischer, G. Hausdorf, A novel approach to temporary stenting: Degradable cardiovascular stents produced from corrodible metal - Results 6-18 months after implantation into New Zealand white rabbits, Heart, 86 (2001) 563-569.

[24] R. Waksman, R. Pakala, R. Baffour, R. Seabron, D. Hellinga, F.O. Tio, Short-term effects of biocorrodible iron stents in porcine coronary arteries, Journal of Interventional Cardiology, 21 (2008) 15-20.

[25] S. Zhu, N. Huang, L. Xu, Y. Zhang, H. Liu, H. Sun, Y. Leng, Biocompatibility of pure iron: In vitro assessment of degradation kinetics and cytotoxicity on endothelial cells, Materials Science and Engineering C, 29 (2009) 1589-1592.

[26] N.E.L. Saris, E. Mervaala, H. Karppanen, J.A. Khawaja, A. Lewenstam, Magnesium: An update on physiological, clinical and analytical aspects, Clinica Chimica Acta, 294 (2000) 1-26.

[27] C. Fox, D. Ramsoomair, C. Carter, Magnesium: its proven and potential clinical significance, Southern medical journal, 94 (2001) 1195-1201.

[28] E.S. Ford, A.H. Mokdad, Dietary Magnesium Intake in a National Sample of U.S. Adults, The Journal of Nutrition, 133 (2003) 2879-2882.

[29] A. Krause, N. Von Der Höh, D. Bormann, C. Krause, F.W. Bach, H. Windhagen, A. Meyer-Lindenberg, Degradation behaviour and mechanical properties of magnesium implants in rabbit tibiae, Journal of Materials Science, 45 (2010) 624-632.

[30] N. Erdmann, N. Angrisani, J. Reifenrath, A. Lucas, F. Thorey, D. Bormann, A. Meyer-Lindenberg, Biomechanical testing and degradation analysis of MgCa0.8 alloy screws: A comparative in vivo study in rabbits, Acta Biomaterialia, 7 (2011) 1421-1428.

[31] Y. He, H. Tao, Y. Zhang, Y. Jiang, S. Zhang, C. Zhao, J. Li, B. Zhang, Y. Song, X. Zhang, Biocompatibility of bio-Mg-Zn alloy within bone with heart, liver, kidney and spleen, Chinese Science Bulletin, 54 (2009) 484-491.

[32] M. Maeng, L.O. Jensen, E. Falk, H.R. Andersen, L. Thuesen, Negative vascular remodelling after implantation of bioabsorbable magnesium alloy stents in porcine coronary arteries: a randomised comparison with bare-metal and sirolimus-eluting stents, Heart, 95 (2009) 241-246.

[33] Y. Ren, J. Huang, B. Zhang, K. Yang, Preliminary study of biodegradation of AZ31B magnesium alloy, Frontiers of Materials Science in China, 1 (2007) 401-404.

[34] F. Witte, J. Fischer, J. Nellesen, C. Vogt, J. Vogt, T. Donath, F. Beckmann, In vivo corrosion and corrosion protection of magnesium alloy LAE442, Acta Biomaterialia, (2009).

[35] F. Witte, V. Kaese, H. Haferkamp, E. Switzer, A. Meyer-Lindenberg, C.J. Wirth, H. Windhagen, In vivo corrosion of four magnesium alloys and the associated bone response, Biomaterials, 26 (2005) 3557-3563.

[36] R. Erbel, C. Di Mario, J. Bartunek, J. Bonnier, B. de Bruyne, F.R. Eberli, P. Erne, M. Haude, B. Heublein, M. Horrigan, C. Ilsley, D. Böse, J. Koolen, T.F. Lüscher, N. Weissman, R. Waksman, Temporary scaffolding of coronary arteries with bioabsorbable magnesium stents: a prospective, non-randomised multicentre trial, Lancet, 369 (2007) 1869-1875.

[37] M. Haude, R. Erbel, P. Erne, S. Verheye, H. Degen, D. Böse, P. Vermeersch, I. Wijnbergen, N. Weissman, F. Prati, R. Waksman, J. Koolen, Safety and performance of the drug-eluting absorbable metal scaffold (DREAMS) in patients with de-novo coronary lesions: 12 month results of the prospective, multicentre, first-in-man BIOSOLVE-I trial, The Lancet, 381 836-844.

[38] P. Peeters, M. Bosiers, J. Verbist, K. Deloose, B. Heublein, Preliminary results after application of absorbable metal stents in patients with critical limb ischemia, Journal of Endovascular Therapy, 12 (2005) 1-5.

[39] R. Waksman, R. Erbel, C. Di Mario, J. Bartunek, B. de Bruyne, F.R. Eberli, P. Erne, M. Haude, M. Horrigan, C. Ilsley, D. Bose, H. Bonnier, J. Koolen, T.F. Luscher, N.J. Weissman, P.-A. Investigators, Early- and long-term intravascular ultrasound and angiographic findings after bioabsorbable magnesium stent implantation in human coronary arteries, Jacc: Cardiovascular Interventions, 2 (2009) 312-320.

[40] A. Atrens, M. Liu, N.I. Zainal Abidin, Corrosion mechanism applicable to biodegradable magnesium implants, Materials Science and Engineering: B, 176 (2011) 1609-1636.

[41] G. Song, A. Atrens, Understanding magnesium corrosion. A framework for improved alloy performance, Advanced Engineering Materials, 5 (2003) 837-858.

[42] G.L. Song, A. Atrens, Corrosion mechanisms of magnesium alloys, Advanced Engineering Materials, 1 (1999) 11-33.

[43] F. Witte, N. Hort, C. Vogt, S. Cohen, K.U. Kainer, R. Willumeit, F. Feyerabend, Degradable biomaterials based on magnesium corrosion, Current Opinion in Solid State and Materials Science, 12 (2008) 63-72.

[44] G.L. Makar, J. Kruger, Corrosion of magnesium, International Materials Reviews, 38 (1993) 138-153.

[45] H. Hornberger, S. Virtanen, A.R. Boccaccini, Biomedical coatings on magnesium alloys – A review, Acta Biomaterialia, 8 (2012) 2442-2455.

[46] W.-D. Mueller, M. Lucia Nascimento, M.F. Lorenzo de Mele, Critical discussion of the results from different corrosion studies of Mg and Mg alloys for biomaterial applications, Acta Biomaterialia, 6 (2010) 1749-1755.

[47] F. Witte, J. Fischer, J. Nellesen, H.A. Crostack, V. Kaese, A. Pisch, F. Beckmann, H. Windhagen, In vitro and in vivo corrosion measurements of magnesium alloys, Biomaterials, 27 (2006) 1013-1018.

[48] Y. Xin, T. Hu, P.K. Chu, Influence of test solutions on in vitro studies of biomedical magnesium alloys, Journal of the Electrochemical Society, 157 (2010) C238-C243.

[49] Y. Xin, T. Hu, P.K. Chu, Degradation behaviour of pure magnesium in simulated body fluids with different concentrations of, Corrosion Science, 53 (2011) 1522-1528.

[50] Y. Xin, K. Huo, H. Tao, G. Tang, P.K. Chu, Influence of aggressive ions on the degradation behavior of biomedical magnesium alloy in physiological environment, Acta Biomaterialia, 4 (2008) 2008-2015.

[51] J. Levesque, H. Hermawan, D. Dube, D. Mantovani, Design of a pseudo-physiological test bench specific to the development of biodegradable metallic biomaterials, Acta Biomaterialia, 4 (2008) 284-295.

[52] W.D. Mueller, M.F. Lorenzo De Mele, M.L. Nascimento, M. Zeddies, Degradation of magnesium and its alloys: Dependence on the composition of the synthetic biological media, Journal of Biomedical Materials Research - Part A, 90 (2009) 487-495.

[53] R. Rettig, S. Virtanen, Time-dependent electrochemical characterization of the corrosion of a magnesium rare-earth alloy in simulated body fluids, Journal of Biomedical Materials Research - Part A, 85 (2008) 167-175.

[54] Y. Chen, Z. Xu, C. Smith, J. Sankar, Recent advances on the development of magnesium alloys for biodegradable implants, Acta Biomaterialia, 10 (2014) 4561-4573.

[55] S. Amira, D. Dubé, R. Tremblay, E. Ghali, Influence of the microstructure on the corrosion behavior of AXJ530 magnesium alloy in 3.5% NaCl solution, Materials Characterization, 59 (2008) 1508-1517.

[56] H.R.B. Rad, M.H. Idris, M.R.A. Kadir, S. Farahany, Microstructure analysis and corrosion behavior of biodegradable Mg–Ca implant alloys, Materials & Design, 33 (2012) 88-97.

[57] G. Song, A. Atrens, M. Dargusch, Influence of microstructure on the corrosion of diecast AZ91D, Corrosion Science, 41 (1998) 249-273.

[58] E. Zhang, D. Yin, L. Xu, L. Yang, K. Yang, Microstructure, mechanical and corrosion properties and biocompatibility of Mg-Zn-Mn alloys for biomedical application, Materials Science and Engineering C, 29 (2009) 987-993.

[59] G. Song, D. StJohn, The effect of zirconium grain refinement on the corrosion behaviour of magnesium-rare earth alloy MEZ, Journal of Light Metals, 2 (2002) 1-16.

[60] Y. Song, E.-H. Han, D. Shan, C.D. Yim, B.S. You, The role of second phases in the corrosion behavior of Mg–5Zn alloy, Corrosion Science, 60 (2012) 238-245.

[61] Y. Song, D. Shan, R. Chen, E.-H. Han, Effect of second phases on the corrosion behaviour of wrought Mg–Zn–Y–Zr alloy, Corrosion Science, 52 (2010) 1830-1837.

[62] Z. Li, G.-L. Song, S. Song, Effect of bicarbonate on biodegradation behaviour of pure magnesium in a simulated body fluid, Electrochimica Acta, 115 (2014) 56-65.

[63] Y. Xin, T. Hu, P.K. Chu, In vitro studies of biomedical magnesium alloys in a simulated physiological environment: A review, Acta Biomaterialia, 7 (2011) 1452-1459.

[64] H.Y. Yang, X.B. Chen, X.W. Guo, G.H. Wu, W.J. Ding, N. Birbilis, Coating pretreatment for Mg alloy AZ91D, Applied Surface Science, 258 (2012) 5472-5481.

[65] A. Oyane, H.M. Kim, T. Furuya, T. Kokubo, T. Miyazaki, T. Nakamura, Preparation and assessment of revised simulated body fluids, Journal of Biomedical Materials Research - Part A, 65 (2003) 188-195.

[66] T. Lei, W. Tang, S.-H. Cai, F.-F. Feng, N.-F. Li, On the corrosion behaviour of newly developed biodegradable Mg-based metal matrix composites produced by in situ reaction, Corrosion Science, 54 (2012) 270-277.

[67] X. Gu, Y. Zheng, Y. Cheng, S. Zhong, T. Xi, In vitro corrosion and biocompatibility of binary magnesium alloys, Biomaterials, 30 (2009) 484-498.

[68] X. Gu, Y. Zheng, S. Zhong, T. Xi, J. Wang, W. Wang, Corrosion of, and cellular responses to Mg-Zn-Ca bulk metallic glasses, Biomaterials, 31 (2010) 1093-1103.

[69] M. Bornapour, N. Muja, D. Shum-Tim, M. Cerruti, M. Pekguleryuz, Biocompatibility and biodegradability of Mg–Sr alloys: The formation of Sr-substituted hydroxyapatite, Acta Biomaterialia, 9 (2013) 5319-5330.

[70] A. Yamamoto, S. Hiromoto, Effect of inorganic salts, amino acids and proteins on the degradation of pure magnesium in vitro, Materials Science and Engineering C, 29 (2009) 1559-1568.

[71] A.C. Hänzi, I. Gerber, M. Schinhammer, J.F. Löffler, P.J. Uggowitzer, On the in vitro and in vivo degradation performance and biological response of new biodegradable Mg-Y-Zn alloys, Acta Biomaterialia, 6 (2010) 1824-1833.

[72] N. Kirkland, J. Waterman, N. Birbilis, G. Dias, T.F. Woodfield, R. Hartshorn, M. Staiger, Buffer-regulated biocorrosion of pure magnesium, Journal of Materials Science: Materials in Medicine, 23 (2012) 283-291.

[73] J.E. Gray-Munro, C. Seguin, M. Strong, Influence of surface modification on the in vitro corrosion rate of magnesium alloy AZ31, Journal of Biomedical Materials Research - Part A, 91 (2009) 221-230.

[74] R. Balint, N.J. Cassidy, S.H. Cartmell, Conductive polymers: Towards a smart biomaterial for tissue engineering, Acta Biomaterialia, 10 (2014) 2341-2353.

[75] P. Deshpande, N. Jadhav, V. Gelling, D. Sazou, Conducting polymers for corrosion protection: a review, J Coat Technol Res, 11 (2014) 473-494.

[76] M. Rohwerder, Conducting polymers for corrosion protection: a review, International Journal of Materials Research, 100 (2009) 1331-1342.

[77] M.C. Turhan, D. Rückle, M.S. Killian, H. Jha, S. Virtanen, Corrosion Behavior of Polypyrrole/AZ91D in Simulated Body Fluid Solutions and Its Functionalization with Albumin Monolayers, Corrosion, 68 (2012) 536-547.

[78] M.C. Turhan, M. Weiser, H. Jha, S. Virtanen, Optimization of electrochemical polymerization parameters of polypyrrole on Mg–Al alloy (AZ91D) electrodes and corrosion performance, Electrochimica Acta, 56 (2011) 5347-5354.

Chapter 2

Background and literature review

2.1 AN OVERVIEW OF Mg BIODEGRADABLE IMPLANTS

The first use of Mg as a biomedical material goes back to 1878, when Huse used some Mg wires as ligatures to stop bleeding vessels of three human patients [1]. In the years following, different investigations in animals and humans reported the use of Mg-based materials for wire ligatures, intestinal and vessel connectors, rods, plates, screws, sutures, anodes for implantable batteries and intravascular wires [1]. However, due to the high reactivity of Mg and its observed high corrosion rate *in vivo*, its use in biomedical applications was soon replaced by more corrosion resistant materials such as stainless steel [1]. Recently, the use of Mg as potential material for biodegradable applications has gained renewed interest as a result of the development of new Mg alloys with improved corrosion resistance and mechanical properties, mainly driven by the needs of the transportation industry [2].

The use of biodegradable materials for temporary implants has recently been suggested as an alternative to avoid complications caused by permanent implants. Metallic implants are suitable for load bearing applications due to their combination of high mechanical strength and fracture toughness. Currently approved most-commonly used biomedical metals include stainless steel, titanium-nickel and cobalt-chromium alloys. However, a disadvantage of these materials is the possible release of toxic metallic ions or particles through corrosion or wear processes [3], leading to inflammatory reactions and decreased implant biocompatibility. Moreover, permanent

implant materials are related to long-term complications in cardiovascular and orthopedic applications, such as restenosis, thrombosis and stress shielding effects [4, 5]. So far, the development of biodegradable materials has focused mainly in two applications: biodegradable stents for the treatment of occlusive arterial disease and biodegradable implants to assist with the repair of bone tissue; however, applications in other areas such as tissue engineering [6] and soft tissue repair are currently being investigated.

2.1.1 Cardiovascular applications

2.1.1.1 Percutaneous coronary intervention

Coronary artery disease (CAD) is a leading cause of mortality worldwide [7]. CAD is often a manifestation of atherosclerosis, a progressive narrowing process of the artery caused by abnormal plaque deposition in the vessel wall [8]. Atherosclerotic plaque limits blood flow and may by erosion or rupture become unstable, eventually leading to thrombosis and heart attack [9].

Percutaneous coronary intervention (PCI) and stenting is currently the first choice for treatment of CAD in selected groups [10], Figure 2.1. Stents are small wire mesh devices used to provide mechanical support and prevent the shrinkage of the arterial wall diameter (negative remodelling) [10, 11]. During this procedure a catheter inserted into the artery, usually in the groin, is conducted to the narrowed site where a balloon tip covered with a stent is inflated. The balloon tip expands the stent and compresses the plaque allowing for improved blood flow. Once the stent is in place, the balloon is deflated and withdrawn (Figure 2.1).

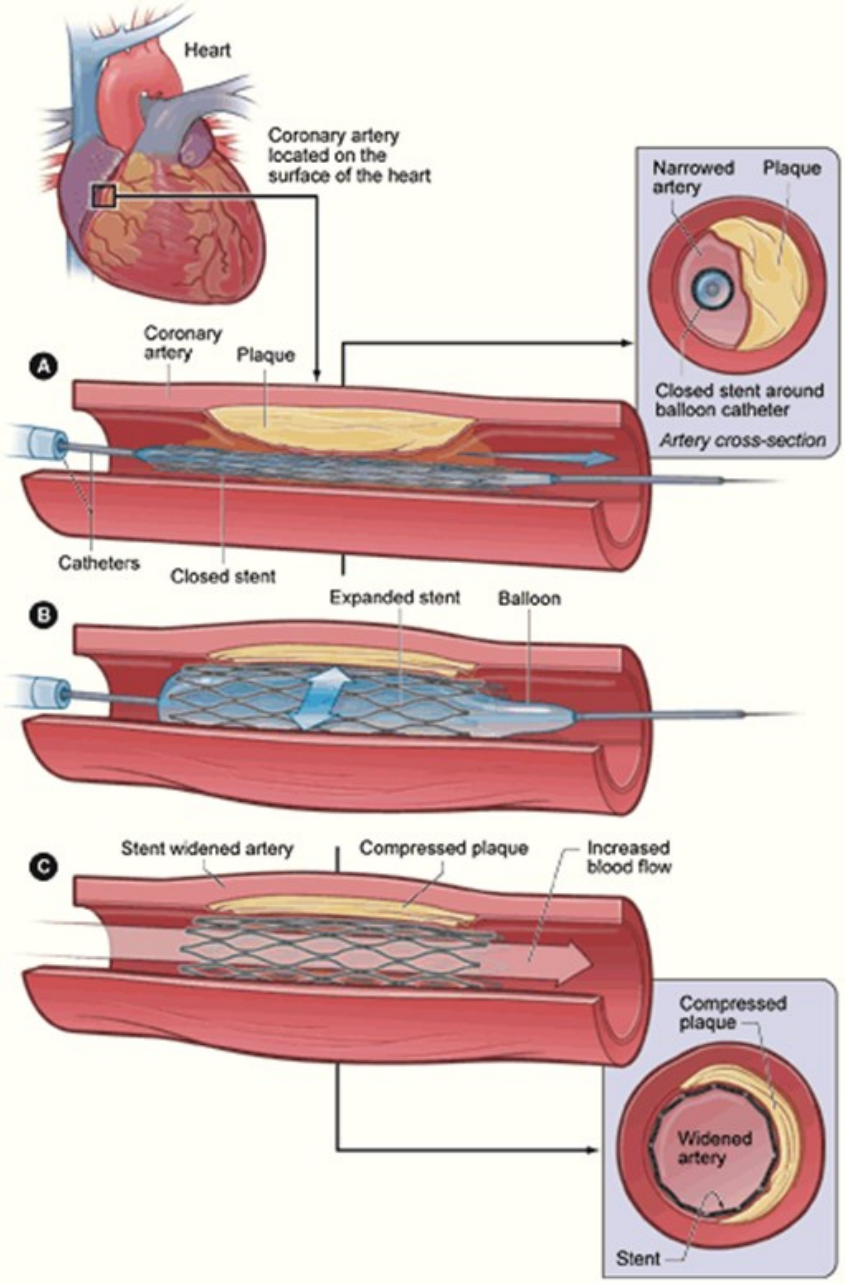

Figure 2.1: Deployment of a stent in a coronary artery with plaque build-up. (A) Insertion of deflated balloon catheter with closed stent, (B) balloon inflation, stent expansion and plaque compression and, (C) normal blood flow restored after stent deployment. Cross sections show the artery before and after stent deployment [12].

Although the use of stents has proven effective in treating coronary and peripheral arterial occlusions, recurrence of arterial narrowing due to in-stent restenosis

(ISR) is still frequent [4]. Restenosis limits the benefits of PCI in many patients, particularly those with diabetes or multi-vessel coronary artery disease [13].

2.1.1.2 Restenosis

The principal limitation of percutaneous coronary intervention is the recurrence of arterial narrowing after treatment, a condition known as *restenosis*. Although the introduction of coronary stents has reduced the incidence of restenosis by providing mechanical support, in-stent restenosis (ISR) still occurs in 20% to 30% of stented vessels (Figure 2.2) [13]. Restenosis, which occurs due to arterial negative remodelling (shrinkage of the arterial wall diameter) and neointimal proliferation (tissue growth inside the artery), is considered a vascular manifestation of the biological response to injury [14]. The high pressure technique of stent deployment triggers an exaggerated tissue repair process as a consequence of trauma [10, 14]. This condition is aggravated by the presence of enmeshed wires which act as a chronic injury/inflammatory stimulus [14].

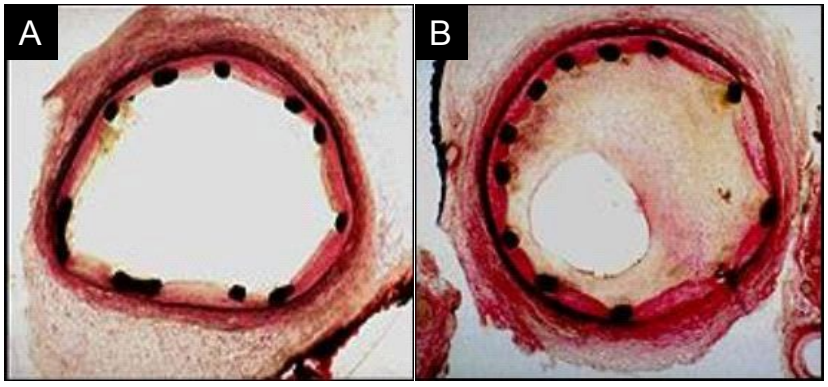

Figure 2.2: Cross-section of coronary artery (A) immediately after implantation of a bare metal stent and (B) six months after implantation of a bare metal stent, showing significant in-stent restenosis [15].

Although many therapies have been developed to manage ISR, its treatment is extremely difficult. The most promising techniques are brachytherapy and drug eluting stents (DES), which target neointimal proliferation [14]. Brachytherapy is based in the use of intracoronary radiation to decrease smooth muscle cell mitosis [13]. This technique has been found to reduce restenosis to 10-15% [14], however the procedure is expensive, requires the services of a radiation oncologist and has been related to deleterious effects such as late thrombosis [13]. The concept of DES is based in the use of stents as vehicles for local intracoronary drug delivery to reduce inflammation and smooth muscle cell replication and migration [16, 17]. A DES generally consists of a metallic stent coated with a thin polymer layer containing the drug [17]. The use of DES has been reported to reduce ISR to 4-15% [14]. However DES have been related to other specific complications such as endothelial dysfunction and late thrombosis associated with the permanent presence of the polymer carrier [10, 18, 19]. This has motivated the use of biodegradable polymer coatings or non-polymeric surfaces for direct loading of drugs [18].

Difficulties in the treatment of ISR and additional drawbacks of permanent implants such as physical irritation, long-term endothelial dysfunction, thrombogenicity, chronic inflammation, disadvantageous characteristics for later surgical revascularization and inability to adapt to growth [20], have limited the more wide spread use of metallic stents.

2.1.1.3 Development of biodegradable Mg stents

The development of biodegradable stents has been suggested as an alternative to avoid the long-term side effects of permanent implants. As biodegradable stents are expected to “fulfill their mission and step away”, their mechanical properties as a function of the degradation time and the nature of the degradation process have to be considered [21]. Ideally, a biodegradable stent will maintain its mechanical properties during the degradation process until the physiological arterial remodelling (after stenting) will be completed, from 6 to 12 months after stent implantation. In addition, the degradation process *in vivo* should not clinically induce negative side effects on the physiology or health of the patient, e.g. must not generate toxic effects or block vessels, and corrosion products should be eliminated by the conventional physiological mechanisms [21].

Polymers such as polylactic acid and polyglycolic acid, and metals such as iron and magnesium have been investigated for the development of biodegradable stents. However, polymers have inferior mechanical properties compared to metals [14] and their relatively bulkiness may limit their use in small vessels such as the coronary arteries [20]. For example, they cannot be used to treat calcified plaque (or blood vessels). Animal studies [22-24] suggest that iron can be safely used as a biodegradable material; however, some limitations are its slow degradation rate [22] and the risk of local toxicity [25].

The largest progress in the development of biodegradable Mg alloy implants has been achieved with cardiovascular stents (Figure 2.3). *In vivo* experiments [20, 26-31]

and clinical trials [32-34] demonstrated the feasibility and safety of biodegradable Mg alloy stents. In the first clinical study of biodegradable coronary stents (PROGRESS-AMS), WE43 Mg alloy stents from the company Biotronik (Germany) were implanted in 63 patients with lesions in the coronary arteries [33, 34]. Observed re-narrowing of the treated arteries was related to neointima proliferation (scar tissue growth) and arterial negative remodelling (arterial shrinking), indicating a limited implant biocompatibility and premature loss of the implant mechanical properties. The latest generation of biodegradable Mg alloy stents (DREAMS) from the company Biotronik consisting of a drug-eluting biodegradable Mg stent is still under clinical trials [35]. The challenge is to develop degradable stents capable of retaining their mechanical properties long enough to avoid vessel recoil and that trigger a minimum local inflammatory/immunological response during the degradation process.

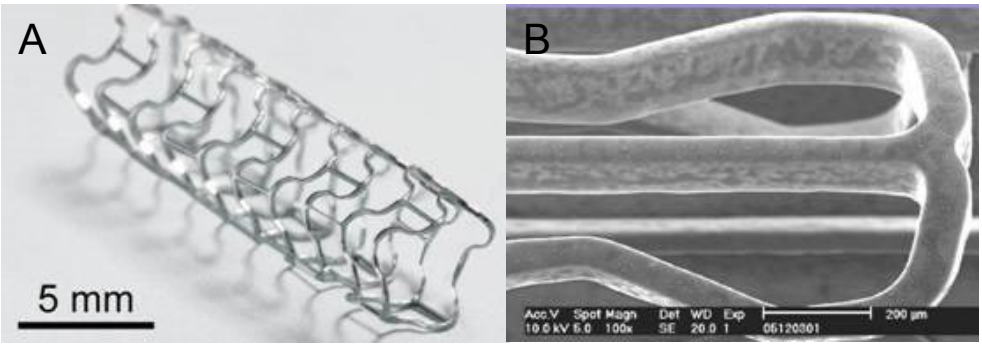

Figure 2.3. (A) Biodegradable WE43 Mg alloy stent fabricated by the company Biotronik and (B) SEM image of the same stent [36].

2.1.2 Orthopaedic applications

Metallic implants made of stainless steel, Ti-alloys, and Co-Cr alloys are widely used in orthopaedic applications to assist with the repair or replacement of bone tissue, e.g.,

plates, screws and pins to fix fractures [37]. These alloys possess good mechanical strength, which is required for load bearing applications; however, their mechanical properties are not well matched with those of natural bone tissue, leading to stress shielding effects that reduce stimulation of new bone formation and remodelling, eventually leading to implant loosening [5]. In addition, removal of permanent implants after the tissue has healed requires a second surgery, which increases health care costs and patient morbidity [38].

Magnesium has mechanical properties comparable to those of human bone and it has shown stimulatory effects on the growth of new bone tissue, which makes it an attractive material for orthopaedic applications. Magnesium has a Young modulus and compressive yield strength closer to natural bone compared to other metallic materials, while its fracture toughness is greater than that of ceramic biomaterials such as hydroxyapatite (Table 2.1) [39]. Regarding fracture treatment, Mg alloys would have the advantage of providing an adapted stabilization depending on its degradation state, thus improving the physiological stimulation of the bone tissue and the healing process [40]. Mg biodegradable implants are expected to maintain their mechanical properties for a time range of 12-18 weeks, eventually being replaced by natural bone tissue [39].

Recent studies suggest a positive role of Mg on the bone cell attachment and tissue growth, probably by promoting precipitation of biologically equivalent apatite ($(Ca_{1-x}Mg_x)_{10}(PO_4)_6OH_2$) [41, 42]. Although several studies have shown the potential of Mg alloys for orthopaedic applications [40, 43-48], control of the implant corrosion rate in the physiological environment, optimization of the implant osseointegration (implant

ability to integrate with bone tissue) and thorough evaluation of the Mg alloys biocompatibility are still required.

Table 2.1: Physical and mechanical properties of various implant materials in comparison to bone [39].

Properties	Natural bone	Magnesium	Ti alloy	Co-Cr alloy	Stainless steel	Synthetic hydroxyapatite
Density (g cm^{-3})	1.8-2.1	1.74-2.0	4.4-4.5	8.3-9.2	7.9-8.1	3.1
Young's modulus (GPa)	3-20	41-45	110-117	230	189-205	73-117
Compressive yield strength (MPa)	130-180	65-100	758-1117	450-1000	170-310	600
Fracture toughness (MPa $m^{1/2}$)	3-6	15-40	55-115	N/A	50-200	0.7

2.2 CORROSION OF Mg AND Mg ALLOYS

Magnesium alloys have a high strength/weight ratio and their development over the last 40 years has been motivated mainly because of their wide applications in the aerospace and transportation industries [49]. The designation system of magnesium alloys generally follows the nomenclature of the American Society for Testing and Materials (ASTM) [50]. In this nomenclature the first two letters identify the two most important alloying elements in the alloy, according to Table 2.2, and the next two digits indicate the nominal concentrations of the alloying elements in wt. %. Thus, WE43 is an alloy nominally containing 4% yttrium and 3% rare earth elements. Magnesium alloys can be divided into three major groups: pure magnesium with traces of other elements, aluminum containing alloys (AZ91, AZ21, AZ31, AE21, LAE442, etc.) and Al-free alloys (WE43, ZE41, Mg-Mn-Zn, Mg-Ca, etc.) [51, 52].

Table 2.2: ASTM codes for identifying alloying elements in Mg alloys [50].

Alloying element	Code
Aluminum	A
Calcium	X
Rare earth	E
Copper	C
Iron	F
Lithium	L
Manganese	M
Nickel	N
Silicon	S
Strontium	J
Yttrium	W
Zinc	Z
Zirconium	K

The corrosion of Mg and Mg alloys has been extensively reviewed [49, 51, 53, 54]. The understanding of the corrosion processes of Mg alloys builds on the understanding of the corrosion of pure magnesium [54]. In aqueous environments magnesium corrosion occurs through electrochemical reaction with water producing magnesium hydroxide and hydrogen gas (reaction 2.1). It has been shown that magnesium corrosion is relatively insensitive to the oxygen concentration [55]. The overall corrosion reaction of magnesium in aqueous environments can be expressed as:

$$Mg + 2H_2O \rightarrow Mg(OH)_2 + H_2 \quad (2.1)$$

The corrosion of Mg is a complex process and different mechanisms have been proposed [49, 56]. In a simplified manner, the overall reaction may be expressed as the sum of the following partial reactions:

$$Mg \rightarrow Mg^{2+} + 2e^{-} \quad \text{(anodic reaction)} \quad (2.2)$$

$$2H_2O + 2e^{-} \rightarrow H_2 + 2OH^{-} \quad \text{(cathodic reaction)} \quad (2.3)$$

$$Mg^{2+} + 2OH^{-} \rightarrow Mg(OH)_2 \quad \text{(product formation)} \quad (2.4)$$

Magnesium has a standard electrode potential (Mg^{+2}/Mg) of -2.37 V vs. NHE and its corrosion potential is usually about -1.7 V vs. NHE in aqueous solutions [54]. The difference in these values is due to the formation of a magnesium hydroxide film, which acts as a protective layer over a wide pH range [54]. The thermodynamic behaviour of magnesium in aqueous solution is described by the Pourbaix diagram (Figure 2.4), which shows that Mg^{2+} is the stable species up to a pH of about 10, above which the formation of a stable $Mg(OH)_2$ layer occurs.

Magnesium hydroxide accumulates on the Mg surface as a corrosion protective layer in water; however, Mg has a poor corrosion resistance in the presence of metallic impurities or aggressive electrolyte species such as Cl^- ions [49], which lead to dissolution of the magnesium hydroxide layer and formation of soluble magnesium chloride. Magnesium and its alloys can suffer a number of different forms of corrosion such as galvanic, pitting and localized corrosion [49]. The hydroxide film on magnesium is much less stable than the passive films formed on metals such as aluminum and stainless steel, and provides only poor pitting resistance [54]. Thus, the corrosion of Mg alloys in neutral or alkaline solutions typically takes the form of pitting [49].

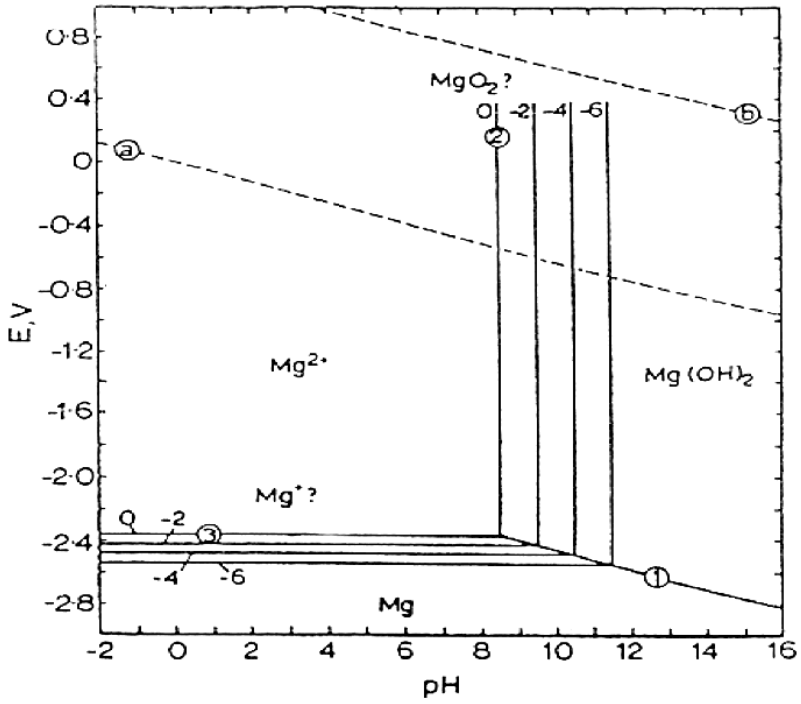

Figure 2.4: Pourbaix diagram for the Mg-H_2O system at 25 ºC [49]. The region of water stability lies between the lines marked (a) and (b). The different regions are separated by the following reactions: (1) $Mg + 2H_2O \rightarrow Mg(OH)_2 + H_2$; (2) $Mg^{2+} + H_2O \rightarrow MgO + 2H^+$; (3) $Mg \rightarrow Mg^{2+} + 2e^-$.

Magnesium is an active metal (Figure 2.5) and thus, Mg alloys are highly susceptible to galvanic corrosion, which is usually observed as localized corrosion near cathodic regions. Macrogalvanic corrosion occurs when magnesium is coupled with another metal (less active). Microgalvanic corrosion occurs due to the presence of metallic impurities, such as Ni, Fe and Cu, and second phases acting as cathodes [54].

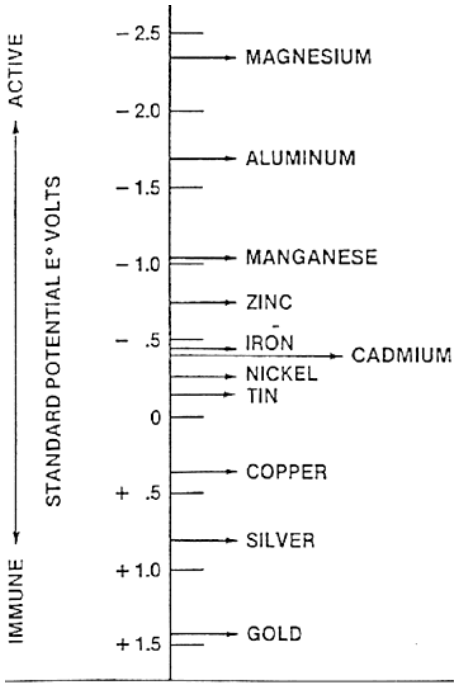

Figure 2.5: Standard electromotive force series [49].

The corrosion behaviour of a metal highly depends on the properties of its corrosion layer. However, the nature of the corrosion layer formed on Mg is still not well understood [49]. The composition and structure of the corrosion layers formed on Mg and Mg alloys has been investigated, showing the presence of MgO and $Mg(OH)_2$ [57-60]. McIntyre et al. [57] observed that corrosion of pure Mg under atmospheric ambient conditions led to formation of a MgO film with a thickness of ca. 2.2 nm after 10 s of exposure. A logarithmic oxide film growth was observed at longer immersion times, with the inclusion of water molecules leading to formation of a hydrated corrosion layer. Nordlien et al. [58, 59, 61] investigated the morphology and structure of Mg oxides formed on pure Mg and Mg-Al alloys by exposure to water. They observed the presence of a three layer-structure, for both pure Mg and Mg-Al alloys, characterized by a hydrated globular inner layer (0.4-0.6 μm), a thin and dense intermediate region (20-40

nm) and a platelet-like outer region (1.8-2.2 μm). They reported that electron beam irradiation during observation led to dehydration of the innermost layer and formation of crystalline MgO zones, while no structural or morphological changes were observed for the dense and platelet-like outer layers. According to a model proposed by Baril et al. [60] to describe the corrosion of pure Mg in Na_2SO_4 solutions, Mg corrosion is controlled by the presence of an inner thin MgO film, with corrosion occurring only at film-free areas. Both the MgO and the film free areas are covered by a thick porous layer of $Mg(OH)_2$. Investigations of the initial film growth on pure Mg by XPS showed the presence of a bilayer structure consisting of an ultra-thin MgO inner layer (ca. 2.5 nm) and a $Mg(OH)_2$ external layer [62, 63].

The corrosion behaviour of Mg described above allows us to understand the rapid corrosion rate of Mg alloys *in vivo*. In the physiological environment, with a pH of 6.8-7.4 and a chloride concentration of about 150 mmol L^{-1}, magnesium hydroxide converts into soluble magnesium chloride and Mg alloy implants can undergo severe pitting corrosion [51]. Pitting of magnesium is observed for Cl^- concentrations above 30 mmol L^{-1} [39]. In addition, the presence of impurities and secondary phases with low hydrogen overpotential leads to fast hydrogen production, thus causing considerable galvanic corrosion and subcutaneous gas accumulation [39].

2.2.1 Negative difference effect (NDE)

Mg and Mg alloys exhibit an abnormal electrochemical behaviour during anodic polarization experiments, a phenomenon known as the negative difference effect [49]. According to the electrochemical theory, anodic polarization leads to an increase in the

anodic reaction rate and a simultaneous decrease in the cathodic reaction rate, i.e., hydrogen evolution reaction. However, in the case of Mg a different behaviour has been observed experimentally; an increase in anodic potential leads to an increase in both the corrosion rate and the hydrogen evolution rate [49, 64]. Additionally, it has been observed that during anodic polarization Mg dissolution occurs faster than expected according to electrochemical theory. In order to explain this contradictory behaviour, four different corrosion mechanisms have been proposed [49]:

1) *Partially protective surface film model.* The NDE is attributed to the presence of a partially protective corrosion layer, which breaks down during anodic polarization, leading to an increase in both the corrosion rate and hydrogen evolution [49, 65].
2) *Mono-valent magnesium ion model.* Since the calculated valence of dissolved Mg has been reported to be in the range from 1.33 to 1.66 [49, 66], the presence of a monovalent magnesium intermediate (Mg^+) has been proposed. This Mg species is produced electrochemically and reacts chemically to produce hydrogen, according to the following equations:

   $$Mg \rightarrow Mg^+ + e^- \quad (2.5)$$

   $$2Mg^+ + 2H^+ \rightarrow 2Mg^{2+} + H_2 \quad (2.6)$$

   Therefore, anodic polarization would lead to an increase in the production of monovalent Mg species and consequently, in the hydrogen evolution rate.
3) *Particle undermining model.* The observed higher than expected corrosion rate is related to the undermining and falling away of second phase particles, which lead to accelerated local corrosion of the surrounding Mg matrix by a galvanic effect

[49, 53]. This results in a mass loss higher that predicted by electrochemical theory.

4) *Magnesium Hydride (MgH_2) model.* It is proposed that MgH_2 formed on the metal surface reacts with water producing Mg^{2+} and H_2, according to the following equation [49, 67]:

$$MgH_2 + 2H_2O \rightarrow Mg^{2+} + 2OH^- + 2H_2 \quad (2.7)$$

Although thermodynamic data predict the stability of MgH_2 and its formation has been proved experimentally [49], this model is in contradiction with electrochemical theory. Since reaction 2.7 is a cathodic reaction, it is expected that anodic polarization would decrease the production rate of hydrogen, which is contrary to the observed experimental behaviour [49].

Recently, Song et al. [49] proposed a new mechanism that combines models 1 and 2 to explain the NDE. According to this mechanism, at corrosion layer-free regions Mg is oxidized to form monovalent Mg intermediates (reaction 5), which then react with water to produce Mg^{2+} and hydrogen, according to the following equation:

$$2Mg^+ + 2H_2O \rightarrow 2Mg^+ + 2OH^- + H_2 \quad (2.8)$$

It is proposed that anodic polarization increases the corrosion layer-free area and thus, an increase in the dissolution of Mg and the production of hydrogen gas is observed.

2.2.2 Metallurgical factors

The corrosion behaviour of Mg and Mg alloys depends on their metallurgy and environmental factors [49]. Metallurgical parameters that have an influence on the corrosion behaviour of Mg alloys include impurity and alloying elements, phase

components and microstructure. Metallurgical manipulation is a conventional approach towards overcoming corrosion problems and provides an effective way to improve the corrosion resistance of magnesium alloys [49].

2.2.2.1 Impurity elements

The corrosion resistance of Mg alloys can be increased by reducing the content of impurity elements such as iron (Fe), copper (Cu), nickel (Ni) and cobalt (Co) [49]. These elements have been found to accelerate the corrosion rate of Mg 10 - 100 fold due to their low solid-solubility limits and because they provide active cathodic sites. Other impurity elements with a more moderate effect on the corrosion rate include silver (Ag), calcium (Ca) and zinc (Zn) [49]. For each of these impurities a tolerance limit can be defined, Cu is limited to 100-300 ppm, Fe to 35-50 ppm and Ni to 20-50 ppm [51]. Different alloys have different tolerance limits because the tolerance limits are influenced by the presence of third elements [54]. For biodegradable implant applications, the amount of these impurities has to be strictly controlled. In addition, Ni should be avoided due to its toxic properties [51].

2.2.2.2 Alloying elements

Common alloying elements of Mg alloys investigated for biodegradable applications include Al, Mn, Zn, Ca, Li, Zr, Y and rare earths [20, 27, 31-33, 39, 40, 43, 51, 68-70]. These elements influence the mechanical, physical and corrosion properties of Mg alloys [51]. They can react with magnesium or among each other to form intermetallic phases which enhance the alloy's strength. In addition, they contribute to corrosion resistance by reducing the effect of impurities, improving the corrosion resistance of the

surface film or increasing grain refinement [49]. The reasons for the use of some of these elements in Mg alloys were reviewed by Song and Witte [49, 51]. Al induces the precipitation of a corrosion resistant phase and increases the corrosion resistance of the hydroxide film formed on the surface. Mn itself does not improve the corrosion resistance, but it reduces the harmful effects of impurities. Zn can increase the tolerance limits and reduce the effect of impurities once the tolerance limit has been exceeded. Zr improves corrosion performance by precipitation of metallic impurities such as Fe and Ni, and is an effective grain refiner agent in Al-free Mg alloys. Ca contributes to solid solution strengthening. RE can strengthen the material by solid solution strengthening and precipitation strengthening, forming intermetallic phases that act as obstacles for the dislocation movement at high temperatures [51]. Furthermore, RE favor the formation of protective corrosion films, which increase the stability of the alloy surface [71]. However, some of these elements are not suitable for biodegradable Mg alloys due to their toxic nature [51, 72]. Elements with potential toxicological problems should be avoided in the design of biodegradable materials, and they should be only used in minimal acceptable amounts if they cannot be excluded from the design [52]. So far, only a small amount of elements that can be tolerated in the human body and can also retard the biodegradation rate of Mg alloys has been considered, namely Sr, Ca, Zn, Mn and perhaps a very small amount of low toxicity rare earth elements [72-74].

2.2.2.3 Phase components and microstructure

The presence of intermetallic phases has an important influence on the corrosion of magnesium alloys [49]. The presence of secondary phases may reduce the corrosion

resistance of the alloy in two ways: 1) by their action as cathodes, accelerating the corrosion of the α-matrix and, 2) by the depletion of alloying elements from the matrix, which results in a less protective surface [71]. As an example, AZ91 alloy usually contains a large fraction of β-phase ($Mg_{17}Al_{12}$) precipitated along the grain boundaries (Figure 2.6). $Mg_{17}Al_{12}$ exhibits a passive behaviour over a wide pH range, was found to be inert to a chloride solution in comparison to the surrounding magnesium matrix, acted as a corrosion barrier and its distribution determined the corrosion resistance of Mg-Al alloys [49]. However, it has been found that β-phase acts as an efficient cathode, increasing the alloy corrosion by a galvanic effect [75]. Song et al. [76] suggested that the β-phase serves as a galvanic cathode and accelerates the alloy corrosion if its volume fraction is small; however, if its volume fraction is high, it could act as an anodic barrier to inhibit the alloy corrosion.

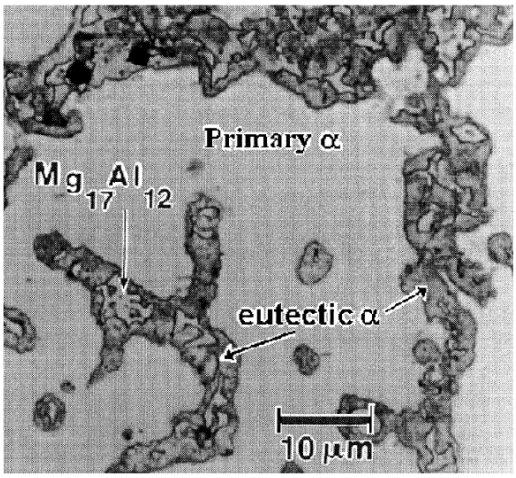

Figure 2.6: Microstructure of die cast AZ91D Mg alloy [49].

Microstructural parameters such as grain size and phase distribution influence the corrosion behaviour of Mg-alloys [49, 77]. Any of the alloying elements in its pure

form or intermetallic phase are less active than magnesium and thus acts as a cathode [51]. Compared to the matrix, a grain boundary is a distorted area with high imperfection and a poor corrosion resistance. Segregation of the alloying elements towards the grain boundary occurs thus incrementing the cathodic behaviour near the boundary. Although the grain boundary is a weak area, small grain magnesium alloys are preferred due to minimized segregation and more homogeneous corrosion behaviour [51]. On the other hand, it has been pointed out that fine, uniformly dispersed cathodic phases were the most detrimental to the corrosion resistance of Mg alloys [49]. The microstructure of Mg alloys and thus their corrosion behaviour can be influenced by the manufacturing process and heat treatment [51, 73, 78-80].

2.2.3 Environmental factors

The corrosion behaviour of Mg alloys depends on environmental factors such as the composition of the corrosion media, pH, temperature and the presence of corrosive electrolyte flow. *In vivo* experiments have shown that the corrosion behaviour of Mg alloy implants depends on the characteristics of the physiological media with two important factors influencing the corrosion rate: the local blood flow and the water content of the surrounding tissues, which are related to the local chloride content and hydrogen diffusion coefficient, respectively [51]. The investigation of the influence of these factors on the degradation process of implants in various anatomical locations might give some information about the underlying corrosion mechanism of the investigated Mg alloys [51]. Analytical methods have been used to determine the elemental components of biodegradable Mg alloys in bone, tissue and body fluids; however, some limitations of currently available methods are insufficient sensitivity, time

consuming sample preparation, availability of the method, lack of sufficient lateral resolution for solid sample analysis and difficulties to overcome interferences during the measuring process [51]. Therefore, there is a need for *in vitro* studies that lead us to a better understanding of the key factors controlling the corrosion process of the Mg alloy implants.

2.2.3.1 Composition of the corrosion media

So far, the physiological medium to which the surface of a biodegradable implant is exposed has been simulated in *in vitro* experiments by electrolytes with similar ionic content to that of the body fluid. Simulated biological fluids used in *in vitro* corrosion experiments include sodium chloride solution, phosphate buffered solution (PBS), Hank's solution, simulated body fluids (SBFs) and Dulbecco's modified eagle medium (DMEM) [81]. Table 2.3 shows the composition of four of these electrolytes. SBF is a very open denomination that allows for variations in the ionic content and buffering strength. Oyane et al. [82] pointed out that conventional SBF (c-SBF) had ionic concentrations not exactly equal to those of blood plasma and prepared new SBFs (r-SBF, i-SBF and m-SBF) with concentrations equal to or closer to those of blood plasma. After analysis of the prepared SBFs at different storage times, it was concluded that, among the different SBFs prepared, m-SBF was optimal in terms of stability and similarity to blood plasma. Xin et al. [81] investigated the influence of different tests solutions (NaCl, PBS, Hank's, c-SBF and DMEM) on the *in vitro* degradation of AZ91 Mg alloy and they reported a dramatically different degradation behaviour in the five solutions investigated. They attributed the observed behaviour to the different composition of the test solutions and mainly to the effect of the buffering agents and

presence of carbonates, which accelerate Mg dissolution. On the other hand, they observed a decrease in the alloy pitting corrosion at higher carbonate concentrations, which was attributed to formation of insoluble carbonates.

Table 2.3: Concentration of simulated biological fluids used in *in vitro* corrosion experiments [81, 82].

Species	Blood plasma	Hank's	DMEM	c-SBF	m-SBF
Na^+ (mM)	142.0	142.0	127.0	142.0	142.0
K^+ (mM)	5.0	5.9	5.3	5.0	5.0
Ca^{2+} (mM)	2.5	1.3	1.8	2.5	2.5
Mg^{2+} (mM)	1.5	0.8	0.8	1.5	1.5
HCO_3^- (mM)	27.0	4.2	44.1	4.2	10.0
Cl^- (mM)	103.0	145.0	90.8	147.8	103.0
HPO_4^{2-} (mM)	1.0	0.8	0.9	1.0	1.0
SO_4^{2-} (mM)	0.5	0.8	0.8	0.5	0.5
TRIS[a] (g L^{-1})	-	-	-	6.06	-
Amino acids (g L^{-1})	variable	-	1.6	-	-
Glucose (g L^{-1})	variable	1	4.5	-	-
Hepes[b] (g L^{-1})	-	-	5.96	-	17.89

[a]TRIS=Tris(hydroxylmethyl)aminomethane
[b]HEPES=2-(4-(2-hydroxyethyl)-1-piperazinyl)ethanesulfonic acid

The pH value of the electrolyte has an important effect on the corrosion rate of Mg alloys [54]. As already mentioned, in acidic or neutral solutions Mg corrodes to form Mg^{2+} ions, causing dissolution of the Mg alloys. During this process, the formation of hydroxyl ions (OH^-) promotes alkalization of the electrolyte. When the pH reaches a value of 10 or higher, the formation of a relatively stable $Mg(OH)_2$ layer occurs, thus inhibiting the corrosion process. A critical parameter observed in *in vitro* experiments is the buffer ability of the electrolyte. Hydroxyl ions produced by the corrosion reaction are

consumed by the buffering agents, with an important effect in the corrosion rate. When Mg alloys are soaked in either sodium chloride or Hank's solution the pH value increases up to approximately 10.5, regardless of the initial pH value of the test solution [73]. In buffered solutions less changes of the surface pH take place and no partial passivation as a result of alkalization occurs. This explains the fact that the polarization resistance, which is inversely proportional to the corrosion resistance, has been found to be significantly smaller in buffered SBFs compared to unbuffered NaCl solutions [83]. It has been observed that after the implant surgery the pH of the tissue surrounding the implant decreases to a value of approximately 5.2 and then recovers after 10 to 15 days [84]. This suggests an initial accelerated corrosion rate of the magnesium implant [73]. Therefore, pH variations of the *in vitro* environment were investigated. It was observed that acidic SBFs (pH=5) formed a short-term stable corrosion layer, but induced a more severe corrosion attack in the long term [84].

An investigation of the effect of aggressive ions (chloride, phosphate, carbonate and sulfate) on the degradation behaviour of Mg alloys in the physiological environment showed that the corrosion rate and the occurrence of pitting corrosion is significantly delayed by precipitation of magnesium phosphate species [85]. The presence of carbonates was related to an initial increase in the corrosion rate, but also to a delay in the occurrence of pitting corrosion due to the precipitation of insoluble magnesium carbonates. Sulfate and chloride ions were found to stimulate the corrosion process and induce pitting corrosion, respectively [85].

It has been observed that Ca and P play an important role in the corrosion mechanism of Mg alloy implants. Witte et al. [43] investigated the *in vivo* degradation of

four Mg alloys (AZ31, AZ91, WE43 and LAE442) and found that the corrosion layers contained high levels of Ca and P. XRD analysis suggested that an amorphous calcium phosphate had formed at the surface of the implants *in vivo*. Rettig et al. [46, 83] investigated the composition of the corrosion layers formed on WE43 Mg alloy immersed in buffered SBF (m-SBF). They used different "partial" SBFs that contained only some of the SBF components to identify the ions that participate in the corrosion layer formation. After 5 days of immersion in SBF, formation of a thick non-protective corrosion layer containing amorphous carbonated calcium phosphate was observed. The corrosion layer reached its final composition after some hours, showing a nearly constant concentration at longer immersion times. Finally, they found that calcium ions are only precipitated together with phosphates forming calcium phosphates, while phosphates can be deposited without calcium.

In an attempt to simulate *in vivo* conditions, the influence of proteins in the corrosion of Mg alloys has been investigated [83, 84, 86, 87]. It is believed that proteins interact and change the corrosion process and metal surface properties by adsorbing on the metallic surface or acting as chelating agents [84]. Their role in the corrosive environment is governed by several factors such as the surface chemistry of the metal, the protein adsorption characteristics, the interaction between protein molecules and other ions present in the electrolyte that produce organic complexes, and the transport of anionic and cationic charges to and away from the local environment [84]. Electrochemical investigations in SBFs containing bovine serum albumin (BSA) in the physiological concentration showed that proteins form a short-term corrosion blocking layer on the surface of Mg alloys in *in vitro* experiments; however, after some hours

their presence has no effect on the corrosion rate [83]. Liu et al. [84] investigated the degradation susceptibility of AZ91 Mg alloy in SBF. They found that the addition of BSA enhanced the short term electrochemical stability and decreased the pitting susceptibility of the alloy by adsorbing on the corrosion layer. They suggested that the adsorbed BSA layer can suppress the dissolution of Mg alloys by a covering and blocking effect. Mueller [87] also proposed that the presence of proteins in SBF inhibits the dissolution of AZ31 and LAE442 alloys. Although it is not clear why the presence of proteins has only a short-term effect on the corrosion process, it has been suggested that the protein layer may be destroyed by the corrosion process or that after some hours it is no longer dominating the electrochemical behaviour [87]. Yamamoto et al. [88] investigated the effect of inorganic salts, amino acids and proteins on the degradation of pure Mg in SBF. They found that protein adsorption and insoluble salt formation retarded Mg degradation, whereas organic compounds such as amino acids encouraged the dissolution of Mg. The effect of amino acids in the dissolution of Mg was suggested to be caused by their chelating effect, which inhibited the formation of insoluble salts.

2.2.3.2 Temperature and flow

Temperature is not considered to be an important factor in the corrosion process of Mg alloys; however, it may influence the adsorption of proteins and thus the corrosion mechanism of the implant *in vivo* [49, 51].

On the other hand, the flow of the corrosive media has been demonstrated to have a significant effect in the corrosion rate of magnesium alloys. Levesque et al. [21]

developed a test bench to investigate the influence of flow on the corrosion behaviour of magnesium alloys for cardiovascular applications. After testing AM60B alloy samples in modified Hank's solution under static and dynamic conditions, they found that the shear stress has a strong influence on the corrosion process. When this stress is low, it protects the surface from localized corrosion; but when it is very high, uniform and localized corrosion occurs. Hiromoto et al. [89] investigated the influence of pH and flow on the corrosion behavior of pure Mg in 0.6 wt.% NaCl borate buffer solutions at pH values of 6.7, 7.6 and 9.3 using a rotating disc electrode. They found that the existence of flow prevented the accumulation of corrosion products and promoted uniform corrosion, regardless of the electrolyte pH. No influence of the electrolyte pH was observed at static conditions; however, under dynamic conditions a higher corrosion rate was observed at lower pH values.

2.3 *IN VITRO* METHODOLOGY FOR THE INVESTIGATION OF THE CORROSION BEHAVIOUR OF Mg ALLOYS FOR BIODEGRADABLE APPLICATIONS

2.3.1 Limitations of current methodology

The development of suitable Mg-based materials for biodegradable applications requires the use of appropriate testing methodology that allows for material screening and best candidate selection. Ideally, *in vitro* tests should be able to provide a strong correlation with *in vivo* experiments, so that long and expensive animal experiments can be minimized. Witte et al. [90] investigated the *in vivo* and *in vitro* corrosion behaviour of AZ91D and LAE442 Mg alloys. They reported that *in vivo* corrosion was about four orders of magnitude lower than *in vitro* corrosion for the alloys tested. They also

observed that the tendency of the corrosion rate values obtained from *in vitro* tests was in the opposite direction as that obtained from the *in vivo* study, suggesting that current *in vitro* methodology cannot be used to predict *in vivo* corrosion rates of Mg alloys. They proposed that the lower corrosion rate observed *in vivo* was the result of a lower concentration of Cl^- ions (compared to the corrosive medium used *in vitro*) and the presence of proteins, which have been shown to adsorb on the implant surface and provide barrier protection. However, they were not able to explain the opposite trend of the corrosion behaviour of *in vivo* and *in vitro* studies. These results led to increased interest in the corrosion mechanisms of Mg alloys *in vivo* and the parameters affecting such behaviour.

Since the corrosion behaviour of Mg alloys depends on the corrosive environment, the observed lack of correlation between *in vivo* and *in vitro* experiments can be attributed to experimental difficulties at simulating physiological conditions. For instance, the concentration of the implant degradation products, i.e., Mg^{2+} and OH^- species, is regulated *in vivo* by homeostatic processes; however, *in vitro* experiments often report a fast increase in the concentration of these species as a result of the corrosion process, leading to an increase in the electrolyte pH and thus, possibly affecting the Mg alloy corrosion mechanisms and degradation rate. Additional limitations of current *in vitro* methodologies are the absence of relevant physiological ions with an effect on the corrosion behaviour, such as phosphates and carbonates [81, 85, 91, 92]; the lack of an appropriate experimental set-up tailored to specific body applications, e.g., the presence of a flow to simulate physiological shear stress inside the arteries [21]; and the absence of important biological components in the corrosive medium, such

as proteins and cells, which have been shown to influence the degradation process [83, 87]. Therefore, in order to improve the performance of biodegradable Mg-based materials it is necessary to first develop a fundamental understanding of the corrosion mechanisms at experimental conditions that resemble the complex nature of the *in vivo* corrosion process and corrosive media the most.

The effect of several parameters on the corrosion behaviour of Mg alloys has been investigated, such as the selection of alloying elements [93, 94], alloy composition [94, 95], microstructure [76, 96-100], electrolyte components [81, 85, 91, 93, 101] and the use of surface pretreatments and protective coatings [2, 102]. However, little information is available regarding the corrosion mechanisms of the investigated Mg alloys in simulated body fluids [56]. Moreover, Mg and its alloys are very reactive and their corrosion behaviour changes with time, ultimately depending on the protective properties and stability of the corrosion layer formed at the corresponding experimental conditions [56]. Therefore, in order to have a better understanding of the parameters determining the corrosion behaviour of Mg alloys *in vivo*, it is necessary to first understand the time-dependence of the corrosion mechanisms and their relationship to the formation, growth and stability of the corrosion layers formed at experimental conditions simulating the physiological environment.

Some reviews on the limitations of current methodologies for the assessment of the corrosion behaviour of biodegradable Mg implants have been published [103, 104]. The experimental parameters and set-up must be understood for the correct interpretation of corrosion results. Regardless of the corrosion test used, the volume-to-surface-area ratio must be considered, since it will have an effect on the pH time-

dependent behaviour and thus, on the corrosion rate. It is recommended to maintain the volume-to-surface-area ratio as large as possible [103].

The different methods to measure corrosion rates can be divided in conventional and electrochemical methods, the latter involving the presence of a corrosion driving force, i.e., potential, which is applied or measured during the test [103, 105]. Conventional tests include weight loss, hydrogen evolution and analytical techniques, while electrochemical tests include potentiodynamic polarization and electrochemical impedance spectroscopy. A brief description of the main techniques used in the investigation of the corrosion behaviour of Mg alloys for biodegradable applications, including their advantages and limitations is provided below.

2.3.2 Weight loss

During this test the sample is weighed before and after immersion in the corrosion medium for certain period of time, after which the sample is withdrawn and the resulting change in weight is calculated. Prior to measuring the final weight, an appropriate cleaning method should be used to remove the corrosion products. A solution containing CrO_3 (chromic acid) and $AgNO_3$ is recommended for the cleaning of corroded Mg alloy samples [106]. This solution is able to dissolve the $MgO/Mg(OH)_2$ corrosion products, while causing negligible corrosion to the metal substrate. The use of the weight loss method in the investigation of biodegradable Mg implants is very common [74, 80, 107-110]. Assuming that localized corrosion is not present, corrosion rate values (mm $year^{-1}$) can be calculated using the following equation [111]:

$$P_w = \frac{kw}{At\rho} \tag{2.9}$$

where P_w is the corrosion rate (mm/year), k is a constant (8.76×10^4), t is the time of exposure (h), A is the area (cm^2), w is the weight loss (g) and ρ is the density ($g\ cm^{-3}$). Weight loss tests are simple to set up and perform, inexpensive, they allow for easy control of the environment and offer the possibility of performing electrochemical measurements. However, corrosion rates calculated by this method correspond to average values for the total immersion time and do not provide information on the corrosion mechanisms nor on the time dependence of the corrosion behaviour. In addition, a considerable amount of corrosion is necessary for precise measurement of the weight loss and multiple samples are needed for accuracy [103].

2.3.3 Hydrogen evolution

According to the overall corrosion reaction of Mg (reaction 2.1), one mole of hydrogen gas is produced by the dissolution (oxidation) of one mole of Mg. According to this reaction, the amount of corroded material and thus, corrosion rate values, can be calculated from the amount of produced hydrogen gas. To collect the produced hydrogen gas, an inverted funnel and burette are usually used (Figure 2.7) [54]. Hydrogen evolution measurements are inexpensive, allow for real-time measurement of corrosion and are not affected by the formation of the corrosion layer [54, 103]. In addition, hydrogen evolution data is of interest for Mg biodegradable applications, since fast production of hydrogen gas can lead to undesired gas accumulation *in vivo*. However, this technique provides little information on the corrosion mechanisms. Furthermore, the increase in the local pH by the formation of a closed system under the funnel and hydrogen gas leaks from the burette can lead to inaccurate corrosion

behaviour data [103]. Corrosion rate values (mm $year^{-1}$) can be calculated from the volume of produced hydrogen gas using the following equation [112]:

$$P_H = kV_H \quad (2.10)$$

where P_H is the corrosion rate (mm $year^{-1}$), k is a constant with a value of 2.279 and V_H is the hydrogen production rate (ml cm^{-2} day^{-1}), where "cm^2" refers to the sample surface area exposed to the corrosive environment.

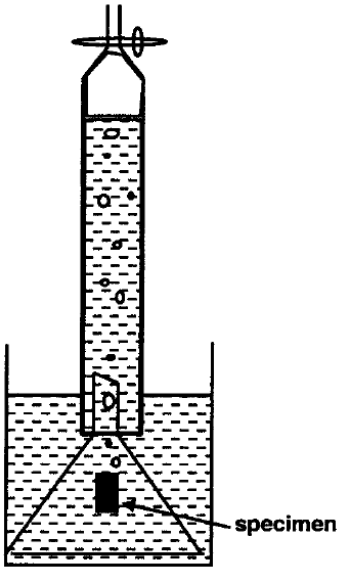

Figure 2.7: Schematic illustration of the procedure to measure the corrosion rate by measuring the volume of hydrogen evolved [54].

Hydrogen evolution tests have often been used in the investigation of Mg biodegradable applications [52, 74, 80, 113, 114]. Although some authors [54, 112] have claimed the suitability of this technique due to the observed good correlation between weight loss and hydrogen evolution tests, a deviation in the stoichiometry ratio of 1:1 in equation 2.1 has also been observed, with some publications reporting this

ratio to vary between 0.22 and 1.31 [80, 103, 109, 110]. Although the reason for such variation is unclear, it might be related to inefficient collection of produced hydrogen gas [103].

2.3.4 ICP-OES

Determination of the concentration of dissolved metals in the corrosive electrolyte solution can be performed by the use of emission spectroscopy techniques such as inductively coupled plasma optical emission spectroscopy (ICP-OES). This method has been used to determine the concentration of dissolved Mg and alloying elements in the electrolyte as a result of the corrosion process [52, 115, 116]. Corrosion rate values can be calculated from the concentration of dissolved magnesium. However, some drawbacks of this technique are the time consuming preparation of samples and the little information provided on the corrosion mechanisms [51]. Furthermore, the presence of Mg in the $Mg(OH)_2$ corrosion layer and insoluble magnesium phosphates and carbonates forming part of the corrosion layer or precipitated in the bulk electrolyte are not taken into account and thus, can lead to inaccurate determination of corrosion rate values [56].

2.3.5 Potentiodynamic polarization

Potentiodynamic polarization (PP) is the most commonly used electrochemical technique for *in vitro* investigation of the corrosion behaviour of Mg alloys [77, 103, 112, 117-119]. By using this technique, the corrosion potential (E_{corr}) and corrosion current density (i_{corr}) can be obtained, as well as information on the kinetics of partial anodic

and cathodic reactions [103]. Average corrosion rate values can be calculated from the corrosion current density (i_{corr}) using the following equation [112]:

$$P_i = k i_{corr} \quad (2.11)$$

where P_i is the corrosion rate (mm year^{-1}), k is a constant with a value of 22.85 (mm cm^2 year^{-1} mA^{-1}) and i_{corr} is the corrosion current density (mA cm^{-2}).

Although PP is a simple and quick technique and thus, widely used, some authors [54, 112] have pointed out that this technique is not appropriate for the determination of the corrosion rate of Mg alloys. Song et al. [54] observed a poor correlation between corrosion rate values obtained for Mg alloys by PP and weight loss technique. They attributed this behaviour to the presence of multiple simultaneous cathodic and anodic reactions occurring on the electrode surface, invalidating the determination of the corrosion rate by this technique. Shi et al. [112] reviewed the use of PP for the determination of the corrosion rate of different Mg alloys and they compared corrosion rates values obtained by PP, hydrogen evolution and weight loss. They observed that corrosion rate values obtained by PP did not agree with the values obtained from weight loss and hydrogen evolution measurements, with a relative deviation in the values obtained by PP ranging from 48% to 96%. Some limitations of PP for the determination of corrosion rates of Mg alloys that might account for the observed deviation are: 1) Evaluation of the Mg alloy corrosion rate is performed soon after specimen immersion, before a steady state has been attained [112]; 2) The corrosion rate of Mg alloys is time-dependent, with gradual formation of a protective corrosion layer and occurrence of localized corrosion contributing to variation in the

corrosion rate, while PP provides instant corrosion rate values which do not reflect the changing nature of the corrosion process [103, 112]; and 3) Variation in the Tafel analysis of the same data by different researchers can result in different corrosion rate values [103]. It should be noted that the PP technique yields an *instantaneous corrosion rate* value and that the technique is usually destructive to the sample.

2.3.6 Electrochemical impedance spectroscopy

Electrochemical impedance spectroscopy (EIS) is an electrochemical method in which an electrical perturbation (usually voltage) is applied and the system impedance response is obtained as a function of frequency. *Impedance* is the term used to describe the alternate current (ac) equivalent of direct current (dc) *resistance*. EIS offers valuable information on a number of phenomena and properties of the metal surface, allowing for the determination of parameters such as electrode capacitance, charge transfer resistance and diffusion resistance [105]. In recent years, this technique has gained popularity in the investigation of Mg alloys for biodegradable applications [60, 83, 103, 120, 121]. Since the applied perturbation is generally in the range of 5-10 mV, EIS measurements are non-destructive, causing only minimal perturbation to the test system [105]. Therefore, EIS allows for multiple recordings without having to re-polish the sample surface and thus, real time monitoring of the corrosion behaviour can be performed [103].

EIS provides instantaneous values of the system impedance, which can be related to the corrosion resistance, i.e., impedance values are inversely proportional to the corrosion rate [103]. Frequently, only a qualitative analysis of the impedance

response is presented, since changes in the impedance response can be related to changes in the corrosion rate. EIS data can also be analysed using a model, such as a reaction mechanism (kinetic model) or an equivalent electrical circuit (EEC) in order to deduce a relationship between electrical components like resistance (*R*) and capacitance (*C*) to the processes occurring at the metal/electrolyte interface, such as charge transfer, diffusion and adsorption [105, 122].

Some limitations of EIS for the investigation of the corrosion of Mg alloys are [103]: 1) multiple equivalent circuits may fit the same data, resulting in significantly different calculated values for the EEC parameters, e.g., charge transfer resistance; 2) some noise at low frequency values is often obtained due to its apparent fast rate of dissolution, 3) it does not provide information on the contribution of anodic/cathodic partial reactions, and 4) since the corrosion of Mg occurs through both electrochemical and chemical reactions, electrochemical measurements are expected to predict a corrosion rate lower than the real value (the same applies to PP).

2.4 CURRENT APPROACHES TO CONTROL THE CORROSION RATE OF Mg ALLOYS FOR BIODEGRADABLE IMPLANT APPLICATIONS

The main limitation of Mg biodegradable implants is their fast corrosion in the physiological environment, often accompanied by the occurrence of localized corrosion, leading to premature loss of the implant mechanical properties. Other drawbacks of Mg alloys are the production of hydrogen gas at a rate the body cannot regulate and the alkalization of the surrounding tissue, which can have deleterious effects.

Current research approaches to improve the biocompatibility and corrosion properties of Mg alloys for biodegradable applications include the development of novel alloys with a composition and microstructure tailored for implant applications and, the formation of protective layers by applying surface treatments and/or coatings [2].

2.4.1 Alloy development

Magnesium alloys currently being investigated as biodegradable materials are mostly commercial alloys developed for the needs in the transportation industry [49]. The observed good corrosion performance of these alloys in industrial applications has been related to the use of alloying elements such as zirconium (Zr), aluminum (Al), zinc (Zn), calcium (Ca), lithium (Li), yttrium (Y) and rare earth (RE) [49, 51]. Following a similar approach, some researchers have developed novel Mg alloys for biodegradable applications containing Y, Al and RE elements. Zhou et al. [123] investigated the mechanical properties, biocorrosion and *in vitro* biocompatibility of Mg-Li-Al-RE alloys for cardiovascular stent applications. Although the addition of Al and RE elements was found to increase the tensile strength of Mg-Li alloys, a decrease in the corrosion resistance was observed due to the presence of intermetallic compounds distributed in the alloy matrix. Mao et al. [124, 125] developed a new Mg alloy with the nominal composition Mg-2.5Nd-0.2Zn-0.4Zr and reported a highly uniform degradation and reduced corrosion rate compared to commercial alloys (WE43 and AZ31). Haenzi et al. [126] investigated the *in vitro* and *in vivo* degradation and biological response of new Mg-Y-Zn alloys for biodegradable stent applications; they reported that the composition Mg-2Y-1Zn showed homogeneous degradation, limited gas formation and good biocompatibility.

Alloy composition is an important issue in terms of biocompatibility; although some alloying elements have been found to improve an alloy performance, their toxic nature can limit the alloy use as implant material. Aluminum has been related to neuronal damage, dementia and Alzheimer's disease [107, 127]. Rare earth elements are apparently hard to resorb by the body and their administration could lead to hepatotoxicity [107, 128]. Excessive yttrium ions have been found to change the expression of some rat genes and to have adverse effects on DNA transcription factors [107, 129]. Therefore, it is necessary to design and develop new Mg alloys with improved biocompatibility. Alloys that consist of trace elements already existing in the human body are promising candidates [51, 95].

Calcium is biocompatible and has a similar density compared to bone, which has motivated the development of calcium-magnesium alloys for orthopaedic biodegradable applications [97, 130, 131]. Li et al. [130] reported that formation of a Mg_2Ca secondary phase led to decreased corrosion resistance; however, the amount of this phase could be decreased by hot rolling and hot extrusion processing treatments. Wan et al. [131] found that the optimum calcium content is 0.6 wt.% in terms of the overall bending and compressive properties and corrosion resistance.

Zinc is an essential element and it is a common alloying element in Mg alloys, contributing to an increase in mechanical properties [95]. Zhang et al. [107] reported that the corrosion rate of Mg-6Zn was lower than that of high-purity Mg in SBF. Sun et al. [132] investigated the mechanical properties, *in vitro* degradation and cytotoxicity of extruded Mg-4Zn-0.2Ca. They showed that the addition of Zn and Ca to the Mg matrix

could enhance the alloy corrosion potential, with corrosion rate values similar to those observed for high-purity Mg in SBF.

Manganese has good biocompatibility and it plays a primary role in the activation of multiple enzymes [95]. Zhang et al. [133] investigated the corrosion behaviour of Mg-Zn-Mn alloys and observed that the increase in Zn content increased the corrosion resistance, with a possible contribution of Zn to formation of a passivation layer. Xu et al. [134] investigated the *in vivo* corrosion behaviour of a high purity Mg-1.2Mn-1Zn alloy implanted in the femora of rats. They observed that at 18 weeks post-operation 54% of the implants had degraded; however, the implants were still fixed with no signs of inflammation. Elemental analysis showed a homogeneous distribution of Mn and Zn in the residual implant, the degradation layer and the surrounding bone tissue.

Strontium is a Group II element that behaves similarly to Ca and Mg. The content of Sr in the body is about 140 mg, with 99% of its total mass located in the bones [95]. Sr is commonly added to Mg as a grain refiner due to its tendency to form compounds that segregate to grain boundaries [135]. Bornapour et al. [74, 118, 119] investigated the corrosion rate in SBF of Mg-Sr alloys, with Sr in the range of 0.3-2.5% and, found that the Mg-0.5Sr alloy had the lowest corrosion rate. The ternary alloy Mg-0.3Sr-0.3Ca showed a good combination of mechanical properties and corrosion resistance.

Since alloying of Mg is challenging due to the low solubility of many elements in Mg, the development of protective coatings is an attractive alternative to control de corrosion of Mg alloys for biodegradable applications.

2.4.2 Protective coatings

The development of surface treatments and protective coatings is an interesting alternative for controlling the corrosion rate and tailoring the surface reactivity of biodegradable Mg implants. Since current commercially-available Mg alloys were mainly developed in response to the needs of the transportation industry, most of the work published on protective Mg alloy coatings envisages industrial applications. Some reviews on the development of coatings and coating technologies can be found in [136-139]. For biomedical applications, coatings should possess, additionally to corrosion protection, other properties such as enhancement of biocompatibility, bioactivity, antibiotic ability, local drug delivery ability and, ideally, they should enable biodegradation at a desired rate, as pointed out by Hornberger et al. [2]. Biocompatible and biodegradable coatings can be classified according to their composition in inorganic and organic. Inorganic coatings include $MgO/Mg(OH)_2$, calcium phosphate and fluoride, while organic coatings include poly lactic acid, caprolactone, chitosan and polypyrrole.

2.4.2.1 Inorganic coatings

2.4.2.1.1 $MgO/Mg(OH)_2$

Partially protective $MgO/Mg(OH)_2$ layers can be formed on Mg alloys by passivation, thermal treatment or anodization [140-142]. Formation of a $MgO/Mg(OH)_2$ passive layer can provide protection during the initial phase of corrosion; however, passivity is quickly lost in the physiological media due to the presence of aggressive Cl^- ions, which promote dissolution of the passive layer and formation of $MgCl_2$ species [2]. An increase in the corrosion resistance of Mg alloys for biomedical applications by the formation of

plasma electrolytic oxidation layers with the incorporation of calcium phosphates and fluorides into the corrosion layer has been reported [143-146].

2.4.2.1.2 Calcium phosphate coatings

Calcium phosphate coatings are the most widely studied coatings for Mg orthopaedic biodegradable applications, mainly due to their excellent biocompatibility, stability and bioactivity [95]. The ability of calcium phosphate coatings to induce bone-like apatite deposition, which is similar to hydroxyapatite (HA), the mineral phase of bone, makes them attractive for orthopaedic applications [2]. Calcium phosphate-containing coatings have been prepared by chemical immersion [95, 140, 146, 147] and electrochemical deposition [148, 149]. Wen et al. [149] prepared hydroxyapatite coatings on AZ31 Mg alloy by cathodic electrodeposition. As-deposited samples were then post-treated with hot alkali solution. It was determined that as-deposited coatings contained dicalcium phosphate dehydrate (DCPD) and hydroxyapatite, while 10 μm-thick hydroxyapatite coatings were observed after alkali treatment. The hydroxyapatite coating slowed down the degradation rate and effectively induced the deposition of Ca-P-Mg apatite in SBF.

2.4.2.1.3 Fluoride coatings

Fluoride-containing coatings have been investigated to decrease the corrosion rate of Mg alloys by the formation of protective MgF_2 layers [69, 150, 151]. However, the coating protective effect is only temporary, due to the dissolution of the fluoride-containing coating [2]. Yan et al. [151] prepared coatings containing MgO and MgF_2 on AZ31B Mg alloy for biodegradable applications. Immersion experiments in SBF showed

an improved corrosion resistance for the fluoride coated samples compared to the bare alloy.

2.4.2.2 Organic coatings

Organic coatings are attractive for biomedical applications due to their favorable properties such as the capacity for drug delivery and their ability to be functionalised with organic biomolecules, in addition to their protective properties [2].

2.4.2.2.1 Poly lactic acid

Poly lactic acid (PLA) is a biocompatible polymer extensively investigated for biomedical applications [121, 152-155]. PLA undergoes hydrolytic degradation in the body fluid and its by-products are non-toxic. The degradation product of PLA is lactic acid, a human metabolic by-product, which breaks down into water and carbon dioxide via the citric acid cycle [156]. Alabbasi et al. [121] formed PLA coatings on AZ91 Mg allow by a spin coating technique for implant applications. Immersion experiments of the coated samples in SBF revealed that the PLA coating enhanced the degradation resistance of the alloy significantly. An increase in the coating thickness led to increased coating resistance, but decreased adhesion. A thin film coating (2-3 μm) showed good adhesion and degradation resistance.

2.4.2.2.2 Polycaprolactone

Polycaprolactone (PCL) has been studied for the development of Mg biodegradable implants [108, 157, 158] and Mg tissue engineering applications [6]. It is nontoxic and it can be blended with a wide range of polymers forming miscible solutions [159].

Compared to other polymers it has a longer degradation time of up to 2 or 3 years, depending on the molecular weight, the degree of crystallinity and the conditions of degradation [160]. Its hydrolysis leads to production of caproic acid that is completely metabolized via the citric acid cycle [156]. Park et al. [158] observed that PCL coatings on Mg led to a decrease in the substrate corrosion rate by about 50 %; however, they observed coating detachment and rapid water absorption at the early stage of corrosion.

2.4.2.2.3 Chitosan

Chitosan is a derivative of chitin, a polysaccharide that can be found in crustaceans and is one of the most abundant natural polymers [156]. Chitosan has been investigated for biomedical applications due to its beneficial properties such as processability, controllable mechanical properties, availability of reactive functional groups, biocompatibility and antimicrobicity [159]. It biodegrades into glucosamine and *in vivo* degradation rates range from a few weeks to 6 months [156]. Major drawbacks of chitosan are its low mechanical strength and insolubility in water [159]. Chitosan has been widely investigated for Mg biodegradable applications [161-164]. Gu et al. [164] investigated the corrosion behaviour of a chitosan-coated Mg-Ca alloy prepared by a dip coating method. They observed that the corrosion resistance of the coated alloy depended on both the chitosan molecular weight and the number of coating layers.

2.4.2.2.4 Polypyrrole

Intrinsically conductive polymers (ICPs) or conductive polymers possess a conjugated backbone, i.e., alternating double and single bonds, that allows for charge transport, Figure 2.8 [165]. Double bonds possess a strong and localized σ-bond and a less

localized π-bond. The p-orbitals in the π-bonds overlap, allowing electrons to delocalize and move freely between the atoms. ICPs are considered synthetic “metals” because they have electrical, magnetic and optical properties typical of metals and semiconductors [165, 166]. ICPs are very attractive for biomedical applications due to their following properties [156, 165]: 1) they can contribute to better integration of the biological tissue with hard metallic biomaterials from electrically conductive devices, such as neural probes, cochlear implants and cardiac pacemakers; 2) they can be easily synthesized and processed to produce smaller devices with electrical stimulus-responsive capabilities; and 3) they can be loaded or functionalized with biological molecules to decrease tissue inflammation and scar formation. Typical conductive polymers used in biomedical applications include polypyrrole (PPy), polythiophene (PT), poly(3,4-ethylenedioxythiophene) (PEDOT) and polyaniline (PANI) [156]. Some of their applications include biosensors, neural implants, drug delivery devices and tissue engineering scaffolds [165].

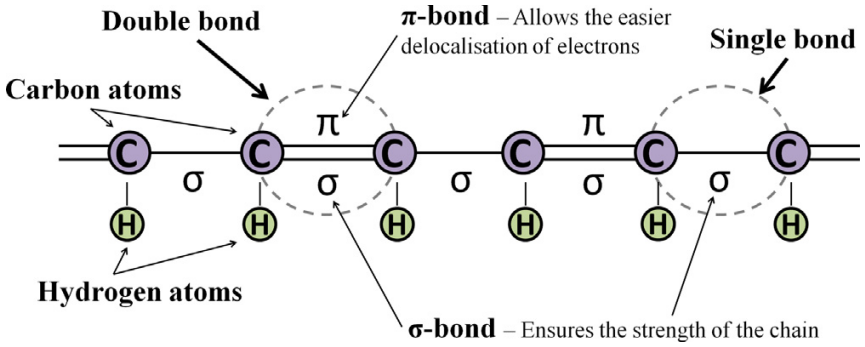

Figure 2.8: A simplified schematic of a conjugated backbone: a chain containing alternating single and double bonds [165].

Polypyrrole (PPy) is probably the most studied conductive polymer, with many interesting properties, which make it a very promising ‘smart’ biomaterial [165]: it has good *in vitro* and *in vivo* biocompatibility, good chemical stability and reasonably high conductivity under physiological conditions. PPy can be easily synthesized at room temperature in a wide range of solvents including water, it can be modified through the incorporation of bioactive molecules and it is stimulus responsive [165]. PPy is used in a wide range of applications including: fuel cells, corrosion protection, computer displays, microsurgical tools, biosensors, drug delivery systems, in neural tissue engineering, neural probes and blood conduits [165]. The chemical structure of PPy is shown in Figure 2.9.

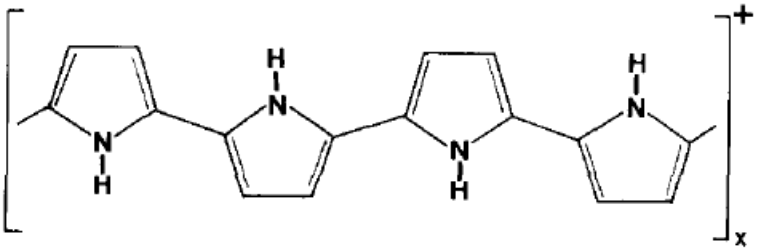

Figure 2.9: Structure of the polypyrrole chain [175].

PPy can be synthesized chemically or electrochemically [166]. Electrochemical synthesis is a relatively straightforward procedure widely used for the preparation of PPy films on metallic surfaces. During electrochemical synthesis, an electrical current is applied through the electrodes, which are placed in the electrolyte containing the pyrrole monomer, the solvent and the doping agent (e.g., an anion). The monomer is oxidized at the working electrode, forming radical cations that react with other monomer or

radical cations, forming polymeric chains on the electrode surface [166]. Electrochemical synthesis of pyrrole can be carried out using potentiostatic, galvanostatic or potentiodynamic methods [167-169].

During the electrochemical synthesis, PPy is synthesized in its oxidized conducting form, leading to the incorporation of dopant agents (anions) into the backbone polymer in order to neutralize the charge [166]. This doping process introduces charge carriers in the form of polarons (i.e., radical ions) or bipolarons (i.e., dianions) into the polymer that, together with electron hopping and the motion of anions or cations, render the polymer conductive [165]. Electron hopping corresponds to the mobility of electrons due to the attraction between the electrons of a polymeric repeat-unit and the nuclei of neighboring units [166]. The doping process is essential for the conductivity of PPy and the process is reversible, this is, a potential applied to the polymer will cause the dopant to leave or re-enter the polymer, switching it between its conductive and insulating redox states [165].

In addition to its interesting properties for biomedical applications, PPy together with other conductive polymers have been extensively investigated for corrosion protection [170, 171]. Although a large number of studies focusing on the corrosion protection of conductive polymers has been published, up to now, little is known about the corrosion protection mechanism of conductive polymers [170]. The following corrosion protection mechanisms have been proposed [170, 171]:

A. *Anodic protection.* According to this mechanism, polarization of the metal substrate over its passivation potential by the conductive polymer leads to

formation of a passive oxide film at the substrate/coating interface, thus preventing corrosion. During the formation of the passive oxide layer, the substrate is oxidized and the polymer is reduced and thus, re-oxidation of the polymer is necessary to maintain its protective properties. It has been proposed that oxygen reduction at the coating/electrolyte interface leads to polymer re-oxidation [170].

B. *Intelligent release of inhibitor anions.* According to this mechanism, in the presence of a coating defect, the oxidized polymer coating will release the dopant anions during its reduction. If the dopant anions possess corrosion inhibiting properties, then its release will result in inhibition of the corrosion within the defect. In this way, a self-healing of the oxide layer might be initiated depending on the nature of the metal and doping anions.

C. *Barrier effect.* The barrier properties of a coating depend on its porosity and on its permeability to water and corrosive ions [170]. A decrease in the coating porosity leads to lower H_2O and O_2 transport rate. A shift of the oxygen reduction site from the metal/coating to the coating/electrolyte interface due to a low coating porosity, prevents coating delamination caused by radical side-products formed during the oxygen reduction reaction [171].

Recently, the use of PPy coatings to control the corrosion rate of Mg alloys for biodegradable applications has been suggested; the rational being the good biocompatibility, drug loading capabilities, possibility of functionalization and attractive corrosion protection mechanisms of PPy [169]. Although PPy is not biodegradable, it is expected that the permanent presence of a thin PPy film would show an adequate

biocompatibility without triggering any negative biological response. Investigations on the corrosion behaviour of PPy coatings on Mg alloys for biodegradable implant applications have demonstrated the potential of PPy coatings for controlling the corrosion rate of Mg implants [169, 172, 173]; however, improvement of the coating properties, e.g., adhesion and barrier effect, is still required. Turhan et al. [169, 173] formed PPy coatings on AZ91D Mg alloy by cyclic voltammetry from aqueous solutions containing pyrrole and sodium salicylate. They optimized the system coating parameters and observed that the coating surface morphology and conductivity are highly affected by the potential range chosen for the electrodeposition, with a potential range from 0 to 1 V vs. Ag/AgCl being the most effective in reducing the corrosion rate. The salicylate-doped PPy coatings remained well adhesive without peeling-off after an immersion time of 10 days in a Na_2SO_4 solution. Srinivasan et al. [174] investigated the effect of monomer concentration on the corrosion resistance properties of electrochemically-formed PPy coatings on AZ31 Mg alloy. They observed that the formation of a uniform coating was achieved only when the pyrrole concentration is above 0.2 M. Immersion experiments in a SBF revealed an increment of one order of magnitude in the corrosion resistance after 45 minutes of immersion, with respect to the bare sample. Turhan et al. [172] investigated the corrosion behaviour of sodium salicylate-doped PPy coatings on AZ91D Mg alloy and its functionalization with albumin monolayers. They reported an increased corrosion resistance of the PPy-coated alloys, which is enhanced by the release of the salicylate dopant anions. Albumin functionalization of the PPy coatings significantly increased the alloy corrosion

resistance. The PPy coatings remained well adhesive over the period of time investigated (1 week).

2.5 REFERENCES

[1] F. Witte, The history of biodegradable magnesium implants: a review, Acta Biomaterialia, 6 (2010) 1680-1692.

[2] H. Hornberger, S. Virtanen, A.R. Boccaccini, Biomedical coatings on magnesium alloys – A review, Acta Biomaterialia, 8 (2012) 2442-2455.

[3] J.J. Jacobs, J.L. Gilbert, R.M. Urban, Corrosion of metal orthopaedic implants, Journal of Bone and Joint Surgery - Series A, 80 (1998) 268-282.

[4] A. Colombo, M. Ferraro, A. Itoh, G. Martini, S. Blengino, L.E.O. Finci, Results of Coronary Stenting for Restenosis, Journal of the American College of Cardiology, 28 (1996) 830-836.

[5] J. Nagels, M. Stokdijk, P.M. Rozing, Stress shielding and bone resorption in shoulder arthroplasty, Journal of Shoulder and Elbow Surgery, 12 (2003) 35-39.

[6] M. Yazdimamaghani, M. Razavi, D. Vashaee, L. Tayebi, Development and degradation behavior of magnesium scaffolds coated with polycaprolactone for bone tissue engineering, Materials Letters, 132 (2014) 106-110.

[7] D. Lloyd-Jones, R. Adams, M. Carnethon, G. De Simone, T.B. Ferguson, K. Flegal, E. Ford, K. Furie, A. Go, K. Greenlund, N. Haase, S. Hailpern, M. Ho, V. Howard, B. Kissela, S. Kittner, D. Lackland, L. Lisabeth, A. Marelli, M. McDermott, J. Meigs, D. Mozaffarian, G. Nichol, C. O'Donnell, V. Roger, W. Rosamond, R. Sacco, P. Sorlie, R. Stafford, J. Steinberger, T. Thorn, S. Wasserthiel-Smoller, N. Wong, J. Wylie-Rosett, Y. Hong, Heart disease and stroke statistics - 2009 update. A report from the American heart association statistics committee and stroke statistics subcommittee, Circulation, 119 (2009) 480-486.

[8] G.K. Hansson, Inflammation, Atherosclerosis, and Coronary Artery Disease, N Engl J Med, 352 (2005) 1685-1695.

[9] M.C. Fishbein, The vulnerable and unstable atherosclerotic plaque, Cardiovascular Pathology, 19 (2010) 6-11.

[10] W.J. Gomes, E. Buffolo, Coronary Stenting and Inflammation: Implications for Further Surgical and Medical Treatment, Annals of Thoracic Surgery, 81 (2006) 1918-1925.

[11] U. Sigwart, J. Puel, V. Mirkovitch, F. Joffre, L. Kappenberger, Intravascular stents to prevent occlusion and restenosis after transluminal angioplasty, N Engl J Med, 316 (1987) 701-706.

[12] "Coronary stent", https://en.wikipedia.org/wiki/Coronary_stent, in, access date: 22/11/2015.

[13] V. Rajagopal, S.G. Rockson, Coronary restenosis: A review of mechanisms and management, American Journal of Medicine, 115 (2003) 547-553.

[14] P. Erne, M. Schier, T.J. Resink, The road to bioabsorbable stents: Reaching clinical reality?, CardioVascular and Interventional Radiology, 29 (2006) 11-16.

[15] "Online Clinical Case Study", http://www.hkma.org/english/cme/clinicalcase /200703ans1.htm, in, access date: 22/11/2015.

[16] G. Mani, M.D. Feldman, D. Patel, C.M. Agrawal, Coronary stents: A materials perspective, Biomaterials, 28 (2007) 1689-1710.

[17] B. O'Brien, W. Carroll, The evolution of cardiovascular stent materials and surfaces in response to clinical drivers: A review, Acta Biomaterialia, 5 (2009) 945-958.

[18] S. Ramcharitar, P.W. Serruys, Fully biodegradable coronary stents: Progress to date, American Journal of Cardiovascular Drugs, 8 (2008) 305-314.

[19] J.J. Wykrzykowska, Y. Onuma, P.W. Serruys, Advances in stent drug delivery: The future is in bioabsorbable stents, Expert Opinion on Drug Delivery, 6 (2009) 113-126.

[20] B. Heublein, R. Rohde, V. Kaese, M. Niemeyer, W. Hartung, A. Haverich, Biocorrosion of magnesium alloys: A new principle in cardiovascular implant technology?, Heart, 89 (2003) 651-656.

[21] J. Levesque, H. Hermawan, D. Dube, D. Mantovani, Design of a pseudo-physiological test bench specific to the development of biodegradable metallic biomaterials, Acta Biomaterialia, 4 (2008) 284-295.

[22] M. Peuster, C. Hesse, T. Schloo, C. Fink, P. Beerbaum, C. von Schnakenburg, Long-term biocompatibility of a corrodible peripheral iron stent in the porcine descending aorta, Biomaterials, 27 (2006) 4955-4962.

[23] M. Peuster, P. Wohlsein, M. Brügmann, M. Ehlerding, K. Seidler, C. Fink, H. Brauer, A. Fischer, G. Hausdorf, A novel approach to temporary stenting: Degradable cardiovascular stents produced from corrodible metal - Results 6-18 months after implantation into New Zealand white rabbits, Heart, 86 (2001) 563-569.

[24] R. Waksman, R. Pakala, R. Baffour, R. Seabron, D. Hellinga, F.O. Tio, Short-term effects of biocorrodible iron stents in porcine coronary arteries, Journal of Interventional Cardiology, 21 (2008) 15-20.

[25] S. Zhu, N. Huang, L. Xu, Y. Zhang, H. Liu, H. Sun, Y. Leng, Biocompatibility of pure iron: In vitro assessment of degradation kinetics and cytotoxicity on endothelial cells, Materials Science and Engineering C, 29 (2009) 1589-1592.

[26] M. Maeng, L.O. Jensen, E. Falk, H.R. Andersen, L. Thuesen, Negative vascular remodelling after implantation of bioabsorbable magnesium alloy stents in porcine coronary arteries: a randomised comparison with bare-metal and sirolimus-eluting stents, Heart, 95 (2009) 241-246.

[27] R. Waksman, R. Pakala, P.K. Kuchulakanti, R. Baffour, D. Hellinga, R. Seabron, F.O. Tio, E. Wittchow, S. Hartwig, C. Harder, R. Rohde, B. Heublein, A. Andreae, K.H. Waldmann, A. Haverich, Safety and efficacy of bioabsorbable magnesium alloy stents in porcine coronary arteries, Catheterization and Cardiovascular Interventions, 68 (2006) 607-617.

[28] T.L. Slottow, R. Pakala, T. Okabe, D. Hellinga, R.J. Lovec, F.O. Tio, A.B. Bui, R. Waksman, Optical coherence tomography and intravascular ultrasound imaging of bioabsorbable magnesium stent degradation in porcine coronary arteries, Cardiovascular Revascularization Medicine, 9 (2008) 248-254.

[29] R. Waksman, R. Pakala, T. Okabe, D. Hellinga, R. Chan, M.O. Tio, E. Wittchow, S. Hartwig, K.H. Waldmann, C. Harder, Efficacy and safety of absorbable metallic stents with adjunct intracoronary beta radiation in porcine coronary arteries, Journal of Interventional Cardiology, 20 (2007) 367-372.

[30] P. Zartner, M. Buettner, H. Singer, M. Sigler, First biodegradable metal stent in a child with congenital heart disease: Evaluation of macro and histopathology, Catheterization and Cardiovascular Interventions, 69 (2007) 443-446.

[31] P. Zartner, R. Cesnjevar, H. Singer, M. Weyand, First successful implantation of a biodegradable metal stent into the left pulmonary artery of a preterm baby, Catheterization and Cardiovascular Interventions, 66 (2005) 590-594.

[32] P. Peeters, M. Bosiers, J. Verbist, K. Deloose, B. Heublein, Preliminary results after application of absorbable metal stents in patients with critical limb ischemia, Journal of Endovascular Therapy, 12 (2005) 1-5.

[33] R. Erbel, C. Di Mario, J. Bartunek, J. Bonnier, B. de Bruyne, F.R. Eberli, P. Erne, M. Haude, B. Heublein, M. Horrigan, C. Ilsley, D. Böse, J. Koolen, T.F. Lüscher, N. Weissman, R. Waksman, Temporary scaffolding of coronary arteries with bioabsorbable magnesium stents: a prospective, non-randomised multicentre trial, Lancet, 369 (2007) 1869-1875.

[34] R. Waksman, R. Erbel, C. Di Mario, J. Bartunek, B. de Bruyne, F.R. Eberli, P. Erne, M. Haude, M. Horrigan, C. Ilsley, D. Bose, H. Bonnier, J. Koolen, T.F. Luscher, N.J. Weissman, P.-A. Investigators, Early- and long-term intravascular ultrasound and angiographic findings after bioabsorbable magnesium stent implantation in human coronary arteries, Jacc: Cardiovascular Interventions, 2 (2009) 312-320.

[35] R. Waksman, F. Prati, N. Bruining, M. Haude, D. Böse, H. Kitabata, P. Erne, S. Verheye, H. Degen, P. Vermeersch, L. Di Vito, J. Koolen, R. Erbel, Serial Observation of Drug-Eluting Absorbable Metal Scaffold: Multi-Imaging Modality Assessment, Circulation: Cardiovascular Interventions, 6 (2013) 644-653.

[36] "Development of bioabsorbable magnesium alloys as implant material for vascular intervention", http://www.metphys.mat.ethz.ch/research/mma/BioMg, in, Swiss Federal Institute of Technology Zurich, access date: 22/11/2015.

[37] M. Geetha, A.K. Singh, R. Asokamani, A.K. Gogia, Ti based biomaterials, the ultimate choice for orthopaedic implants – A review, Progress in Materials Science, 54 (2009) 397-425.

[38] J.B. Park, R.S. Lakes, Biomaterials an introduction, in, Springer, New York, NY, 2007.

[39] M.P. Staiger, A.M. Pietak, J. Huadmai, G. Dias, Magnesium and its alloys as orthopedic biomaterials: A review, Biomaterials, 27 (2006) 1728-1734.

[40] A. Krause, N. Von Der Höh, D. Bormann, C. Krause, F.W. Bach, H. Windhagen, A. Meyer-Lindenberg, Degradation behaviour and mechanical properties of magnesium implants in rabbit tibiae, Journal of Materials Science, 45 (2010) 624-632.

[41] L. Li, J. Gao, Y. Wang, Evaluation of cyto-toxicity and corrosion behavior of alkali-heat-treated magnesium in simulated body fluid, Surface and Coatings Technology, 185 (2004) 92-98.

[42] H. Kuwahara, Y. Al-Abdullat, N. Mazaki, S. Tsutsumi, T. Aizawa, Precipitation of magnesium apatite on pure magnesium surface during immersing in Hank's solution, Materials Transactions, 42 (2001) 1317-1321.
[43] F. Witte, V. Kaese, H. Haferkamp, E. Switzer, A. Meyer-Lindenberg, C.J. Wirth, H. Windhagen, In vivo corrosion of four magnesium alloys and the associated bone response, Biomaterials, 26 (2005) 3557-3563.

[44] F. Witte, J. Fischer, J. Nellesen, C. Vogt, J. Vogt, T. Donath, F. Beckmann, In vivo corrosion and corrosion protection of magnesium alloy LAE442, Acta Biomaterialia, (2009).

[45] Y. Liao, D. Chen, J. Niu, J. Zhang, Y. Wang, Z. Zhu, G. Yuan, Y. He, Y. Jiang, In vitro degradation and mechanical properties of polyporous CaHPO4-coated Mg–Nd–Zn–Zr alloy as potential tissue engineering scaffold, Materials Letters, 100 (2013) 306-308.

[46] S. Zhang, J. Li, Y. Song, C. Zhao, X. Zhang, C. Xie, Y. Zhang, H. Tao, Y. He, Y. Jiang, Y. Bian, In vitro degradation, hemolysis and MC3T3-E1 cell adhesion of biodegradable Mg-Zn alloy, Materials Science and Engineering C, 29 (2009) 1907-1912.

[47] H. Windhagen, K. Radtke, A. Weizbauer, J. Diekmann, Y. Noll, U. Kreimeyer, R. Schavan, C. Stukenborg-Colsman, H. Waizy, Biodegradable magnesium-based screw clinically equivalent to titanium screw in hallux valgus surgery: Short term results of the first prospective, randomized, controlled clinical pilot study, BioMedical Engineering Online, 12 (2013).

[48] K.F. Farraro, K.E. Kim, S.L.Y. Woo, J.R. Flowers, M.B. McCullough, Revolutionizing orthopaedic biomaterials: The potential of biodegradable and bioresorbable magnesium-based materials for functional tissue engineering, Journal of Biomechanics, 47 (2014) 1979-1986.

[49] G.L. Song, A. Atrens, Corrosion mechanisms of magnesium alloys, Advanced Engineering Materials, 1 (1999) 11-33.

[50] ASTM Standard B951-11, "Standard practice for codification of unalloyed magnesium and magnesium alloys, cast and wrought", ASTM International, West Conshohocken, PA, 2011, in.

[51] F. Witte, N. Hort, C. Vogt, S. Cohen, K.U. Kainer, R. Willumeit, F. Feyerabend, Degradable biomaterials based on magnesium corrosion, Current Opinion in Solid State and Materials Science, 12 (2008) 63-72.

[52] X. Gu, Y. Zheng, Y. Cheng, S. Zhong, T. Xi, In vitro corrosion and biocompatibility of binary magnesium alloys, Biomaterials, 30 (2009) 484-498.

[53] G.L. Makar, J. Kruger, Corrosion of magnesium, International Materials Reviews, 38 (1993) 138-153.

[54] G. Song, A. Atrens, Understanding magnesium corrosion. A framework for improved alloy performance, Advanced Engineering Materials, 5 (2003) 837-858.
[55] G. Baril, N. Pébère, Corrosion of pure magnesium in aerated and deaerated sodium sulphate solutions, Corrosion Science, 43 (2001) 471-484.

[56] A. Atrens, G.-L. Song, M. Liu, Z. Shi, F. Cao, M.S. Dargusch, Review of Recent Developments in the Field of Magnesium Corrosion, Advanced Engineering Materials, 17 (2015) 400-453.

[57] N.S. McIntyre, C. Chen, Role of impurities on Mg surfaces under ambient exposure conditions, Corrosion Science, 40 (1998) 1697-1709.

[58] J.H. Nordlien, K. Nisancioglu, S. Ono, N. Masuko, Morphology and Structure of Water-Formed Oxides on Ternary MgAl Alloys, Journal of the Electrochemical Society, 144 (1997) 461-466.

[59] J.H. Nordlien, K. Nişancioğlu, S. Ono, N. Masuko, Morphology and structure of oxide films formed on MgAl alloys by exposure to air and water, Journal of the Electrochemical Society, 143 (1996) 2564-2572.

[60] G. Baril, G. Galicia, C. Deslouis, N. Pebere, B. Tribollet, V. Vivier, An Impedance Investigation of the Mechanism of Pure Magnesium Corrosion in Sodium Sulfate Solutions, Journal of the Electrochemical Society, 154 (2007) C108-C113.

[61] J.H. Nordlien, S. Ono, N. Masuko, K. Nisancioglu, Morphology and structure of oxide films formed on magnesium by exposure to air and water, Journal of the Electrochemical Society, 142 (1995) 3320-3322.

[62] M. Santamaria, F. Di Quarto, S. Zanna, P. Marcus, Initial surface film on magnesium metal: A characterization by X-ray photoelectron spectroscopy (XPS) and photocurrent spectroscopy (PCS), Electrochimica Acta, 53 (2007) 1314-1324.

[63] M. Liu, S. Zanna, H. Ardelean, I. Frateur, P. Schmutz, G. Song, A. Atrens, P. Marcus, A first quantitative XPS study of the surface films formed, by exposure to water, on Mg and on the Mg–Al intermetallics: Al3Mg2 and Mg17Al12, Corrosion Science, 51 (2009) 1115-1127.

[64] G. Song, A. Atrens, D. Stjohn, J. Nairn, Y. Li, The electrochemical corrosion of pure magnesium in 1 N NaCl, Corrosion Science, 39 (1997) 855-875.

[65] R. Tunold, H. Holtan, M.-B.H. Berge, A. Lasson, R. Steen-Hansen, The corrosion of magnesium in aqueous solution containing chloride ions, Corrosion Science, 17 (1977) 353-365.

[66] M.D. Rausch, W.E. McEwen, J. Kleinberg, The Anodic Oxidation of Some Active Metals in Pyridine, Journal of the American Chemical Society, 77 (1955) 2093-2096.
[67] G.G. Perrault, The potential-pH diagram of the magnesium-water system, Journal of Electroanalytical Chemistry and Interfacial Electrochemistry, 51 (1974) 107-119.

[68] L. Xu, E. Zhang, D. Yin, S. Zeng, K. Yang, In vitro corrosion behaviour of Mg alloys in a phosphate buffered solution for bone implant application, Journal of Materials Science: Materials in Medicine, 19 (2008) 1017-1025.

[69] F. Witte, J. Fischer, J. Nellesen, C. Vogt, J. Vogt, T. Donath, F. Beckmann, In vivo corrosion and corrosion protection of magnesium alloy LAE442, Acta Biomaterialia, 6 (2010) 1792-1799.

[70] D. Schranz, P. Zartner, I. Michel-Behnke, H. Akintürk, Bioabsorbable metal stents for percutaneous treatment of critical recoarctation of the aorta in a newborn, Catheterization and Cardiovascular Interventions, 67 (2006) 671-673.

[71] A.E. Coy, F. Viejo, P. Skeldon, G.E. Thompson, Susceptibility of rare-earth-magnesium alloys to micro-galvanic corrosion, Corrosion Science, 52 (2010) 3896-3906.

[72] G. Song, Control of biodegradation of biocompatable magnesium alloys, Corrosion Science, 49 (2007) 1696-1701.

[73] R. Zeng, W. Dietzel, F. Witte, N. Hort, C. Blawert, Progress and challenge for magnesium alloys as biomaterials, Advanced Engineering Materials, 10 (2008) B3-B14+702.

[74] M. Bornapour, N. Muja, D. Shum-Tim, M. Cerruti, M. Pekguleryuz, Biocompatibility and biodegradability of Mg–Sr alloys: The formation of Sr-substituted hydroxyapatite, Acta Biomaterialia, 9 (2013) 5319-5330.

[75] N. Pebere, C. Riera, F. Dabosi, Investigation of magnesium corrosion in aerated sodium sulfate solution by electrochemical impedance spectroscopy, Electrochimica Acta, 35 (1990) 555-561.

[76] G. Song, A. Atrens, M. Dargusch, Influence of microstructure on the corrosion of diecast AZ91D, Corrosion Science, 41 (1998) 249-273.

[77] Y. Liu, D. Liu, C. You, M. Chen, Effects of grain size on the corrosion resistance of pure magnesium by cooling rate-controlled solidification, Front. Mater. Sci., 9 (2015) 247-253.

[78] H. Wang, Y. Estrin, Z. Zúberová, Bio-corrosion of a magnesium alloy with different processing histories, Materials Letters, 62 (2008) 2476-2479.

[79] L. Xu, C. Liu, Y. Wan, X. Wang, H. Xiao, Effects of heat treatments on microstructures and mechanical properties of Mg–4Y–2.5Nd–0.7Zr alloy, Materials Science and Engineering: A, 558 (2012) 1-6.

[80] N. Hort, Y. Huang, D. Fechner, M. Störmer, C. Blawert, F. Witte, C. Vogt, H. Drücker, R. Willumeit, K.U. Kainer, F. Feyerabend, Magnesium alloys as implant materials - Principles of property design for Mg-RE alloys, Acta Biomaterialia, (2009).

[81] Y. Xin, T. Hu, P.K. Chu, Influence of test solutions on in vitro studies of biomedical magnesium alloys, Journal of the Electrochemical Society, 157 (2010) C238-C243.

[82] A. Oyane, H.M. Kim, T. Furuya, T. Kokubo, T. Miyazaki, T. Nakamura, Preparation and assessment of revised simulated body fluids, Journal of Biomedical Materials Research - Part A, 65 (2003) 188-195.

[83] R. Rettig, S. Virtanen, Time-dependent electrochemical characterization of the corrosion of a magnesium rare-earth alloy in simulated body fluids, Journal of Biomedical Materials Research - Part A, 85 (2008) 167-175.

[84] C. Liu, Y. Xin, X. Tian, P.K. Chu, Degradation susceptibility of surgical magnesium alloy in artificial biological fluid containing albumin, Journal of Materials Research, 22 (2007) 1806-1814.

[85] Y. Xin, K. Huo, H. Tao, G. Tang, P.K. Chu, Influence of aggressive ions on the degradation behavior of biomedical magnesium alloy in physiological environment, Acta Biomaterialia, 4 (2008) 2008-2015.

[86] W.D. Müller, M.L. Nascimento, M. Zeddies, M. Córsico, L.M. Gassa, M.A.F.L. de Mele, Magnesium and its alloys as degradable biomaterials. Corrosion studies using potentiodynamic and EIS electrochemical techniques, Materials Research, 10 (2007) 5-10.

[87] W.D. Mueller, M.F. Lorenzo De Mele, M.L. Nascimento, M. Zeddies, Degradation of magnesium and its alloys: Dependence on the composition of the synthetic biological media, Journal of Biomedical Materials Research - Part A, 90 (2009) 487-495.

[88] A. Yamamoto, S. Hiromoto, Effect of inorganic salts, amino acids and proteins on the degradation of pure magnesium in vitro, Materials Science and Engineering C, 29 (2009) 1559-1568.

[89] S. Hiromoto, A. Yamamoto, N. Maruyama, H. Somekawa, T. Mukai, Influence of pH and flow on the polarisation behaviour of pure magnesium in borate buffer solutions, Corrosion Science, 50 (2008) 3561-3568.

[90] F. Witte, J. Fischer, J. Nellesen, H.A. Crostack, V. Kaese, A. Pisch, F. Beckmann, H. Windhagen, In vitro and in vivo corrosion measurements of magnesium alloys, Biomaterials, 27 (2006) 1013-1018.

[91] Y. Xin, T. Hu, P.K. Chu, In vitro studies of biomedical magnesium alloys in a simulated physiological environment: A review, Acta Biomaterialia, 7 (2011) 1452-1459.

[92] Y. Xin, T. Hu, P.K. Chu, Degradation behaviour of pure magnesium in simulated body fluids with different concentrations of, Corrosion Science, 53 (2011) 1522-1528.

[93] Y. Chen, Z. Xu, C. Smith, J. Sankar, Recent advances on the development of magnesium alloys for biodegradable implants, Acta Biomaterialia, 10 (2014) 4561-4573.

[94] Y.F. Zheng, X.N. Gu, F. Witte, Biodegradable metals, Materials Science and Engineering: R: Reports, 77 (2014) 1-34.

[95] N. Li, Y. Zheng, Novel Magnesium Alloys Developed for Biomedical Application: A Review, Journal of Materials Science & Technology, 29 (2013) 489-502.

[96] S. Amira, D. Dubé, R. Tremblay, E. Ghali, Influence of the microstructure on the corrosion behavior of AXJ530 magnesium alloy in 3.5% NaCl solution, Materials Characterization, 59 (2008) 1508-1517.

[97] H.R.B. Rad, M.H. Idris, M.R.A. Kadir, S. Farahany, Microstructure analysis and corrosion behavior of biodegradable Mg–Ca implant alloys, Materials & Design, 33 (2012) 88-97.

[98] G. Song, D. StJohn, The effect of zirconium grain refinement on the corrosion behaviour of magnesium-rare earth alloy MEZ, Journal of Light Metals, 2 (2002) 1-16.

[99] Y. Song, E.-H. Han, D. Shan, C.D. Yim, B.S. You, The role of second phases in the corrosion behavior of Mg–5Zn alloy, Corrosion Science, 60 (2012) 238-245.

[100] Y. Song, D. Shan, R. Chen, E.-H. Han, Effect of second phases on the corrosion behaviour of wrought Mg–Zn–Y–Zr alloy, Corrosion Science, 52 (2010) 1830-1837.

[101] Z. Li, G.-L. Song, S. Song, Effect of bicarbonate on biodegradation behaviour of pure magnesium in a simulated body fluid, Electrochimica Acta, 115 (2014) 56-65.

[102] H.Y. Yang, X.B. Chen, X.W. Guo, G.H. Wu, W.J. Ding, N. Birbilis, Coating pretreatment for Mg alloy AZ91D, Applied Surface Science, 258 (2012) 5472-5481.

[103] N.T. Kirkland, N. Birbilis, M.P. Staiger, Assessing the corrosion of biodegradable magnesium implants: A critical review of current methodologies and their limitations, Acta Biomaterialia, 8 (2012) 925-936.

[104] W.-D. Mueller, M. Lucia Nascimento, M.F. Lorenzo de Mele, Critical discussion of the results from different corrosion studies of Mg and Mg alloys for biomaterial applications, Acta Biomaterialia, 6 (2010) 1749-1755.

[105] E. Ghali, Conventional and Electrochemical Methods of Investigation, in: Corrosion Resistance of Aluminum and Magnesium Alloys, John Wiley & Sons, Inc., 2010, pp. 565-620.

[106] ASTM Standard G1-03, "Standard practice for preparing, cleaning and evaluating corrosion test specimens", ASTM International, West Conshohocken, PA, 2011., in.

[107] S. Zhang, X. Zhang, C. Zhao, J. Li, Y. Song, C. Xie, H. Tao, Y. Zhang, Y. He, Y. Jiang, Y. Bian, Research on an Mg-Zn alloy as a degradable biomaterial, Acta Biomaterialia, 6 (2010) 626-640.

[108] H.M. Wong, K.W.K. Yeung, K.O. Lam, V. Tam, P.K. Chu, K.D.K. Luk, K.M.C. Cheung, A biodegradable polymer-based coating to control the performance of magnesium alloy orthopaedic implants, Biomaterials, 31 (2010) 2084-2096.

[109] Y. Ren, J. Huang, B. Zhang, K. Yang, Preliminary study of biodegradation of AZ31B magnesium alloy, Frontiers of Materials Science in China, 1 (2007) 401-404.

[110] Y.C. Xin, Corrosion behavior of biomedical AZ91 magnesium alloy in simulated body fluids, Journal of Materials Research, 22 (2007) 2004-2011.

[111] ASTM Standard G31-72, "Standard practice for laboratory immersion corrosion testing of metals", ASTM International, West Conshohocken, PA, 2004., in.

[112] Z. Shi, M. Liu, A. Atrens, Measurement of the corrosion rate of magnesium alloys using Tafel extrapolation, Corrosion Science, 52 (2010) 579-588.

[113] E. Ghali, W. Dietzel, K.U. Kainer, Testing of general and localized corrosion of magnesium alloys: A critical review, Journal of Materials Engineering and Performance, 13 (2004) 517-529.

[114] G. Song, S. Song, A possible biodegradable magnesium implant material, Advanced Engineering Materials, 9 (2007) 298-302.

[115] X. Gu, Y. Zheng, S. Zhong, T. Xi, J. Wang, W. Wang, Corrosion of, and cellular responses to Mg-Zn-Ca bulk metallic glasses, Biomaterials, 31 (2010) 1093-1103.

[116] H.X. Zhang, Q. Li, L.Q. Li, J.C. Zhou, S.Y. Wang, F. Liu, P. Zhang, In vitro studies of hydrothermally treated magnesium alloy in common simulated body fluid, Transactions of the IMF, 91 (2013) 141-149.

[117] M.I. Jamesh, G. Wu, Y. Zhao, D.R. McKenzie, M.M.M. Bilek, P.K. Chu, Electrochemical corrosion behavior of biodegradable Mg–Y–RE and Mg–Zn–Zr alloys in Ringer's solution and simulated body fluid, Corrosion Science, 91 (2015) 160-184.

[118] M. Bornapour, M. Celikin, M. Pekguleryuz, Thermal exposure effects on the in vitro degradation and mechanical properties of Mg-Sr and Mg-Ca-Sr biodegradable implant alloys and the role of the microstructure, Materials Science and Engineering C, 46 (2015) 16-24.

[119] M. Bornapour, M. Celikin, M. Cerruti, M. Pekguleryuz, Magnesium implant alloy with low levels of strontium and calcium: The third element effect and phase selection

improve bio-corrosion resistance and mechanical performance, Materials Science and Engineering: C, 35 (2014) 267-282.

[120] M.I. Jamesh, G. Wu, Y. Zhao, D.R. McKenzie, M.M.M. Bilek, P.K. Chu, Effects of zirconium and oxygen plasma ion implantation on the corrosion behavior of ZK60 Mg alloy in simulated body fluids, Corrosion Science, 82 (2014) 7-26.

[121] A. Alabbasi, S. Liyanaarachchi, M.B. Kannan, Polylactic acid coating on a biodegradable magnesium alloy: An in vitro degradation study by electrochemical impedance spectroscopy, Thin Solid Films, 520 (2012) 6841-6844.

[122] M.E. Orazem, B. Tribollet, Equivalent Circuit Analogs, in: Electrochemical Impedance Spectroscopy, John Wiley & Sons, Inc., 2008, pp. 153-162.

[123] W.R. Zhou, Y.F. Zheng, M.A. Leeflang, J. Zhou, Mechanical property, biocorrosion and in vitro biocompatibility evaluations of Mg–Li–(Al)–(RE) alloys for future cardiovascular stent application, Acta Biomaterialia, 9 (2013) 8488-8498.

[124] L. Mao, L. Shen, J. Niu, J. Zhang, W. Ding, Y. Wu, R. Fan, G. Yuan, Nanophasic biodegradation enhances the durability and biocompatibility of magnesium alloys for the next-generation vascular stents, Nanoscale, 5 (2013) 9517-9522.

[125] L. Mao, G. Yuan, S. Wang, J. Niu, G. Wu, W. Ding, A novel biodegradable Mg–Nd–Zn–Zr alloy with uniform corrosion behavior in artificial plasma, Materials Letters, 88 (2012) 1-4.

[126] A.C. Hänzi, I. Gerber, M. Schinhammer, J.F. Löffler, P.J. Uggowitzer, On the in vitro and in vivo degradation performance and biological response of new biodegradable Mg–Y–Zn alloys, Acta Biomaterialia, 6 (2010) 1824-1833.

[127] C.H. Ku, D.P. Pioletti, M. Browne, P.J. Gregson, Effect of different Ti-6Al-4V surface treatments on osteoblasts behaviour, Biomaterials, 23 (2002) 1447-1454.

[128] Y. Nakamura, Y. Tsumura, Y. Tonogai, T. Shibata, Y. Ito, Differences in behavior among the chlorides of seven rare earth elements administered intravenously to rats, Toxicological Sciences, 37 (1997) 106-116.

[129] W. Yang, P. Zhang, J. Liu, Y. Xue, Effect of long-term intake of Y3+ in drinking water on gene expression in brains of rats, Journal of Rare Earths, 24 (2006) 369-373.

[130] Z. Li, X. Gu, S. Lou, Y. Zheng, The development of binary Mg-Ca alloys for use as biodegradable materials within bone, Biomaterials, 29 (2008) 1329-1344.

[131] Y. Wan, G. Xiong, H. Luo, F. He, Y. Huang, X. Zhou, Preparation and characterization of a new biomedical magnesium–calcium alloy, Materials & Design, 29 (2008) 2034-2037.

[132] Y. Sun, B. Zhang, Y. Wang, L. Geng, X. Jiao, Preparation and characterization of a new biomedical Mg–Zn–Ca alloy, Materials & Design, 34 (2012) 58-64.

[133] E. Zhang, D. Yin, L. Xu, L. Yang, K. Yang, Microstructure, mechanical and corrosion properties and biocompatibility of Mg-Zn-Mn alloys for biomedical application, Materials Science and Engineering C, 29 (2009) 987-993.

[134] L. Xu, G. Yu, E. Zhang, F. Pan, K. Yang, In vivo corrosion behavior of Mg-Mn-Zn alloy for bone implant application, Journal of Biomedical Materials Research - Part A, 83 (2007) 703-711.

[135] H.S. Brar, J. Wong, M.V. Manuel, Investigation of the mechanical and degradation properties of Mg-Sr and Mg-Zn-Sr alloys for use as potential biodegradable implant materials, Journal of the Mechanical Behavior of Biomedical Materials, 7 (2012) 87-95.

[136] X.B. Chen, N. Birbilis, T.B. Abbott, Review of Corrosion-Resistant Conversion Coatings for Magnesium and Its Alloys, Corrosion, 67 (2011) 035005-035001-035005-035016.

[137] J.E. Gray, B. Luan, Protective coatings on magnesium and its alloys — a critical review, Journal of Alloys and Compounds, 336 (2002) 88-113.

[138] S. Pommiers, J. Frayret, A. Castetbon, M. Potin-Gautier, Alternative conversion coatings to chromate for the protection of magnesium alloys, Corrosion Science, 84 (2014) 135-146.

[139] C. Zhong, F. Liu, Y. Wu, J. Le, L. Liu, M. He, J. Zhu, W. Hu, Protective diffusion coatings on magnesium alloys: A review of recent developments, Journal of Alloys and Compounds, 520 (2012) 11-21.

[140] C. Lorenz, J.G. Brunner, P. Kollmannsberger, L. Jaafar, B. Fabry, S. Virtanen, Effect of surface pre-treatments on biocompatibility of magnesium, Acta Biomaterialia, 5 (2009) 2783-2789.

[141] A.C. Hänzi, P. Gunde, M. Schinhammer, P.J. Uggowitzer, On the biodegradation performance of an Mg-Y-RE alloy with various surface conditions in simulated body fluid, Acta Biomaterialia, 5 (2009) 162-171.

[142] L. Guo, K. Liu, S. Zhang, J. Huang, L. Tan, K. Yang, Cytotoxicity of AZ31B magnesium alloy covering with magnesium oxide, Xiyou Jinshu Cailiao Yu Gongcheng/Rare Metal Materials and Engineering, 37 (2008) 1027-1031.

[143] P.B. Srinivasan, J. Liang, C. Blawert, M. Störmer, W. Dietzel, Characterization of calcium containing plasma electrolytic oxidation coatings on AM50 magnesium alloy, Applied Surface Science, 256 (2010) 4017-4022.

[144] Z. Yao, L. Li, Z. Jiang, Adjustment of the ratio of Ca/P in the ceramic coating on Mg alloy by plasma electrolytic oxidation, Applied Surface Science, 255 (2009) 6724-6728.

[145] P. Shi, W.F. Ng, M.H. Wong, F.T. Cheng, Improvement of corrosion resistance of pure magnesium in Hanks' solution by microarc oxidation with sol-gel TiO2 sealing, Journal of Alloys and Compounds, 469 (2009) 286-292.

[146] J.H. Jo, J.Y. Hong, K.S. Shin, H.E. Kim, Y.H. Koh, Enhancing biocompatibility and corrosion resistance of Mg implants via surface treatments, Journal of Biomaterials Applications, 27 (2012) 469-476.

[147] S. Hiromoto, A. Yamamoto, High corrosion resistance of magnesium coated with hydroxyapatite directly synthesized in an aqueous solution, Electrochimica Acta, 54 (2009) 7085-7093.

[148] Y.W. Song, D.Y. Shan, E.H. Han, Electrodeposition of hydroxyapatite coating on AZ91D magnesium alloy for biomaterial application, Materials Letters, 62 (2008) 3276-3279.

[149] C. Wen, S. Guan, L. Peng, C. Ren, X. Wang, Z. Hu, Characterization and degradation behavior of AZ31 alloy surface modified by bone-like hydroxyapatite for implant applications, Applied Surface Science, 255 (2009) 6433-6438.

[150] M. Carboneras, M.C. García-Alonso, M.L. Escudero, Biodegradation kinetics of modified magnesium-based materials in cell culture medium, Corrosion Science, 53 (2011) 1433-1439.

[151] T. Yan, L. Tan, D. Xiong, X. Liu, B. Zhang, K. Yang, Fluoride treatment and in vitro corrosion behavior of an AZ31B magnesium alloy, Materials Science and Engineering C, 30 (2010) 740-748.

[152] J.E. Gray-Munro, C. Seguin, M. Strong, Influence of surface modification on the in vitro corrosion rate of magnesium alloy AZ31, Journal of Biomedical Materials Research - Part A, 91 (2009) 221-230.

[153] A. Abdal-hay, N.A.M. Barakat, J.K. Lim, Influence of electrospinning and dip-coating techniques on the degradation and cytocompatibility of Mg-based alloy, Colloids and Surfaces A: Physicochemical and Engineering Aspects, 420 (2013) 37-45.

[154] R.M. Rasal, A.V. Janorkar, D.E. Hirt, Poly(lactic acid) modifications, Progress in Polymer Science, 35 (2010) 338-356.

[155] M.B. Kannan, S. Liyanaarachchi, Hybrid coating on a magnesium alloy for minimizing the localized degradation for load-bearing biodegradable mini-implant applications, Materials Chemistry and Physics, 142 (2013) 350-354.

[156] G. Rohman, Materials Used in Biomaterial Applications, in: Biomaterials, John Wiley & Sons, Inc., 2014, pp. 27-81.

[157] J. Degner, F. Singer, L. Cordero, A.R. Boccaccini, S. Virtanen, Electrochemical investigations of magnesium in DMEM with biodegradable polycaprolactone coating as corrosion barrier, Applied Surface Science, 282 (2013) 264-270.

[158] M. Park, J. Lee, C. Park, S. Lee, H. Seok, Y. Choy, Polycaprolactone coating with varying thicknesses for controlled corrosion of magnesium, J Coat Technol Res, 10 (2013) 695-706.

[159] X. Tang, S.K. Thankappan, P. Lee, S.E. Fard, M.D. Harmon, K. Tran, X. Yu, Chapter 21 - Polymeric Biomaterials in Tissue Engineering and Regenerative Medicine, in: S.G.K.T.L. Deng (Ed.) Natural and Synthetic Biomedical Polymers, Elsevier, Oxford, 2014, pp. 351-371.

[160] M. Labet, W. Thielemans, Synthesis of polycaprolactone: A review, Chemical Society Reviews, 38 (2009) 3484-3504.

[161] B.-D. Hahn, D.-S. Park, J.-J. Choi, J. Ryu, W.-H. Yoon, J.-H. Choi, H.-E. Kim, S.-G. Kim, Aerosol deposition of hydroxyapatite–chitosan composite coatings on biodegradable magnesium alloy, Surface and Coatings Technology, 205 (2011) 3112-3118.

[162] K. Bai, Y. Zhang, Z. Fu, C. Zhang, X. Cui, E. Meng, S. Guan, J. Hu, Fabrication of chitosan/magnesium phosphate composite coating and the in vitro degradation properties of coated magnesium alloy, Materials Letters, 73 (2012) 59-61.

[163] J. Zhang, C.-S. Dai, J. Wei, Z.-H. Wen, Study on the bonding strength between calcium phosphate/chitosan composite coatings and a Mg alloy substrate, Applied Surface Science, 261 (2012) 276-286.

[164] X.N. Gu, Y.F. Zheng, Q.X. Lan, Y. Cheng, Z.X. Zhang, T.F. Xi, D.Y. Zhang, Surface modification of an Mg-1Ca alloy to slow down its biocorrosion by chitosan, Biomedical materials (Bristol, England), 4 (2009) 044109.

[165] R. Balint, N.J. Cassidy, S.H. Cartmell, Conductive polymers: Towards a smart biomaterial for tissue engineering, Acta Biomaterialia, 10 (2014) 2341-2353.

[166] N.K. Guimard, N. Gomez, C.E. Schmidt, Conducting polymers in biomedical engineering, Progress in Polymer Science, 32 (2007) 876-921.

[167] N. Sheng, M. Ueda, T. Ohtsuka, The formation of polypyrrole film on zinc-coated AZ91D alloy under constant current characterized by Raman spectroscopy, Progress in Organic Coatings, 76 (2013) 328-334.

[168] T.F. Otero, C. Santamaría, Dependence of polypyrrole production on potential, Synthetic Metals, 51 (1992) 313-319.

[169] M.C. Turhan, M. Weiser, M.S. Killian, B. Leitner, S. Virtanen, Electrochemical polymerization and characterization of polypyrrole on Mg–Al alloy (AZ91D), Synthetic Metals, 161 (2011) 360-364.

[170] M. Rohwerder, Conducting polymers for corrosion protection: a review, International Journal of Materials Research, 100 (2009) 1331-1342.

[171] P. Deshpande, N. Jadhav, V. Gelling, D. Sazou, Conducting polymers for corrosion protection: a review, J Coat Technol Res, 11 (2014) 473-494.

[172] M.C. Turhan, D. Rückle, M.S. Killian, H. Jha, S. Virtanen, Corrosion Behavior of Polypyrrole/AZ91D in Simulated Body Fluid Solutions and Its Functionalization with Albumin Monolayers, Corrosion, 68 (2012) 536-547.

[173] M.C. Turhan, M. Weiser, H. Jha, S. Virtanen, Optimization of electrochemical polymerization parameters of polypyrrole on Mg–Al alloy (AZ91D) electrodes and corrosion performance, Electrochimica Acta, 56 (2011) 5347-5354.

[174] A. Srinivasan, P. Ranjani, N. Rajendran, Electrochemical polymerization of pyrrole over AZ31 Mg alloy for biomedical applications, Electrochim Acta, 88 (2013) 310-321.

[175] S. Asavapiriyanont, G.K. Chandler, G.A. Gunawardena, D. Pletcher, The electrodeposition of polypyrrole films from aqueous solutions, Journal of Electroanalytical Chemistry and Interfacial Electrochemistry, 177 (1984) 229-244.

Chapter 3

Statement of Objectives

As demonstrated in Chapter 2, Mg-based materials are promising candidates for the development of biodegradable implants; however, their corrosion rate needs to be controlled and their biocompatibility improved before they can be approved and commercialized for clinical use. Faster and more efficient development of suitable Mg-based biodegradable materials is hampered by the lack of complete understanding of the Mg alloy corrosion mechanisms *in vivo* and by difficulties at simulating such environment *in vitro*. *In vivo* experiments are expensive, time consuming and pose some limitations for the investigation and monitoring of the implant corrosion behavior and thus, the use of adequate and reliable *in vitro* methodologies is crucial for the development and optimization of new Mg alloys. The effect of several experimental parameters such as alloy composition and microstructure, electrolyte composition and the use of surface pretreatments and protective coatings on the corrosion behaviour of Mg alloys has been investigated by researchers. However, up to the present date, little information has been provided regarding the time-dependence of the corrosion mechanisms of the investigated Mg alloys. Furthermore, a lack of correlation observed between *in vivo* and *in vitro* corrosion results has been attributed to limitations of current *in vitro* methodologies, such as the omission of important electrolyte components and the accumulation of corrosion products that lead to a fast increase in the electrolyte pH, possibly affecting the Mg alloys corrosion mechanisms.

Consequently, in an attempt to gain better fundamental understanding of the corrosion mechanisms of Mg alloys at experimental conditions relevant to biodegradable applications, this PhD project addressed the following objectives:

(i) Investigate the corrosion kinetics and mechanisms of WE43 Mg alloy in a modified simulated body fluid (m-SBF) for an immersion time up to five days,

(ii) Investigate the effect of electrolyte renewal, as a method to better simulate physiological homeostasis, on the corrosion behaviour of WE43 Mg alloy in m-SBF, and

(iii) Investigate the short-term (up to five days) corrosion behaviour of a polypyrrole-coated WE43 Mg alloy in m-SBF with daily electrolyte renewal.

The approach employed was the following: WE43 Mg alloy was used as a model alloy due to its good corrosion resistance, which led to its use in clinical trials by the company Biotronik (Germany) for the development of biodegradable cardiovascular stents. WE43 Mg alloy is thus an important reference often used as a control in the investigation of the corrosion behaviour of Mg-based biodegradable materials. The m-SBF was selected as the corrosive medium due to the combination of its ionic composition that is closer to that of blood plasma and its higher stability, compared to other available simulated body fluids. The pH of freshly-prepared m-SBF was adjusted to 7.4 (physiological value). HEPES was chosen as a buffer in order to better control the increase in the electrolyte pH as a result of the corrosion process. Immersion experiments were carried out for a time period up to 5 days at the average body temperature of 37 ºC and at an initial pH of 7.4, corresponding to the physiological value.

In (ii) above, complete renewal of the electrolyte was performed on a daily basis in order to better control accumulation of corrosion products and the increase in electrolyte pH as a result of the corrosion process, thereby better simulating physiological homeostasis.

In (iii) above, PPy coatings were electrochemically synthesized on WE43 Mg alloy by a galvanostatic method in a solution containing pyrrole and sodium salicylate. PPy was selected as coating material due to its well-known biocompatibility, its interesting corrosion protection mechanisms and its drug-loading and surface-functionalization capabilities. In addition, electrochemical formation of PPy films on metallic materials is a relatively simple task. The reason for the use of sodium salicylate was threefold: 1) it contributes to the formation of a partially protective Mg-salicylate layer on the Mg alloy surface, thereby decreasing its corrosion rate and allowing for PPy nucleation and growth, 2) salicylate species are incorporated into the PPy coating as dopant species, acting as corrosion inhibitors during its gradual release and, 3) sodium salicylate is biocompatible and has anti-inflammatory properties, which is of relevance for biodegradable applications.

Interfacial processes and corrosion mechanisms of both bare WE43 and PPy-coated WE43 Mg alloy were investigated by electrochemical impedance spectroscopy (EIS). The WE43 corrosion kinetics was investigated by analytical and hydrogen evolution techniques, and the corrosion products layer composition and morphology were analyzed by a series of surface characterization techniques.

This PhD project addressed the following specific objectives:

(i) Investigate the effect of immersion time on the WE43 corrosion kinetics and corrosion mechanisms, the variation in the electrolyte composition and pH, the production of hydrogen gas and the protective properties of the formed corrosion layer.

(ii) Investigate the effect of electrolyte renewal and the corresponding variation in the electrolyte composition and pH on the WE43 corrosion kinetics and corrosion mechanisms, the production of hydrogen gas and the protective properties of the formed corrosion layer.

(iii) Investigate the composition, thickness and surface morphology of corrosion products formed on WE43 Mg alloy in m-SBF with and without electrolyte renewal.

(iv) Synthesize PPy coatings on a WE43 Mg alloy surface by electrochemical techniques and investigate the composition, thickness, morphology and surface adhesion of the formed PPy coatings.

(v) Investigate the corrosion kinetics and corrosion mechanisms of a PPy-coated WE43 Mg alloy in m-SBF with daily electrolyte renewal, the production of hydrogen gas and the composition, thickness and surface morphology of the corrosion products.

The following chapters in the thesis will address the specific objectives mentioned above. Namely, Chapter 4 will discuss the effect of immersion time on the corrosion kinetics and corrosion mechanisms of WE43 Mg alloy in m-SBF, and on the composition, thickness and morphology of the formed corrosion layer. In addition, the relationship between the time-dependent shape of the impedance response and the

corresponding corrosion mechanism taking place will be discussed. In Chapter 5, the effect of daily electrolyte renewal on the corrosion kinetics and corrosion mechanisms of WE43 Mg alloy in m-SBF will be discussed, taking into account the resulting variation in the electrolyte composition and pH and their effect on the corrosion layer protective properties. In addition, the corrosion behaviour observed with and without daily electrolyte renewal will be compared. In Chapter 6, PPy coatings are electrochemically synthesized on WE43 Mg alloy and the corrosion behaviour of PPy-coated WE43 Mg alloy in m-SBF and the corresponding corrosion mechanisms are discussed. Finally, an investigation of the corrosion behaviour of WE43 Mg alloy in m-SBF under continuous electrolyte flow conditions will be presented in the appendix.

Each of the following four chapters is written in a manuscript-based style, so the reader can follow the results and the corresponding discussion more easily. In this way, the connection between the above outlined objectives and the research results are more clearly presented.

Chapter 4

An investigation of the corrosion mechanisms of WE43 Mg alloy in a modified simulated body fluid solution: The influence of immersion time

M. Ascencio[1], M. Pekguleryuz[2] and S. Omanovic[1]

(1) Department of Chemical Engineering, (2) Department of Mining and Materials Engineering
McGill University, Montreal, Quebec, H3A 0C5, Canada

PREFACE

This chapter is comprised of one published journal manuscript. As is was explained in the previous chapters, the understanding of the corrosion mechanisms at *in vitro* experimental conditions resembling the physiological environment is necessary for an accurate assessment and prediction of the *in vivo* performance of potential Mg alloy materials. The focus of this part of the study is to investigate the effect of immersion time on the corrosion kinetics and mechanisms of a model WE43 Mg alloy in a modified simulated body fluid (m-SBF). The production of hydrogen gas, the variation in the electrolyte pH and concentration of magnesium, calcium and phosphate ions, and the morphology and composition of the corrosion products layer were also investigated. Immersion experiments were performed for a time period up to five days at 37 ºC and at an initial pH of 7.4, corresponding to physiological conditions. Interfacial processes such as charge transfer, adsorption of Mg intermediates and diffusion of Mg^{2+} ions were investigated and monitored after different immersion times by electrochemical impedance spectroscopy (EIS). Normalized corrosion rate values calculated by EIS,

hydrogen evolution and ICP-OES are compared and their variation with time is discussed. The corrosion products layer composition and morphology were investigated by SEM, EDS, XRD, ATR-FTIR and XPS. Finally, a corrosion mechanism as a function of immersion time was proposed taking into account the analysis of the corrosion kinetics results, the EIS time-dependent fitting parameters and the characterization of the corrosion products layer.

The co-authors of the manuscript presented in this chapter are listed above. The contributions of each author were the following: Mario Ascencio designed the experiments, prepared samples, performed the experimental work, analyzed results and wrote the manuscript. Prof. Mihriban Pekguleryuz provided samples and contributed in the interpretation and discussion of results. Prof. Sasha Omanovic provided guidance, contributed in the interpretation and discussion of results and corrected the manuscript.

The authors gratefully acknowledge the financial support from the Natural Science and Engineering Research Council of Canada (NSERC) and the National Council of Science and Technology of Mexico (CONACyT). The contribution of Pierre Vermette in the casting of the Mg alloy samples is also acknowledged.

An investigation of the corrosion mechanisms of WE43 Mg alloy in a modified simulated body fluid solution: The influence of immersion time

This section has been published as: M. Ascencio, M. Pekguleryuz, S. Omanovic, An investigation of the corrosion mechanisms of WE43 Mg alloy in a modified simulated body fluid solution: The influence of immersion time, Corrosion Science, 87 (2014) 489-503.

4.1 ABSTRACT

The corrosion mechanisms and kinetics of WE43 Mg alloy in a modified simulated body fluid (m-SBF) are investigated by electrochemical, hydrogen evolution and analytical techniques. The changes in the impedance response over time are related to four corrosion stages involving the formation of a partially protective corrosion layer and adsorption of Mg intermediates, formation of an inner passive MgO layer with increasing coverage over time, rupture of the corrosion layer and lateral growth of stable pits. ATR-FTIR, XRD and XPS results show the presence of an amorphous carbonated apatite/$Mg(OH)_2$ mixed corrosion layer.

4.2 INTRODUCTION

The development of biodegradable implants for orthopaedic and cardiovascular applications has gained considerable attention as an alternative to avoid long-term complications caused by permanent implants. A biodegradable device should be able to

provide adequate mechanical support until the surrounding tissue has healed and then dissolve/biodegrade without causing any important inflammatory/immunological response.

Magnesium is a promising material for such applications mainly due to its biocompatibility and adequate mechanical properties. In addition, the degradation products of Mg are expected to be physiologically beneficial. Magnesium is an essential element and its importance in many metabolic reactions and physiological functions has been reviewed [1-4]. The recommended dietary allowance (RDA) of Mg is 330-420 mg/day for adult males and 225-320 mg/day for adult females [5]. Mg depletion has been linked to the development of cardiovascular disease, hypertension and diabetes mellitus [2, 5]. Mg is absorbed by the intestine and its availability is regulated mainly by the kidney [6]. In the absence of renal failure, severe side effects due to Mg intake are extremely rare [3].

In addition to its good biocompatibility, Mg has mechanical properties similar to those of human bone and this makes it an attractive material for orthopaedic applications. Mg and its alloys have a similar Young's modulus and a favorable compression and tensile strength with respect to the cortical bone [7]. Furthermore, the superior mechanical properties of Mg alloys in comparison to polymeric materials make them good candidates for stent applications in small vessels such as the coronary arteries, where a high strength to bulk ratio is required [1, 8]. Biodegradable stents offer the possibility of more physiological repair, reconstitution of local vascular compliance and the possibility for blood vessel growth without the danger of stent dislocation as with permanently implanted stents, which makes them relevant for pediatric applications [8].

The feasibility and safety of biodegradable Mg alloy implants have been demonstrated in *in vivo* experiments [9-17] and clinical trials [18, 19]. However, the main drawbacks related to the use of Mg alloys as implants are (*i*) their fast corrosion rate in the physiological environment, leading to premature loss of mechanical properties and implant failure, and (*ii*) the production of hydrogen gas at a rate the body cannot regulate, inducing subcutaneous hydrogen accumulation.

The corrosion of Mg has been extensively investigated [20-28]. In aqueous environments, Mg dissolution occurs by an electrochemical reaction, producing magnesium hydroxide and hydrogen gas (reaction (4.1)), a mechanism that is relatively insensitive to oxygen concentration differences [29]. The overall Mg corrosion reaction may be expressed as:

$$Mg + 2H_2O \rightarrow Mg(OH)_2 + H_2 \qquad (4.1)$$

However, the corrosion mechanism of Mg is actually quite complex and proceeds in steps. Thus, up to the present date, no agreement regarding the Mg partial corrosion reactions (steps) has been reached. It has been observed that Mg corrodes at a higher rate than expected during anodic polarization experiments and that the cathodic-reaction rate (hydrogen evolution) increases when the anodic potential is increased, a behaviour that is contradictory to the electrochemical theory. This anomalous phenomenon is known as the negative difference effect (NDE) and several mechanisms have been proposed to explain it [24]. Song et al. [22] proposed a corrosion mechanism in which Mg is first oxidised to Mg^+ intermediate species (reaction (4.3), below) which then react chemically with water producing hydrogen and Mg^{2+} species (reaction (4.4),

below). According to Song, this reaction occurs only on the corrosion-layer-free surface or on the corrosion-layer-broken areas, which increase at higher anodic potentials. The mechanism proposed considered the following partial reactions [22]

$2H_2O + 2e^- \rightarrow H_2 + 2OH^-$ (cathodic reaction) (4.2)

$2Mg \rightarrow 2Mg^+ + 2e^-$ (anodic reaction) (4.3)

$2Mg^+ + 2H_2O \rightarrow 2Mg^{2+} + 2OH^- + H_2$ (chemical reaction) (4.4)

$2Mg + 4H_2O \rightarrow 2Mg^{2+} + 4OH^- + 2H_2$ (overall reaction) (4.5)

$Mg^{2+} + 2OH^- \rightarrow Mg(OH)_2$ (product formation) (4.6)

Magnesium hydroxide produced in reaction (4.6) accumulates on the substrate surface forming a protective corrosion layer that decreases or prevents further corrosion of the underlying Mg substrate.

However, Mg has a poor corrosion resistance in the presence of metallic impurities or aggressive electrolyte species such as Cl^- ions and under these conditions different forms of corrosion can be observed, e.g., general, pitting and galvanic [21, 26, 30, 31]. In neutral or alkaline solution Mg corrosion typically takes the form of pitting [24]. Microgalvanic corrosion occurs due to the presence of metallic impurities, such as Ni, Fe and Cu, and second phases, which act as cathode sites [32, 33].

In the physiological environment, at pH of 6.8-7.4 and a chloride concentration of about 0.15 M, magnesium hydroxide converts into soluble magnesium chloride (reaction (4.7)) and the surface of the Mg sample can undergo severe pitting corrosion [34].

$$Mg(OH)_2 + 2Cl^- \rightarrow Mg^{2+} + 2Cl^- + 2OH^- \quad (4.7)$$

Several Mg alloys with improved mechanical and corrosion properties have been investigated for biodegradable implants applications, however, up to the present date no Mg alloy with an adequate corrosion resistance and biocompatibility for such applications has been developed. Faster and more efficient development of Mg alloys is limited due to a lack of both a complete understanding of the Mg alloy corrosion mechanisms and of a standard protocol that allows for alloy performance evaluation and composition optimization.

The corrosion behaviour of Mg alloys for biomedical applications is often investigated *in vitro* by performing immersion experiments in a simulated body fluid and carrying out electrochemical, analytical and hydrogen evolution measurements after different immersion times. Among the electrochemical techniques, electrochemical impedance spectroscopy (EIS) has been extensively used due to its high suitability for the assessment of the corrosion resistance and its capabilities in the investigation of interfacial processes. In addition, its non-destructive properties make it a suitable technique for the monitoring of the corrosion process *in situ*. An interesting approach for the investigation of the biodegradation process of Mg alloys is the monitoring of the impedance behaviour at longer immersion times and the interpretation of the corrosion process by the analysis of the impedance response time-dependent fitting parameters. Some authors have investigated the long term corrosion behaviour of Mg alloys by carrying out a qualitative analysis of the time dependent impedance response [35-39]. Others have proposed an equivalent circuit to interpret the EIS data and have explained the corrosion process as a function of the fitting parameters, e.g., charge transfer

resistance, film resistance and double layer capacitance [29, 40-44]. However, these results are not sufficient for a better understanding of the Mg alloys biodegradation process since the experiments have been carried out using rather simple electrolytes, e.g., NaCl or Na_2SO_4, only the analysis of the high frequency impedance data has been presented and/or the measurements have been performed for a short period of time. Furthermore, little information has been provided regarding the analysis of the impedance response at intermediate frequencies (second capacitive loop) and the relationship between the shape of the impedance response presented in the complex plane and the corresponding corrosion mechanism taking place.

The aim of the present work is to report our results on the investigation of the corrosion behaviour of a commercially available yttrium-rare earth Mg alloy (WE43) in a modified simulated body fluid (m-SBF). Interfacial processes such as charge transfer, diffusion and adsorption of species were investigated and monitored by EIS. The corrosion kinetics was also investigated by hydrogen evolution and analytical measurements and the results were compared to the data obtained by EIS. Finally, a corrosion mechanism is proposed taking into account the corrosion kinetics results, the analysis of the impedance response time-dependent fitting parameters and the characterization of the corrosion products and Mg alloy substrate.

4.3 EXPERIMENTAL SECTION

4.3.1 Sample preparation and electrolyte

WE43 Mg alloy supplied by Magnesium Elektron, USA was die cast into rods using an electrical induction furnace (Norax, Canada) and a boron nitride-coated steel die. CO_2 with 0.5% SF_6 was used at a flow rate of 1.1 dm^3 min^{-1} to prevent oxidation during the melting and casting processes. A K-type Chromel-Alumel thermocouple (Omega, USA) was used to monitor the temperature. Prior to the casting process, the steel die was heated to 400 °C using a Lindberg/Blue M crucible furnace (Thermal Product Solutions, USA). As-cast WE43 Mg alloy rods were machined to a diameter of 1.59 cm and cut into coins with a thickness of 0.5 cm. Electrodes were prepared by fixing an insulated copper wire to the coins using conductive silver epoxy (Chemtronics Circuitworks, USA) and embedding the coins in epoxy resin (Epofix, Struers, USA), leaving a metal-exposed area of 1.98 cm^2. Before the experiments, the exposed electrode surface was wet-ground using SiC paper up to 1200-grit and then fine-polished with diamond paste to a final polishing particle roughness of 1 μm. Finally, to remove polishing residue and degrease the surface, the samples were ultrasonically cleaned in ethanol for 10 minutes, rinsed with acetone and dried in argon. This procedure ensured a reproducible surface state of the working electrodes. The nominal composition of the WE43 Mg alloy is given in Table 4.1.

In order to better simulate the physiological environment, a buffered modified simulated body fluid (m-SBF) as defined by Oyane et al. [45], with a pH of 7.4 was used as electrolyte. The m-SBF was prepared using reagent grade chemicals and deionized

water with a resistivity of 18.2 MΩ cm. The amounts of chemicals used and the ionic composition of the m-SBF are shown in Table 4.2 and Table 4.3, respectively. In contrast with the procedure proposed by Oyane, only 10 ml of 1 M NaOH solution were necessary to adjust the pH to a final value of 7.4 and thus, the prepared m-SBF had a sodium concentration about 14% lower than that of blood plasma.

Table 4.1: Nominal composition of WE43 Mg alloy.

Element	Mass Fraction (wt. %)
Yttrium	3.7-4.3
Rare earths (mainly Nd)	2.4-4.4
Zirconium	Min. 0.4
Magnesium	Balance

Table 4.2: Amounts of reagents used to prepare 1000 ml of m-SBF [45].

Reagents[a]	Purity / %	Amount
NaCl	>99.5	5.4030 g
$NaHCO_3$	>99.5	0.5040 g
Na_2CO_3	>99	0.4260 g
KCl	>99	0.2250 g
K_2HPO_4	>98	0.1756 g
$MgCl_2 \times 6H_2O$	>99.4	0.3110 g
HEPES[b]	>99.5	17.8920 g[c]
$CaCl_2 \times 2H_2O$	>99	0.3881 g
Na_2SO_4	>99.2	0.0720 g
1.0 M NaOH	---	10 ml

[a] Listed in sequence of dissolution
[b] HEPES, 2-(4-(2-hydroxyethyl)-1-piperazinyl) ethanesulfonic acid
[c] HEPES was previously dissolved in 100 ml of 0.2M NaOH

Table 4.3: Nominal concentration of m-SBF and blood plasma [45].

Ion	Concentration / mM	
	Blood plasma	m-SBF
Na^+	142	122.5
K^+	5	5
Mg^{2+}	1.5	1.5
Ca^{2+}	2.5	2.5
Cl^-	103	103
HCO_3^-	27	10
HPO_4^{2-}	1	1
SO_4^{2-}	0.5	0.5

4.3.2. Experimental set-up

WE43 Mg alloy electrodes were immersed in m-SBF for a time period up to 5 days. Independent experiments at different immersion times were performed in which (*i*) the amount of hydrogen gas produced was measured, (*ii*) the electrolyte analysis was performed by inductively coupled plasma optical emission spectroscopy (ICP-OES), and (*iii*) electrochemical measurements were performed. All the experiments were carried out at the average human body temperature (37 °C). The electrolyte temperature was maintained using a water bath equipped with a thermostat. The volume of the electrolyte in the corrosion cell was 100 ml and all the experiments were done in triplicates. The amount of hydrogen produced was measured using an inverted funnel and a burette as described by Song et al. [22]. During the immersion experiments the pH of the electrolyte was monitored. At the end of the immersion experiments the samples were removed from the electrochemical cell, rinsed with distilled water and dried with argon gas. After surface characterization of the corrosion products, the

corrosion layer was dissolved by immersion in chromic acid (180 g CrO_3/dm^3) for 5-10 min in order to analyse the morphology of the underlying (corroded) Mg alloy substrate.

4.3.3 Electrochemical techniques

Electrochemical experiments were performed in a standard three-electrode electrochemical cell. WE43 Mg alloy samples were used as working electrode, a graphite rod as counter electrode and a commercial saturated calomel electrode (SCE, Fisher Scientific Accumet, USA) as reference electrode. All potentials in this paper are referred to the SCE. Electrochemical measurements were carried out using a potentiostat/galvanostat (Autolab PGSTAT30, Netherlands) equipped with a frequency response analyser. Open circuit potential measurements were performed over a time period of 5 days. Electrochemical impedance measurements were carried out at open circuit potential with AC amplitude of 10 mV over a frequency range from 10 mHz to 100 kHz.

4.3.4 Electrolyte analysis and corrosion products characterization

Inductively coupled plasma optical emission spectroscopy (ICP-OES, Thermo Jarrell Ash Trace Scan, USA) was used to measure the electrolyte concentration of magnesium, calcium and phosphate species at wavelengths of 285.2, 422 and 178.2 nm, respectively. The morphology and composition of the sample surface were characterized by scanning electron microscopy (FE-SEM, Philips XL-30, Netherlands) equipped with an energy-disperse spectrometer (EDS). The corrosion layer thickness was measured by cross-sectional SEM analysis of the sample. Attenuated total

reflectance Fourier transform infrared spectroscopy (ATR-FTIR, Bruker Hyperion, USA) analysis was performed to investigate the presence of chemical groups in the corrosion product layers. The corrosion layer phase composition was investigated by X-ray diffraction analysis (XRD , Bruker D8 X-ray diffractometer, USA) with Cu Kα radiation and with a current and voltage of 40 mA and 40 kV, respectively. The chemical composition of the corrosion layer was investigated by X-ray photoelectron spectroscopy (XPS, Thermo Scientific K-alpha, USA) using an X-ray source of Al Kα (1486.6 eV) with a spot size of 100 μm in diameter.

4.4 RESULTS AND DISCUSSION

4.4.1 Sample substrate and corrosion layer morphology

In order to assess the Mg alloy surface morphology prior to the immersion experiments surface-polished samples (freshly-prepared surfaces) were examined under a scanning electron microscope. Figure 4.1 shows the SEM-EDS analysis of a polished WE43 Mg alloy sample. It can be observed that the surface is relatively smooth, with a microstructure consisting of α-Mg matrix (darker areas) and some dispersed intermetallic (second phase) precipitates of varying size (lighter areas, see the arrow). EDS analysis showed the presence of carbon, oxygen and magnesium elements (Table 4.4). Yttrium and rare-earth (RE) elements present in the Mg alloy were not detected, probably due to their low content. Point/spot EDS analyses of second phase precipitates and of the α-Mg matrix revealed a similar composition, the latter, however, showing a higher oxygen content, probably due to a preferential oxidation over the intermetallic phases, indicating the formation of a thicker native oxide film. The

presence of carbon corresponds to incorporation of impurities from the atmosphere. The microstructure of commercial WE43 Mg alloy has already been investigated and RE-rich second phase precipitates with different structure and composition have been identified. The microstructure of this alloy consists of α-Mg matrix, a second phase Mg_{12}(RE,Y) segregated at the grain boundaries [46], a needle-like β-phase ($Mg_{14}Nd_2Y$) [36, 46, 47] within the matrix and irregular Y-rich (MgY, $Mg_{24}Y_5$) [36, 46, 47], Nd-rich ($Mg_{41}Nd_5$, $Mg_{12}Nd$) [36, 47] and Zr-rich precipitates [46] distributed within the matrix and around the second phase. It has also been found that Zr-rich precipitates exhibit a greater potential difference with respect to the matrix (by about +170 mV), followed by Y-rich (by about +50 mV), Mg_{12}(RE,Y) (by about +25 mV) and β-phase (by about +15 mV) [46]. It is known that microstructural parameters such as grain size and phase distribution influence the corrosion behaviour of Mg alloys [24, 48-52]. Any alloying element in its pure form or intermetallic phase is less active than magnesium and thus acts as a cathode, promoting galvanic corrosion [34, 53, 54]. The effect of grain size on the corrosion properties [55] and the micro-galvanic corrosion [46] of WE43 Mg alloy have been investigated. Since the current work was focused on the WE43 Mg alloy general corrosion process, microstructural characterization of the Mg alloy was not carried out and the local effect of the intermetallic precipitates on the corrosion mechanism was not investigated.

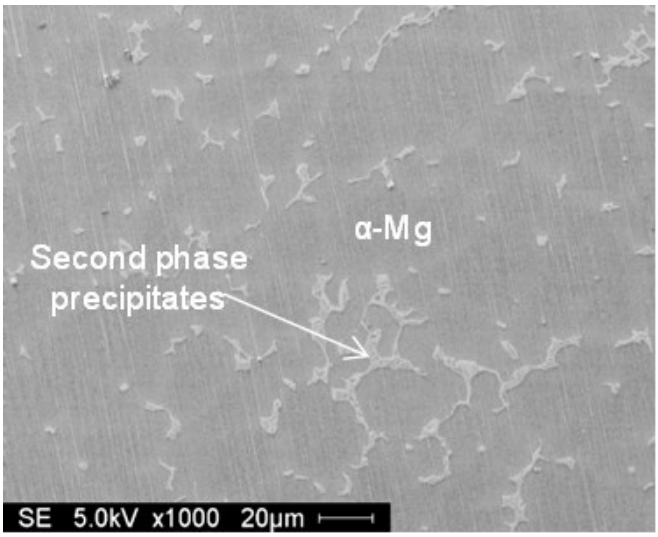

Figure 4.1: SEM analysis of WE43 Mg alloy showing the presence of second phase precipitates and α-Mg matrix on the surface of a polished WE43 Mg alloy sample.

Table 4.4: Elemental composition of WE43 Mg alloy samples obtained by EDS.

Sample	Elemental composition at. %							Ca/P
	C	O	Na	Mg	P	Ca	Cl	
WE43 clean	14.25	8.09	-	77.66	-	-	-	-
WE43 corroded surface (A)	32.31	53.13	0.91	5.52	6.51	1.62	-	0.25
WE43 corroded surface (B)	21.54	52.05	0.69	7.30	7.26	11.16	-	1.54

The corrosion layer surface morphology after different immersion times is shown in Figure 4.2. A cracked-mud surface morphology can be observed on most of the surface, but continuous non-cracked regions are also apparent (some of these are bordered by a white line in Figure 4.2a in the upper left corner, but the regions are visible across the whole surface presented). The cracks were, most likely, formed due to dehydration of the corrosion layer by the vacuum atmosphere created during the SEM analysis. Continuous, white-bordered regions can be related to the formation of a corrosion layer

on second phase precipitates, while the cracked area corresponds to the formation of a corrosion layer due to preferential attack on the α-Mg matrix (Figure 2a-d). At longer immersion times, formation of a thicker corrosion layer was observed and second phase precipitate regions could no longer be clearly distinguished (Figure 2e). White rounded volcano-like precipitates of different sizes formed on the corrosion layer were observed after 1h of immersion and during the entire experiment. The holes observed at the center of these precipitates were formed due to hydrogen gas production during the immersion experiment, suggesting the presence of cathodic regions underneath the precipitates. Figure 2f shows a corrosion layer defect observed after 48h of immersion, suggesting the presence of a localized corrosion process.

Figure 4.3a shows a Mg alloy sample surface after 5 days of immersion in m-SBF. A completely corroded surface, with some white precipitates of a maximum diameter of about 1.5 mm, can be seen. The occurrence of localized corrosion was evidenced by the presence of large pits partially filled with corrosion products. Cross-sectional observation of the corroded sample revealed a non-uniform corrosion layer with a thickness in the range of 15-40 μm (Figure 4.3b). To better assess the characteristics of the corrosion attack, the corrosion products were removed and the sample substrate was then analysed. Figure 4.3c shows the sample substrate after dissolving the corrosion layer in chromic acid. A relatively uniformly-corroded surface and some pits with a length of about 2-4 mm can be observed. It was noticed that the substrate surface underneath the volcano-like precipitates (see Figure 4.2) was not corroded, which was further confirmed by SEM observation (Figure 4.3d). The formation of bubbles at these precipitates, observed during the immersion experiments, and the

presence of a non-corroded surface underneath the precipitates, confirmed that these regions correspond to cathodic zones where reduction of water and formation of hydrogen gas take place. These results are in agreement with the corrosion layer morphology results reported in the literature for WE43 Mg alloy exposed to different simplified SBF's [56], where the formation of round precipitates with a diameter of up to 500 μm and with a hole in the center, was attributed to the presence of cathodic regions. It was also showed that formation of these round precipitates did not occur on WE43 Mg alloy in m-SBF, which is in contrast with the present results. Coy et al. [46] observed the formation of white-rounded precipitates on the rare-earth containing Mg alloys WE43 and ZE41 in 3.5 wt. % NaCl solution. They showed that these precipitates corresponded to a large amount of corrosion products, identified as $Mg(OH)_2$, formed due to localised galvanic attack occurring at areas adjacent to Zr-rich cathodic phases, which had the largest potential difference with respect to the α-Mg matrix. They also showed that other micro-constituent phases, such as Y-rich, $Mg_{12}(RE,Y)$ and β-phase, did not have a significant effect on the WE43 Mg alloy galvanic corrosion.

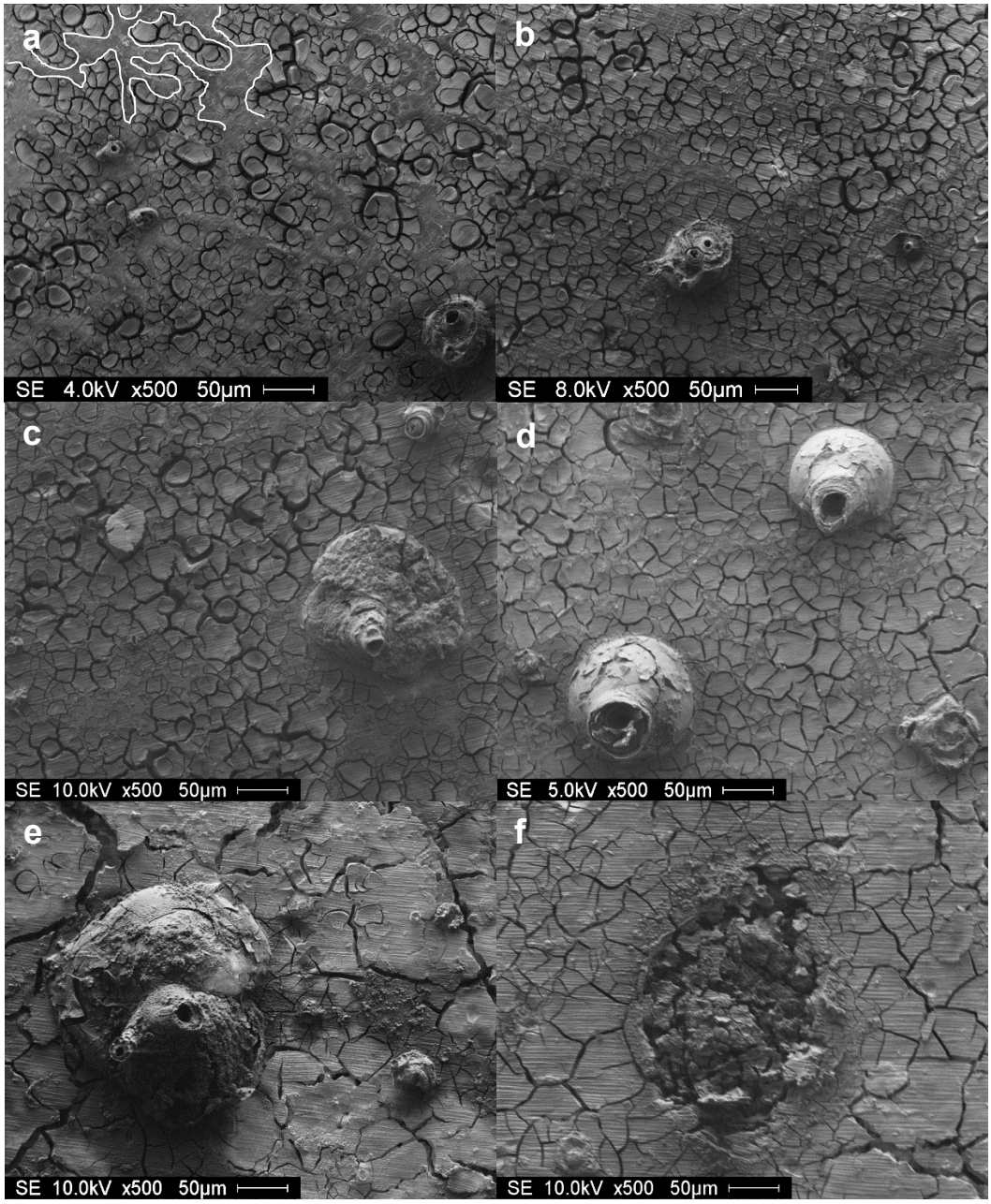

Figure 4.2: SEM images of the corroded surface of WE43 Mg alloy in m-SBF after (a) 1 h (b) 2 h (c) 4 h (d) 8 h and (e) 24 h. (f) Corrosion layer defect observed after 48 h. The white line in (a) outlines the location of second phase precipitates.

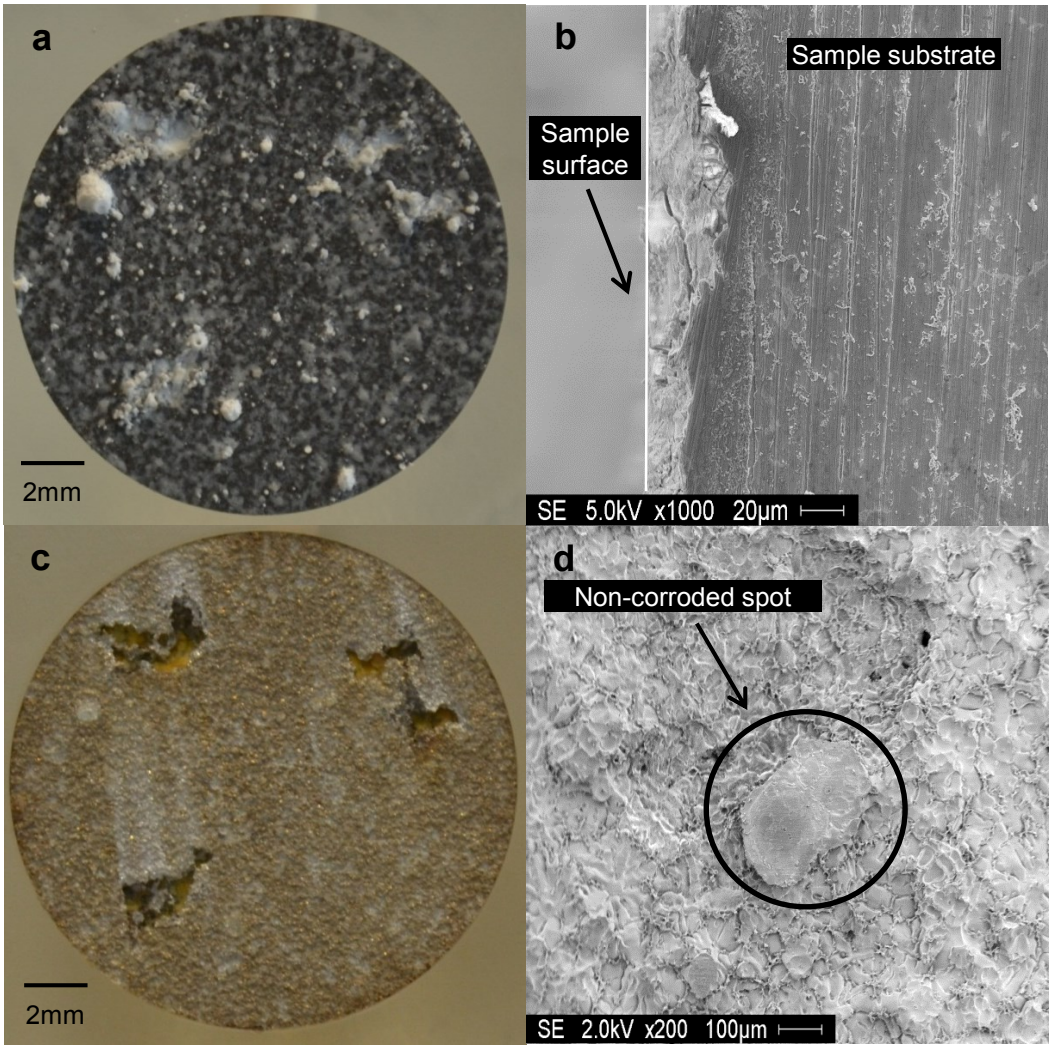

Figure 4.3: Pictures of WE43 Mg alloy in m-SBF after 5 days of immersion. Optical images of (a) a corroded surface and (c) a sample substrate surface after dissolving the corrosion layer, and SEM images of (b) a sample cross-sectional view and (d) a sample substrate showing a non-corroded spot (circled area).

4.4.2 Electrochemical experiments

Figure 4.4a shows the open circuit potential (OCP) time dependence of a WE43 Mg alloy electrode immersed in m-SBF. OCP measurements provide information on the "natural" corrosion behaviour of the system in the absence of any external current or potential bias. A rather steep increase in the OCP to more positive values can be

observed until a time of 4 h, followed by a slower increase to finally reach a constant value of ca. -1.62 V after a time of 48 h. The increase in OCP can be related to the formation of a corrosion layer with increasing protective properties over time. The constant OCP value after 48 h suggests that equilibrium has been reached and/or that a constant surface coverage by the corrosion layer has been reached.

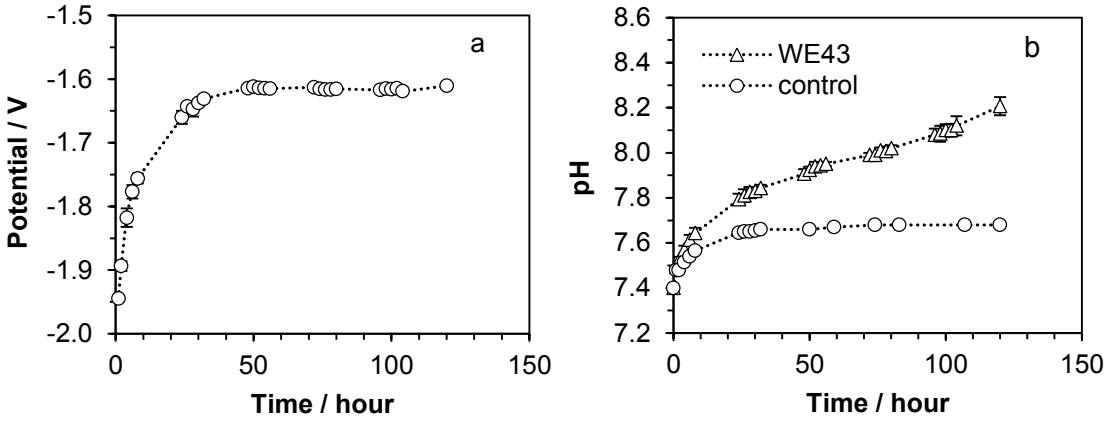

Figure 4.4: Time dependent behaviour of (a) open circuit potential (OCP) and (b) electrolyte pH of WE43 Mg alloy in m-SBF.

The formation of a protective corrosion layer was accompanied by an increase in the electrolyte pH from an initial value of 7.4 to a value of 8.2, after an immersion time of 120 h (Figure 4.4b; note that the figure also shows the time-dependent variation of pH of the electrolyte in the absence of WE43 sample immersed in it - control). A fast pH increase during the first 8 h of immersion was observed for the solution with the corroding sample (triangles), followed by a quasi-linear increase from 30-120 h. On the other hand, the initial increase in pH of the control (circles) is slower, and after 24 h it levels off into a plateau. The pH increase in the presence of corroding sample can thus be attributed to the production of OH^- species as a result of the corrosion process

(reaction (4.5)) and to the release of CO_2 to the atmosphere according to reaction (4.8) [30]:

$$H_2CO_{3(aq)} \leftrightarrow CO_{2(g)} + H_2O_{(aq)} \quad (4.8)$$

Therefore, the fast pH increase observed during the first 24 h corresponds to the combined effect of a fast initial corrosion rate and the release of CO_2 gas to the atmosphere, whereas the pH increase after 24 h corresponds only to the increase in the OH^- ions concentration due to the corrosion process. These results evidence the difficulties to maintain a constant pH even if a buffered media is used. It has been shown that the electrolyte pH has an important effect on the corrosion rate of Mg alloys [22]. According to thermodynamic data [24], the formation of a stable $Mg(OH)_2$ layer occurs above a pH of about 10, whereas in acidic or neutral solutions Mg dissolution occurs to form Mg^{2+} ions. Therefore, at the experimental conditions in the current work, the formation of a corrosion layer is the result of a competition between the following processes: (i) production of OH^- ions and precipitation of $Mg(OH)_2$ on the sample surface, and (ii) neutralization of produced OH^- ions and dissolution of the $Mg(OH)_2$ layer due to the presence of the buffering agent. The observed formation of a corrosion layer at a relatively neutral pH can be related to the presence of a local alkaline pH due to stagnant electrolyte conditions close to the surface, and to a slower $Mg(OH)_2$ dissolution kinetics with respect to the $Mg(OH)_2$ formation kinetics. The present results suggest that the constant OCP observed after 48 h corresponds to a dynamic equilibrium between the corrosion layer formation and dissolution processes. It is interesting to observe that the increase in the electrolyte pH after a time of 48 h does

not have an effect on the OCP value, and thus, on the protective ability of the corrosion layer.

Electrochemical impedance spectroscopy (EIS) was then applied to investigate the electrode corrosion resistance and to gain information about the processes occurring at the electrode/electrolyte interface. Figure 4.5 shows the impedance response of the WE43 Mg alloy in m-SBF after 24 h of immersion. The presentation of the data in the form of a Nyquist plot reveals the presence of two capacitive loops at high and medium frequencies and an inductive loop at low frequencies, corresponding to three time constants (τ_1, τ_2 and τ_3), i.e., three different interfacial processes. These results are in agreement with the data reported in the literature for pure Mg [29, 57, 58] and Mg alloys [35, 40]. The capacitive loop at high frequencies (τ_1) has been related to charge transfer and electrochemical double-layer/oxide-film effects; the capacitive loop at medium frequencies (τ_2) has been related to mass transport relaxation due to diffusion of Mg^{2+} ions through the corrosion layer, while the inductive loop at low frequencies (τ_3) has been related to relaxation of coverage due to adsorption of Mg^{+} intermediates [58]. Thus, a three-time constant electrical equivalent circuit (EEC) was used to fit the impedance response (Figure 4.6). By using this EEC a good fit was obtained (Figure 4.7) with an average value of $\chi^2=2.7\text{x}10^{-4} \pm 1.3\text{x}10^{-4}$. In order to better fit the experimental data, a constant phase element (CPE) was used to model the electrode capacitive behaviour. CPE's are often used to describe a non-ideal capacitive behaviour due to different factors such as surface roughness and heterogeneities, electrode porosity, variation of coating composition, slow adsorption reactions or a non-uniform

potential and current distribution [59]. The impedance of a CPE is given by the following equation [60]:

$$Z_{CPE} = Q^{-1}(j\omega)^{-n} \qquad \text{with} \quad -1 \le n \le 1 \tag{4.9}$$

where Z_{CPE} is the CPE impedance (Ωcm^2), Q is a constant ($\Omega^{-1}cm^{-2}s^n$), n is a dimensionless constant in the range $-1 \le n \le 1$, j is the imaginary number $j=(-1)^{0.5}$ and ω is the angular frequency ($\omega=2\pi f$, f being the frequency). An ideal capacitor behaviour yields n =1, a resistor yields n =0 and an inductor yields n =-1, while n =0.5 represents the response of mass-transport processes.

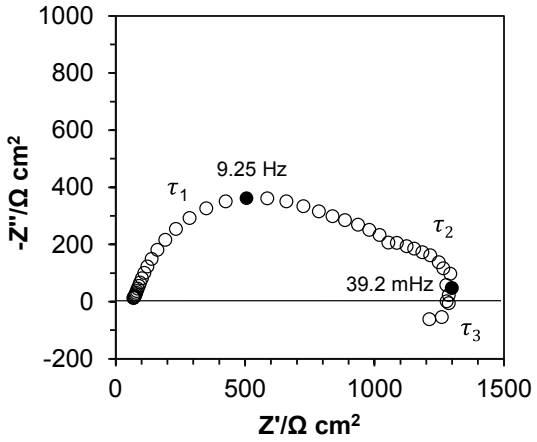

Figure 4.5: Nyquist plot of the WE43 Mg alloy electrode in m-SBF, recorded after 48 h.

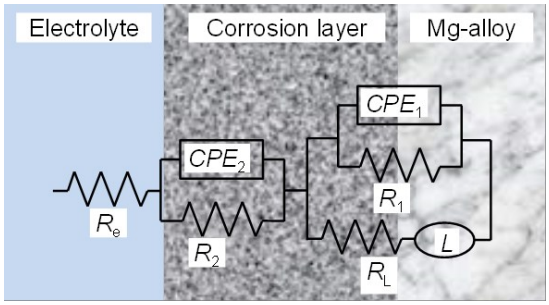

Figure 4.6: Equivalent electrical circuit (EEC) used to fit the EIS data obtained on WE43 Mg alloy in m-SBF.

The understanding of the corrosion mechanisms of pure Mg provides the basis for the understanding of the corrosion of Mg alloys. Song et al. showed that the α-Mg phase in the AZ21, AZ501 and AZ91 Mg alloys follows the same corrosion mechanism as pure magnesium [22]. They also pointed out that the matrix α phase always corrodes preferentially, while other constituents usually act as cathodes. Pebere et al. [61] also showed that, at the corrosion potential and for short immersion times, the corrosion behaviour of AM50 and AZ91 was close to that of pure magnesium. It has been reported that the corrosion layer formed on Mg consists of an outer porous $Mg(OH)_2$ layer and a thin dehydrated MgO inner layer responsible for the passive (protective) corrosion behaviour. McIntyre et al. [62] found that the oxide formed on pure magnesium exposed to ambient conditions corresponds to MgO with a thickness of ca. 2.2 nm after 10 seconds, and that the film thickness increases logarithmically with time forming a hydrated corrosion layer. Investigations on the oxide films formed on Mg in aqueous media revealed a three layer structure consisting in an inner cellular structure, a dense intermediate region and a platelet-like outer layer [63]. It was also proposed that the inner layer was responsible for the passivity of the surface [64]. Baril et al. [57] investigated the corrosion mechanism of pure magnesium in sodium sulfate solutions. They proposed the formation of a double layer corrosion film; a thin barrier film of MgO in contact with the metal substrate, and a relatively thick porous layer of $Mg(OH)_2$ on top of the barrier film. They attributed the increase in the impedance response to an increasing ratio of the inner MgO barrier film-covered surface and the film free areas, underneath the $Mg(OH)_2$ porous layer. They calculated the MgO inner layer thickness to be of about 1 nm; according to them, the low MgO layer thickness and the presence of

the outer $Mg(OH)_2$ layer are the reasons for the MgO not being observed by surface analyses. In agreement with the models proposed by Song [22] and Baril [57] the EEC fitting parameters in Figure 4.6 were physically interpreted as follows: R_1 and CPE_1 describe respectively the charge transfer resistance and the electrochemical double layer/MgO barrier film capacitance at the substrate/electrolyte interface; R_2 and CPE_2 describe the diffusion of Mg^{2+} species through the outer $Mg(OH)_2$ corrosion layer; L and R_L describe respectively the inductance and inductance resistance due to the adsorption of intermediate species at the corrosion-layer-free surface; and R_e describes the electrolyte resistance between the working and reference electrode. An inductive behaviour is related to a current signal following a potential perturbation with a phase delay (ϕ=90° for a pure inductor). The inductance related to the adsorption of intermediate species can be interpreted as the time it takes, after a potential perturbation, before the new steady-state coverage is established and the corresponding current flows [65].

Figure 4.7 shows the impedance response obtained after different immersion times up to 120 h. A progressive increase in the impedance response was observed until a time of 48 h. At longer immersion times, an inverse trend was observed. The increase in the impedance response until 48 h is due to the formation of a corrosion layer with increasing protective properties over time. The decrease in the impedance response after 48 h can be related to an increase in the corrosion rate due to rupture of the protective layer and to presence of a localized corrosion process, i.e., pitting. Xin et al. [37] investigated the corrosion behaviour of AZ91 Mg alloy in a non-buffered SBF and they attributed the decrease in the impedance response and the presence of only

one capacitive loop at longer immersion times to the occurrence of pitting corrosion. The relative change in the size of the three time constants, i.e., different shape of the impedance response on the complex plane, suggests the presence of different corrosion stages with a changing corrosion mechanism, which will be discussed in detail later in the paper.

To better understand the corrosion process and to investigate the time dependence of the WE43 Mg alloy corrosion mechanisms, the impedance response fitting parameters were analysed as a function of time. Table 4.5 shows the EIS fitting parameters obtained after different immersion times. Figure 4.8a shows R_1 and R_2 time dependent values. An initial gradual increase in the charge transfer resistance (R_1) was observed, reaching a value of about 1050 $\Omega\,cm^2$ around a time of 48 h and then gradually decreasing after 72 h. On the other hand, during the first 8 h the diffusion resistance (R_2) remained low (see also Table 4.5), followed by a linear increase to reach a maximum value of about 430 Ωcm^2 at 32 h, and then decreasing to reach an almost constant value after 56 h. The initial increase in R_1 can be related to the formation of a corrosion layer with increasing protective properties, whereas its decrease after 72 h can be related to an increase in exposure of the underlying substrate surface to the electrolyte, due to the rupture of the corrosion layer. The R_2 behaviour shows the presence of a partially protective corrosion layer with low diffusion resistance during the first 8 h of immersion, followed by an increase in the diffusion resistance, probably due to formation of a more compact corrosion layer at a higher pH (Figure 4.4). The decrease in the diffusion resistance (R_2) after 32 h can be related to partial dissolution of the corrosion layer induced by adsorption of Cl^- ions, whereas the

quasi-constant R_2 value after 56 h suggests the presence of a non-protective corrosion layer, probably due to the occurrence of localized corrosion (Figure 4.2f).

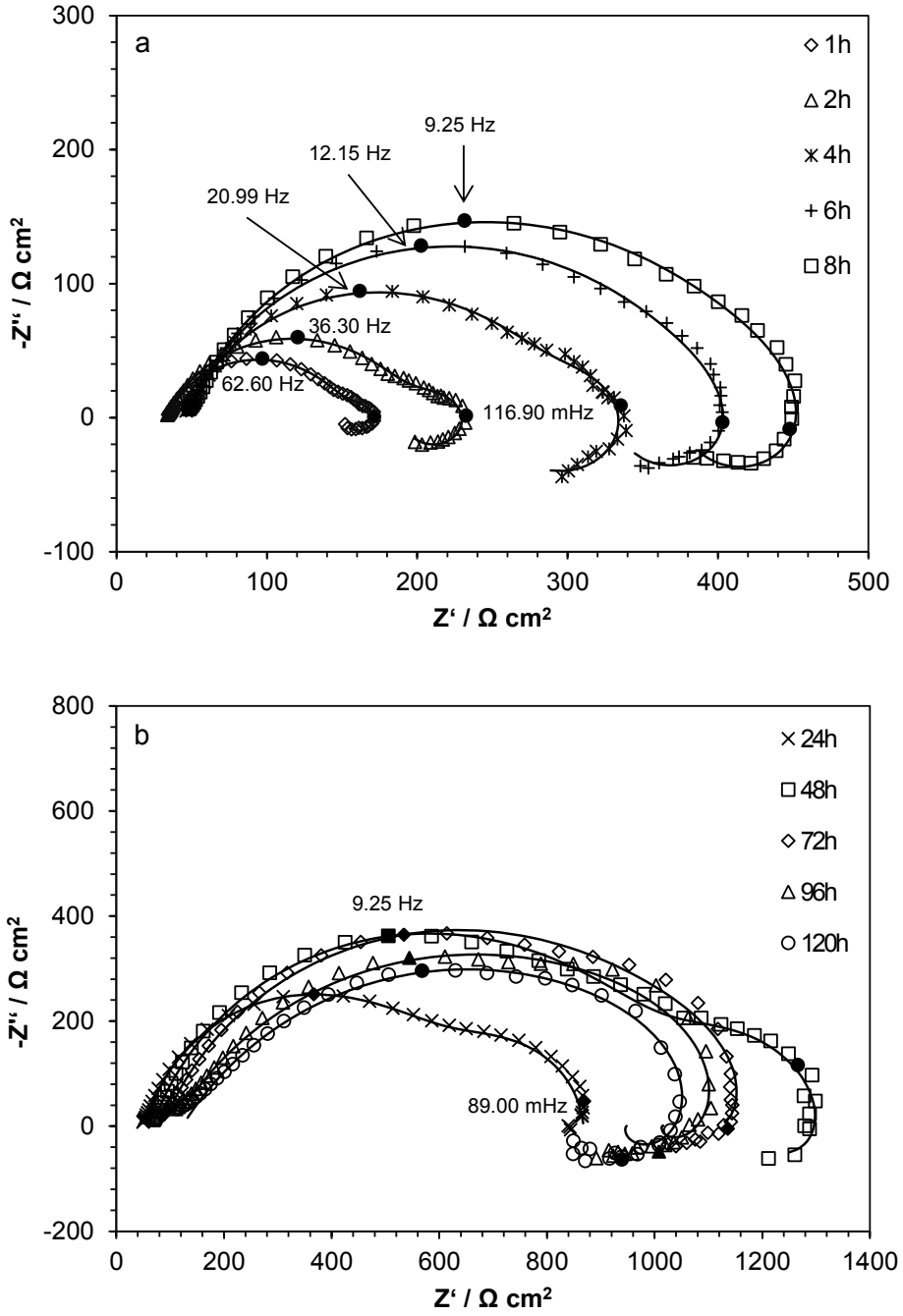

Figure 4.7: Electrochemical impedance response of WE43 Mg alloy in m-SBF after different immersion times: (a) 1-8 h, (b) 24-120 h. Symbols represent experimental values, whereas lines represent simulated spectra.

Table 4.5: Fitting parameters for WE43 Mg alloy in m-SBF after different immersion times.

Time / h	R_e / Ω cm^2	Q_1 / Ω^{-1} cm^{-2} s^n	n_1	C_1 / F cm^{-2}	R_1 / Ω cm^2	Q_2 / Ω^{-1} cm^{-2} s^n	n_2	R_2, / Ω cm^2
1	31.2	3.80×10^{-3}	0.42	1.12×10^{-4}	66.5	4.90×10^{-5}	0.88	90.8
8	45.6	3.46×10^{-4}	0.67	4.01×10^{-5}	299.9	1.02×10^{-4}	1.00	145.3
24	55.6	5.77×10^{-5}	0.83	1.71×10^{-5}	672.0	9.94×10^{-4}	0.91	273.3
32	63.6	5.29×10^{-5}	0.81	1.36×10^{-5}	820.3	9.68×10^{-4}	0.82	429.7
48	76.5	4.72×10^{-5}	0.80	1.08×10^{-5}	1009.0	1.91×10^{-3}	0.96	208.6
56	82.3	5.08×10^{-5}	0.78	1.04×10^{-5}	1043.3	1.98×10^{-3}	0.98	113.8
72	114.3	5.95×10^{-5}	0.74	9.85×10^{-6}	1080.0	1.63×10^{-3}	1.00	108.6
80	112.3	6.50×10^{-5}	0.73	9.67×10^{-6}	1010.7	1.45×10^{-3}	1.00	94.1
96	118.4	9.52×10^{-5}	0.63	6.25×10^{-6}	1005.3	1.41×10^{-3}	1.00	126.1
104	95.8	1.07×10^{-4}	0.62	6.12×10^{-6}	865.5	1.27×10^{-3}	1.00	132.0
120	103.9	9.86×10^{-5}	0.63	5.97×10^{-6}	816.0	1.61×10^{-3}	1.00	118.0

Thus, the combined R_1 and R_2 behavior suggest initial formation of a porous corrosion layer, probably $Mg(OH)_2$, with an increasing protective ability as a result of the increase in the solution pH and thus a reduced film porosity. After 24 h, the increase in R_2 can be related to the increase in the corrosion layer thickness and protective ability, whereas the increase in R_1 can be related to formation of a protective inner MgO film, with an increasing coverage over time. The R_2 decrease after 32 h can be related to local dissolution of the outer $Mg(OH)_2$ layer due to the presence of Cl^- ions leading to subsequent destruction of the protective inner MgO film and thus a decrease in R_1 after 72 h. The continuous R_1 increase after 32 h suggests an increase in the MgO coverage after the onset of localized corrosion. The formation of a protective inner MgO is further evidenced by a decrease in the size of the inductive loop (τ_3) observed between 24 h and 32 h (Figure 4.16), suggesting a decrease in the formation of adsorbed Mg^+ intermediates due to a decrease in the film-free area (i.e. the area of substrate exposed

directly to the electrolyte). An inverse process, with an increasing size of the inductive loop observed after 32 h, can be related to the film rupture and the destruction of the MgO inner layer, with the subsequent increase in the production of adsorbed Mg^+ intermediates (Figure 4.7).

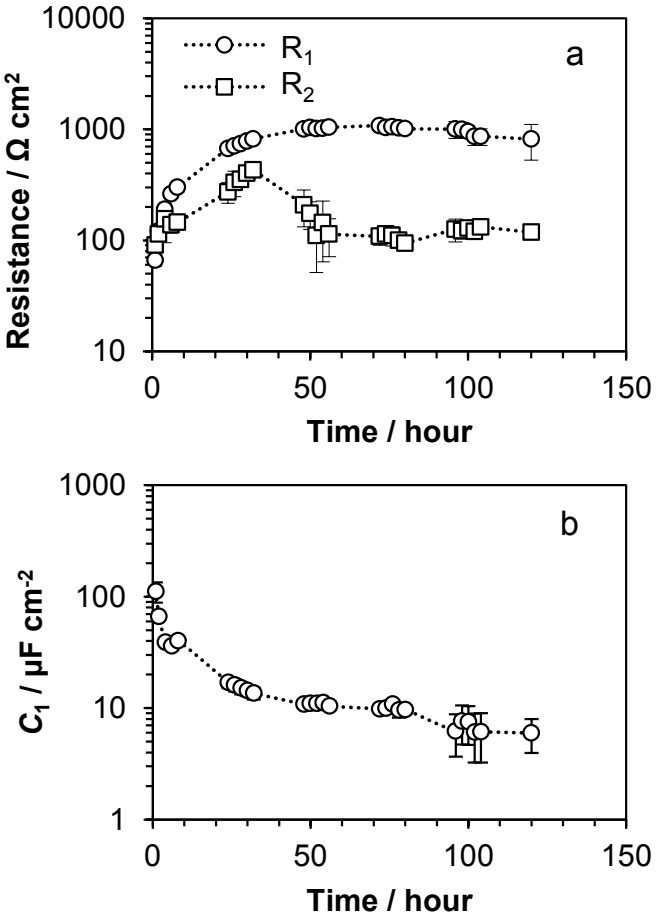

Figure 4.8: Time dependent behaviour of (a) charge transfer resistance (R_1) and diffusion resistance (R_2), and (b) electrochemical double-layer / MgO barrier film capacitance, (C_1) of WE43 Mg alloy in m-SBF.

It has been shown that the CPE parameter *Q* cannot be always used to represent pure capacitance in cases when its power, *n*, substantially deviates from unity. Equations to express the relationship between *Q* and the interfacial capacitance

according to a surface or axial distribution of time constants have been proposed [66-68]. A surface distribution of time constants was assumed for the WE43 Mg alloy due to the presence of second phases, due to the MgO inner layer with increasing coverage, and due to the occurrence of localized corrosion. Therefore, the electrochemical double layer / MgO barrier film capacitance values, C_1 (F cm^{-2}), were calculated using Brug's equation [66]:

$$C_1 = Q_1^{-n_1}\left(\frac{R_e R_1}{R_e + R_1}\right)^{(1-n_1)/n_1} \quad (4.10)$$

where Q_1 is the CPE_1 constant (Ω^{-1} cm^{-2} s^n), R_e is the electrolyte resistance (Ω cm^2), R_1 is the charge transfer resistance (Ω cm^2) and n_1 is the CPE_1 dimensionless exponent. Figure 4.8b shows that C_1 decreases with time, from an initial value of 112 μF cm^{-2} to a final value of 6 μF cm^{-2}, after 120 h. The decrease in C_1 can be related to the thickening of the corrosion layer that spreads and blocks the surface. The C_1 values obtained are in agreement with data reported in the literature for Mg alloys [57, 69].

4.4.3 Hydrogen evolution

Figure 4.9 shows the cumulative volume of hydrogen produced by the WE43 Mg alloy corrosion after different immersion times. A variable hydrogen production rate was observed over time, with a gradual decrease observed during the first 48 h, followed then by a gradual increase at longer times. This behaviour is in agreement with the formation of hydrogen gas occurring mainly at the substrate/electrolyte interface. Hydrogen gas is produced electrochemically by water reduction occurring predominantly at cathodic intermetallic regions (reaction (4.2)) and chemically by the

reaction of water with adsorbed intermediate Mg^+ species at MgO film-free regions (reaction (4.4)). At shorter times, the formation of a porous corrosion layer allows water to access the substrate/electrolyte interface through the corrosion layer and thus, hydrogen is produced at a high rate. However, at longer immersion times the formation of a thicker and more protective corrosion layer occurs, decreasing the access of water to the substrate surface and its intermetallic regions thus decreasing the production of hydrogen. At times past 48 h, an increasing corroding area and water access to intermetallic regions due to the formation and growth of pits, are responsible for the increasing hydrogen production rate (Figure 4.9). The larger error bars observed at longer immersion times can be related to the stochastic nature of the pit formation and growth processes.

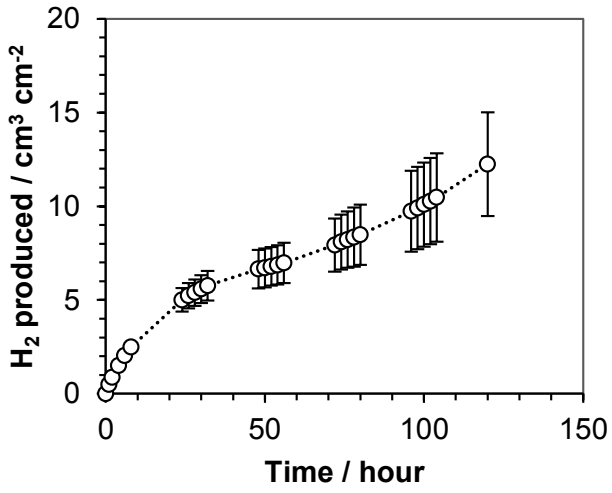

Figure 4.9: Cumulative evolution of hydrogen produced by corrosion of WE43 Mg alloy in m-SBF expressed in terms of hydrogen gas volume per WE43 Mg alloy sample surface area.

4.4.4 Electrolyte analysis

Figure 4.10a shows the concentration of Mg, Ca and P in the electrolyte as a function of corrosion time, measured by ICP-OES. A gradual increase in the Mg concentration over time was observed as a result of the corrosion process. A somewhat linear increase in the Mg concentration was observed until 24 h, followed by a minor increase from 24-48 h and then a faster increase from 48-120 h. These results are in agreement with the behaviour observed for the production of hydrogen gas (Figure 4.9), with an initial increase in the Mg concentration due to formation of a porous corrosion layer and thus, a higher initial corrosion rate. The increase in the protective ability of the corrosion layer after 24 h results in a decreased corrosion rate and thus a lower Mg dissolution rate (Figure 4.10a). Then, the faster increase in the Mg concentration after 48 h corresponds to the onset of localized corrosion (Figure 4.2f and Figure 4.8a). On the other hand, a quasi-constant Ca and P concentration can be observed during the first 48 h, followed by a significant decrease in concentration after 120 h. The latter can be related to the formation of insoluble Ca and P compounds precipitated on the Mg alloy sample, forming part of the corrosion layer, and to the formation of precipitates in the electrolyte solution. The m-SBF is supersaturated and saturated with respect to formation of apatite [$Ca_{10}(PO_4)_6(Cl,OH)_2$] and calcite ($CaCO_3$), respectively [70]. In addition, formation of insoluble precipitates can be enhanced by the electrolyte solution supersaturation as a result of the increase in pH and concentration of dissolved corrosion products, i.e., OH^- and Mg^{2+} ions. In order to test the stability of the m-SBF in the absence of corroding sample, the Mg, Ca and P electrolyte concentrations were monitored by ICP-OES. Figure 4.10b shows that their values do not change over the

time interval tested, thus confirming that the changes presented in Figure 4.10a are solely the result of the alloy corrosion.

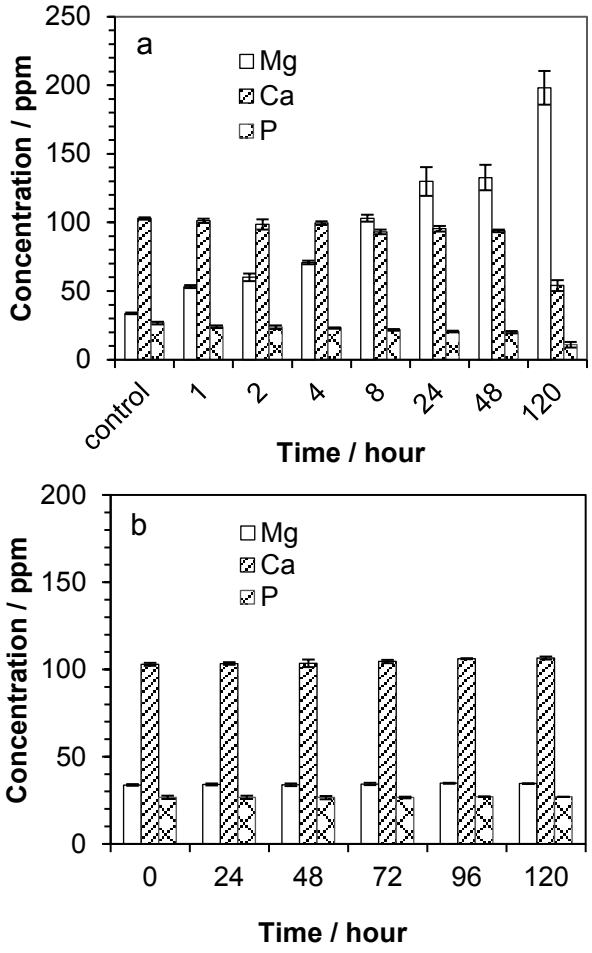

Figure 4.10: Time dependence of concentration of Mg, Ca and P ions dissolved in m-SBF (a) during the immersion of WE43 Mg alloy in m-SBF and (b) without WE43 Mg alloy immersed in m-SBF (control), obtained by ICP-OES.

4.4.5 Corrosion rate

To better assess the time dependent corrosion rate behaviour and to compare/use the results obtained by the different techniques utilized, normalized corrosion rate values

were calculated from EIS, hydrogen evolution and ICP-OES data. Normalized corrosion rate values were calculated according to the following equation:

$$P_{norm} = \frac{P}{P_{\max}} \tag{4.11}$$

where P_{norm} is the normalized corrosion rate, P is the corrosion rate at any time (mm year^{-1}) and P_{max} is the largest measured corrosion rate (mm year^{-1}). The corrosion rate is inversely proportional to the corrosion resistance and thus, instantaneous relative corrosion rate values were obtained from EIS by calculating the inverse of R_{CT} (R_1) values presented in Figure 4.8a. Further, time-dependent Mg concentration data obtained by ICP-OES (Figure 4.10a) were fitted (smoothing spline, *SSE*=121.2, R^2=0.9964) and instantaneous corrosion rate values were calculated using the following equation:

$$P_{ICP} = \frac{8.76C}{\rho A} \tag{4.12}$$

where P_{ICP} is the corrosion rate (mm year^{-1}), 8.76 is a constant (dm^3 mm g h mg^{-1} year^{-1} cm^{-1}), C is the fitting curve slope (ppm h^{-1}), ρ is the Mg density (1.74 g cm^{-3}) and A is the sample area (cm^2). Similarly, hydrogen production data in Figure 4.9 were also fitted (polynomial degree 5, *SSE*=0.0259, R^2=0.9999) and instantaneous corrosion rate values were then calculated using the following equation [71]:

$$P_{HE} = 2.279V_H \tag{4.13}$$

where P_{HE} is the corrosion rate (mm year^{-1}), 2.279 is a constant (mm day cm^{-1} year^{-1}) and V_H is the fitting curve slope (cm^3 cm^{-2} day^{-1}). It was assumed that one mole of

hydrogen (22.4 $dm^3 mol^{-1}$) is produced for each mole of corroded Mg metal (24.32 $g mol^{-1}$). All fittings were performed using the application Curve Fitting Toolbox (MathWorks, 2012).

Figure 4.11 shows the time dependent normalized corrosion rate calculated from EIS, hydrogen evolution experiments and ICP-OES. The highest corrosion rate was observed during the first 8 h of sample immersion, followed by a decrease in the corrosion rate. Results obtained in hydrogen evolution experiments and by ICP-OES showed a minimum corrosion rate value around a time of 48 h, followed by a gradual corrosion rate increase thereafter. EIS results showed a minimum corrosion rate at 32 h followed by a gradual increase at longer times, although this is not evident on the plot due to the large ordinate scale. The observed corrosion behaviour is in agreement with the formation of a corrosion layer with an increasing protective ability during the first 48 h followed by an increase in the corrosion rate due to onset of a localized corrosion process around a time of 48 h. This is also in agreement with the OCP results, where a quasi-constant corrosion potential was reached after a time of about 48 h. However, the onset of the localized corrosion process did not produce a decrease in the OCP, probably due to the pitting-related non-uniform potential and current distribution.

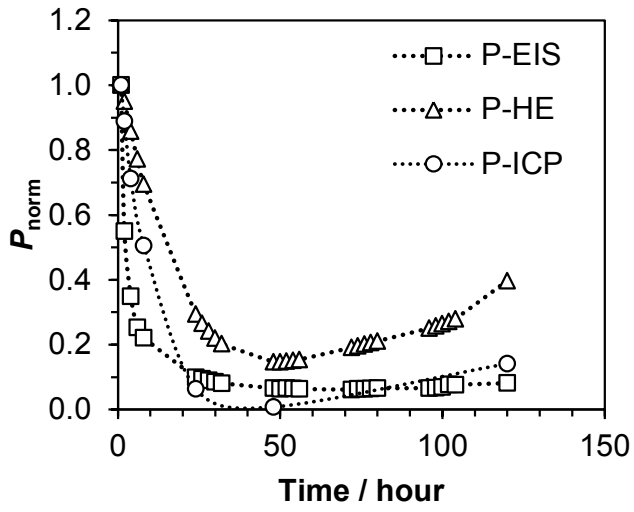

Figure 4.11: Time dependent normalized corrosion rate ($P_{norm} = P/P_{max}$) of WE43 Mg alloy in m-SBF calculated from EIS (P-EIS), hydrogen evolution (P-HE) and ICP-OES (P-ICP) data.

4.4.6 Corrosion products characterization

Table 4.4 shows the corrosion layer composition obtained by EDS analysis after 8 h of immersion. The presence of Mg, Ca, Na, P, O and C was detected, implying the presence of a Ca/Mg-phosphate/carbonate-containing Mg-oxide/hydroxide corrosion layer (Figure 4.12). SEM-EDS analysis after different immersion times showed a constant corrosion layer composition during the complete immersion experiment (not shown). It was observed that the volcano-like deposits had the same elemental composition as the rest of the corrosion layer, but a significantly higher calcium content (Table 4.4). The Ca/P ratio found on the cracked surface is about 0.25 while that found on the volcano-like deposits is 1.5; the latter indicates the presence of $Ca_3(PO_4)_2$. These results show that the incorporation of Ca and P into the corrosion layer as insoluble

precipitates contributes to the electrolyte concentration decrease observed for these species by ICP-OES (Figure 4.10a).

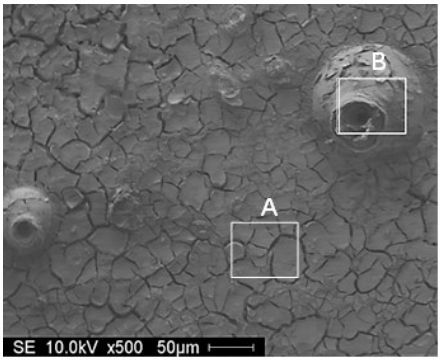

Figure 4.12: SEM image of WE43 Mg alloy in m-SBF after 8 h of immersion. Quantitative EDS analysis data of the corrosion layer (A) and volcano-like deposit (B) are shown in Table 4.4.

Figure 4.13 shows ATR-FTIR microscopy spectra obtained after different immersion times. The spectra evidence the presence of phosphate and carbonate species in the corrosion layer. Characteristic phosphate absorption bands were observed at about 1030 cm^{-1} and 580 cm^{-1} corresponding to *v*3 and *v*4 vibrational modes, respectively [44, 72]. The peaks at about 1485 cm^{-1}, 1430 cm^{-1} (*v*3 mode) and 850 cm^{-1} (*v*2 mode) correspond to the stretching and bending vibrations of CO_3^{2-} ions, respectively [44, 72]. The peak at 1600 cm^{-1} corresponds to the bending vibration mode of water molecules, suggesting the presence of hydrated species in the corrosion layer [44]. The peak at about 710 cm^{-1} corresponds probably to OH^- species and the peak at 470 cm^{-1}, observed for the control sample, can be related to the Mg-O stretching vibration of a native MgO layer [73]. The presence of wide peaks at PO_4^{3-} and CO_3^{2-} characteristic absorption bands suggests the formation of a poorly crystalline

carbonated apatite on the sample surface [73]. A decrease in the size of the PO_4^{3-} peak at 600 cm^{-1} can be observed after 1 h, accompanied by an increase in the peak of the water bending vibration at 1600 cm^{-1}, suggesting the formation of a hydrated apatite-containing corrosion layer. The m-SBF has been found to be optimal for *in-vitro* bioactivity assessment of artificial materials and for biomimetic production of bone-like apatite [45]. After 120 h, a decrease in the water bending vibration and CO_3^{2-} peaks can be observed; the latter occurring probably due to a decrease in the CO_3^{2-} concentration in solution due to release of CO_2 into the atmosphere (reaction (4.8)) and thus the shift of equilibrium towards the dissolution of carbonate layer.

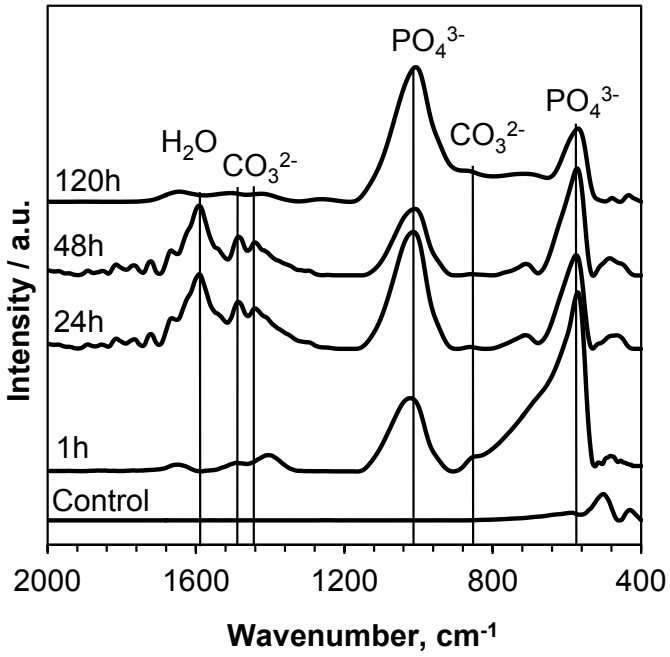

Figure 4.13: ATR-FTIR spectra of WE43 Mg alloy in m-SBF after different immersion times showing the presence of carbonate and phosphate functional groups. A clean polished WE43 sample was used as control.

Figure 4.14a-b shows the corrosion layer X-ray diffraction (XRD) patterns obtained after different immersion times. Analysis of a control sample showed diffraction peaks

corresponding to α-Mg, β, Mg-Y and Mg-Nd [74]. For the samples immersed in the m-SBF only the α-Mg and β phases underneath the corrosion layer could be distinguished, which revealed the amorphous nature of the corrosion layer. The decrease in the diffraction peaks intensity at longer immersion times was related to the corrosion layer thickness increase. Therefore, a gradual increase in the corrosion layer thickness during the first 48 h can be observed, followed by a slow thickening process from 48-120 h. This was in agreement with the OCP (Figure 4.4a), R_1 (Figure 4.8a) and C_1 (Figure 4.8b) behaviour, which showed a quasi-constant value after 48 h of immersion. Furthermore, the smallest corrosion rate was observed around a time of 48 h (Figure 4.11), providing additional evidence for a slower corrosion layer growth.

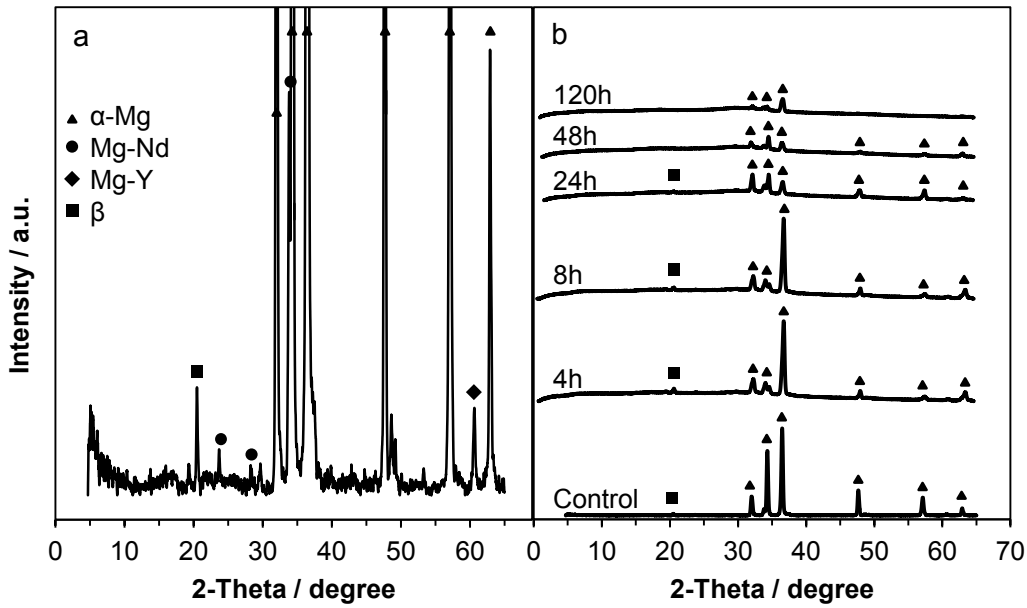

Figure 4.14: XRD patterns of (a) control Mg alloy sample and (b) of WE43 Mg alloy corroded in m-SBF after different immersion times.

Figure 4.15 shows the C 1s, O 1s, P 2p, Ca 2p and Mg 1s XPS spectra of the Mg alloy surface after 120 days of immersion in m-SBF. The Mg 1s and P 2p spectra were

detected as single peaks at 1303.9 and 132.9 eV, respectively. The Ca 2p spectrum was detected as doublet peaks at 347 and 350.7 eV. From the binding energies of P 2p and Ca 2p it can be concluded that phosphorous exists in the form of phosphate [75]. The O 1s peak could be resolved into two spectra with peaks at 531 and 532.1 eV which have been attributed to the presence of $Mg(OH)_2$ and CO_3^{-2} species [76], respectively. The presence of carbonate was further confirmed by the C 1s peak at 288.9 eV [76, 77]. The C 1s peak at 284.6 eV corresponds to adventitious carbon and the peak at 286.5 eV may be related to the presence of C-O groups [77]. Combined with ATR-FTIR and XRD results shown in Figure 4.13 and Figure 4.14, it can be concluded that the top-most corrosion layer is composed of an amorphous $Mg(OH)_2$ and carbonated apatite mixture.

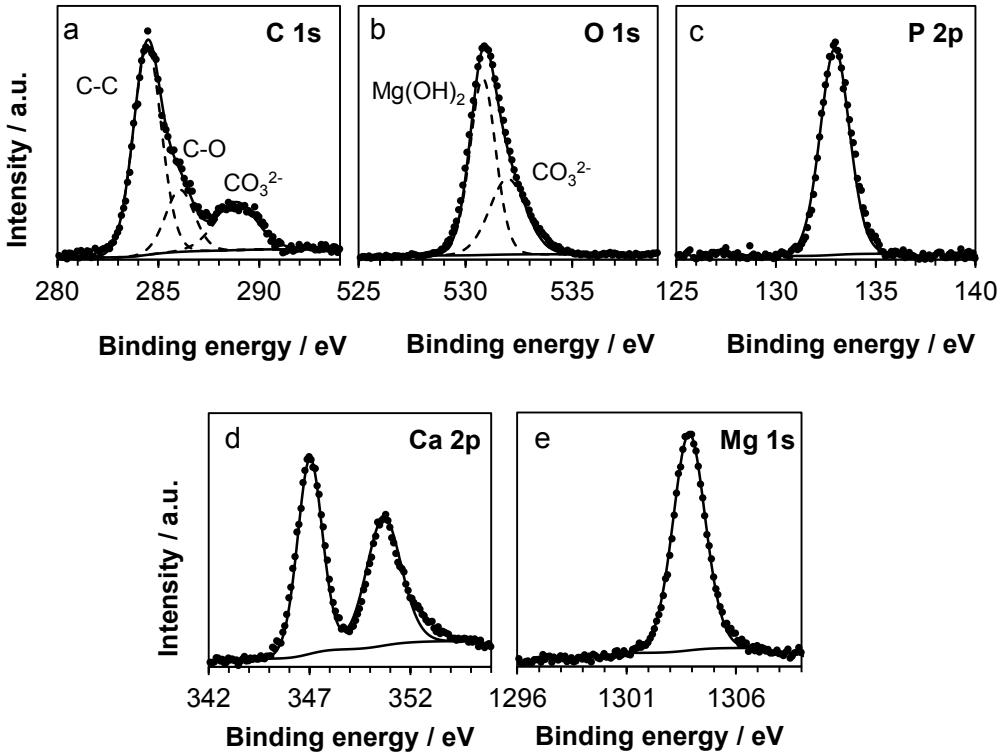

Figure 4.15: XPS spectra of the WE43 Mg alloy corrosion layer after 120 h of immersion in m-SBF. (a) C 1s, (b) O 1s, (c) P 2p, (d) Ca 2p and (e) Mg 1s.

The corrosion layer composition and structure results are in agreement with the results reported in the literature for biodegradable Mg alloys. Witte et al. investigated the *in vivo* degradation of four Mg alloys (AZ31, AZ91, WE43 and LAE442) and found that the corrosion layers contained high levels of Ca and P in the form of an amorphous calcium phosphate [17]. Retig el al. [56] studied the corrosion layer composition of a WE43 Mg alloy in m-SBF and found that it consisted of an amorphous carbonated calcium/magnesium phosphate. They found that a corrosion layer with a thickness of 20-40 μm was formed after 5 days and that its composition was almost constant after 6 h of immersion. Bornapour et al. [78] investigated the corrosion of pure Mg and Mg-Sr alloys in a SBF and found that the corrosion layer was composed of $Mg(OH)_2$ and hydroxyapatite, $Ca_{10}(PO_4)_6(OH)_2$. They also showed the presence of $CaCO_3$ and a Sr-substituted hydroxyapatite in the corrosion layer of a Mg-Sr alloy.

4.4.7 Corrosion mechanism

On the basis of the experimental results and literature data the following corrosion mechanism for WE43 Mg alloy in m-SBF is proposed (Figure 4.16a-d):

Stage 1, Figure 4.16a (1-8 h). Electrochemical oxidation of α-Mg matrix to produce adsorbed Mg^+ intermediates and chemical reaction of the latter with water to form Mg^{2+} and hydrogen gas, according to reactions (4.3) and (4.4), respectively. In parallel with reaction (4.3), electrochemical hydrogen reduction and formation of hydrogen gas (reaction (4.2)) occurs preferentially on intermetallic regions. The presence of cathodic intermetallic regions is evidenced by the formation of white volcano-like precipitates (see Figure 4.2). The initial fast corrosion rate leads to an increase in the local

concentration of Mg^{2+} and OH^- ions (increase in pH, Figure 4.4b) leading to formation of a mixed carbonated apatite/$Mg(OH)_2$ porous corrosion layer (reaction (4.6)) with an increasing thickness over time. Initially, a porous layer is formed due to an initial high buffering capacity of the electrolyte, which promotes neutralization of OH^- ions and dissolution of the corrosion layer. Therefore, the corrosion layer growth is the result of a dynamic dissolution equilibrium controlled by the local Mg^{2+} and OH^- ions concentration and by the availability of hydrogen discharging cathodic regions (intermetallic precipitates). The formation of a porous partially-protective corrosion layer is evidenced by an initial low diffusion resistance (R_2, Figure 4.8a). The faster formation over dissolution kinetics leads to a gradual thickening of the corrosion layer and to an increase in its protective ability, evidenced by a gradual increase in R_1 (Figure 4.8a) and a decrease in C_1 (Figure 4.8b). It has been proposed that the dissolution rate of Mg is controlled by the availability of hydrogen discharging sites. Therefore, the increase in R_1 is also the result of a decreased availability of hydrogen discharging sites (intermetallic precipitates) as a result of thickening of a corrosion layer.

Stage 2, Figure 4.16b (8-32 h). The formation of a corrosion layer with an increasing thickness and protective ability leads to a decreased water access to the substrate/corrosion layer interface and thus, to a decreased water availability for the chemical reaction with adsorbed Mg^+ intermediates (reaction (4.4)). Therefore, $Mg(OH)_2$ undergoes a dehydration process to form MgO:

$$Mg(OH)_2 \leftrightarrow MgO + H_2O \qquad (4.14)$$

which produces H_2O needed for further chemical reaction with Mg^+ intermediates (reaction (4.4)). This process leads to (i) a gradual formation of a dehydrated insulating MgO inner corrosion layer (Figure 4.16b, dark areas), which is thought to have passive properties and, also to (ii) a decreased substrate/electrolyte interfacial area. As a consequence, a decrease in the production of adsorbed Mg^+ intermediates and thus in the chemical production of hydrogen gas (reaction (4.4)), occur. However, the occurrence of a reaction that involves direct production of Mg^{2+} ions is also possible:

$$Mg \rightarrow Mg^{2+} + 2e^- \quad (4.15)$$

The increase in the corrosion layer protective ability due to the formation of the inner MgO layer is evidenced by the increase in OCP (Figure 4.4b), R_1 and R_2 (Figure 4.8a) values and the decrease in C_1 (Figure 4.8b). The decrease in the rate of production of adsorbed Mg^+ intermediates and thus in the chemical production of hydrogen (Figure 4.9) is evidenced by the gradual decrease in the low frequency inductive loop (τ_3) (see EIS spectra in Figure 4.16b). The corrosion layer protective ability is probably further enhanced by the precipitation of carbonated apatite species, as shown by ATR-FTIR (Figure 4.13).

Stage 3, Figure 4.16c (32-72 h). During this stage, the maximum corrosion layer resistance is observed. Also, equilibrium in the corrosion layer formation and dissolution rates is reached. However, the increase in OCP (Figure 4.4) and the presence of aggressive Cl^- species in the solution, which promote dissolution/rupture of the corrosion layer (reaction (4.7)), contribute to the onset of a localized corrosion process, i.e., pit formation. This is accompanied by an increased water access to the rupture

sites and thus, by an increased production of adsorbed Mg^+ intermediates and H_2 gas, according to reactions (4.2-4.4). The onset of localized corrosion was evidenced by the decrease in the diffusion resistance (R_2) after 32 h (Figure 4.8a) and by observation of corrosion layer defects after 48 h in SEM analysis (Figure 4.2f). The decrease in the diffusion resistance (R_2) is also accompanied by a decrease in the intermediate frequency capacitive loop (τ_2, EIS in Figure 4.16c), whereas an increase in the production of adsorbed Mg^+ intermediates as a result of the corrosion layer dissolution/rupture is evidenced by an increase in the low frequency inductive loop (τ_3, EIS in Figure 4.16c).

Stage 4, Figure 4.16d (72-120 h). During this stage, a lateral growth of stable pits occurs, leading to an increase in substrate/electrolyte interfacial area exposed to the electrolyte and, thus, to an increased corrosion rate and hydrogen production, through reactions (4.2-4.6). It has been proposed that localized corrosion of magnesium has an inherent tendency to be self-limiting, due to the production of OH^- and concomitant stabilization of the local $Mg(OH)_2$ film [22]. However, local production of hydrogen gas at intermetallic precipitates promotes the diffusion of corrosion products away from the surface and, thus, impedes the formation of a stable corrosion layer. This process is enhanced by dissolution of α-Mg matrix along grain boundaries, leading to a larger intermetallic-exposed area and, thus, to increased hydrogen production. Film rupture and lateral pit growth is accompanied by increased water access to the substrate/corrosion layer interface leading to conversion of MgO into $Mg(OH)_2$ according to reaction (4.14). A decrease in the protective properties of the corrosion film due to both the pit growth and the destruction of the MgO inner layer, is evidenced by a

decrease in the charge transfer resistance (R_1) after 72 h (Figure 4.8a), whereas the formation of a porous $Mg(OH)_2$ layer inside the pit cavity is evidenced by the quasi-constant R_2 value after 52 h (Figure 4.8a). Pit growth can be identified on the impedance diagrams as the quasi-constant size of the intermediate and low frequency loops (τ_2 and τ_3) and the decrease in size of the high frequency loop (τ_1), Figure 4.16.

The present investigation outlines the corrosion mechanism of WE43 in a m-SBF, with the aim of providing some insight into the corrosion mechanisms of this alloy in the real physiological environment. Knowledge of the corrosion susceptibility and the corresponding corrosion mechanisms is fundamental for the assessment of prospective implant materials. However, some limitations of this investigation are the use of a stagnant electrolyte and the corresponding accumulation of corrosion products in the electrolyte, i.e., Mg^{2+} and OH^- ions, which lead to an increase in the electrolyte pH above the physiological range, the loss of carbonate species in solution due to the release of CO_2 into the atmosphere and, the lack of organic and biological components; all of which can have an effect on the alloy corrosion behaviour. Experimental conditions that allow for a better control of the electrolyte composition and pH, simulating physiological homeostasis, combined with the presence of relevant organic molecules, such as proteins, are necessary for a better understanding of the Mg alloy corrosion mechanisms *in vivo*.

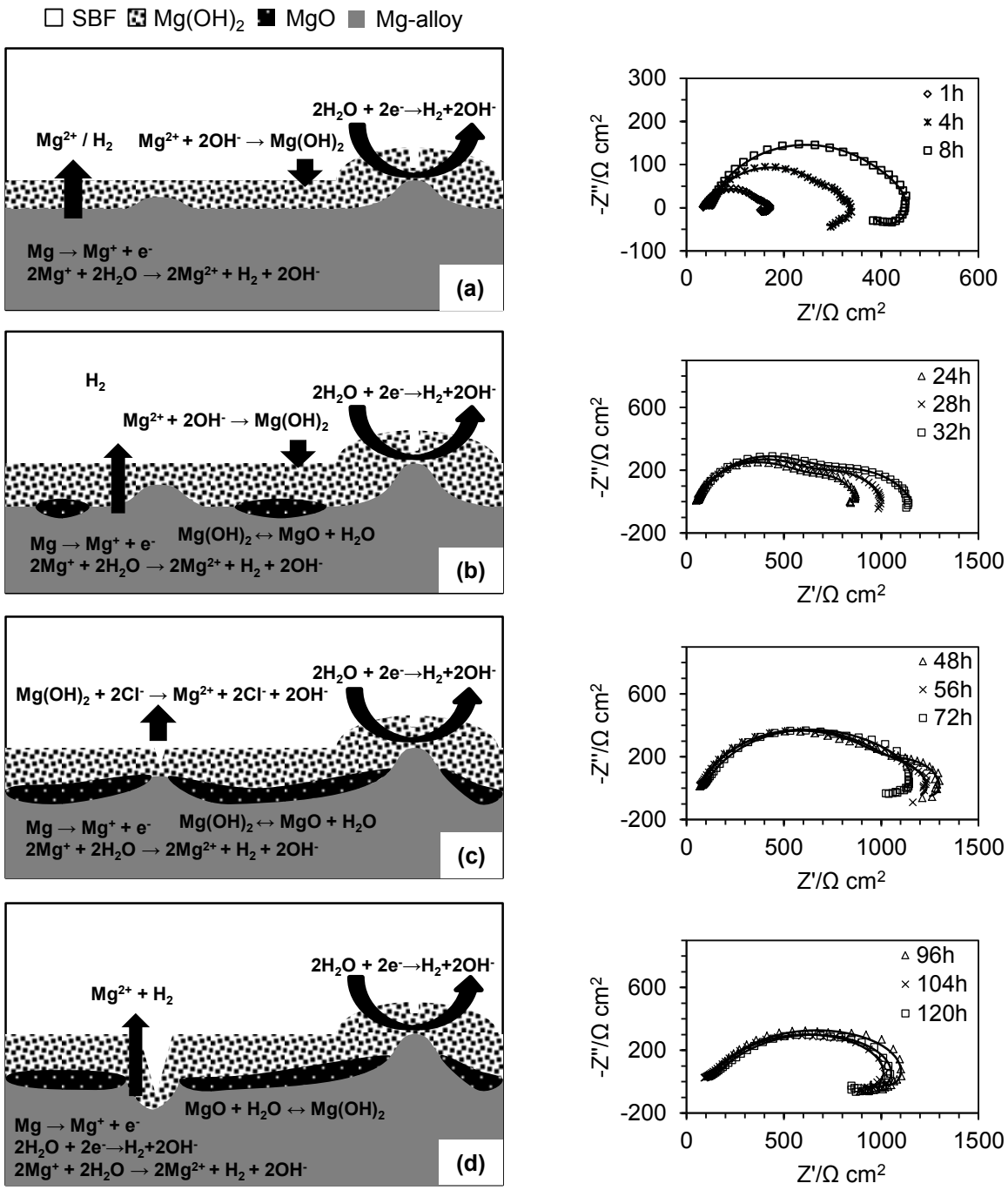

Figure 4.16: Corrosion mechanism stages of WE43 Mg alloy in m-SBF, and their corresponding impedance response: (a) Stage 1: Formation of a $Mg(OH)_2$ porous layer with a growing thickness; (b) Stage 2: Increased corrosion layer resistance and decreased hydrogen production due to formation of a MgO passive inner layer; (c) Stage 3: High substrate coverage by the MgO inner layer and onset of localized corrosion, i.e., pit formation; and (d) Stage 4: Increased corrosion rate and hydrogen production due to pit growth.

4.5 CONCLUSIONS

An investigation of the corrosion mechanisms and kinetics of WE43 Mg alloy in m-SBF was conducted over a time period of 5 days using a range of experimental techniques. Comparison of the corrosion kinetics obtained by electrochemical, hydrogen evolution and analytical techniques showed a good agreement. Four corrosion stages were identified: (1) electrochemical oxidation of the α-Mg matrix with the formation of adsorbed Mg^+ intermediates and production of hydrogen gas, chemically by the reaction of water with adsorbed Mg^+ intermediates and electrochemically on intermetallic cathodic regions. This is accompanied by the formation of an amorphous carbonated apatite/$Mg(OH)_2$ mixed corrosion layer with increasing thickness; (2) Increase in the corrosion layer thickness and protective ability leading to a decreased water access to the substrate/$Mg(OH)_2$ interface. Continued chemical reaction of adsorbed Mg^+ intermediates leads to dehydration of the $Mg(OH)_2$ inner layer and to the subsequent formation of a MgO protective film with increasing coverage; (3) A decreased corrosion rate due to the increased MgO inner layer coverage leads to an equilibrium in the formation and dissolution of the corrosion layer. A higher OCP and the presence of aggressive Cl^- ions lead to local dissolution of the corrosion layer and onset of a localized corrosion process; and (4) Lateral growth of stable pits due to an increased intermetallic region area and local production of hydrogen gas, with the subsequent increase in water access and gradual destruction of the MgO inner layer.

The present study provides a mechanism for the corrosion of WE43 Mg alloy in m-SBF under the investigated conditions over a period of 5 days. In addition, the investigation presented provides additional indirect evidence on the presence of a

protective dehydrated inner MgO film and the formation of adsorbed Mg intermediates at the film-free regions.

4.6 REFERENCES

[1] P. Erne, M. Schier, T.J. Resink, The road to bioabsorbable stents: Reaching clinical reality?, CardioVascular and Interventional Radiology, 29 (2006) 11-16.

[2] C. Fox, D. Ramsoomair, C. Carter, Magnesium: its proven and potential clinical significance, Southern medical journal, 94 (2001) 1195-1201.

[3] N.E.L. Saris, E. Mervaala, H. Karppanen, J.A. Khawaja, A. Lewenstam, Magnesium: An update on physiological, clinical and analytical aspects, Clinica Chimica Acta, 294 (2000) 1-26.

[4] R. Zeng, W. Dietzel, F. Witte, N. Hort, C. Blawert, Progress and challenge for magnesium alloys as biomaterials, Advanced Engineering Materials, 10 (2008) B3-B14+702.

[5] E.S. Ford, A.H. Mokdad, Dietary Magnesium Intake in a National Sample of U.S. Adults, The Journal of Nutrition, 133 (2003) 2879-2882.

[6] A. Yamamoto, S. Hiromoto, Effect of inorganic salts, amino acids and proteins on the degradation of pure magnesium in vitro, Materials Science and Engineering C, 29 (2009) 1559-1568.

[7] A. Krause, N. Von Der Höh, D. Bormann, C. Krause, F.W. Bach, H. Windhagen, A. Meyer-Lindenberg, Degradation behaviour and mechanical properties of magnesium implants in rabbit tibiae, Journal of Materials Science, 45 (2010) 624-632.

[8] B. Heublein, R. Rohde, V. Kaese, M. Niemeyer, W. Hartung, A. Haverich, Biocorrosion of magnesium alloys: A new principle in cardiovascular implant technology?, Heart, 89 (2003) 651-656.

[9] N. Erdmann, N. Angrisani, J. Reifenrath, A. Lucas, F. Thorey, D. Bormann, A. Meyer-Lindenberg, Biomechanical testing and degradation analysis of MgCa0.8 alloy screws: A comparative in vivo study in rabbits, Acta Biomaterialia, 7 (2011) 1421-1428.

[10] Y. He, H. Tao, Y. Zhang, Y. Jiang, S. Zhang, C. Zhao, J. Li, B. Zhang, Y. Song, X. Zhang, Biocompatibility of bio-Mg-Zn alloy within bone with heart, liver, kidney and spleen, Chinese Science Bulletin, 54 (2009) 484-491.

[11] M. Maeng, L.O. Jensen, E. Falk, H.R. Andersen, L. Thuesen, Negative vascular remodelling after implantation of bioabsorbable magnesium alloy stents in porcine coronary arteries: a randomised comparison with bare-metal and sirolimus-eluting stents, Heart, 95 (2009) 241-246.

[12] Y. Ren, J. Huang, B. Zhang, K. Yang, Preliminary study of biodegradation of AZ31B magnesium alloy, Frontiers of Materials Science in China, 1 (2007) 401-404.

[13] T.L. Slottow, R. Pakala, T. Okabe, D. Hellinga, R.J. Lovec, F.O. Tio, A.B. Bui, R. Waksman, Optical coherence tomography and intravascular ultrasound imaging of bioabsorbable magnesium stent degradation in porcine coronary arteries, Cardiovascular Revascularization Medicine, 9 (2008) 248-254.

[14] R. Waksman, R. Pakala, P.K. Kuchulakanti, R. Baffour, D. Hellinga, R. Seabron, F.O. Tio, E. Wittchow, S. Hartwig, C. Harder, R. Rohde, B. Heublein, A. Andreae, K.H. Waldmann, A. Haverich, Safety and efficacy of bioabsorbable magnesium alloy stents in porcine coronary arteries, Catheterization and Cardiovascular Interventions, 68 (2006) 607-617.

[15] R. Waksman, R. Pakala, T. Okabe, D. Hellinga, R. Chan, M.O. Tio, E. Wittchow, S. Hartwig, K.H. Waldmann, C. Harder, Efficacy and safety of absorbable metallic stents with adjunct intracoronary beta radiation in porcine coronary arteries, Journal of Interventional Cardiology, 20 (2007) 367-372.

[16] F. Witte, J. Fischer, J. Nellesen, C. Vogt, J. Vogt, T. Donath, F. Beckmann, In vivo corrosion and corrosion protection of magnesium alloy LAE442, Acta Biomaterialia, (2009).

[17] F. Witte, V. Kaese, H. Haferkamp, E. Switzer, A. Meyer-Lindenberg, C.J. Wirth, H. Windhagen, In vivo corrosion of four magnesium alloys and the associated bone response, Biomaterials, 26 (2005) 3557-3563.

[18] R. Erbel, C. Di Mario, J. Bartunek, J. Bonnier, B. de Bruyne, F.R. Eberli, P. Erne, M. Haude, B. Heublein, M. Horrigan, C. Ilsley, D. Böse, J. Koolen, T.F. Lüscher, N. Weissman, R. Waksman, Temporary scaffolding of coronary arteries with bioabsorbable magnesium stents: a prospective, non-randomised multicentre trial, Lancet, 369 (2007) 1869-1875.

[19] P. Peeters, M. Bosiers, J. Verbist, K. Deloose, B. Heublein, Preliminary results after application of absorbable metal stents in patients with critical limb ischemia, Journal of Endovascular Therapy, 12 (2005) 1-5.

[20] E. Ghali, W. Dietzel, K.U. Kainer, General and Localized Corrosion of Magnesium Alloys: A Critical Review, Journal of Materials Engineering and Performance, 13 (2004) 7-23.

[21] G.L. Makar, J. Kruger, Corrosion of magnesium, International Materials Reviews, 38 (1993) 138-153.

[22] G. Song, A. Atrens, Understanding magnesium corrosion. A framework for improved alloy performance, Advanced Engineering Materials, 5 (2003) 837-858.

[23] G. Song, A. Atrens, Recent insights into the mechanism of magnesium corrosion and research suggestions, Advanced Engineering Materials, 9 (2007) 177-183.

[24] G.L. Song, A. Atrens, Corrosion mechanisms of magnesium alloys, Advanced Engineering Materials, 1 (1999) 11-33.

[25] H.H. Uhlig, R. Winston Revie, Uhlig's Corrosion Handbook, 2nd ed., Wiley, New York, 2000.

[26] G. Song, A. Atrens, D.S. John, X. Wu, J. Nairn, The anodic dissolution of magnesium in chloride and sulphate solutions, Corrosion Science, 39 (1997) 1981-2004.

[27] G. Song, A. Atrens, D. Stjohn, J. Nairn, Y. Li, The electrochemical corrosion of pure magnesium in 1 N NaCl, Corrosion Science, 39 (1997) 855-875.

[28] H. Inoue, K. Sugahara, A. Yamamoto, H. Tsubakino, Corrosion rate of magnesium and its alloys in buffered chloride solutions, Corrosion Science, 44 (2002) 603-610.

[29] G. Baril, N. Pébère, Corrosion of pure magnesium in aerated and deaerated sodium sulphate solutions, Corrosion Science, 43 (2001) 471-484.

[30] M.-C. Zhao, M. Liu, G.-L. Song, A. Atrens, Influence of pH and chloride ion concentration on the corrosion of Mg alloy ZE41, Corrosion Science, 50 (2008) 3168-3178.

[31] H. Matsubara, Y. Ichige, K. Fujita, H. Nishiyama, K. Hodouchi, Effect of impurity Fe on corrosion behavior of AM50 and AM60 magnesium alloys, Corrosion Science, 66 (2013) 203-210.

[32] Y. Song, D. Shan, R. Chen, E.-H. Han, Effect of second phases on the corrosion behaviour of wrought Mg–Zn–Y–Zr alloy, Corrosion Science, 52 (2010) 1830-1837.

[33] Y. Song, E.-H. Han, D. Shan, C.D. Yim, B.S. You, The role of second phases in the corrosion behavior of Mg–5Zn alloy, Corrosion Science, 60 (2012) 238-245.

[34] F. Witte, N. Hort, C. Vogt, S. Cohen, K.U. Kainer, R. Willumeit, F. Feyerabend, Degradable biomaterials based on magnesium corrosion, Current Opinion in Solid State and Materials Science, 12 (2008) 63-72.

[35] R. Rettig, S. Virtanen, Time-dependent electrochemical characterization of the corrosion of a magnesium rare-earth alloy in simulated body fluids, Journal of Biomedical Materials Research - Part A, 85 (2008) 167-175.

[36] R. Arrabal, E. Matykina, F. Viejo, P. Skeldon, G.E. Thompson, Corrosion resistance of WE43 and AZ91D magnesium alloys with phosphate PEO coatings, Corrosion Science, 50 (2008) 1744-1752.

[37] Y.C. Xin, Corrosion behavior of biomedical AZ91 magnesium alloy in simulated body fluids, Journal of Materials Research, 22 (2007) 2004-2011.

[38] S. Feliu Jr, A. Samaniego, A.A. El-Hadad, I. Llorente, The effect of NaHCO3 treatment time on the corrosion resistance of commercial magnesium alloys AZ31 and AZ61 in 0.6M NaCl solution, Corrosion Science, 67 (2013) 204-216.

[39] T. Lei, W. Tang, S.-H. Cai, F.-F. Feng, N.-F. Li, On the corrosion behaviour of newly developed biodegradable Mg-based metal matrix composites produced by in situ reaction, Corrosion Science, 54 (2012) 270-277.

[40] F. Zucchi, V. Grassi, A. Frignani, C. Monticelli, G. Trabanelli, Electrochemical behaviour of a magnesium alloy containing rare earth elements, Journal of Applied Electrochemistry, 36 (2006) 195-204.

[41] Y. Song, D. Shan, R. Chen, F. Zhang, E.-H. Han, Biodegradable behaviors of AZ31 magnesium alloy in simulated body fluid, Materials Science and Engineering: C, 29 (2009) 1039-1045.

[42] M. Jamesh, S. Kumar, T.S.N. Sankara Narayanan, Corrosion behavior of commercially pure Mg and ZM21 Mg alloy in Ringer's solution – Long term evaluation by EIS, Corrosion Science, 53 (2011) 645-654.

[43] Y. Zhang, C. Yan, F. Wang, W. Li, Electrochemical behavior of anodized Mg alloy AZ91D in chloride containing aqueous solution, Corrosion Science, 47 (2005) 2816-2831.

[44] M.I. Jamesh, G. Wu, Y. Zhao, D.R. McKenzie, M.M.M. Bilek, P.K. Chu, Effects of zirconium and oxygen plasma ion implantation on the corrosion behavior of ZK60 Mg alloy in simulated body fluids, Corrosion Science, 82 (2014) 7-26.

[45] A. Oyane, H.M. Kim, T. Furuya, T. Kokubo, T. Miyazaki, T. Nakamura, Preparation and assessment of revised simulated body fluids, Journal of Biomedical Materials Research - Part A, 65 (2003) 188-195.

[46] A.E. Coy, F. Viejo, P. Skeldon, G.E. Thompson, Susceptibility of rare-earth-magnesium alloys to micro-galvanic corrosion, Corrosion Science, 52 (2010) 3896-3906.

[47] T. Rzychon, A. Kielbus, Microstructure of WE43 casting magnesium alloy, Journal of Achievements in Materials and Manufacturing Engineering, 21 (2007) 31-34.

[48] Y. Deng, Z. Yin, K. Zhao, J. Duan, J. Hu, Z. He, Effects of Sc and Zr microalloying additions and aging time at 120°C on the corrosion behaviour of an Al–Zn–Mg alloy, Corrosion Science, 65 (2012) 288-298.

[49] H.-Y. Ha, J.-Y. Kang, S.G. Kim, B. Kim, S.S. Park, C.D. Yim, B.S. You, Influences of metallurgical factors on the corrosion behaviour of extruded binary Mg–Sn alloys, Corrosion Science, 82 (2014) 369-379.

[50] N.I. Zainal Abidin, A.D. Atrens, D. Martin, A. Atrens, Corrosion of high purity Mg, Mg2Zn0.2Mn, ZE41 and AZ91 in Hank's solution at 37°C, Corrosion Science, 53 (2011) 3542-3556.

[51] G.R. Argade, S.K. Panigrahi, R.S. Mishra, Effects of grain size on the corrosion resistance of wrought magnesium alloys containing neodymium, Corrosion Science, 58 (2012) 145-151.

[52] M. Liu, P. Schmutz, P.J. Uggowitzer, G. Song, A. Atrens, The influence of yttrium (Y) on the corrosion of Mg–Y binary alloys, Corrosion Science, 52 (2010) 3687-3701.

[53] N.I. Zainal Abidin, B. Rolfe, H. Owen, J. Malisano, D. Martin, J. Hofstetter, P.J. Uggowitzer, A. Atrens, The in vivo and in vitro corrosion of high-purity magnesium and magnesium alloys WZ21 and AZ91, Corrosion Science, 75 (2013) 354-366.

[54] Y. Song, E.-H. Han, D. Shan, C.D. Yim, B.S. You, The effect of Zn concentration on the corrosion behavior of Mg–xZn alloys, Corrosion Science, 65 (2012) 322-330.

[55] K.V. Kutniy, I.I. Papirov, M.A. Tikhonovsky, A.I. Pikalov, S.V. Sivtzov, L.A. Pirozhenko, V.S. Shokurov, V.A. Shkuropatenko, Influence of grain size on mechanical and corrosion properties of magnesium alloy for medical implants. Einfluss der Korngröße auf die mechanischen und korrosionstechnischen Eigenschaften von Magnesiumlegierungen für medizinische Implantate, Materialwissenschaft und Werkstofftechnik, 40 (2009) 242-246.

[56] R. Rettig, S. Virtanen, Composition of corrosion layers on a magnesium rare-earth alloy in simulated body fluids, Journal of Biomedical Materials Research - Part A, 88 (2009) 359-369.

[57] G. Baril, G. Galicia, C. Deslouis, N. Pebere, B. Tribollet, V. Vivier, An Impedance Investigation of the Mechanism of Pure Magnesium Corrosion in Sodium Sulfate Solutions, Journal of the Electrochemical Society, 154 (2007) C108-C113.

[58] N. Pebere, C. Riera, F. Dabosi, Investigation of magnesium corrosion in aerated sodium sulfate solution by electrochemical impedance spectroscopy, Electrochimica Acta, 35 (1990) 555-561.

[59] J.B. Jorcin, M.E. Orazem, N. Pébère, B. Tribollet, CPE analysis by local electrochemical impedance spectroscopy, Electrochimica Acta, 51 (2006) 1473-1479.

[60] P. Zoltowski, On the electrical capacitance of interfaces exhibiting constant phase element behaviour, Journal of Electroanalytical Chemistry, 443 (1998) 149-154.

[61] G. Galicia, N. Pébère, B. Tribollet, V. Vivier, Local and global electrochemical impedances applied to the corrosion behaviour of an AZ91 magnesium alloy, Corrosion Science, 51 (2009) 1789-1794.

[62] N.S. McIntyre, C. Chen, Role of impurities on Mg surfaces under ambient exposure conditions, Corrosion Science, 40 (1998) 1697-1709.

[63] J.H. Nordlien, S. Ono, N. Masuko, K. Nisancioglu, Morphology and structure of oxide films formed on magnesium by exposure to air and water, Journal of the Electrochemical Society, 142 (1995) 3320-3322.

[64] J.H. Nordlien, S. Ono, N. Masuko, K. Nisancioglu, A tem investigation of naturally formed oxide films on pure magnesium, Corrosion Science, 39 (1997) 1397-1414.

[65] J.T. Müller, P.M. Urban, W.F. Hölderich, Impedance studies on direct methanol fuel cell anodes, Journal of Power Sources, 84 (1999) 157-160.

[66] G.J. Brug, A.L.G. Van Den Eeden, M. Sluyters-Rehbach, J.H. Sluyters, The analysis of electrode impedances complicated by the presence of a constant phase element, Journal of Electroanalytical Chemistry, 176 (1984) 275-295.

[67] B. Hirschorn, M.E. Orazem, B. Tribollet, V. Vivier, I. Frateur, M. Musiani, Determination of effective capacitance and film thickness from constant-phase-element parameters, Electrochimica Acta, 55 (2010) 6218-6227.

[68] C.H. Hsu, F. Mansfeld, Technical Note: Concerning the Conversion of the Constant Phase Element Parameter Y0 into a Capacitance, Corrosion, 57 (2001) 747-748.

[69] E. Ghali, W. Dietzel, K.U. Kainer, Testing of general and localized corrosion of magnesium alloys: A critical review, Journal of Materials Engineering and Performance, 13 (2004) 517-529.

[70] A. Oyane, K. Onuma, A. Ito, H.M. Kim, T. Kokubo, T. Nakamura, Formation and growth of clusters in conventional and new kinds of simulated body fluids, Journal of Biomedical Materials Research - Part A, 64 (2003) 339-348.

[71] Z. Shi, M. Liu, A. Atrens, Measurement of the corrosion rate of magnesium alloys using Tafel extrapolation, Corrosion Science, 52 (2010) 579-588.

[72] A. Slósarczyk, Z. Paszkiewicz, C. Paluszkiewicz, FTIR and XRD evaluation of carbonated hydroxyapatite powders synthesized by wet methods, Journal of Molecular Structure, 744-747 (2005) 657-661.

[73] Y. Zhu, G. Wu, Y.H. Zhang, Q. Zhao, Growth and characterization of Mg(OH)2 film on magnesium alloy AZ31, Applied Surface Science.

[74] L. Xu, C. Liu, Y. Wan, X. Wang, H. Xiao, Effects of heat treatments on microstructures and mechanical properties of Mg–4Y–2.5Nd–0.7Zr alloy, Materials Science and Engineering: A, 558 (2012) 1-6.

[75] L. Xu, F. Pan, G. Yu, L. Yang, E. Zhang, K. Yang, In vitro and in vivo evaluation of the surface bioactivity of a calcium phosphate coated magnesium alloy, Biomaterials, 30 (2009) 1512-1523.

[76] D.K. Aswal, K.P. Muthe, S. Tawde, S. Chodhury, N. Bagkar, A. Singh, S.K. Gupta, J.V. Yakhmi, XPS and AFM investigations of annealing induced surface modifications of MgO single crystals, Journal of Crystal Growth, 236 (2002) 661-666.

[77] N.I. Zainal Abidin, D. Martin, A. Atrens, Corrosion of high purity Mg, AZ91, ZE41 and Mg2Zn0.2Mn in Hank's solution at room temperature, Corrosion Science, 53 (2011) 862-872.

[78] M. Bornapour, N. Muja, D. Shum-Tim, M. Cerruti, M. Pekguleryuz, Biocompatibility and biodegradability of Mg–Sr alloys: The formation of Sr-substituted hydroxyapatite, Acta Biomaterialia, 9 (2013) 5319-5330.

Chapter 5

An investigation of the corrosion mechanisms of WE43 Mg alloy in a modified simulated body fluid solution: The effect of electrolyte renewal

M. Ascencio[1], M. Pekguleryuz[2] and S. Omanovic[1]

(1) Department of Chemical Engineering, (2) Department of Mining and Materials Engineering
McGill University, Montreal, Quebec, H3A 0C5, Canada

PREFACE

This chapter is comprised of one published journal manuscript. It was shown in previous chapters that difficulties at emulating the physiological environment *in vitro* due to the fast increase of the electrolyte pH and the accumulation of corrosion products, among other factors, limit the significance of current *in vitro* methodologies for the investigation of the corrosion behaviour of Mg-based biodegradable materials. The focus of this part of the study is to investigate the effect of daily electrolyte renewal on the corrosion kinetics and mechanisms of WE43 Mg alloy in a modified simulated body fluid (m-SBF) solution. Daily electrolyte renewal was performed as a method to control the increase in the electrolyte pH and the accumulation of corrosion products, thereby better simulating physiological homeostasis. The production of hydrogen gas, the variation in the electrolyte pH and concentration of magnesium, calcium and phosphate ions, and the morphology and composition of the corrosion products layer were also investigated. Immersion experiments were performed for a time period up to five days at 37 ºC and at an initial pH of 7.4, corresponding to physiological conditions. Complete electrolyte

renewal was performed on a daily basis. Interfacial processes such as charge transfer, adsorption of Mg intermediates and diffusion of Mg^{2+} ions were investigated and monitored after different immersion times by electrochemical impedance spectroscopy (EIS). Normalized corrosion rate values calculated by EIS, hydrogen evolution and ICP-OES are compared and their variation with time is discussed. The corrosion products layer composition and morphology were investigated by SEM, EDS, XRD, ATR-FTIR and XPS. Finally, a corrosion mechanism as a function of immersion time was proposed taking into account the analysis of the corrosion kinetics results, the EIS time-dependent fitting parameters and the characterization of the corrosion products layer.

The co-authors of the manuscript presented in this chapter are listed above. The contributions of each author were the following: Mario Ascencio designed the experiments, prepared samples, performed the experimental work, analyzed results and wrote the manuscript. Prof. Mihriban Pekguleryuz provided samples and contributed in the interpretation and discussion of results. Prof. Sasha Omanovic provided guidance, contributed in the interpretation and discussion of results and corrected the manuscript.

The authors gratefully acknowledge the financial support from the Natural Science and Engineering Research Council of Canada (NSERC) and the National Council of Science and Technology of Mexico (CONACyT). The contribution of Pierre Vermette in the casting of the Mg alloy samples is also acknowledged.

An investigation of the corrosion mechanisms of WE43 Mg alloy in a modified simulated body fluid solution: The effect of electrolyte renewal

This section has been published as: M. Ascencio, M. Pekguleryuz, S. Omanovic, An investigation of the corrosion mechanisms of WE43 Mg alloy in a modified simulated body fluid solution: The effect of electrolyte renewal, Corrosion Science, 91 (2015) 297-310.

5.1 ABSTRACT

The effect of daily electrolyte renewal on the corrosion mechanisms and kinetics of WE43 Mg alloy in a modified simulated body fluid (m-SBF) is investigated by electrochemical, hydrogen evolution, analytical and surface characterization techniques. It is shown that by performing electrolyte renewal, physiological control of corrosion products and concentration of relevant electrolyte components such as calcium, phosphate and carbonate species, can be better emulated. Electrolyte renewal affects the corrosion mechanism by promoting partial dissolution of the corrosion layer and increasing mass transport, thereby delaying the increase in the corrosion layer protective ability and the occurrence of localized corrosion.

5.2 INTRODUCTION

Bioabsorbable implants have emerged as an alternative to avoid long term complications caused by permanent implants in applications that require a device with a

temporary short function, such as endovascular stents and bone repair implants. Mg and some of its alloys are biocompatible and have good mechanical properties, which make them good candidates for biodegradable applications [1-4]. *In vivo* experiments and clinical trials have demonstrated the feasibility of Mg-based bioabsorbable implants [5-13]. However, the main limitations of Mg alloy implants remain their fast biodegradation rate, with the concomitant decrease in their mechanical properties, and the fast production of hydrogen gas, leading to subcutaneous gas accumulation [14]. An additional concern is the presence of potentially toxic elements in commercially available Mg alloys, whose development has been mainly driven by the needs of the transportation industry [15].

Magnesium biodegradation occurs by corrosion and therefore, knowledge of the implant corrosion susceptibility and related corrosion mechanisms is fundamental for the assessment of prospective implant materials. The corrosion of Mg is a complex process and different mechanisms have been proposed [16]. According to Song et al. [16] the corrosion of Mg in an aqueous media occurs through the following partial reactions:

$2H_2O + 2e^- \rightarrow H_2 + 2OH^-$ (cathodic reaction) (5.1)

$2Mg \rightarrow 2Mg^+ + 2e^-$ (anodic reaction) (5.2)

$2Mg^+ + 2H_2O \rightarrow 2Mg^{2+} + 2OH^- + H_2$ (chemical reaction) (5.3)

$2Mg + 4H_2O \rightarrow 2Mg^{2+} + 4OH^- + 2H_2$ (overall reaction) (5.4)

$Mg^{2+} + 2OH^- \rightarrow Mg(OH)_2$ (product formation) (5.5)

At the substrate/electrolyte interface Mg is oxidized to Mg^{+} intermediate species (reaction (5.2)), which then react chemically with water forming H_2 gas, Mg^{2+} and OH^{-} species (reaction (5.3)). Electrochemical water reduction (reaction (5.1)) also contributes to formation of H_2 gas and OH^{-} species. The corrosion behaviour of Mg alloys is affected by the surrounding electrolyte pH [17-19]. During the corrosion process, the electrolyte pH near the electrode surface increases due to the accumulation of OH^{-} ions, leading to formation of a $Mg(OH)_2$ corrosion layer (reaction (5.5)), which provides partial corrosion protection by preventing mass diffusion between the alloy substrate and the electrolyte. However, Mg alloys have a poor corrosion resistance in neutral solutions and in the presence of aggressive electrolyte species such as Cl^{-} ions, which promote the dissolution of the protective $Mg(OH)_2$ layer (reaction (5.6)) and the occurrence of localized corrosion [16, 20-22].

$$Mg(OH)_2 + 2Cl^{-} \rightarrow Mg^{2+} + 2Cl^{-} + 2OH^{-} \quad (5.6)$$

Current research efforts aim at the development of new Mg alloys with improved corrosion resistance and biocompatibility. However, this is limited by the lack of a complete understanding of the Mg alloy corrosion mechanisms in the real physiological environment and by difficulties at emulating such environment *in vitro*. For instance, the concentration of the implant corrosion products in the body fluid, i.e., Mg^{2+} and OH^{-}, is regulated by homeostatic processes; however, in *in vitro* experiments, a fast increase in the electrolyte concentration of these ions as a result of the rapid corrosion rate often occurs, leading to an increase in the electrolyte pH and thus, possibly affecting the Mg alloy corrosion mechanisms and degradation rate. These limitations might be one of the reasons for the discrepancies observed in the corrosion performance of Mg alloys by *in*

vitro and *in vivo* investigations [23]. It has been shown that the selection of the electrolyte composition, the use of buffering agents to control the electrolyte pH and the electrolyte-volume/sample-surface ratio have an impact on the *in vitro* corrosion behaviour of Mg alloys [24-26]. Control of the electrolyte pH has been attempted by the use of buffering reagents such as TRIS and HEPES; however, an increase in the electrolyte pH beyond the physiological range, with pH values above 8, has been reported [27-31], or the pH increase has not at all been reported [32-36]. The increase in the electrolyte pH and concentration of Mg^{2+} ions can also affect the solubility equilibrium of relevant electrolyte components such as calcium, phosphate and carbonate species, which play a role in the protective ability of the corrosion layer and the occurrence of localized corrosion. An alternative to control the increase in the electrolyte pH and concentration of Mg^{2+} ions is by performing daily electrolyte renewal. By using this method, physiological homeostasis, i.e., physiological control of electrolyte pH and Mg^{2+} ions concentration, can be better simulated compared to long-term stagnant immersion experiments. Yamamoto et al. performed daily partial electrolyte renewal in the investigation of the degradation of pure Mg in different electrolytes [25]. However, a systematic investigation of the effect of electrolyte renewal and the corresponding variation in pH and electrolyte components concentration on the Mg alloy corrosion behaviour has not yet been reported.

The present work reports our results on the effect of daily electrolyte renewal, with the aim to better simulate physiological homeostasis, on the short-term (up to 5 days) corrosion behaviour of a commercial WE43 Mg alloy in a modified simulated body fluid (m-SBF). The selected electrolyte has a composition similar to that of blood plasma

and is buffered with HEPES to better control changes in the electrolyte pH. Interfacial processes and corrosion mechanisms are investigated by electrochemical impedance spectroscopy (EIS). The electrode degradation kinetics is investigated by analytical and hydrogen-evolution techniques and the results are compared to those obtained by EIS. Finally, a corrosion mechanism is proposed taking into account the degradation kinetics results, the analysis of the EIS fitting parameters and the corrosion products characterization.

5.3 EXPERIMENTAL SECTION

5.3.1 Sample preparation

Commercial WE43 Mg alloy (Magnesium Elektron, USA) with a chemical composition of 3.48 wt.% yttrium, 2.0 wt.% neodymium, 0.5 wt.% gadolinium, 0.15 wt.% praseodymium, magnesium balance, was die cast into rods using an electrical induction furnace (Norax, Canada) and a boron nitride-coated steel die. In order to prevent oxidation of the alloy during the melting and casting processes, CO_2 with 0.5% SF_6 was supplied at a flow rate of 1.1 dm^3 min^{-1}. The temperature was monitored using a K-type Chromel-Alumel thermocouple (Omega, USA). Prior to the casting process, the steel die was heated to 400 °C using a Lindberg/Blue M crucible furnace (Thermal Product Solutions, USA). As-cast WE43 Mg alloy rods were machined to a diameter of 1.59 cm and cut into coins with a thickness of 0.5 cm. Electrodes for immersion experiments were prepared by attaching an insulated copper wire to the coins using conductive silver epoxy (Chemtronics Circuitworks, USA) and embedding the coins in epoxy resin (Epofix, Struers, USA). The final exposed area of the samples was 1.98 cm^2. Before the

immersion experiments, the electrode surface was wet-abraded using SiC paper up to 1200-grit and then fine-polished with diamond paste to a final polishing particle roughness of 1 μm. Finally, the samples were ultrasonically cleaned in ethanol for 10 minutes to remove polishing residue, rinsed with acetone and dried in argon. This procedure ensured a reproducible surface state of the working electrodes.

5.3.2 Immersion experiments

Modified simulated body fluid (m-SBF), as defined by Oyane et al. [37], with a final pH of 7.4 was prepared using reagent grade chemicals and deionized water with a resistivity of 18.2 MΩ cm. The amounts of chemicals used are shown in Table 5.1. In contrast with the recipe provided by Oyane, only 10 cm^3 of 1M NaOH solution were needed to adjust the final pH to a value of 7.4. Table 5.2 shows the nominal concentration of m-SBF and blood plasma. Immersion experiments were performed for a time period up to 5 days. The electrolyte-volume/sample-surface ratio was 50 cm^3/cm^2 and the electrolyte was in contact with air. All the experiments were done in triplicates. In order to closer simulate physiological homeostasis, the m-SBF electrolyte was completely renewed every 24h. Electrochemical measurements were performed after different immersion times and electrolyte samples were collected for inductively coupled plasma optical emission spectroscopy (ICP-OES) analysis. From independent immersion experiments, the amount of hydrogen gas produced was measured using the method proposed in the literature [38]. All the experiments were carried out at the average human body temperature of 37 °C. The electrolyte temperature was controlled using a water bath equipped with a thermostat. At the end of the immersion experiments, the samples were removed from the electrochemical cell, rinsed with

distilled water and dried with argon gas. After surface characterization of the corrosion products, the corrosion layer was dissolved by immersion in chromic acid (180 g CrO_3/dm^3) for 5-10 min in order to analyse the morphology of the underlying (corroded) Mg alloy substrate.

Table 5.1: Amounts of reagents used to prepare 1000 ml of m-SBF [37].

Reagents[a]	Purity / %	Amount
NaCl	>99.5	5.4030 g
$NaHCO_3$	>99.5	0.5040 g
Na_2CO_3	>99	0.4260 g
KCl	>99	0.2250 g
K_2HPO_4	>98	0.1756 g
$MgCl_2 \times 6H_2O$	>99.4	0.3110 g
HEPES[b]	>99.5	17.8920 g[c]
$CaCl_2 \times 2H_2O$	>99	0.3881 g
Na_2SO_4	>99.2	0.0720 g
1.0 M NaOH	---	10 ml

[a] Listed in sequence of dissolution
[b] HEPES, 2-(4-(2-hydroxyethyl)-1-piperazinyl) ethanesulfonic acid
[c] HEPES was previously dissolved in 100 ml of 0.2M NaOH

Table 5.2: Nominal concentration of m-SBF and blood plasma [37].

Ion	Concentration / mM	
	Blood plasma	m-SBF
Na^+	142	122.5
K^+	5	5
Mg^{2+}	1.5	1.5
Ca^{2+}	2.5	2.5
Cl^-	103	103
HCO_3^-	27	10
HPO_4^{2-}	1	1
SO_4^{2-}	0.5	0.5

5.3.3 Electrochemical techniques

Electrochemical experiments were performed in a standard three-electrode electrochemical cell. WE43 Mg alloy samples were used as working electrodes, a graphite rod as counter electrode and a saturated calomel electrode (SCE, Fisher Scientific Accumet, USA) as reference electrode. All potentials in this paper are referred to the SCE. Electrochemical measurements were carried out using a potentiostat/galvanostat (Autolab PGSTAT30, Netherlands) equipped with a frequency response analyser. Open circuit potential measurements were performed over a time period of 5 days. Electrochemical impedance measurements were carried out at open circuit potential with an AC amplitude of 10 mV over a frequency range from 100 kHz to 10 mHz.

5.3.4 Electrolyte analysis and corrosion products characterization

Inductively coupled plasma optical emission spectroscopy (ICP-OES, Thermo Jarrell Ash Trace Scan, USA) was used to measure the electrolyte concentration of magnesium, calcium and phosphate species at wavelengths of 285.2, 422 and 178.2 nm, respectively. The morphology and composition of the sample surface were characterized by scanning electron microscopy (FE-SEM, Philips XL-30, Netherlands) equipped with an energy-disperse spectrometer (EDS). The corrosion layer thickness was measured by cross-sectional SEM analysis of the sample.

5.4 RESULTS AND DISCUSSION

5.4.1 Electrochemical Experiments

Figure 5.1 shows the open circuit potential (OCP) and pH time-dependent behaviour of the Mg alloy electrode during the 5-day immersion in m-SBF, with daily electrolyte renewal. OCP values describe the Mg alloy electrode free corrosion potential in the absence of any external current or potential bias. A fast increase in OCP during the first 8h can be observed, followed by a gradual approach of OCP to a quasi-constant value of ca. -1.6 V vs. SCE, reached after 100h of immersion. The trend is also characterized by an alternating decrease/increase behaviour occurring after each renewal of the electrolyte. The OCP of a polarizable electrode is conventionally explained by the mixed potential theory; however, in the case of a corroding electrode, formation of a non-conductive corrosion layer alters the electrolyte double layer and thus, the corrosion layer surface coverage effect has also to be considered [39]. The observed increase in OCP can thus be related to the formation of a $MgO/Mg(OH)_2$ corrosion layer with increasing coverage/protective properties over time, while its intermittent decrease after each electrolyte renewal, can be related to a temporary reduction in the corrosion layer coverage/protective ability. Changes in the electrolyte pH and concentration of Mg^{+2} ions after electrolyte renewal can affect the solubility of the corrosion layer. Equation (5.7) shows a solubility equilibrium equation for $Mg(OH)_2$ in an aqueous medium [40]:

$$\log[Mg^{2+}]=16.95-2pH \qquad (5.7)$$

From this equation, a decrease in the electrolyte pH from 7.8 to 7.4, which was observed after electrolyte renewal at 24 h, leads to a sixfold increase in the Mg^{2+}

equilibrium concentration, with the respective increase in the $Mg(OH)_2$ solubility. The equilibrium solubility of carbonate and phosphate species precipitated into the corrosion layer is also affected by electrolyte renewal (discussed later in the paper). This suggests that partial dissolution of the corrosion layer after electrolyte renewal leads to a decrease in the corrosion layer surface coverage and/or increase in its porosity, enhancing mass diffusion between the substrate surface and the electrolyte and thereby, causing a shift in the corrosion potential to more negative values (Figure 5.1). The decreasing effect of electrolyte renewal on OCP values observed at longer immersion times and the quasi-constant OCP values observed after 96h suggest a gradual increase in the corrosion layer coverage until a constant coverage is reached. This behaviour can be related to changes in coverage of an inner MgO barrier film formed underneath the $Mg(OH)_2$ corrosion layer, as will be discussed subsequently in the text.

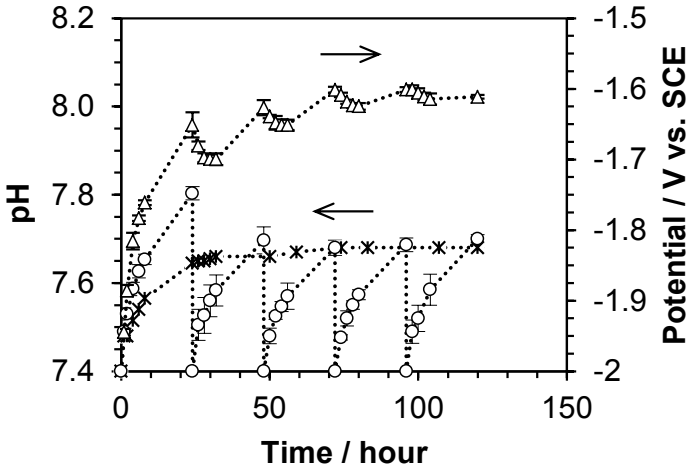

Figure 5.1: Time-dependent open circuit potential (triangles) and pH (circles) behaviour of WE43 Mg alloy in m-SBF with daily electrolyte renewal. Asterisks show the pH change of m-SBF without corroding sample.

Similarly to the OCP behaviour, an alternating increase/decrease in pH values can be observed, with decreases corresponding to electrolyte renewal. The largest pH increase, of about 0.4 units, was observed during the first day of immersion, followed by a repetitive daily pH increase of about 0.3 units at subsequent immersion times. It has been shown that the release of CO_2 to the atmosphere and the corresponding decrease in the concentration of carbonate species (reaction (5.8)) leads to an increase in the SBF pH [37].

$$H_2CO_{3(aq)} \leftrightarrow CO_{2(g)} + H_2O_{(aq)} \quad (5.8)$$

Thus, the observed daily increase in the electrolyte pH corresponds to the combined effect of the WE43 alloy corrosion reaction and the release of CO_2. A control experiment performed to test the electrolyte pH stability without the corroding sample, showed that the electrolyte pH increases to a value of ca. 7.7 after 24 h, followed by a quasi-constant pH at longer immersion times (Figure 5.1, asterisks). Thus, the difference in the behaviour between the two pH trends in Figure 5.1 indicates that the faster corrosion rate during the first 24 h induces the larger initial increase in pH, while the subsequent repetitive increases in the electrolyte pH at longer immersion times can be related mainly to the release of CO_2 and the corresponding decrease in the concentration of carbonates; note that the initial pH increase rate in the control experiment (asterisks) is similar to those obtained after electrolyte renewal with the corroding WE43 alloy sample (circles). It has been shown that carbonates induce fast passivation of Mg alloys at corrosion sites, suppressing pitting corrosion [35, 41]; however, the effect of carbonate concentration variations due to the release of CO_2 on the Mg alloys corrosion mechanisms is usually not considered in *in vitro* investigations.

In this regard, electrolyte renewal contributes to maintenance of an electrolyte carbonate concentration close to the physiological value; however, experimental conditions that allow for a constant carbonate concentration are necessary to better simulate the physiological environment.

In order to gain a better insight into the Mg alloy corrosion process, electrochemical impedance spectroscopy (EIS) was used to investigate the electrode corrosion resistance and to obtain information on the processes occurring at the electrode/electrolyte interface before and after electrolyte renewal. Figure 5.2 shows Nyquist and Bode plots for the impedance response of WE43 Mg alloy in m-SBF after 1h of immersion. Three time constants can be distinguished (τ_1, τ_2 and τ_3), corresponding to two capacitive loops at high and medium frequencies and one inductive loop at low frequencies, respectively. The capacitive loop at high frequencies (τ_1) can be related to charge transfer and electrochemical double-layer/oxide film effects; the capacitive loop at medium frequencies (τ_2) can be related to mass transport relaxation due to diffusion of Mg^{2+} ions through the corrosion layer and, the inductive loop at low frequencies (τ_3) can be related to a relaxation process due to adsorption of Mg^{+} intermediate species [42]. A three-time-constant electrical equivalent circuit (EEC) was used to fit the impedance response (Figure 5.3). By using this EEC a good fit was obtained with an average value of $\chi^2=1.5x10^{-4} \pm 1.9x10^{-4}$. A constant phase element (CPE) was used to model the electrode capacitive behaviour. CPE's are often used to describe a non-ideal capacitive behaviour due to different factors such as distributed surface reactivity, surface inhomogeneity, roughness or fractal geometry, electrode

porosity and non-uniform current and potential distributions [43]. The impedance of a CPE is given by the following equation:

$$Z_{CPE} = Q^{-1}(j\omega)^{-n} \qquad \text{with} \quad -1 \le n \le 1 \tag{5.9}$$

where Z is the CPE impedance (Ωcm^2), Q is a constant with units $\Omega^{-1}\,cm^{-2}\,s^n$, n is a dimensionless constant in the range $-1 \le n \le 1$, j is the imaginary number $j=(-1)^{0.5}$ and ω is the angular frequency ($\omega = 2\pi f$, f being the frequency in Hz). An ideal capacitor behaviour yields $n = 1$, a resistor yields $n = 0$ and an inductor yields $n = -1$, while $n = 0.5$ represents the response of mass-transport processes.

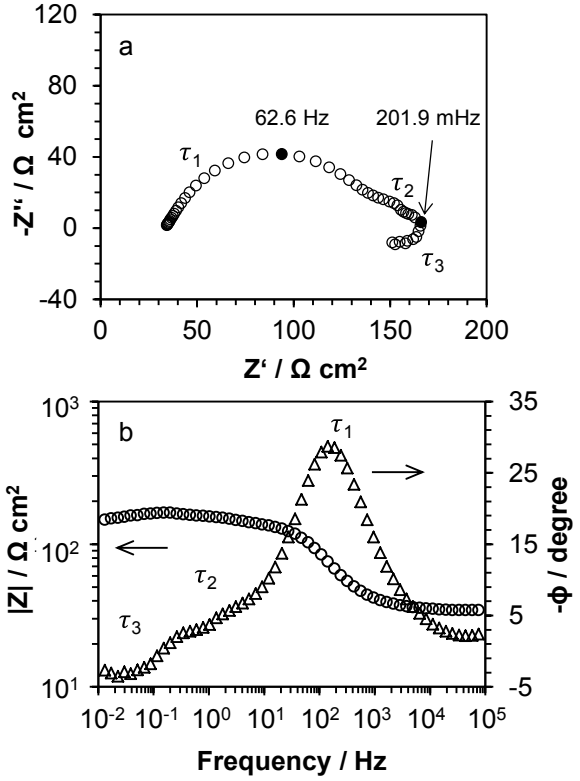

Figure 5.2: (a) Nyquist and (b) Bode plots of WE43 Mg alloy in m-SBF, recorded at OCP after 1 h of immersion.

The microstructure of the WE43 Mg alloy has been previously described by the authors [28]. The EEC physical interpretation was elaborated according to the following data reported in the literature for the corrosion of pure Mg and assuming that the WE43 Mg alloy α-Mg matrix has a corrosion behaviour similar to that of pure Mg, as has been pointed out by some authors for other Mg alloys [44, 45]: 1) the corrosion layer is composed of a thin MgO barrier film in contact with the substrate metal and a relatively thick $Mg(OH)_2$ layer covering the MgO film and the film-free areas [46]; and 2) Mg corrosion occurs on the corrosion film-free areas with the formation of adsorbed Mg intermediates (reaction (5.2)) [21]. Thus, CPE-1 and R_1 describe, respectively, the charge transfer resistance and the combined electrochemical double layer/MgO barrier film capacitance at the substrate/electrolyte interface; R_2 and CPE-2 describe the diffusion of Mg^{2+} species through the outer $Mg(OH)_2$ corrosion layer; L and R_L describe, respectively, the inductance and inductance resistance due to the adsorption of intermediate species at the MgO film-free surface; and R_e describes the electrolyte resistance between the working and reference electrodes.

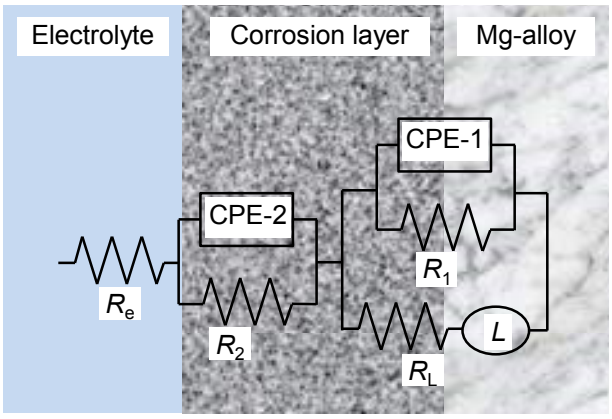

Figure 5.3: Equivalent electrical circuit (EEC) used to fit the EIS data obtained from WE43 Mg alloy in m-SBF.

Figure 5.4 shows the impedance response of the Mg alloy electrode after different immersion times up to 120 h. A progressive increase in the impedance response during the first 24 h of immersion can be observed (Figure 5.4a-b), corresponding to an increase in the corrosion layer protective properties over time. At immersion times longer than 24 h (Figure 5.4b-e) an initial decrease in the impedance response after every electrolyte renewal was observed, followed by a subsequent increase in impedance. In addition, changes in the relative size of the capacitive and inductive loops can be observed. Figure 5.4b-e shows the impedance response right before electrolyte renewal (squares), 8 hours after electrolyte renewal (circles) and 24 h after electrolyte renewal (triangles). The observed decrease in the impedance response occurred gradually, reaching its minimum value ca. 8 h after electrolyte renewal. After 24 h and 48 h, the impedance response changed from two capacitive loops before electrolyte renewal, to only one capacitive loop and one inductive loop 8 h after electrolyte renewal, and then it increased again showing two capacitive loops 24 h after electrolyte renewal. After 72 h and 96 h, a smaller decrease in the impedance response after electrolyte renewal can be seen, with an almost constant shape of the impedance response after 80 h, showing only one capacitive loop and one inductive loop. Thus, it appears that the electrolyte renewal had a decreasing effect over time on the impedance response, with the largest decrease observed after the first electrolyte renewal (24 h after immersion), and the smallest decrease observed after the last electrolyte renewal (96 h after immersion). The changes observed in the size and shape of the impedance response reveal a variation in the corrosion layer protective ability and corrosion mechanisms over time, as a result of electrolyte renewal. In our previous

publication [28], which reported results on the corrosion of WE43 Mg alloy without electrolyte renewal, the corrosion mechanism of WE43 Mg alloy in m-SBF was investigated as a function of immersion time. In the same work, the increase in the size of the impedance response and the change in its shape over time were related respectively to formation of an inner MgO barrier film with increasing coverage and, to the presence of four different corrosion stages. We can adopt the same explanation for the behaviour in Figure 5.4, in the current work.

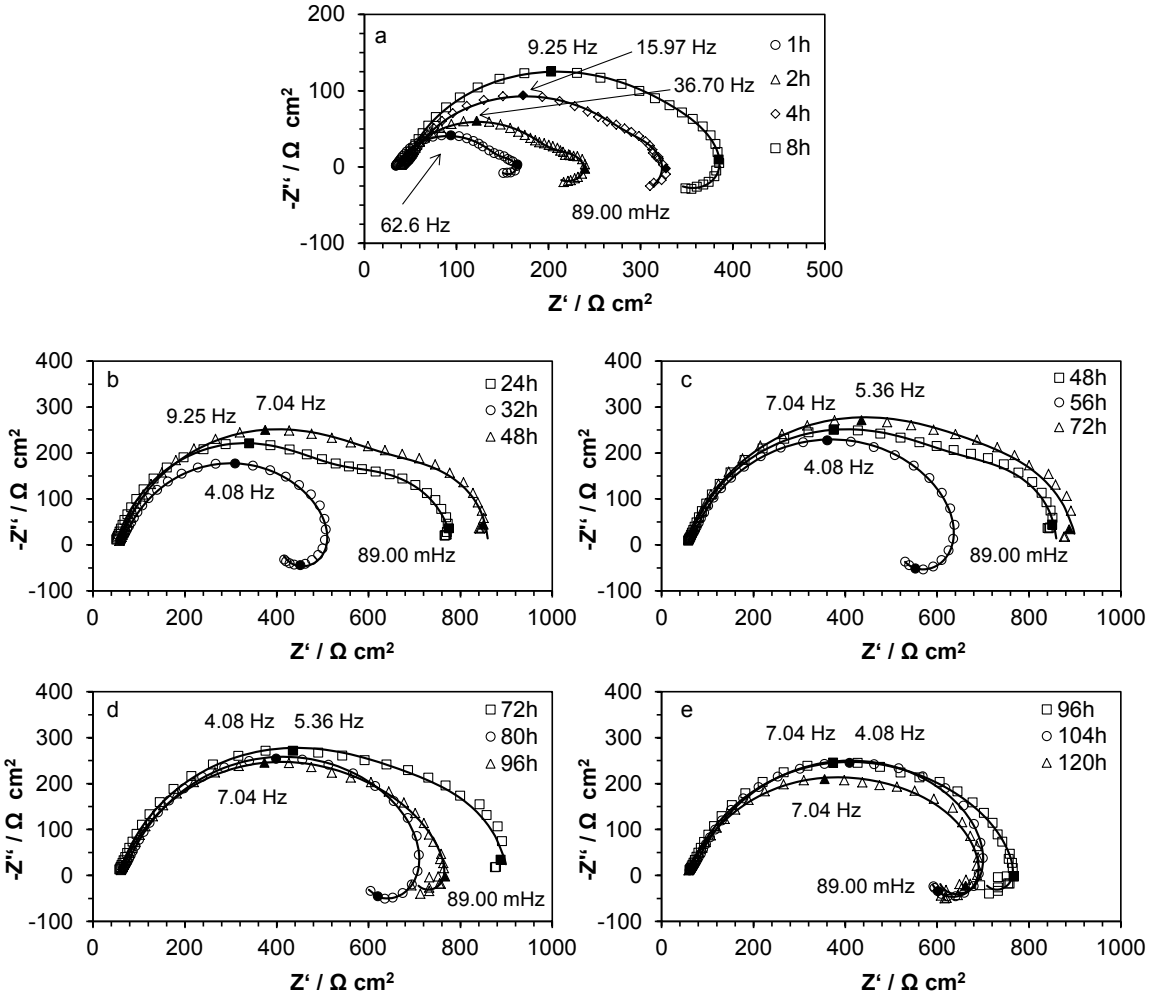

Figure 5.4: Electrochemical impedance response of WE43 Mg alloy in m-SBF with daily electrolyte renewal after different immersion times: (a) 1-8 h, (b) 24-48 h, (c) 48-72 h,

(d) 72-96 h and (e) 96-120 h. Symbols represent experimental values, whereas continuous lines represent simulated spectra.

To better understand the corrosion process and to obtain more information on the changes occurring at the electrode/electrolyte interface after electrolyte renewal, the impedance response fitting parameters were analysed as a function of time. Table 5.3 shows the EIS fitting parameters obtained for some selected immersion times. Figure 5.5 shows the variation of R_1 and R_2 with immersion time. A general increase in R_1 with time can be observed, with an intermittent increase/decrease pattern corresponding to electrolyte renewal, until a quasi-constant value of ca. 1 kΩ cm^2 is reached after 72 h. R_2 also shows the intermittent increase/decrease pattern, with values in the range of 18-251 Ω cm^2 during the first 72 h and then decreasing to 17-60 Ω cm^2 at longer immersion times. The increase in R_1 and R_2 corresponds to the increase in the protective properties of the corrosion layer over time, while their intermittent decrease indicates a temporary reduction in the corrosion layer resistance as a result of electrolyte renewal. The overall increase in R_1 can be related to formation of an inner MgO passive film with increasing coverage over time, reaching a quasi-constant coverage after 72 h. The behaviour displayed by R_1 follows the same trend observed for OCP values (Figure 5.1), demonstrating that the OCP depends on the MgO barrier film coverage. On the other hand, the increase in the diffusion resistance (R_2) can be related to a decrease in the porosity of the $Mg(OH)_2$ layer due to the increase in pH and the precipitation of phosphate and carbonate species (discussed later in the paper), found to enhance the corrosion layer protective properties. The decrease in the diffusion resistance (R_2) after electrolyte renewal can be related to partial dissolution of the corrosion layer as a result

of the lower electrolyte pH and Mg^{2+} concentration, leading to increased mass transfer through the $Mg(OH)_2$ layer and possibly to partial destruction of the inner MgO barrier film, with the corresponding decrease in R_1. The smaller R_2 values observed from 72-120 h can be related to the occurrence of a localized corrosion process, i.e., pitting, with a decreased diffusion resistance due to rupture of the $Mg(OH)_2$ corrosion layer (Figure 5.11c).

Table 5.3: Fitting parameters for WE43 Mg alloy in m-SBF after different immersion times.

Time/ h	R_e/ $\Omega\,cm^2$	$Q_1\times10^5$/ $\Omega^{-1}cm^{-2}s^n$	n_1	C_{dl}/ $\mu F cm^{-2}$	R_1/ $\Omega\,cm^2$	$Q_2\times10^5$/ $\Omega^{-1}cm^{-2}s^n$	n_2	R_2/ $\Omega\,cm^2$
1	35.3	4.77	0.90	115.98	67.1	318.50	0.43	79.3
8	46.5	10.43	1.00	42.66	276.0	36.80	0.66	134.9
24	57.3	111.66	0.94	16.46	609.7	5.56	0.83	251.1
32	48.2	82.34	0.50	45.87	500.7	13.58	0.82	21.9
48	58.8	122.83	1.00	19.55	721.0	7.20	0.81	221.6
56	55.2	13.87	0.75	36.56	738.0	11.27	0.82	18.4
72	77.2	127.77	1.00	21.33	996.7	7.45	0.81	219.9
80	62.9	9.13	0.78	33.07	904.0	10.25	0.82	17.1
96	67.1	179.48	0.98	20.95	954.0	8.33	0.79	59.1
104	61.6	6.81	0.83	29.49	928.0	10.43	0.80	19.6
120	74.8	150.08	1.00	20.55	935.3	9.59	0.77	48.4

The CPE's parameter *Q* cannot be used to represent pure capacitance when its power "*n*" substantially deviates from unity [47]. Therefore, electrochemical double layer/MgO barrier film capacitance values, C_1 (F cm^{-2}), were calculated using Brug's equation [48]:

$$C_1 = Q_1^{-n_1}\left(\frac{R_e R_1}{R_e + R_1}\right)^{(1-n_1)/n_1} \tag{5.10}$$

where Q_1 is the CPE-1 constant ($\Omega^{-1}\,cm^{-2}\,s^n$), R_e is the electrolyte resistance ($\Omega\,cm^2$), R_1 is the charge transfer resistance ($\Omega\,cm^2$) and n_1 is the CPE-1 dimensionless exponent. Figure 5.6 shows the variation of C_1 with time. A fast decrease in C_1 during the first 24 h of immersion can be observed, followed by the alternating increase/decrease pattern as a result of electrolyte renewal, with a decreasing effect over time. The overall decrease in C_1 is in agreement with the formation of a corrosion layer with increasing protective properties over time and with increasing coverage. The increase in C_1 after electrolyte renewal is in agreement with partial dissolution of the corrosion layer and the subsequent decrease in the barrier film coverage, as was also proposed to explain the variation of OCP (Figure 5.1) and resistance (Figure 5.5) values over time. The decreasing effect of electrolyte renewal on OCP, R_1 and C_1 values, observed at longer immersion times (note the decrease in amplitude variation), can be related to a decreasing MgO film-free substrate surface over time, to an increase in the $Mg(OH)_2$ corrosion layer thickness and to onset of a localized corrosion process, with the corresponding change in the corrosion mechanism.

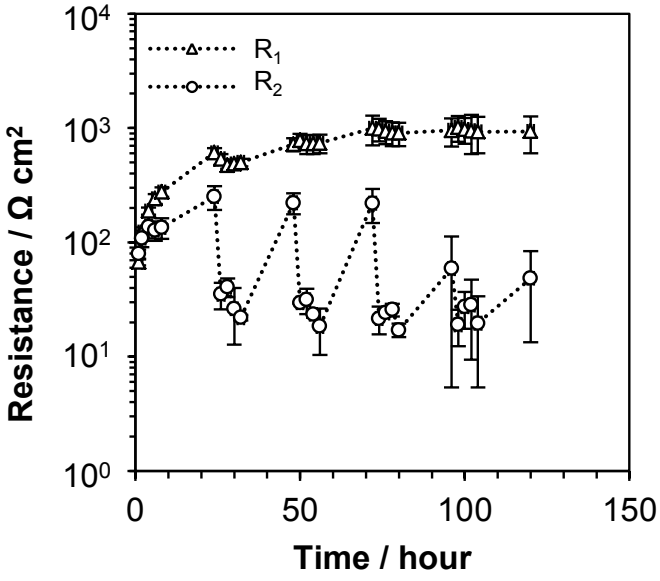

Figure 5.5: Time-dependent behaviour of the charge transfer resistance (R_1) and diffusion resistance (R_2) of WE43 Mg alloy in m-SBF with daily electrolyte renewal.

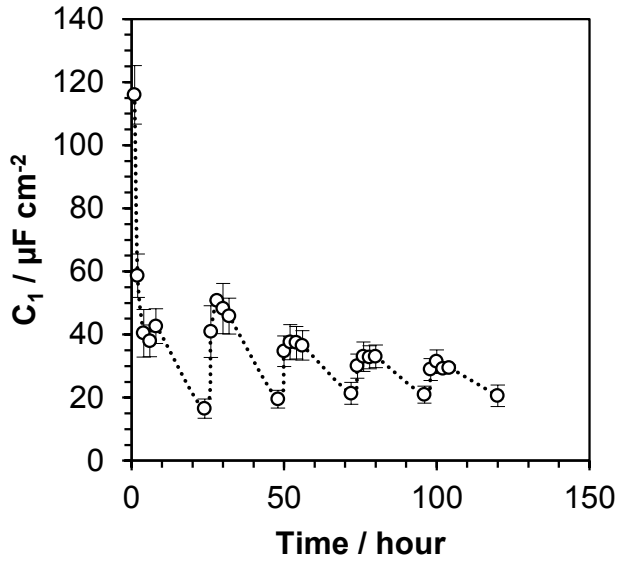

Figure 5.6: Time-dependent behaviour of the electrochemical double layer / MgO barrier film capacitance (C_1) of WE43 Mg alloy in m-SBF with daily electrolyte renewal.

5.4.2 Electrolyte analysis

In order to investigate the variation in electrolyte concentration after electrolyte renewal and the corresponding effect on the corrosion mechanism, daily concentrations of Mg, Ca and P species were monitored. Figure 5.7 shows the time-dependent electrolyte concentration of Mg, Ca and P species. A cumulative increase in the Mg^{2+} electrolyte concentration with respect to the control (no Mg alloy sample was present in the electrolyte) can be observed as a result of the corrosion process (Figure 5.7a, hollow bars). A daily variation in Mg^{2+} concentration values (Figure 5.7a, shaded bars) shows that the highest increase in concentration was reached during the first 24 h of immersion, followed by a decrease in daily-released Mg^{2+} and levelling to a constant value after 48 h of immersion. The decrease in the daily-released Mg^{2+} is in agreement with the formation of a corrosion layer with increasing protective properties over time. Daily Ca and P amounts (Figure 5.7b) are respectively lower by about 87% and 75% in comparison to the control values, indicating removal of the two species from the electrolyte as a result of the Mg alloy corrosion, and their, at least partial, incorporation into the corrosion layer. Indeed, it has been shown that Ca and P in SBF's effectively improve the corrosion resistance of Mg alloys by the formation of insoluble precipitates, e.g., Ca/Mg-phosphates, incorporated into the corrosion layer [25, 49]. Xin et al. found that pitting corrosion of die-cast AZ91 Mg alloy in a SBF is significantly delayed due to precipitation of magnesium phosphates [41]. SBF's such as conventional (c-SBF), revised (r-SBF), ionized (i-SBF) and modified (m-SBF) are supersaturated with respect to formation of apatite [$Ca_{10}(PO_4)_6(Cl,OH)_2$] [37] and thus, the increase in pH and Mg^{2+} concentration during the corrosion process can lead not only to formation of insoluble

precipitates incorporated into the corrosion layer but also to particle formation in the bulk electrolyte [50], with the corresponding decrease in the concentration of P and Ca species, possibly affecting the corrosion process. In our previous investigation of WE43 Mg alloy corrosion without m-SBF electrolyte renewal [28] we reported a five-fold increase in the electrolyte Mg^{2+} concentration and a decrease in the concentration of Ca and P species to respectively 53% and 41% with respect to the control (physiological) values, after 5 days of immersion. The previous information shows the relevance of electrolyte renewal in the maintenance of the electrolyte components concentration to values close to the physiological range during *in-vitro* investigations of the biodegradation behaviour of Mg alloys.

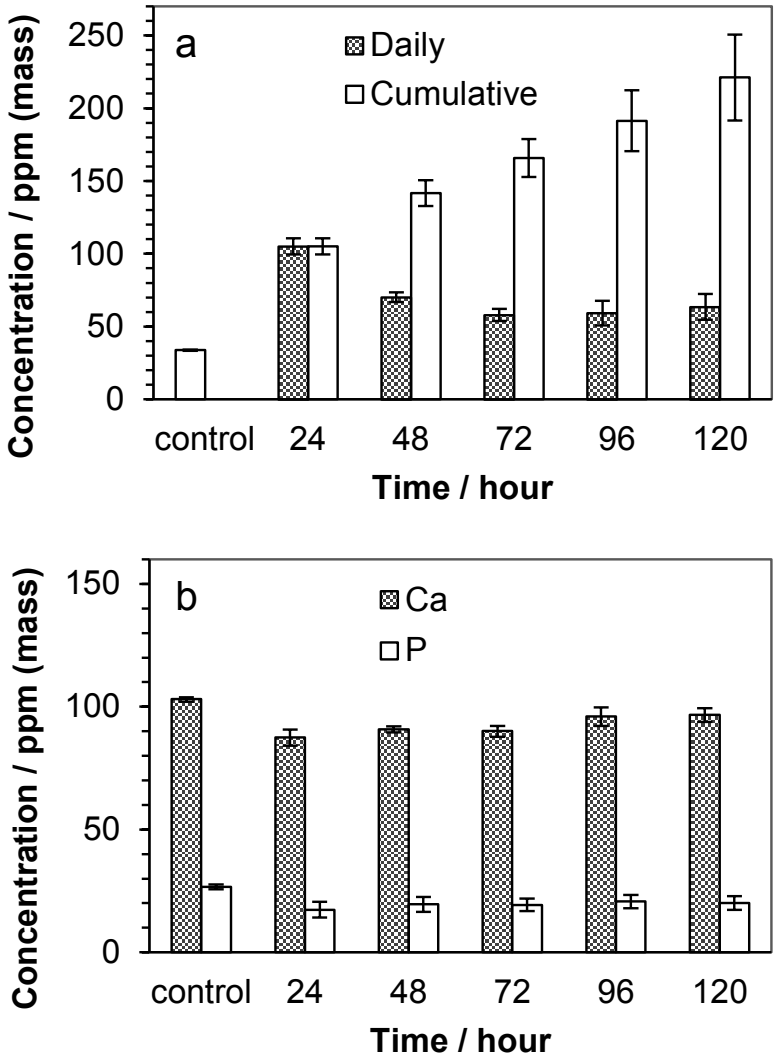

Figure 5.7: Time-dependent behaviour of (a) daily and cumulative Mg concentration, and (b) daily Ca and P electrolyte concentration of WE43 Mg alloy in m-SBF with daily electrolyte renewal.

5.4.3 Hydrogen evolution

The effect of electrolyte renewal on the formation of hydrogen gas was also investigated. Figure 5.8 shows daily and cumulative volume values of hydrogen produced after different immersion times. Daily values (Figure 5.8a) show that the largest amount of hydrogen gas was produced during the first 24 h of immersion,

followed by a decreasing volume of produced hydrogen at longer immersion times. This is in agreement with the trends in Figure 5.1 and Figures 5.5 - 5 . 7. Cumulative values (Figure 5.8b) show a gradual increase in the volume of produced hydrogen, with a faster rate of production (larger slope) observed during the first 8 h and then gradually decreasing at longer immersion times. Hydrogen gas is produced by (1) electrochemical reduction of water (reaction (5.1)), occurring preferentially at impurities and second phase precipitates with low hydrogen evolution overvoltage [28, 51-53] and (2) chemical reaction of adsorbed Mg^{+} intermediates with water occurring at MgO film-free areas (reaction (5.3)) [16, 38]. The observed decrease in the hydrogen gas production rate at longer immersion times can thus be related to an increasing coverage of the MgO barrier film and the corresponding reduction in the free Mg alloy substrate/electrolyte interfacial area, in agreement with the trend observed with OCP, R_{ct} and daily Mg^{2+} concentration values (Figures 5.1, 5.5 and 5.7a). Although it cannot be clearly appreciated on the provided plot (Figures 5.8), electrolyte renewal caused a temporary (initial) increase in the hydrogen production rate, which was evidenced by an increase in the formation of hydrogen bubbles during the immersion experiment and confirmed later by the shape of the hydrogen produced data best-fit curve. It has been proposed that water reduction occurs mostly at the Mg alloy substrate/electrolyte interface, not on the surface of the insulating corrosion layer and, that availability of hydrogen discharge sites becomes the controlling factor in the corrosion reaction rate [54]. Therefore, the initial increase in the hydrogen gas production rate after electrolyte renewal can be related to the observed decrease in the diffusion resistance (Figure 5.5) and the corresponding increased water access to the metal substrate and second phase precipitates [28]. An

expected increase in the production rate of hydrogen gas due to the occurrence of localized corrosion after 72 h (Figures 5.5 and 5.10) was not observed probably due to (1) hydrogen production data being obtained from an independent experiment and, (2) interruption of the experiment at an early stage of the localized corrosion process.

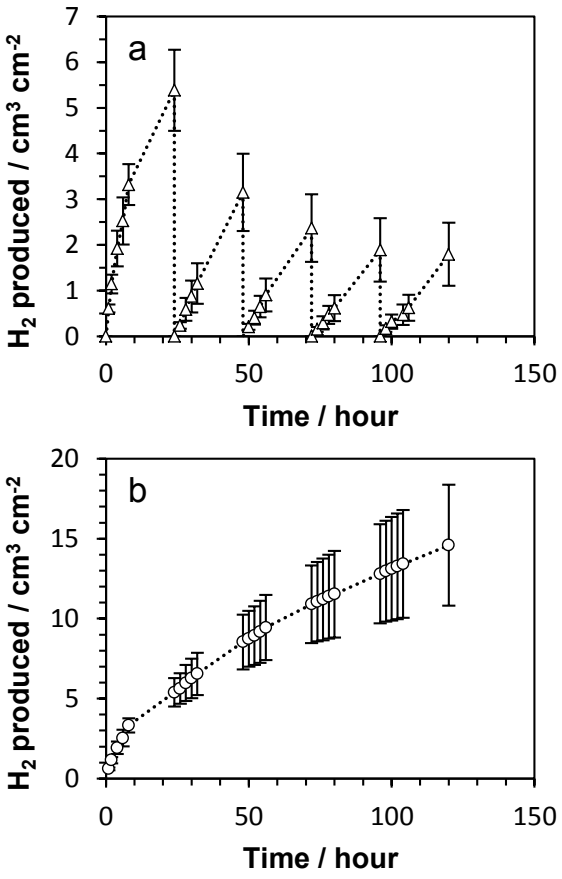

Figure 5.8: (a) Daily and (b) cumulative hydrogen produced by corrosion of WE43 Mg alloy in m-SBF with daily electrolyte renewal.

5.4.4 Corrosion rate

Normalized corrosion rate values were calculated from EIS, hydrogen evolution and ICP-OES data. Normalized corrosion rate values were calculated according to the following equation:

$$P_{norm} = \frac{P}{P_{max}} \quad (5.11)$$

Instantaneous relative corrosion rate values were obtained from EIS data by calculating the inverse of R_{ct} (R_1) values (Figure 5.5). Cumulative Mg^{2+} concentration values obtained by ICP-OES (Figure 5.7) were fitted (polynomial degree 3, *SSE*=14.29, R^2=0.9994) and instantaneous corrosion rate values were calculated using the following equation:

$$P_{ICP}=8.76C\rho^{-1}A^{-1} \quad (5.12)$$

where P_{ICP} is the corrosion rate (mm $year^{-1}$), 8.76 is a constant for the conversion of units (dm^3 mm g h mg^{-1} $year^{-1}$ cm^{-1}), C is the fitting curve slope (ppm h^{-1}), ρ is the Mg density (1.74 g cm^{-3}) and A is the sample area (cm^2). Cumulative hydrogen volume values (Figure 5.8b) were also fitted (smoothing spline, *SSE*=0.0166, R^2=0.9999) and instantaneous corrosion rate values were calculated using the following equation [55]:

$$P_{HE}=2.279V_H \quad (5.13)$$

where P_{HE} is the corrosion rate (mm $year^{-1}$), 2.279 is a constant (mm day cm^{-1} $year^{-1}$) and V_H is the fitting curve slope (cm^3 cm^{-2} day^{-1}). It was assumed that one mole of hydrogen is produced for each mole of corroded Mg metal (24.32 g mol^{-1}). All fittings

and slope calculations were performed using the application Curve Fitting Toolbox (MathWorks, 2012).

Figure 5.9 shows normalized corrosion rate values calculated by the EIS, ICP-OES and hydrogen evolution techniques. Since no concentration values were measured at immersion times below 24 h for ICP-OES, the corresponding normalized corrosion rate values (P-ICP) were obtained with respect to the highest instantaneous corrosion rate value calculated from hydrogen evolution measurements (26.87 mm/year). A relatively good agreement between the three techniques was obtained. The largest corrosion rate is observed at the beginning of the immersion experiment. A fast decrease in the corrosion rate can be observed during the first 24 h, followed by a slower decrease at longer immersion times, in agreement with the formation of a MgO barrier film with increasing coverage. Corrosion rate values obtained from ICP-OES show that the corrosion rate again starts increasing after 72 h, probably corresponding to local dissolution of the corrosion layer and occurrence of localized corrosion; however, this trend is not observed for the corrosion rate values obtained by EIS and HE techniques, where a quasi-constant corrosion rate can be observed after 72 h. The relatively larger corrosion rate values and the larger effect of electrolyte renewal observed on the corrosion rate values from hydrogen evolution (P-HE) can be related to the combined chemical and electrochemical formation of hydrogen at MgO film-free areas (reactions (5.1) and (5.3)), which cannot be accounted for by EIS that measures only the electrochemical corrosion reactions (reactions (5.1) and (5.2)) and by ICP-OES that measures dissolved Mg^{2+} (reaction (5.3)). The trends in the corrosion rate values with electrolyte renewal obtained in this investigation (Figure 5.9) follow a trend similar

to that one reported in our previous investigation without electrolyte renewal (Figure 5.9, continuous line); however, the latter evidenced an increase in corrosion rate after 48h due to the occurrence of localized corrosion. The difference in behaviour observed for the OCP, R_{ct}, C_1 and corrosion rate values (Figures 5.1, 5.5, 5.6 and 5.9, respectively) between the experiments with and without electrolyte renewal (in chapter 4: Figures 4.4a, 4.8a, 4.8b and 4.11, respectively) show that electrolyte renewal contributes to both a delay in the MgO barrier film coverage increase and to the onset of localized corrosion. This is of relevance in terms of the expected difference in the Mg alloy corrosion behaviour between immersion experiments with conventional stagnant conditions and those with a set-up allowing for better resemblance of physiological homeostasis, e.g., in the presence of a continuous m-SBF flow.

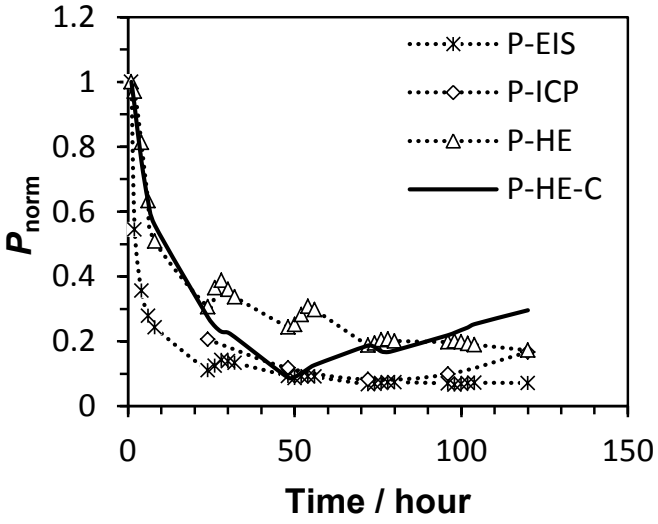

Figure 5.9: Time-dependent normalized corrosion rate ($P_{norm}=P/P_{max}$) of WE43 Mg alloy in m-SBF with daily electrolyte renewal calculated from EIS (P-EIS), hydrogen evolution (P-HE) and ICP-OES (P-ICP) data. The continuous line (R-HE-C) shows corrosion rate values calculated from hydrogen evolution for WE43 in m-SBF without electrolyte renewal [28].

5.4.5 Corrosion products characterization

Figure 5.10 shows optical and SEM images of a corroded Mg alloy sample after 120 h of immersion in m-SBF, before and after removing the corrosion products. A completely corroded sample surface can be observed, with some whitish corrosion products distributed all over the corrosion layer (Figure 5.10a). Larger white rounded deposits, with a diameter of about 1.3 mm scattered over the corrosion layer, can also be observed. Formation of hydrogen gas bubbles on these deposits was observed during the immersion experiments, revealing that the substrate areas underneath the deposits correspond to cathodic regions. Removal of the corrosion layer by chromic acid revealed the occurrence of general and localized corrosion, with the presence of large localized corrosion areas with a maximum length of about 4 mm (Figure 5.10b). It was also observed that the surface underneath the bigger rounded white deposits was not corroded, indicating that these regions correspond to cathodic areas. Namely, SEM images of the substrate corroded surface after removal of the corrosion products revealed the presence of circular non-corroded spots of different areas (Fig. 5.10c), corresponding to cathodic regions underneath the white deposits. A picture of a non-corroded spot taken at a higher magnification (Fig. 5.10d) shows the evidence that some pitting corrosion occurred at the center.

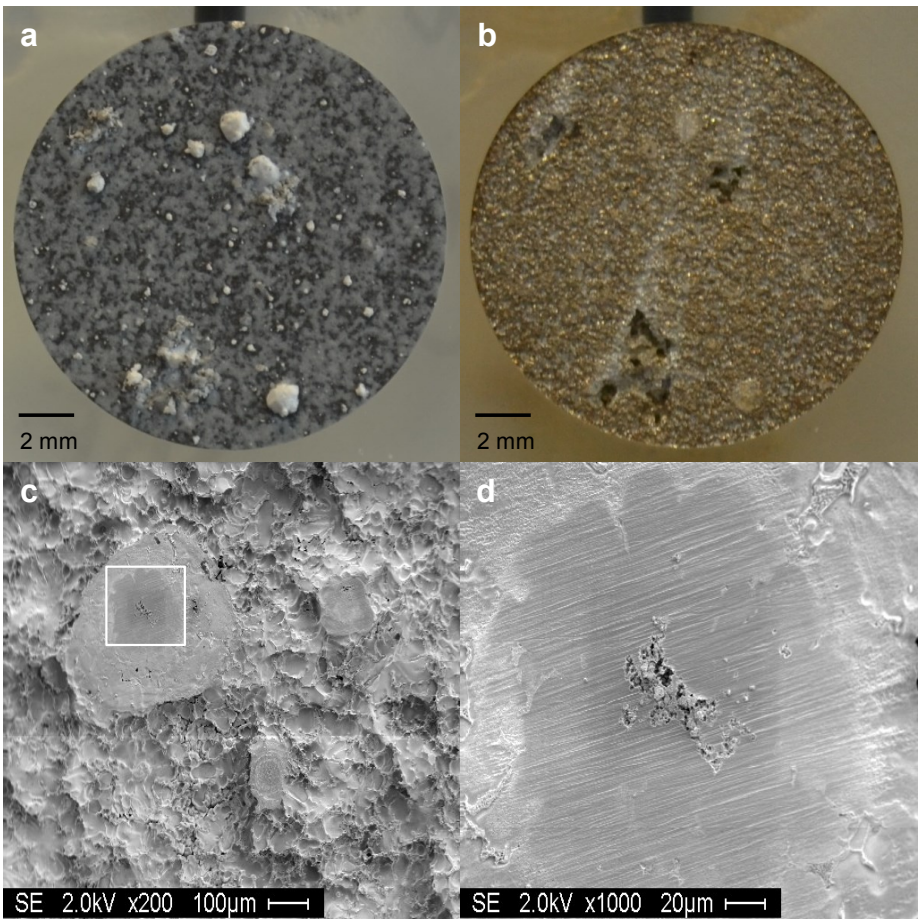

Figure 5.10: Pictures of WE43 Mg alloy in m-SBF with daily electrolyte renewal after 5 days of immersion. Optical images of (a) a corroded surface and (b) a sample substrate surface after dissolving the corrosion layer, and SEM images of (c) a sample substrate surface showing some non-corroded spots and (d) a non-corroded spot at higher magnification corresponding to the white rectangle on (c).

Figure 5.11 shows SEM images of the Mg alloy corroded sample after different immersion times. White rectangles show the areas where EDS analysis was performed (Table 5.4). Figure 5.11a shows the corroded surface after 24 h; a relatively uniform surface with some cracks and a rounded deposit with a hole on the top side (volcano-like) can be observed. The cracks are formed due to dehydration of the corrosion layer during the analysis in vacuum. Formation of the hole occurred probably due to

production of hydrogen gas at cathodic sites underneath the deposit. Formation of deposits with a similar morphology on Mg alloys exposed to different electrolytes has been attributed to precipitation of large amounts of corrosion products due to the presence of galvanic corrosion occurring at cathodic second phases [49, 56]. WE43 Mg alloy contains rare-earth-rich second phase precipitates with different size and morphology [56-58] that are nobler with respect to the α-Mg matrix and therefore act as cathodes [28, 59]. Fast reduction of water (reaction (5.1)) on second phase precipitates leads to a fast increase in the local pH under stagnant conditions promoting precipitation of magnesium hydroxide and Ca/Mg-carbonates/phosphates due to electrolyte super-saturation and saturation with respect to apatite and calcite [37], respectively. Table 5.4 shows the elemental composition and Ca/P ratio of the corrosion layer after different immersion times. It was observed the presence of C, O, Na, Mg, P, Ca and C; it was also observed that the volcano-like deposits have the same elemental composition as the rest of the corrosion layer, but a higher Ca content (Figure 5.11a). Ca/P atomic ratio values of 1.07 and 0.60 were obtained for the volcano-like deposit and the rest of the corrosion layer, respectively. Analysis of the Mg alloy corroded sample after 32 h, the time at which the lowest impedance response was observed after the first electrolyte renewal (Figure 5.4), showed ruptured volcano-like deposits (Figure 5.11b), evidencing partial dissolution of the corrosion layer as a result of electrolyte renewal; however, EDS analysis did not show any significant difference in the corrosion layer chemical composition before and after electrolyte renewal, with only a slightly higher Ca/P ratio observed (Table 5.4). Figure 5.11c shows a localized corrosion region on the Mg alloy corroded surface after 120 h. Some small volcano-like deposits can be

observed, revealing local formation of hydrogen gas probably due to the presence of second phase precipitates underneath. EDS analysis showed the presence of Cl species at the localized corrosion site (Table 5.4), revealing the contribution of chloride ions in the onset and development of localized corrosion. Cross-sectional analysis of the corroded sample showed a non-uniform corrosion layer, with a thickness varying from 25-140 μm (Figure 5.11d); this is in contrast with the results obtained from immersion experiments of WE43 in m-SBF without electrolyte renewal, where a corrosion layer thickness in the range of 20-40 μm was observed after 5 days of immersion [28, 49] . The observed difference in thickness shows that electrolyte renewal promotes formation of a thicker corrosion layer, probably due to increased mass transport as a result of the corrosion layer partial dissolution.

Table 5.4: Elemental composition of the WE43 Mg alloy corrosion layer obtained by EDS. Spots 1-4 are indicated in Figure 5.11.

	Elemental composition at. %							
Immersion time / h	C	O	Na	Mg	P	Ca	Cl	Ca/P
24 (corrosion layer, spot 1)	19.64	56.19	1.05	5.93	10.73	6.46	-	0.60
24 (volcano-like precipitate, spot 2)	15.58	57.68	0.69	7.63	8.90	9.52	-	1.07
32 (corrosion layer, spot 3)	18.24	55.26	0.69	6.88	10.96	7.97	-	0.73
120 (localized corrosion, spot 4)	11.38	37.93	-	24.69	14.03	-	11.97	-

Analysis of the corrosion layer by ATR-FTIR, XRD and XPS (not showed) and the results obtained by SEM (Figure 5.11) and EDS (Table 5.4), reveal the presence of an amorphous corrosion layer containing $Mg(OH)_2$ and a carbonated apatite. These results are in agreement with the corrosion layer composition reported by our group for WE43 Mg alloy after 5 days of immersion in m-SBF without electrolyte renewal [28]. A

similar composition has also been reported by other groups for Mg alloys immersed in SBF's. Rettig et al. showed that the corrosion layer of WE43 Mg alloy after 5 days of immersion in m-SBF consisted of an amorphous carbonated calcium/magnesium phosphate [49]. Bornapour et al. found that a mixed $Mg(OH)_2$ and hydroxyapatite [$Ca_{10}(PO_4)_6(OH)_2$] corrosion layer formed on Mg-0.5Sr and Mg-0.3Sr-0.3Ca alloys immersed in Hanks solution [60, 61].

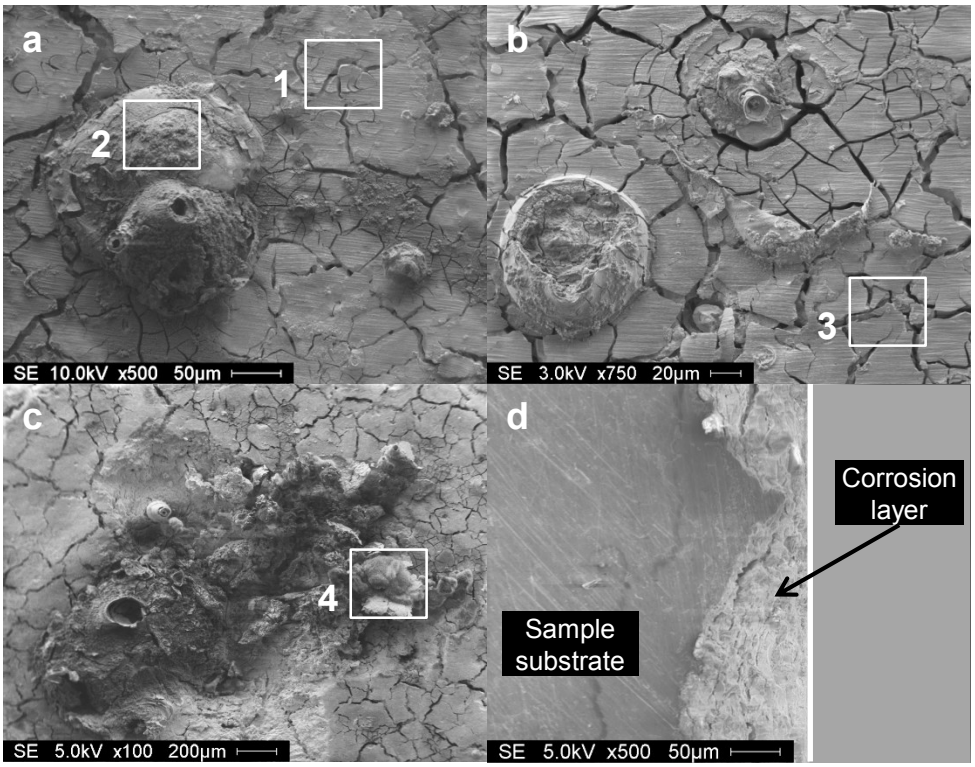

Figure 5.11: SEM images of WE43 Mg alloy in m-SBF with daily electrolyte renewal. Corroded surface after (a) 24 h, (b) 32 h and (c) 120 h. (d) Sample cross-sectional view after 120 h. Numbered white squares (1-4) on SEM images correspond to areas where EDS analysis was performed (Table 5.4).

Characterization of the Mg alloy corroded surface by ATR-FTIR and EDS after 24 h and 32 h of immersion did not show any significant difference in the corrosion layer

composition; however, destruction of volcano-like deposits after 32 h (Figure 5.11b) reveals partial dissolution of the corrosion layer after electrolyte renewal. It was already discussed previously in the text that $Mg(OH)_2$ solubility increases as a result of the decrease in the electrolyte pH after electrolyte renewal. The initial decrease in pH (Figure 5.1) and Mg^{2+} electrolyte concentration (Figure 5.7a) accompanying electrolyte renewal can also disturb the solubility equilibrium of phosphate and carbonate species, promoting dissolution of the corrosion layer. The solubility of insoluble carbonate and phosphate salts precipitated into the corrosion layer and found to enhance the corrosion layer protective properties depends on the concentration of the ions involved in the solubility product (K_{sp}) and also on the electrolyte acid-base equilibrium. Due to diprotic and triprotic equilibria in H_2CO_3 and H_3PO_4 systems, respectively, variations in pH alter the relative concentrations of the respective protonated forms and thus the chemical composition and amount of precipitates formed [62]. For instance, the solubility of $MgCO_3$ can be estimated by the following equations:

$$K_{sp}(MgCO_3) = [Mg^{2+}]\left[{CO_3}^{2-}\right] \tag{5.14}$$

$$\left[{CO_3}^{2-}\right] = \frac{C_{total}({CO_3}^{2-})K_{a1}K_{a2}}{[H^+]^2+[H^+]K_{a1}+K_{a1}K_{a2}} \tag{5.15}$$

where $K_{sp}(MgCO_3)$ is the solubility product constant of $MgCO_3$, K_{a1} and K_{a2} are the dissociation constants of H_2CO_3 and HCO_3^-, respectively, $C_{total}(CO_3^{2-})$ is the total concentration of CO_3^{2-} species and square brackets denote concentration values (M) of Mg^{2+}, CO_3^{2-} and H^+ species. In the same way, the solubility of $Mg_3(PO_4)_2$ can be estimated by the following equations:

$$K_{sp}\{Mg_3(PO_4)_2\} = [Mg^{2+}]^3\left[{PO_4}^{3-}\right]^2 \quad (5.16)$$

$$\left[{PO_4}^{3-}\right] = \frac{C_{total}({PO_4}^{3-})K_{a1}K_{a2}K_{a3}}{[H^+]^3+[H^+]^2K_{a1}+[H^+]K_{a1}K_{a2}+K_{a1}K_{a2}K_{a3}} \quad (5.17)$$

where $K_{sp}\{Mg_3(PO_4)_2\}$ is the solubility product constant of $Mg_3(PO_4)_2$, K_{a1}, K_{a2} and Ka_3 are the dissociation constants of H_3PO_4, $H_2PO_4^-$ and HPO_4^-, respectively, $C_{total}(PO_4^{3-})$ is the total concentration of PO_4^{3-} species and square brackets denote concentration values (M) of Mg^{2+}, PO_4^{3-} and H^+ species. Using K_{sp}, K_{a1} and K_{a2} values of $MgCO_3$ as $6.82x10^{-6}$, $4.47x10^{-7}$ and $4.68x10^{-11}$ [25], respectively; K_{sp}, K_{a1}, K_{a2} and K_{a3} values of $Mg_3(PO_4)_2$ as $1.04x10^{-24}$, $6.92x10^{-3}$, $6.17x10^{-8}$ and $4.79x10^{-13}$ [25], respectively; and the total concentration values of CO_3^{2-} and PO_4^{3-} species in the control m-SBF electrolyte as 10 mM and 1 mM (Table 5.2), a two-fold increase in the equilibrium concentration of Mg^{2+} with respect to both $MgCO_3$ and $Mg_3(PO_4)_2$ due to a decrease in the electrolyte pH from 7.8 to 7.4, can be obtained according to equations (5.14)-(5.17). However, a bigger solubility perturbation might occur after electrolyte renewal at cathodic sites with higher local pH value changes due to the formation of OH^- ions (reaction (5.1)), with the subsequent increase in the solubility of deposited phosphate compounds. The solubility of calcium phosphates, in particular hydroxyapatite, has been extensively investigated due to their importance in biological processes such as formation and resorption of hard tissues as well as pathological conditions [62]. Determination of accurate solubility values of calcium phosphates is limited due to the presence of several different phases, e.g., hydroxyapatite, tricalcium phosphate (TCP), dicalcium phosphate dehydrate (DCPD), octacalcium phosphate (OCP) and amorphous calcium phosphate (ACP), and the possibility of phase transformations [63]. Amorphous carbonated apatite showed the

highest dissolution rate among several calcium phosphate phases in pure water at a temperature of 37°C and pH=4.4 [64]. Biological apatites are non-stoichiometric and contain significant amounts of foreign anions such as CO_3^{2-}, Mg^{2+}, Na^+ and F^-, leading to structural disorder and higher solubility [65]. It was found that Mg-substituted hydroxyapatite had a significantly higher solubility than stoichiometric hydroxyapatite in Hank's balanced salt solution in dynamic conditions at 37 °C [66]. The previous information suggests that the presence of soluble calcium phosphate phases precipitated at cathodic sites contributes to local dissolution of the corrosion layer after electrolyte renewal, without significant changes in the general composition of the corrosion layer. Local dissolution of calcium phosphate deposits at cathodic sites can lead to a decrease in the corrosion layer resistance by exposing non-corroded substrate areas underneath the deposits to the electrolyte and, by increasing the access of water to intermetallic second phases. The observed rupture of volcano-like deposits (Figure 5.11b) at cathodic sites might also be mechanically enhanced by faster production of hydrogen gas as a result of increased water access to the alloy substrate surface.

5.4.6 Corrosion mechanism

On the basis of the experimental results and the corrosion mechanism proposed for WE43 Mg alloy in m-SBF without electrolyte renewal [28], the following corrosion mechanism is proposed for WE43 with electrolyte renewal (Figure 5.12a-f):

Figure 5.12a (0-8 h). Right after immersion, the Mg alloy sample undergoes electrochemical oxidation with formation of adsorbed Mg^+ intermediates (reaction (5.2)). Simultaneously, hydrogen gas is produced both electrochemically, through reduction of

water (reaction (5.1), black arrows on Figure 5.12), and chemically, by the reaction of adsorbed Mg^+ intermediates and water (reaction (5.3), white arrows on Figure 5.12). Production of OH^- ions as a result of electrochemical and chemical reactions leads to an increase in the electrolyte pH (Figure 5.1) and to the formation of a mixed $Mg(OH)_2$/carbonated apatite corrosion layer with increasing protective properties over time. Fast production of OH^- ions at second phase precipitates, which have a nobler potential with respect to the α-Mg phase, leads to a fast local pH increase, inducing the deposition of large amounts of corrosion products and formation of volcano-like deposits (Figure 5.11a) onto second phase cathodic regions. The increase in the corrosion layer protective properties, mostly due to an increase in the layer thickness, is evidenced by the increase in OCP and R_{ct} values (Figures 5.1 and 5.5) and by the decrease in C_1 (Figure 5.6). Formation of adsorbed Mg^+ intermediates and thus chemical production of hydrogen gas is evidenced by the presence of the inductive loop on the Nyquist plot (Figure 5.4a).

Figure 5.12b (8-24 h). The increase in the corrosion layer protective properties over time is accompanied by an increase in the corrosion layer diffusion resistance (Figure 5.5, R_2) leading to decreased water access to the sample substrate. Water consumption by adsorbed Mg^+ intermediates (reaction (5.3)) and decreased water access due to increased diffusion resistance leads to dehydration of the $Mg(OH)_2$ inner layer and formation of an inner MgO barrier film with increasing coverage (reaction (5.18)). Water molecules produced by this reaction are then available for subsequent reaction with adsorbed Mg^+ intermediates. The increase in the MgO barrier film coverage over time leads to a decrease in the formation of adsorbed Mg^+ intermediates,

evidenced by the decrease in the size of the inductive loop at 24h (Figure 5.4a), and thus, to decreased chemical production of hydrogen gas. Formation of Mg^{2+} through direct electrochemical oxidation of magnesium is also possible (reaction 5.19).

$$Mg(OH)_2 \leftrightarrow MgO + H_2O \quad (5.18)$$

$$Mg \rightarrow Mg^{2+} + 2e^- \quad (5.19)$$

Figure 5.12c (at 24 h, after electrolyte renewal). Partial dissolution of the corrosion layer as a result of electrolyte renewal leads to a decrease in the corrosion layer protective properties, evidenced by a decrease in R_1 and R_2 values (Figure 5.5). The decrease in diffusion resistance (R_2) leads to increased mass transfer through the $Mg(OH)_2$ layer, possibly causing the destruction of the MgO barrier film by shifting the equilibrium of reaction (5.18) to the left, and thus increasing the formation of Mg^+ intermediates and chemical production of hydrogen gas (reactions (5.2) and (5.3)). Partial dissolution of the corrosion layer and a decrease in the MgO barrier film surface coverage after electrolyte renewal are evidenced by the decrease in charge transfer resistance (R_1) (Figure 5.5) and OCP values (Figure 5.1) and by the increase in C_1 values (Figure 5.6). Dissolution of volcano-like deposits at cathodic regions (Figure 5.11b), probably corresponding to dissolution of amorphous calcium phosphates, leads to increased water access to second phase precipitates and thus to increased electrochemical hydrogen production (reaction (5.1)). The dissolution and/or rupture of volcano-like deposits might be enhanced by fast formation of hydrogen gas at second phase precipitates. Dissolution of volcano-like deposits also contributes to a decrease in R_1 and R_2 values by exposing non-corroded substrate surface areas to the electrolyte

(Figures 5.10c and 5.11b). The increase in the MgO film-free areas leads thus to an increase in hydrogen formation and corrosion rates (Figure 5.9).

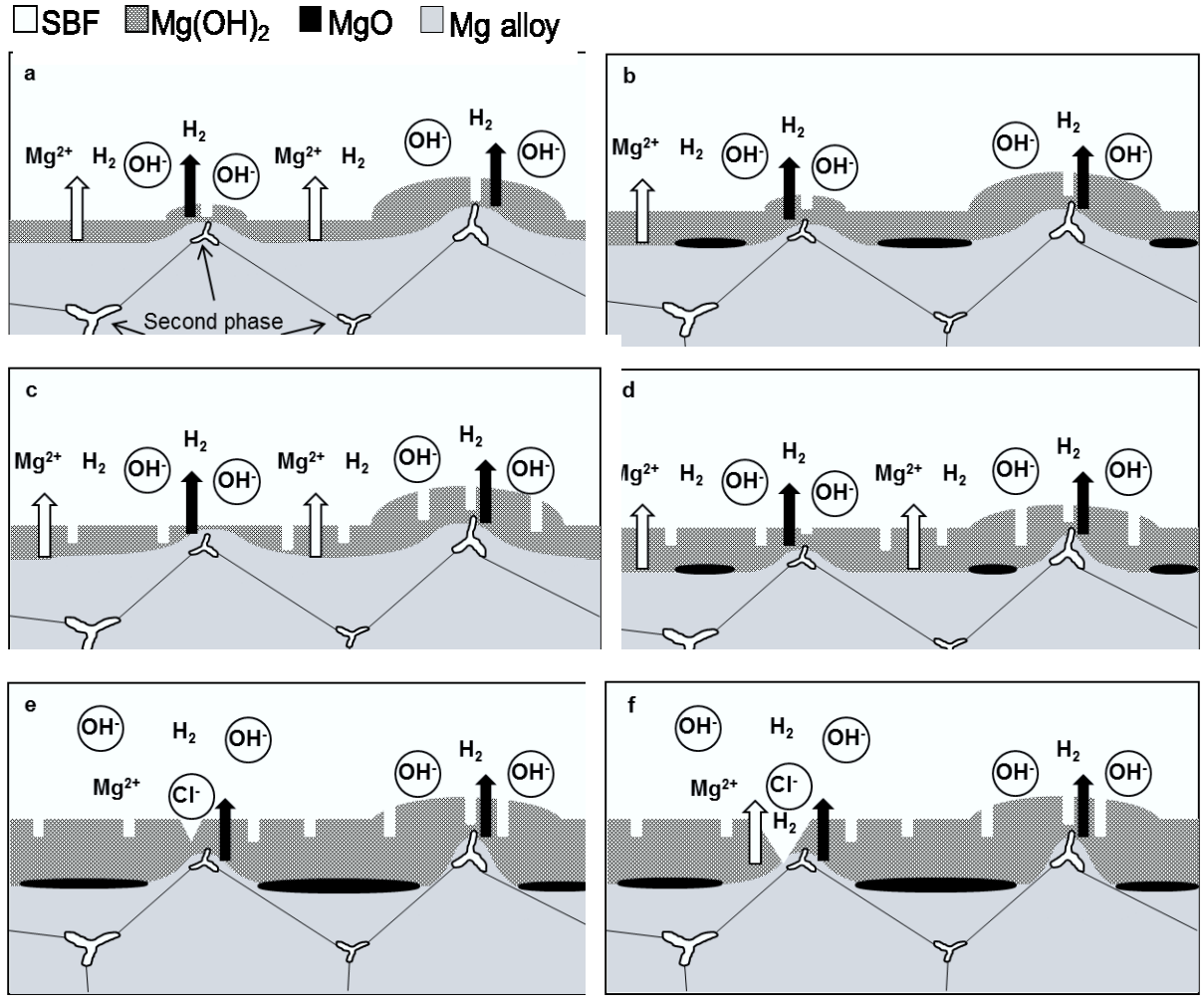

Figure 5.12: Corrosion mechanism for WE43 Mg alloy in m-SBF with daily electrolyte renewal: (a) Formation of a $Mg(OH)_2$ porous layer with a growing thickness ; (b) Increased corrosion resistance and decreased hydrogen production due to formation of a MgO inner barrier film; (c) Decreased corrosion resistance and increased hydrogen formation due to partial dissolution of the corrosion layer after electrolyte renewal; (d) Increased corrosion resistance due to corrosion layer thickening and increased MgO film coverage; (e) Increased MgO film coverage and onset of localized corrosion induced by aggressive Cl^- ions; and (f) Pit formation and spreading of stable pits.

Figure 5.12d (at 48h, after electrolyte renewal). Partial dissolution of the corrosion layer and a decrease in its protective properties after electrolyte renewal is evidenced by the decrease in R_1 and R_2 values (Figure 5.5). The effect of electrolyte renewal is smaller than that observed after 24 h, probably due to the smaller pH perturbation (Figure 5.1) and also due to an increased corrosion layer thickness and MgO barrier film coverage after 48 h, evidenced by the increase in OCP (Figure 5.1) and R_1 (Figure 5.5). Therefore, the increase in mass transfer after electrolyte renewal, evidenced by the decrease in R_2 (Figure 5.5) leads to a smaller decrease (compared to the decrease observed after 24 h) in the MgO barrier film coverage and to a smaller increase in corrosion rate and hydrogen production (Figure 5.9). The decrease in MgO coverage is evidenced by the decrease in OCP (Figure 5.1) and R_1 (Figure 5.5) values and by the increase in C_1 (Figure 5.6).

Figure 5.12e (at 72 h, after electrolyte renewal). The effect of electrolyte renewal on the corrosion process is similar to that observed after 48h. The increase in OCP (Figure 5.1) and R_1 (Figure 5.5) values at 72 h indicate an increase in the MgO barrier film coverage. The quasi-constant R_2 values observed after 72 h (Figure 5.5) suggest rupture of the $Mg(OH)_2$ corrosion layer and onset of a localized corrosion process, probably occurring close to cathodic regions covered by a thinner corrosion layer. The presence of chloride species at localized corrosion regions (Figure 5.11c, Table 5.4) indicates the participation of chloride ions in the dissolution of the corrosion layer (reaction (5.6)).

Figure 5.12f (at 96h, after electrolyte renewal). Electrolyte renewal has the smallest effect on the corrosion process after 96h. Quasi-constant OCP, R_1 and

corrosion rate values (Figures 5.1, 5.5 and 5.9, respectively) indicate that a constant MgO barrier film coverage has been reached. Spreading of stable pits occurs probably due to (*i*) the presence of aggressive Cl^- species promoting the dissolution of the corrosion layer and (*ii*) fast formation of hydrogen gas at localized corrosion sites, which increases mass transfer and prevents the formation of a protective corrosion layer.

5.5 CONCLUSIONS

The mechanisms and kinetics of corrosion of WE43 Mg alloy in m-SBF were investigated over a 5-day period time with daily electrolyte renewal with the aim to better resemble (simulate) physiological homeostasis. Normalized corrosion rate values obtained by EIS, hydrogen evolution and ICP-OES techniques show a relatively good agreement. A fast decrease in the Mg alloy corrosion rate during the first 24 h of immersion, followed by a slower decrease and a quasi-constant corrosion rate after 72 h can be related to formation of a corrosion layer with increasing protective properties over time. The increase in the corrosion layer protective properties is proposed to occur through the formation of an inner MgO barrier film with increasing coverage over time, underneath the porous $Mg(OH)_2$ corrosion layer. An increase in the corrosion rate after 96h, observed by ICP-OES, can be related to rupture of the corrosion layer and occurrence of a localized corrosion process. Onset of localized corrosion and spreading of stable pits can be related, respectively, to dissolution of the corrosion layer promoted by adsorption of aggressive Cl^- species and, to fast formation of hydrogen gas at localized corrosion areas, increasing the mass transfer and hampering the formation of a protective corrosion layer.

In conclusion, it was found that by performing electrolyte renewal, physiological control of corrosion products and concentration of relevant electrolyte components such as calcium, phosphate and carbonate species, can be better emulated. Electrolyte renewal affects the corrosion mechanism by promoting partial dissolution of the corrosion layer and by increasing mass transport through the corrosion layer, thereby delaying the increase in the MgO barrier film coverage and the occurrence of localized corrosion. The effect of electrolyte renewal on the overall corrosion behaviour of WE43 in m-SBF is small, compared to stagnant immersion conditions. However, this effect is expected to be larger in the presence of a continuous flow with constant electrolyte renewal. This shows the need of an improved experimental set-up for a more accurate determination of the corrosion kinetics and behaviour of Mg alloys for biodegradable applications.

The present results provide a corrosion mechanism for WE43 Mg alloy at conditions that better resemble physiological homeostasis and show the relevance of taking into account the changes in the corrosion layer protective properties over time and the influence of electrolyte pH and relevant electrolyte components such as calcium, carbonate and phosphate species in the corrosion process.

5.6 REFERENCES

[1] N.E.L. Saris, E. Mervaala, H. Karppanen, J.A. Khawaja, A. Lewenstam, Magnesium: An update on physiological, clinical and analytical aspects, Clinica Chimica Acta, 294 (2000) 1-26.

[2] C. Fox, D. Ramsoomair, C. Carter, Magnesium: its proven and potential clinical significance, Southern medical journal, 94 (2001) 1195-1201.

[3] B. Heublein, R. Rohde, V. Kaese, M. Niemeyer, W. Hartung, A. Haverich, Biocorrosion of magnesium alloys: A new principle in cardiovascular implant technology?, Heart, 89 (2003) 651-656.

[4] M.P. Staiger, A.M. Pietak, J. Huadmai, G. Dias, Magnesium and its alloys as orthopedic biomaterials: A review, Biomaterials, 27 (2006) 1728-1734.

[5] R. Erbel, C. Di Mario, J. Bartunek, J. Bonnier, B. de Bruyne, F.R. Eberli, P. Erne, M. Haude, B. Heublein, M. Horrigan, C. Ilsley, D. Böse, J. Koolen, T.F. Lüscher, N. Weissman, R. Waksman, Temporary scaffolding of coronary arteries with bioabsorbable magnesium stents: a prospective, non-randomised multicentre trial, Lancet, 369 (2007) 1869-1875.

[6] P. Peeters, M. Bosiers, J. Verbist, K. Deloose, B. Heublein, Preliminary results after application of absorbable metal stents in patients with critical limb ischemia, Journal of Endovascular Therapy, 12 (2005) 1-5.

[7] N. Erdmann, N. Angrisani, J. Reifenrath, A. Lucas, F. Thorey, D. Bormann, A. Meyer-Lindenberg, Biomechanical testing and degradation analysis of MgCa0.8 alloy screws: A comparative in vivo study in rabbits, Acta Biomaterialia, 7 (2011) 1421-1428.

[8] M. Maeng, L.O. Jensen, E. Falk, H.R. Andersen, L. Thuesen, Negative vascular remodelling after implantation of bioabsorbable magnesium alloy stents in porcine coronary arteries: a randomised comparison with bare-metal and sirolimus-eluting stents, Heart, 95 (2009) 241-246.

[9] T.L. Slottow, R. Pakala, T. Okabe, D. Hellinga, R.J. Lovec, F.O. Tio, A.B. Bui, R. Waksman, Optical coherence tomography and intravascular ultrasound imaging of bioabsorbable magnesium stent degradation in porcine coronary arteries, Cardiovascular Revascularization Medicine, 9 (2008) 248-254.

[10] R. Waksman, R. Pakala, P.K. Kuchulakanti, R. Baffour, D. Hellinga, R. Seabron, F.O. Tio, E. Wittchow, S. Hartwig, C. Harder, R. Rohde, B. Heublein, A. Andreae, K.H. Waldmann, A. Haverich, Safety and efficacy of bioabsorbable magnesium alloy stents in porcine coronary arteries, Catheterization and Cardiovascular Interventions, 68 (2006) 607-617.

[11] R. Waksman, R. Pakala, T. Okabe, D. Hellinga, R. Chan, M.O. Tio, E. Wittchow, S. Hartwig, K.H. Waldmann, C. Harder, Efficacy and safety of absorbable metallic stents with adjunct intracoronary beta radiation in porcine coronary arteries, Journal of Interventional Cardiology, 20 (2007) 367-372.

[12] F. Witte, J. Fischer, J. Nellesen, C. Vogt, J. Vogt, T. Donath, F. Beckmann, In vivo corrosion and corrosion protection of magnesium alloy LAE442, Acta Biomaterialia, (2009).

[13] F. Witte, V. Kaese, H. Haferkamp, E. Switzer, A. Meyer-Lindenberg, C.J. Wirth, H. Windhagen, In vivo corrosion of four magnesium alloys and the associated bone response, Biomaterials, 26 (2005) 3557-3563.

[14] E.D. McBRIDE, ABSORBABLE METAL IN BONE SURGERY: A FURTHER REPORT ON THE USE OF MAGNESIUM ALLOYS, J Am Med Assoc, 111 (1938) 2464-2467.

[15] S. Zhang, X. Zhang, C. Zhao, J. Li, Y. Song, C. Xie, H. Tao, Y. Zhang, Y. He, Y. Jiang, Y. Bian, Research on an Mg-Zn alloy as a degradable biomaterial, Acta Biomaterialia, 6 (2010) 626-640.

[16] G.L. Song, A. Atrens, Corrosion mechanisms of magnesium alloys, Advanced Engineering Materials, 1 (1999) 11-33.

[17] G.L. Makar, J. Kruger, Corrosion of magnesium, International Materials Reviews, 38 (1993) 138-153.

[18] H. Inoue, K. Sugahara, A. Yamamoto, H. Tsubakino, Corrosion rate of magnesium and its alloys in buffered chloride solutions, Corrosion Science, 44 (2002) 603-610.

[19] M.-C. Zhao, M. Liu, G.-L. Song, A. Atrens, Influence of pH and chloride ion concentration on the corrosion of Mg alloy ZE41, Corrosion Science, 50 (2008) 3168-3178.

[20] G. Song, A. Atrens, D.S. John, X. Wu, J. Nairn, The anodic dissolution of magnesium in chloride and sulphate solutions, Corrosion Science, 39 (1997) 1981-2004.

[21] G. Song, A. Atrens, D. Stjohn, J. Nairn, Y. Li, The electrochemical corrosion of pure magnesium in 1 N NaCl, Corrosion Science, 39 (1997) 855-875.

[22] Y. Zhang, C. Yan, F. Wang, W. Li, Electrochemical behavior of anodized Mg alloy AZ91D in chloride containing aqueous solution, Corrosion Science, 47 (2005) 2816-2831.

[23] F. Witte, J. Fischer, J. Nellesen, H.A. Crostack, V. Kaese, A. Pisch, F. Beckmann, H. Windhagen, In vitro and in vivo corrosion measurements of magnesium alloys, Biomaterials, 27 (2006) 1013-1018.

[24] N.T. Kirkland, N. Birbilis, M.P. Staiger, Assessing the corrosion of biodegradable magnesium implants: A critical review of current methodologies and their limitations, Acta Biomaterialia, 8 (2012) 925-936.

[25] A. Yamamoto, S. Hiromoto, Effect of inorganic salts, amino acids and proteins on the degradation of pure magnesium in vitro, Materials Science and Engineering C, 29 (2009) 1559-1568.

[26] Y. Xin, T. Hu, P.K. Chu, Influence of test solutions on in vitro studies of biomedical magnesium alloys, Journal of the Electrochemical Society, 157 (2010) C238-C243.

[27] T. Lei, W. Tang, S.-H. Cai, F.-F. Feng, N.-F. Li, On the corrosion behaviour of newly developed biodegradable Mg-based metal matrix composites produced by in situ reaction, Corrosion Science, 54 (2012) 270-277.

[28] M. Ascencio, M. Pekguleryuz, S. Omanovic, An investigation of the corrosion mechanisms of WE43 Mg alloy in a modified simulated body fluid solution: The influence of immersion time, Corrosion Science, 87 (2014) 489-503.

[29] X. Gu, Y. Zheng, S. Zhong, T. Xi, J. Wang, W. Wang, Corrosion of, and cellular responses to Mg-Zn-Ca bulk metallic glasses, Biomaterials, 31 (2010) 1093-1103.

[30] X. Gu, Y. Zheng, Y. Cheng, S. Zhong, T. Xi, In vitro corrosion and biocompatibility of binary magnesium alloys, Biomaterials, 30 (2009) 484-498.

[31] M. Jamesh, S. Kumar, T.S.N. Sankara Narayanan, Corrosion behavior of commercially pure Mg and ZM21 Mg alloy in Ringer's solution - Long term evaluation by EIS, Corrosion Science, 53 (2011) 645-654.

[32] R. Rettig, S. Virtanen, Time-dependent electrochemical characterization of the corrosion of a magnesium rare-earth alloy in simulated body fluids, Journal of Biomedical Materials Research - Part A, 85 (2008) 167-175.

[33] M.I. Jamesh, G. Wu, Y. Zhao, D.R. McKenzie, M.M.M. Bilek, P.K. Chu, Effects of zirconium and oxygen plasma ion implantation on the corrosion behavior of ZK60 Mg alloy in simulated body fluids, Corrosion Science, 82 (2014) 7-26.

[34] G. Song, Control of biodegradation of biocompatable magnesium alloys, Corrosion Science, 49 (2007) 1696-1701.

[35] Y. Xin, T. Hu, P.K. Chu, Degradation behaviour of pure magnesium in simulated body fluids with different concentrations of, Corrosion Science, 53 (2011) 1522-1528.

[36] N.I. Zainal Abidin, D. Martin, A. Atrens, Corrosion of high purity Mg, AZ91, ZE41 and Mg2Zn0.2Mn in Hank’s solution at room temperature, Corrosion Science, 53 (2011) 862-872.

[37] A. Oyane, H.M. Kim, T. Furuya, T. Kokubo, T. Miyazaki, T. Nakamura, Preparation and assessment of revised simulated body fluids, Journal of Biomedical Materials Research - Part A, 65 (2003) 188-195.

[38] G. Song, A. Atrens, Understanding magnesium corrosion. A framework for improved alloy performance, Advanced Engineering Materials, 5 (2003) 837-858.

[39] Z. Chen, The Open-Circuit Potential of a Polarizable and Reactive Electrode, ECS Transactions, 6 (2008) 1-15.

[40] G.G. Perrault, The potential-pH diagram of the magnesium-water system, Journal of Electroanalytical Chemistry and Interfacial Electrochemistry, 51 (1974) 107-119.

[41] Y. Xin, K. Huo, H. Tao, G. Tang, P.K. Chu, Influence of aggressive ions on the degradation behavior of biomedical magnesium alloy in physiological environment, Acta Biomaterialia, 4 (2008) 2008-2015.

[42] N. Pebere, C. Riera, F. Dabosi, Investigation of magnesium corrosion in aerated sodium sulfate solution by electrochemical impedance spectroscopy, Electrochimica Acta, 35 (1990) 555-561.

[43] J.B. Jorcin, M.E. Orazem, N. Pébère, B. Tribollet, CPE analysis by local electrochemical impedance spectroscopy, Electrochimica Acta, 51 (2006) 1473-1479.

[44] G. Baril, C. Blanc, N. Pébère, AC Impedance Spectroscopy in Characterizing Time-Dependent Corrosion of AZ91 and AM50 Magnesium Alloys Characterization with Respect to Their Microstructures, Journal of The Electrochemical Society, 148 (2001) B489-B496.

[45] G. Song, A. Atrens, X. Wu, B. Zhang, Corrosion behaviour of AZ21, AZ501 and AZ91 in sodium chloride, Corrosion Science, 40 (1998) 1769-1791.

[46] G. Baril, G. Galicia, C. Deslouis, N. Pebere, B. Tribollet, V. Vivier, An Impedance Investigation of the Mechanism of Pure Magnesium Corrosion in Sodium Sulfate Solutions, Journal of the Electrochemical Society, 154 (2007) C108-C113.

[47] B. Hirschorn, M.E. Orazem, B. Tribollet, V. Vivier, I. Frateur, M. Musiani, Determination of effective capacitance and film thickness from constant-phase-element parameters, Electrochimica Acta, 55 (2010) 6218-6227.

[48] G.J. Brug, A.L.G. Van Den Eeden, M. Sluyters-Rehbach, J.H. Sluyters, The analysis of electrode impedances complicated by the presence of a constant phase element, Journal of Electroanalytical Chemistry, 176 (1984) 275-295.

[49] R. Rettig, S. Virtanen, Composition of corrosion layers on a magnesium rare-earth alloy in simulated body fluids, Journal of Biomedical Materials Research - Part A, 88 (2009) 359-369.

[50] A. Oyane, K. Onuma, A. Ito, H.M. Kim, T. Kokubo, T. Nakamura, Formation and growth of clusters in conventional and new kinds of simulated body fluids, Journal of Biomedical Materials Research - Part A, 64 (2003) 339-348.

[51] H. Matsubara, Y. Ichige, K. Fujita, H. Nishiyama, K. Hodouchi, Effect of impurity Fe on corrosion behavior of AM50 and AM60 magnesium alloys, Corrosion Science, 66 (2013) 203-210.

[52] Y. Song, E.-H. Han, D. Shan, C.D. Yim, B.S. You, The role of second phases in the corrosion behavior of Mg–5Zn alloy, Corrosion Science, 60 (2012) 238-245.

[53] Y. Song, D. Shan, R. Chen, E.-H. Han, Effect of second phases on the corrosion behaviour of wrought Mg–Zn–Y–Zr alloy, Corrosion Science, 52 (2010) 1830-1837.

[54] E. Ghali, W. Dietzel, K.U. Kainer, General and Localized Corrosion of Magnesium Alloys: A Critical Review, Journal of Materials Engineering and Performance, 13 (2004) 7-23.

[55] Z. Shi, M. Liu, A. Atrens, Measurement of the corrosion rate of magnesium alloys using Tafel extrapolation, Corrosion Science, 52 (2010) 579-588.

[56] A.E. Coy, F. Viejo, P. Skeldon, G.E. Thompson, Susceptibility of rare-earth-magnesium alloys to micro-galvanic corrosion, Corrosion Science, 52 (2010) 3896-3906.

[57] R. Arrabal, E. Matykina, F. Viejo, P. Skeldon, G.E. Thompson, Corrosion resistance of WE43 and AZ91D magnesium alloys with phosphate PEO coatings, Corrosion Science, 50 (2008) 1744-1752.

[58] F. Zucchi, V. Grassi, A. Frignani, C. Monticelli, G. Trabanelli, Electrochemical behaviour of a magnesium alloy containing rare earth elements, Journal of Applied Electrochemistry, 36 (2006) 195-204.

[59] A.D. Südholz, N.T. Kirkland, R.G. Buchheit, N. Birbilis, Electrochemical Properties of Intermetallic Phases and Common Impurity Elements in Magnesium Alloys, Electrochemical and Solid-State Letters, 14 (2011) C5-C7.

[60] M. Bornapour, N. Muja, D. Shum-Tim, M. Cerruti, M. Pekguleryuz, Biocompatibility and biodegradability of Mg–Sr alloys: The formation of Sr-substituted hydroxyapatite, Acta Biomaterialia, 9 (2013) 5319-5330.

[61] M. Bornapour, M. Celikin, M. Cerruti, M. Pekguleryuz, Magnesium implant alloy with low levels of strontium and calcium: The third element effect and phase selection improve bio-corrosion resistance and mechanical performance, Materials Science and Engineering: C, 35 (2014) 267-282.

[62] L. Wang, G.H. Nancollas, Calcium orthophosphates: crystallization and dissolution, Chemical Reviews, (2008) 4628-4669.

[63] H.B. Pan, B.W. Darvell, Calcium Phosphate Solubility: The Need for Re-Evaluation, Crystal Growth & Design, 9 (2008) 639-645.

[64] D. Tadic, F. Peters, M. Epple, Continuous synthesis of amorphous carbonated apatites, Biomaterials, 23 (2002) 2553-2559.

[65] E. Boanini, M. Gazzano, A. Bigi, Ionic substitutions in calcium phosphates synthesized at low temperature, Acta Biomaterialia, 6 (2010) 1882-1894.

[66] E. Landi, G. Logroscino, L. Proietti, A. Tampieri, M. Sandri, S. Sprio, Biomimetic Mg-substituted hydroxyapatite: from synthesis to in vivo behaviour, Journal of Materials Science: Materials in Medicine, 19 (2008) 239-247.

Chapter 6

Corrosion behaviour of polypyrrole-coated WE43 Mg alloy in a modified simulated body fluid solution

M. Ascencio[1], M. Pekguleryuz[2] and S. Omanovic[1]

(1) Department of Chemical Engineering, (2) Department of Mining and Materials Engineering
McGill University, Montreal, Quebec, H3A 0C5, Canada

PREFACE

This chapter is comprised of a manuscript that will be submitted for publication in a peer-reviewed scientific journal. It was shown in Chapter 2 that the development of protective coatings is an attractive approach to control the corrosion rate and improve the biocompatibility of Mg-based biodegradable materials. The focus of this part of the study is to investigate the corrosion kinetics and mechanisms of polypyrrole-coated WE43 Mg alloy in a modified simulated body fluid (m-SBF) solution with daily electrolyte renewal. The production of hydrogen gas, the variation in the electrolyte pH and concentration of magnesium ions, and the morphology and composition of the corrosion products layer were also investigated. Polypyrrole (PPy) coatings were synthesized on WE43 Mg alloy samples by cyclic voltammetry in a solution containing pyrrole and sodium salicylate. Immersion experiments were performed for a time period up to five days at 37 ºC and at an initial pH of 7.4, corresponding to physiological conditions. Complete electrolyte renewal was performed on a daily basis to better simulate physiological homeostasis. Interfacial processes such as charge transfer, adsorption of

Mg intermediates and diffusion of Mg^{2+} ions were investigated and monitored after different immersion times by electrochemical impedance spectroscopy (EIS). The corrosion products layer composition and morphology were investigated by SEM, EDS, and ATR-FTIR. Finally, a corrosion mechanism as a function of immersion time was proposed taking into account the analysis of the corrosion kinetics results, the EIS time-dependent fitting parameters and the characterization of the corrosion products layer.

The co-authors of the manuscript presented in this chapter are listed above. The contributions of each author were the following: Mario Ascencio designed the experiments, prepared samples, performed the experimental work, analyzed results and wrote the manuscript. Prof. Mihriban Pekguleryuz contributed in the interpretation and discussion of results. Prof. Sasha Omanovic provided guidance, contributed in the interpretation and discussion of results and corrected the manuscript.

The authors gratefully acknowledge the financial support from the Natural Science and Engineering Research Council of Canada (NSERC) and the National Council of Science and Technology of Mexico (CONACyT).

Corrosion behaviour of polypyrrole-coated WE43 Mg alloy in a modified simulated body fluid solution

M. Ascencio[1*], M. Pekguleryuz[2] and S. Omanovic[1]

(1) Department of Chemical Engineering, (2) Department of Mining and Materials Engineering
McGill University, Montreal, Quebec, H3A 0C5, Canada

6.1 ABSTRACT

The corrosion mechanisms and kinetics of PPy-coated WE43 Mg alloy in a modified simulated body fluid (m-SBF) solution with daily electrolyte renewal are investigated by electrochemical, hydrogen evolution and analytical techniques. It is shown that the PPy coating effectively contributes to a decrease in the corrosion rate of WE43 Mg alloy and production of H_2 gas. An increase in the PPy coating protective properties observed after every electrolyte renewal is attributed to: 1) a decrease in the coating conductivity by the adsorption of CO_2 species, and to 2) substrate/coating decoupling due to uncompensated coating positive charging and misalignment of the substrate and coating Fermi levels.

6.2 INTRODUCTION

Magnesium alloys are attractive materials for the development of bioabsorbable implants mainly due to their relatively good biocompatibility and favorable mechanical properties, compared to polymeric biodegradable materials [1-4]. *In-vivo* experiments have demonstrated the feasibility of Mg-based bioabsorbable implants for

cardiovascular and orthopaedic applications [5-12], with recent clinical trials confirming the safety of Mg-based bioabsorbable stents [13-16]. However, the fast degradation of Mg-based implants in the physiological environment and concomitant premature decrease in the implant mechanical properties remain the main limitations for their commercialization and widespread use. Another issue is the production of hydrogen gas during the corrosion process at a rate the human body cannot regulate, leading to subcutaneous gas accumulation and delay in the healing process.

The corrosion of Mg is a complex process and different mechanisms have been proposed [17]. According to Song and Atrens [18], corrosion of Mg in an aqueous media occurs through the following reactions:

$2Mg \rightarrow 2Mg^{+} + 2e^{-}$ (anodic reaction) (6.1)

$2H_2O + 2e^{-} \rightarrow H_2 + 2OH^{-}$ (cathodic reaction) (6.2)

$2Mg^{+} + 2H_2O \rightarrow 2Mg^{2+} + 2OH^{-} + H_2$ (chemical reaction) (6.3)

$2Mg + 4H_2O \rightarrow 2Mg^{2+} + 4OH^{-} + 2H_2$ (overall reaction) (6.4)

$Mg^{2+} + 2OH^{-} \rightarrow Mg(OH)_2$ (product formation) (6.5)

According to this mechanism, corrosion of Mg involves the formation of Mg^{+} intermediates (reaction (6.1)) at the substrate/electrolyte interface and the production of OH^{-} species and H_2 gas through both electrochemical (reaction (6.2)) and chemical (reaction(6.3)) water reduction reactions. Accumulation of OH^{-} species, and the corresponding pH increase near the metal surface, leads to formation of an insulating Mg-oxide/hydroxide corrosion layer (reaction(5)), which provides partial corrosion

protection by limiting water penetration to the metal substrate. However, Mg has a poor corrosion resistance in neutral solutions and in the presence of aggressive electrolyte species such as Cl^- ions [17, 19-21], which lead to dissolution of the protective corrosion layer according to the following reaction:

$$Mg(OH)_2 + 2Cl^- \rightarrow Mg^{2+} + 2Cl^- + 2OH^- \quad (6.6)$$

Current research efforts are directed towards the development of methods to control the corrosion rate of Mg-based implants and to, ideally, tailor the implant degradation kinetics to specific body applications. Most of these efforts are oriented in two directions: (*i*) tailoring the composition and microstructure of Mg alloys for improved biocompatibility and targeted corrosion resistance rate and, (*ii*) the development of protective biocompatible coatings. The use of protective coatings is an attractive method to decrease the corrosion rate of Mg alloys. A variety of coatings and coating technologies have been developed to decrease the corrosion rate of Mg alloys, with some reviews recently published [22-25]; however, most of these techniques respond to the needs of the transportation industry and their use for biodegradable applications is not suitable. Only in recent years the development of protective coatings tailored to biomedical applications has gained interest. A general overview of biomedical coatings and coating techniques for Mg-based bioabsorbable applications was given by Hornberger et al. [26]. In addition to reducing the degradation rate of implants and improving their initial biocompatibility, desired functionalities of coatings for biomedical applications include bioactivity, antibiotic ability, local drug delivery and, in the case of orthopaedic applications, osseointegration. Furthermore, these coatings should allow for controlled degradation at the desired rate and thus, they should offer only a limited

barrier protection. A wide range of coatings on Mg and Mg alloys have been found to reduce the substrate corrosion rate to certain extent, including inorganic coatings containing Mg-oxide/hydroxide [27-29], calcium-phosphates [30-32], fluoride [33-35] and organic coatings containing polylactic acid (PLA) [36-38], polycaprolactone (PCL) [39, 40] and chitosan [41, 42]. However, critical factors such as surface chemistry, corrosion rate, corrosion process uniformity, coating adhesion and coating morphology still need to be optimized. Moreover, investigation of the long-term degradation process of prospective coated-alloys and development of appropriate test methods to accurately obtain information on the corrosion behaviour are still required.

Recently, the use of polypyrrole (PPy) coatings for controlling the degradation rate of Mg alloys for bioabsorbable applications has been suggested. PPy is an electrically-conductive polymer with well-known biocompatibility and it offers the possibility of controlled release of a variety of drugs and enzymes, which can be incorporated in the coating as dopant species [43]. Current biomedical applications of PPy include the development of artificial muscles [44], neural recording [45], stimulation of nerve regeneration [46], biosensors [47] and controlled drug release [48]. Furthermore, polypyrrole has a promising potential for intelligent corrosion protection. Intrinsically conductive polymers (ICPs) such as polythiophene, polyaniline (PANI) and polypyrrole have been extensively investigated for the corrosion protection of metals [49-51]. Although the suitability of ICPs for corrosion protection in practical applications has recently been questioned [52], a number of promising corrosion protection mechanisms have been identified, including anodic protection, intelligent release of corrosion inhibiting anions, and the shift of the oxygen reduction site from the

substrate/coating to the coating/electrolyte interface [51]. In a recent investigation by Turhan et al. [53], electrochemically-formed salicylate-doped polypyrrole coatings on AZ91D Mg alloy showed good corrosion protection properties in Na_2SO_4 solutions; according to the authors, such coatings have a high potential for controlling the degradation rate of Mg-based implants, since all components (substrate, coating and dopant) are non-toxic. In an investigation by the same group, optimization of salicylate-doped PPy coatings on AZ91D showed good corrosion properties after 10 days of immersion in Na_2SO_4 solutions, with the PPy coatings displaying good adhesion properties during the whole immersion time [54]. Srinivasan et al. [55] investigated the corrosion behaviour of salicylate-doped PPy coatings on AZ31 Mg alloys after 45 min of immersion in a simulated body fluid (SBF) and an increase in the corrosion resistance for the PPy-coated alloy of about one order of magnitude with respect to the bare alloy, was reported. The corrosion behaviour of salicylate-doped PPy/AZ91D Mg alloy in a simulated body fluid (SBF5) and the effect of the coating functionalization with protein albumin (Alb) monolayers was investigated [56]. According to this study, the corrosion resistance of the alloys increased in the order: AZ91D < PPy/AZ91D < Alb/PPy/AZ91D, with the corrosion protection of the coatings being attributed to a self-healing effect by the release of dopant salicylate ions. Thus, the previous investigations evidence the potential of PPy coatings for controlling the corrosion resistance of Mg-based biomedical implants; however, further improvement of the coating properties, e.g., corrosion protection and coating adhesion, is still required. Moreover, little information is available on the corrosion behaviour of PPy-coated Mg alloys in SBFs at longer immersion times and also on the corresponding corrosion mechanisms.

The aim of the present work is to report results on the corrosion behaviour of PPy-coated WE43 Mg alloy in a modified simulated body fluid (m-SBF) at 37 ºC for an immersion time up to 120 h. Daily electrolyte renewal was performed with the aim to better simulate physiological homeostasis. Interfacial processes and corrosion mechanisms are investigated by electrochemical impedance spectroscopy (EIS), and the time-variation of the EIS fitting parameters obtained by equivalent electrical circuit modelling is discussed. The PPy/WE43 electrode corrosion kinetics was also investigated by monitoring the electrolyte concentration of dissolved Mg^{2+} species and the production of H_2 gas. The effect of electrolyte renewal and the variation in the conductive properties of the PPy coating on the corrosion behaviour are discussed. Finally, a corrosion mechanism is proposed taking into account the PPy/WE43 corrosion kinetics, the analysis of the EIS results and the characterization of the PPy coating, corrosion products and Mg alloy substrate.

6.3 EXPERIMENTAL SECTION

6.3.1 Sample preparation

Commercial WE43 Mg alloy rods (Magnesium Elektron, USA) with the chemical composition shown in Table 6.1, were machined down to a diameter of 1.6 cm and cut into coins with a thickness of 0.5 cm. Working electrodes (test specimen) were prepared by attaching an insulated copper wire to a Mg alloy coin using conductive silver epoxy (Chemtronics Circuitworks, USA) and embedding the coin in epoxy resin (Epofix Struers, USA). The area of the sample exposed to the corrosive electrolyte was 1.98 cm^2. Prior to the coating procedure, the electrode surface was wet-abraded using SiC

paper up to 1200-grit and then fine-polished with diamond paste to a final polishing particle roughness of 1 μm. The samples were ultrasonically cleaned in ethanol for 10 minutes to remove any polishing residue, rinsed with acetone and dried in argon. This procedure ensured a reproducible surface state of the working electrodes.

Table 6.1: Chemical composition of WE43 Mg alloy.

Element	Mass Fraction (wt %)
Yttrium	4.0
Neodymium	2.2
Zirconium	0.54
Other rare earths	0.91
Magnesium	Balance

6.3.2 Electrochemical polymerization of pyrrole

Polypyrrole (PPy) coatings were electrochemically synthesized on WE43 samples from an aqueous solution containing 0.1 M pyrrole (Sigma-Aldrich) and 0.5 M sodium salicylate (Sigma-Aldrich), using cyclic voltammetry at a scan rate of 20 mV s^{-1} over 20 cycles. The previous parameters where chosen based on the work by Turhan et al. [54], who optimized the parameters for electrochemical polymerization of PPy on AZ91D Mg alloy. In order to optimize the electropolymerization potential range, electrodeposition experiments were performed in three different potential regions: 0 to 1 V, 0 to 1.25 V and 0 to 1.5 V, while keeping the other parameters constant. Following the completion of the electropolymerization procedure, the electrodes were withdrawn from the electrolyte solution, rinsed with deionized water and dried with argon gas.

6.3.3 Adhesion test

Adhesion of the PPy coating to the WE43 substrate was evaluated using an adhesive tape (Scotch Transparent Tape 600). Six parallel vertical and horizontal cuts were made, cutting through the coating and reaching the substrate in one steady motion, resulting in a grid of small squares. Afterwards, the sample surface was gently brushed to remove any detached flakes. The adhesive tape was then placed over the sample surface and good contact was ensured by rubbing the tape firmly with an eraser. Finally, after about 90 s the tape was rapidly removed by pulling it at an angle of 180º to the coating surface.

6.3.4 Immersion experiments

Modified simulated body fluid (m-SBF) [57], with a pH of 7.4 was prepared using reagent grade chemicals and deionized water with a resistivity of 18.2 MΩ cm. Table 6.2 shows the amount of chemicals used. Immersion experiments were performed for a time period up to 120 h. The electrolyte-volume/sample-surface ratio was 50 cm^3/cm^2 and the electrolyte was in contact with air. In order to closer simulate physiological homeostasis, the m-SBF electrolyte was completely renewed every 24 h. All the experiments were performed at the physiological body temperature of 37 °C. The electrolyte temperature was controlled using a water bath equipped with a thermostat. Electrochemical measurements were performed after different immersion times and electrolyte samples were collected on a daily basis for subsequent analysis of the concentration of dissolved Mg species. From independent immersion experiments, the amount of hydrogen gas produced by corrosion of the Mg alloy was measured using the

method proposed in the literature [18]. At the end of the immersion experiments, the samples were removed from the electrochemical cell, rinsed with distilled water and dried with argon gas. All the experiments were done in triplicates. After surface characterization of the corrosion products, the corrosion layer was dissolved by immersion in chromic acid (concentration, 180 g dm^{-3}) for 5-10 min in order to analyse the morphology of the underlying (corroded) Mg alloy substrate.

Table 6.2: Amounts of reagents used to prepare 1000 ml of m-SBF [57].

Reagents[a]	Purity / %	Amount
NaCl	>99.5	5.403g
$NaHCO_3$	>99.5	0.504g
Na_2CO_3	>99	0.426g
KCl	>99	0.225g
K_2HPO_4	>98	0.1756g
$MgCl_2*6H_2O$	>99.4	0.311g
HEPES[b]	>99.5	17.892g[c]
$CaCl_2*2H_2O$	>99	0.3881g
Na_2SO_4	>99.2	0.072g
1.0 M NaOH	---	10 ml

[a]Listed in sequence of dissolution; [b]HEPES, 2-(4-(2-hydroxyethyl)-1-piperazinyl)ethanesulfonic acid; [c]HEPES was previously dissolved in 100 ml of 0.2M NaOH.

6.3.5 Electrochemical techniques

Electrochemical experiments were performed in a standard three-electrode electrochemical cell. WE43 Mg alloy samples were used as working electrodes, a graphite rod as a counter electrode and a saturated calomel electrode (SCE, Fisher Scientific Accumet, USA) as a reference electrode. All potentials in this paper are

referred to SCE. Electrochemical measurements were carried out using a potentiostat/galvanostat (Autolab PGSTAT30, Netherlands) equipped with a frequency response analyser. Electrochemical impedance spectroscopy measurements were carried out at open circuit potential with an AC amplitude of 10 mV over a frequency range from 100 kHz to 10 mHz. Open circuit potential values from impedance measurements were recorded during the complete immersion time.

6.3.6 Electrolyte analysis and substrate surface and corrosion products characterization

Inductively coupled plasma optical emission spectroscopy (ICP-OES, Thermo Jarrell Ash Trace Scan, USA) was used to measure the electrolyte concentration of dissolved Mg species at a wavelength of 285.2 nm. The morphology and composition of the samples surface were characterized by scanning electron microscopy (FE-SEM, Philips XL-30, Netherlands) equipped with an energy-disperse spectrometer (EDS). The corrosion layer thickness was measured by cross-sectional SEM analysis of the sample. Attenuated total reflectance Fourier transform infrared spectroscopy (ATR-FTIR, Bruker Hyperion, USA) analysis, with an ATR objective mounted on an FTIR microscope, was performed to investigate the presence of chemical groups in the PPy coating and of the corrosion products layer.

6.4 RESULTS AND DISCUSSION

6.4.1 Electrochemical polymerization of pyrrole on WE43 Mg alloy

Magnesium has a very negative corrosion potential and a fast dissolution rate in aqueous solutions, making direct electropolymerization of pyrrole (Py) on its surface a

challenging task. To overcome this problem, passivation of the Mg substrate is necessary prior to the electropolymerization step. This could be done, for instance, by first coating the magnesium alloy surface with a thin metal film that is more resistant to anodic dissolution, as proposed by Jian et al. [58], who applied an electroless Cu and Ni plating pretreatment before Py electropolymerization on AZ91 Mg alloy. Following a different approach, sodium salicylate (SS) has recently been used for direct electropolymerization of Py on Zn-Al-Mg alloys, without any pretreatment of the surface [53-56]. Formation of a thin Mg-salicylate protective layer contributes to passivation of the Mg alloy substrate, allowing for subsequent formation of the PPy layer [59, 60]. It has been proposed that SS is the most suitable candidate for the formation of adherent and homogenous PPy films on oxidizable metals by electrochemical polymerization [53, 60]. Figure 6.1 shows cyclic voltammograms for WE43 Mg alloy in 0.5 M aqueous SS solution without the dissolved Py monomer and in the presence of Py in the solution, recorded in three different potential regions: 0 to 1 V, 0 to 1.25 V and 0 to 1.5 V. Inset figures show the first (solid line) and second (dashed line) polarization cycles. Polarization of the Mg alloy electrode in the SS solution without Py monomer (Figure 6.1a) showed two anodic peaks/shoulders in the forward direction at potentials around 0.2 and 0.7 V, in agreement with data reported in the literature for other Mg alloys [53-55]. The first peak has been related to anodic dissolution of the Mg alloy substrate and subsequent precipitation of an insoluble Mg-salicylate layer, while the second peak has been related to salicylate oxidation, which leads to formation of an insulating layer [61, 62]. Reverse scans show an initial low current density that increases at a potential negative of 0.8 V, indicating the reactivation of the electrode dissolution process. The

decrease in current density observed after the first polarization cycle (compare the solid and dashed lines in the inset to Figure 6.1a) supports the formation of a protective Mg-salicylate layer, while the gradual increase in current density observed after the third polarization cycle indicates an increase in the substrate dissolution rate with the number of cycles. Removal of the Mg alloy electrode from the SS solution at the end of the experiment revealed the presence of a thin yellowish film on the electrode surface, which can be related to the formation of the Mg-salicylate protective layer.

Cyclic voltammograms recorded in the presence of Py (Figure 6.1b-d) show an initial behaviour similar to that observed for the Py-free solution (insets), with anodic peaks/shoulders around 0.2 and 0.7 V corresponding to the Mg alloy electrode anodic dissolution and salicylate oxidation processes, respectively. However, a different electrochemical behaviour was observed in subsequent cycles, depending on the upper (anodic) polarization potential limit. Cyclic voltammograms obtained from 0 to 1 V (Figure 6.1b) show a small decrease in the current density with repetitive cycling and a delay in the current density increase during the reverse scan, compared to the response obtained for the Py-free solution (Figure 6.1a). This behaviour suggests that incorporation of Py into the Mg-salicylate layer contributes to a gradual decrease in the Mg alloy electrode dissolution rate and to a delay in its reactivation during the reverse scan, with respect to the behaviour observed for the Py-free SS solution (Figure 6.1a). However, even after 20 cycles, the results evidence the still poor protective properties of the formed coating. Removal of the Mg alloy electrode from the electrolyte solution revealed the presence of a greenish-brown coating, suggesting the formation of a thin PPy layer. Asavapiriyanont et al. [63] pointed out that polarization of almost any

electrode in an aqueous Py solution to a potential above 0.6 V vs. SCE results in the formation of a PPy film. They also stated that the appearance and color of the PPy film depends on the concentration of pyrrole, pH, potential and time of oxidation but, in general, thick PPy films are black and thin ones are yellow. Cyclic voltammograms recorded from 0 to 1.25 V (Figure 6.1c) show a gradual current density decrease in the forward scan direction at potentials negative of 0.8 V, indicating a progressive decrease in the electrode dissolution rate. Simultaneously, a gradual current density increase positive of 0.8 V can be observed, corresponding to the oxidation of Py and formation of a PPy layer with an increasing thickness [53, 54]. Removal of the Mg alloy electrode from the electrolyte solution revealed the presence of a black uniform coating corresponding to PPy, as shown by SEM (Figure 6.2) and ATR-FTIR (Figure 6.13) analyses. Cyclic voltammograms recorded from 0 to 1.5 V (Figure 6.1d) show, simultaneously, a fast current density decrease in the potential region below 0.8 V, corresponding to the decreased Mg alloy electrode anodic dissolution and SS oxidation processes, and a gradual current density increase in the potential region positive of 0.8 V, corresponding to the Py oxidation process. Removal of the Mg alloy electrode from the electrolyte solution revealed the presence of a thick black coating with some blister-like structures, suggesting the formation of gas cavities underneath the coating. Posterior rinsing of the electrode with deionized water led to partial removal of the coating, revealing a weak coating adhesion. A decrease in the adhesion of PPy coatings on platinum and glassy carbon electrodes has been related to PPy overoxidation at anodic potentials above 1 V vs SCE [54, 64, 65]. PPy overoxidation leads to a decrease in the coating electrochemical activity and conductivity and is thus

accompanied by a decrease in the current density [64, 65]. Since cyclic voltammograms in the potential regions from 0 to 1.25 V and 0 to 1.5 V show a gradual increase in the current density at potentials positive of 0.8 V, a decrease in the coating adhesion as a result of PPy overoxidation is unlikely. Therefore, the poorer adhesion observed for the PPy coatings prepared in the potential region from 0 to 1.5 V can be rather attributed to the increase in the PPy coating thickness.

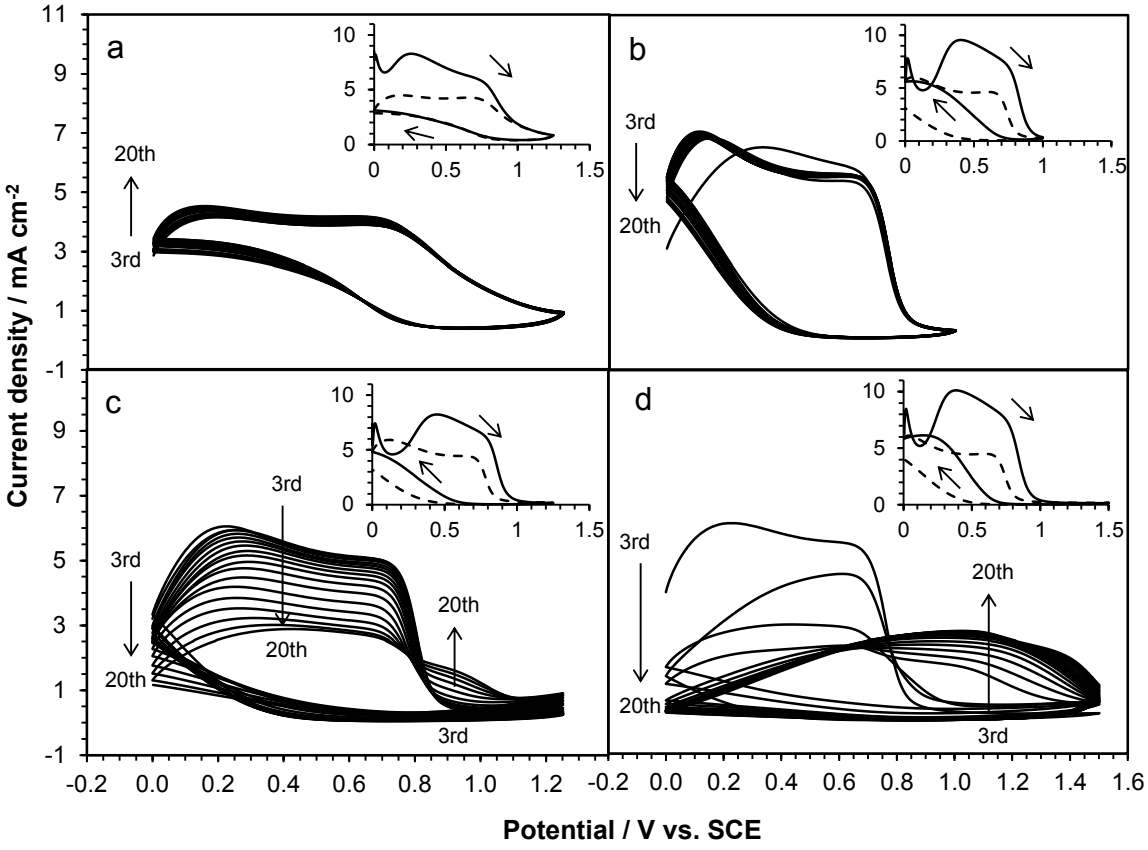

Figure 6.1: Cyclic voltammograms of WE43 Mg alloy in 0.5 M sodium salicylate (a) without Py monomer and (b-d) in the presence of 0.1 M Py in different potential regions: (b) 0-1 V, (c) 0-1.25 V and (d) 0-1.5 V. Inset figures show the first (solid line) and second (dashed line) polarization cycles. Scan rate = 20 mV s^{-1}.

It can be concluded that, among the potential regions investigated, electropolymerization in the potential region from 0 to 1.25 V produces the PPy layer with the most suitable adhesion and protective properties on WE43 Mg alloy. Therefore, PPy coatings prepared in this potential region were used for subsequent PPy layer characterization and immersion experiments in m-SBF.

6.4.2 Surface morphology and adherence of PPy coating layer

Figure 6.2 shows the surface morphology of bare WE43 and PPy/WE43 Mg alloys examined by SEM. The bare sample (Figure 6.2a) shows a uniform surface, while the PPy/WE43 sample revealed a thin PPy layer (Figure 6.2b), through which the grinding/polishing striations can be distinguished. Scattered granular structures and some interconnected lines along grain boundaries can also be observed, which can be related to the presence of PPy nucleation sites and to formation of the PPy film probably occurring at a different rate on the grain boundaries, respectively. Figure 6.2c shows a higher magnification picture of a region identified as a PPy nucleation site, in which the characteristic PPy cauliflower morphology with globules of less than 1 μm diameter can be observed. The presence of islands of PPy with globular structure reveals an early stage of the PPy deposition. The presence of PPy was further confirmed by ATR-FTIR analysis (Figure 6.13). Figure 6.2d shows a PPy coating with a fairly uniform thickness of 1.7 ± 0.2 μm (measured at seven different locations).

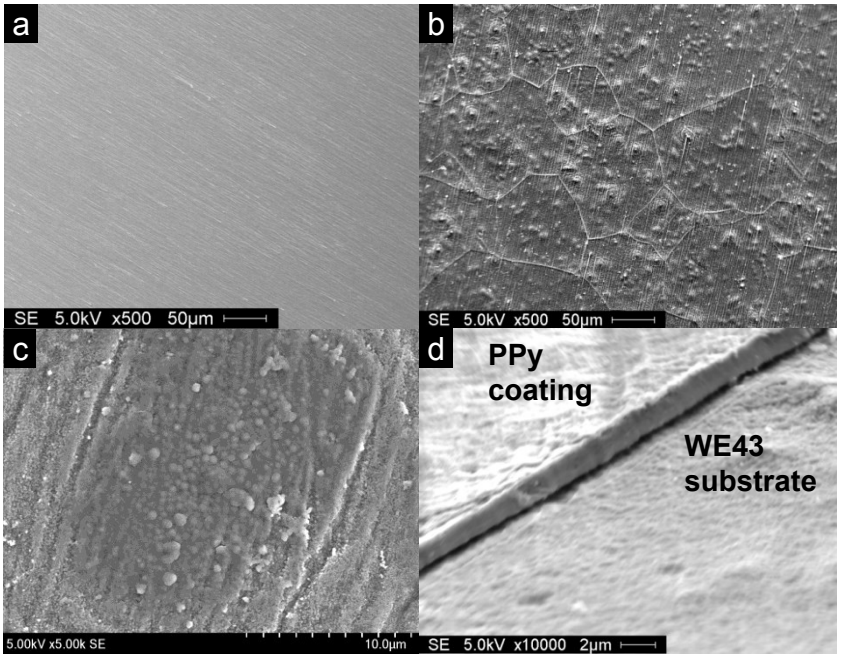

Figure 6.2: SEM images of (a) the surface of bare WE43 and (b) PPy/WE43 Mg alloy electrodes, (c) a PPy nucleation site with globular morphology and (d) a tilted PPy/WE43 electrode showing the PPy coating thickness.

Adhesion of the PPy coating to the Mg alloy substrate was evaluated using a tape test. Figure 6.3 shows the PPy/WE43 Mg alloy surface before and after the adhesion test. It was observed that the coating detached along the top edge of the electrodes with an average affected area of 21 ±6 % obtained by triplicates. All the samples tested showed a similar behaviour. Although the reason of the non-uniform coating adhesion is not clear, it might be related to a non-uniform potential and current distribution during the PPy electrodeposition.

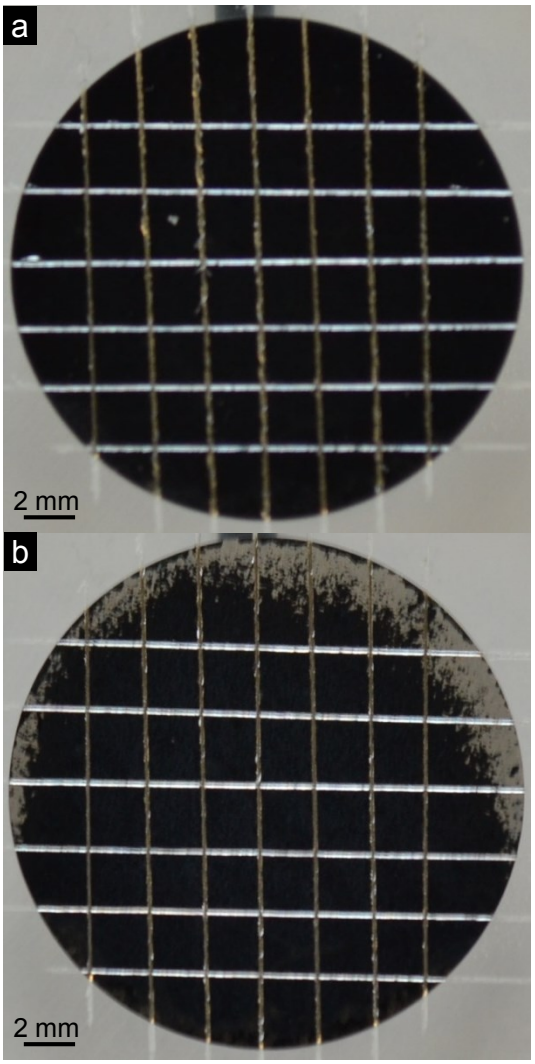

Figure 6.3: Pictures of a PPy/WE43 electrode surface (a) before and (b) after the adhesion test.

6.4.3 Electrochemical experiments

Figure 6.4 shows the open circuit potential (OCP) and electrolyte pH time-dependent behaviour of bare WE43 and PPy/WE43 Mg alloy electrodes in m-SBF with daily electrolyte renewal. An initial fast increase in OCP during the first 8 h can be observed, with OCP values of both the bare and coated substrates fairly similar. At immersion times between 8 h and 24 h, the OCP of the bare sample continues increasing,

reaching a value of -1.75 V after 24 h, while the OCP of the coated sample reached a value of -1.82 V. The initial increase in OCP of both the bare and coated samples can be related to the formation of a corrosion layer with increasing protective properties over time, while the indication of relative OCP stabilization at 24 h can be related to quasi-equilibrium conditions. After every electrolyte renewal, a temporary decrease in the OCP of the bare sample to more negative potentials was observed, while the OCP of PPy/WE43 showed the opposite behaviour, temporarily increasing to the OCP values of the bare sample and then decreasing again. This OCP fluctuation observed for both the bare and coated electrodes can be related to a perturbation of the electrode surface as a result of the change in the electrolyte composition and pH after electrolyte renewal, as will be discussed in more detail later in the paper. It is well known that the corrosion behaviour of Mg is affected by the electrolyte pH. It has also been pointed out that during immersion experiments in SBFs, variations in the electrolyte pH and concentration of Mg^{2+} ions affect the solubility equilibrium of phosphate and carbonate species, which play a role in the protective ability of the corrosion layer [66]. Electrolyte renewal has recently been proposed as a way to better control the increase in the electrolyte pH and the change in the concentration of electrolyte components, and thus, to better simulate physiological homeostasis [66, 67]. Figure 6.4 shows the time-dependent pH behaviour of bare WE43 and PPy/WE43 Mg alloys in m-SBF. An alternating increase/decrease in the pH values can be observed, with the decrease in pH corresponding to the electrolyte renewal. A control experiment to investigate the pH variation of m-SBF without the corroding sample (Figure 6.4, solid line) showed a gradual pH increase, reaching a quasi-constant value of about 7.65 after 24 h. It has

been shown that this pH increase corresponds to a decrease in the concentration of carbonate species by the release of CO_2 to the atmosphere, according to the following reaction [57]:

$$H_2CO_{3(aq)} \leftrightarrow CO_{2(g)} + H_2O_{(aq)} \quad (6.7)$$

Thus, the increase in the electrolyte pH observed in Figure 6.4 for bare WE43 and PPy/WE43 Mg alloys can be related to the combination of the increase in the concentration of OH^- species as a result of the corrosion process, and the decrease in the concentration of carbonate species by the gradual release of CO_2 to the atmosphere. The highest pH increase was observed for the bare WE43 electrode, reaching a value of about 7.7 after 24 h. At longer immersion times, both bare WE43 and WE43/PPy electrodes showed a similar behaviour, with a maximum daily pH value close to that observed for the control experiment (7.65). The smaller pH increase observed for PPy/WE43 during the first 24 h can be related to the protective properties of the PPy coating; however, the protection extent of the coating at longer immersion times is not evident from the pH values.

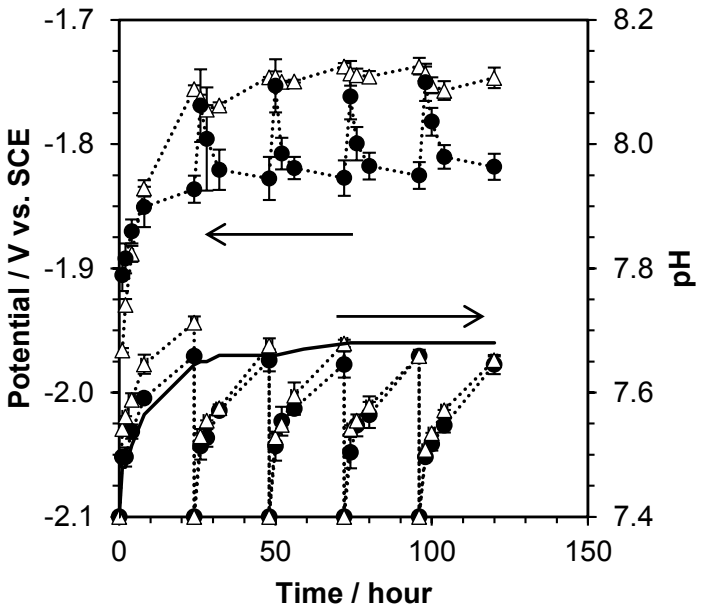

Figure 6.4: Time-dependent open circuit potential (OCP) and electrolyte pH behaviour of bare WE43 (triangles) and PPy/WE43 (circles) Mg alloy electrodes in m-SBF. The solid line shows the pH change of m-SBF without corroding sample.

It has been shown in [51, 68-70] that galvanic coupling between intrinsically conductive polymer (ICP) coatings and substrates such as iron, mild steel and stainless steel, leads to formation of a passive oxide layer at the substrate/coating interface; a process that is accompanied by ennoblement of the OCP to the equilibrium potential of the corresponding conductive polymer. It is proposed that ICPs provide corrosion protection by stabilising or even improving the protective oxide layer, by an anodic protection mechanism. The extent of the coating protection depends on the experimental conditions and on the presence of coating defects; with coating failure usually related to a shift in the OCP to more negative values. During the formation of the substrate passive oxide layer, the conductive coating, which is initially in its oxidized state, undergoes a reduction process, leading to a decrease in its conductivity and thus,

protective properties. However, it has been observed that ICPs such as PANI and PPy can be re-oxidized in the presence of oxygen [51, 71], thus regenerating its protective properties. According to this mechanism, the reduction of PPy coatings during the Mg-substrate corrosion process and its re-oxidation in the presence of oxygen can be expressed by the following equations, as proposed in [71]:

$$½\,Mg + 1/m\,[PPy^{m+}(mA^-)] \rightarrow ½\,Mg^{2+} + 1/m\,PPy^0 + A^- \quad (6.9)$$

$$1/m\,PPy^0 + ¼\,O_2 + ½\,H_2O + A^- \rightarrow 1/m\,[PPy^{m+}(mA^-)] + OH^- \quad (6.10)$$

The reduction of PPy is usually accompanied by the release of its dopant anions, denoted by A- in equation 6.9, in some cases possessing corrosion inhibiting properties, e.g., salicylate, while its re-oxidation is accompanied by the uptake of anions such as Cl^- and OH^- to maintain the polymer electroneutrality.

The OCP behavior displayed by PPy/WE43 in Figure 6.4 clearly shows the absence of an anodic protection mechanism, with OCP values overall more negative than those observed for the bare electrode. The absence of the OCP ennoblement for ICP-coatings on active metals such as zinc and magnesium has already been observed and different explanations have been provided [71-73]. Williams and McMurray [72] observed that coatings containing polyaniline emeraldine salt (ES) induce oxide growth and OCP ennoblement on Fe and Al, but not on Mg and Zn. They attributed such behaviour to the low acidity of the Mg-oxide and Zn-oxide cations, which deprotonate ES, leading to its inactivation, i.e., loss of conductivity. Rohwerder et al. [73] investigated the corrosion at the buried interface between the metal and conductive polymer-based coatings. They observed that while a PPy-containing coating led to a

potential ennoblement on iron and aluminum, on a zinc-coated electrode the low potential of metallic zinc was obtained, although the PPy-coating seemed still to be in its oxidized state. They attributed this phenomenon to a misalignment of the Zn substrate and PPy coating Fermi-levels, due to corrosion-induced formation of a non-conducting film at the substrate/coating interface and to positive coating charging due to uncompensated cation uptake. Thus, in view of the studies performed by Williams and Rohwerder, the following explanation is proposed for the observed more negative OCP behaviour for PPy/WE43 with respect to the bare sample: corrosion-induced reduction of PPy and alkalization of the substrate/coating interface lead to formation of a non-conducting PPy interfacial film. The presence of an insulating film limiting the substrate/coating electrical contact might be enhanced by the formation of a corrosion layer at the substrate/coating interface and by corrosion-induced release of salicylate ions and precipitation of Mg-salicylate species, as explained in section 3.1. Under these conditions, passivation and full polarization of the metal substrate to the PPy potential does not occur; however, formation of a weak galvanic couple by the diffusion of water and ions to the interface may polarize the substrate towards increased corrosion and thus, exhibit a more negative OCP, as proposed in [73]. However, OCP values are thermodynamic data and do not provide information on the corrosion charge transfer and mass transport kinetics and thus, other techniques need to be used to assess the coating protective properties.

In order to obtain more information on the corrosion process and to evaluate the protective properties of the PPy coating, electrochemical impedance spectroscopy (EIS) was used to investigate the corrosion resistance of bare WE43 and PPy/WE43 Mg

alloys. Figure 6.5 shows Nyquist plots for the impedance response of bare WE43 Mg alloy after different immersion times up to 120 h. Three time constants can be identified: two capacitive loops at high and medium frequencies and one inductive loop at low frequencies, in agreement with data reported in the literature for pure Mg [74-76] and Mg alloys [77, 78]. The capacitive loop at high frequencies has been related to charge transfer (electron transfer) and electrochemical double-layer/barrier film effects; the capacitive loop at medium frequencies has been related to mass transport relaxation due to diffusion of Mg^{2+} ions through the corrosion layer and, the inductive loop at low frequencies has been related to relaxation of coverage due to adsorption of Mg^{+} intermediates [76]. The gradual increase in the impedance response observed during the first 24 h (Figure 6.5a-b) can be related to formation of a corrosion layer with increasing protective properties over time. At longer immersion times, a temporary decrease in the impedance response was observed after every electrolyte renewal, reaching the smallest value 4 h after electrolyte renewal and then increasing again. Figure 6.5c-f shows the impedance response right before, 4 h after and 24 h after electrolyte renewal. A change in the relative size of the capacitive and inductive loops can be seen, with the impedance response changes observed after electrolyte renewal corresponding mainly to changes in the size of the capacitive loop at medium frequencies. In agreement with our previous investigation on the influence of electrolyte renewal on the corrosion behaviour of cast WE43 in m-SBF [66], the temporary decrease in the impedance response and OCP (Figure 6.4) observed after electrolyte renewal can be attributed to partial dissolution of the corrosion layer and the

corresponding increase in mass transport, as a result of the decrease in the electrolyte pH and concentration of Mg^{2+} species.

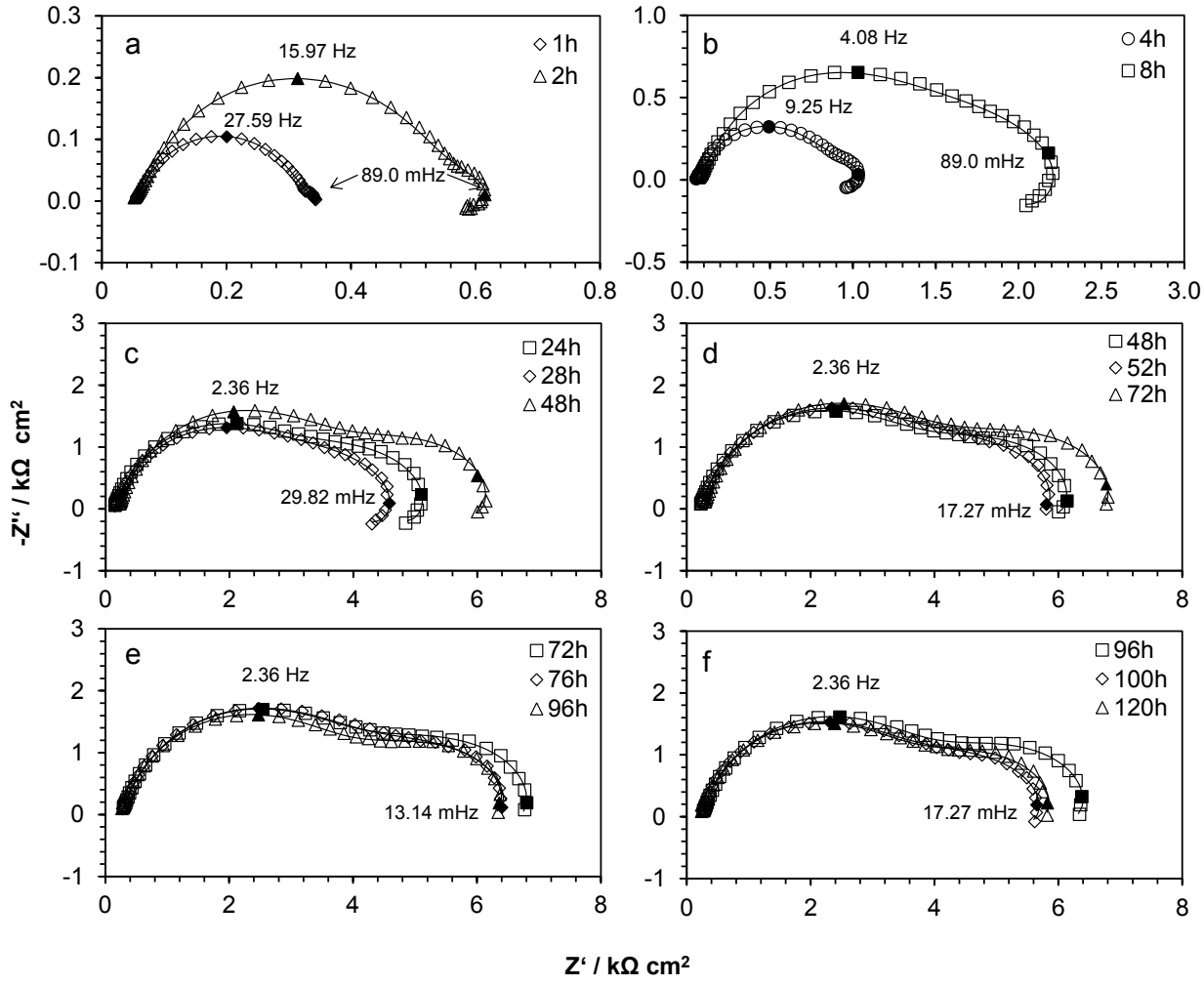

Figure 6.5: Electrochemical impedance response of WE43 Mg alloy in m-SBF with daily electrolyte renewal after different immersion times: (a) 1-2 h, (b) 4-8 h, (c) 24-48 h, (d) 48-72 h, (e) 72-96 h and (f) 96-120 h. Symbols represent experimental values, whereas continuous lines represent simulated spectra.

Figure 6.6 shows the impedance response of PPy/WE43 Mg alloy after different immersion times up to 120 h. Similarly to the behaviour observed for the bare electrode,

an increase in the impedance response observed during the first 8 h (Figure 6.6a) can be attributed to the formation of a corrosion layer with increasing protective properties over time. However, a small decrease in the impedance response was observed at the 24^{th} hour, suggesting a decreasing effect of the coating protective properties over time. In agreement with the OCP behaviour (Figure 6.4) and contrary to the effect observed for the bare alloy, a temporary increase in the impedance response was observed after every electrolyte renewal, reaching its maximum value 2 h after electrolyte renewal and subsequently decreasing again. Figure 6b-c shows the impedance response right before, 2 h after and 24 h after electrolyte renewal. It was observed a temporary change in the shape of the impedance response after every electrolyte renewal, changing from two capacitive loops and one inductive loop, before electrolyte renewal, to one capacitive loop and one inductive loop up to 8 h after electrolyte renewal and then recovering its initial shape 24 h after electrolyte renewal. This behaviour was confirmed by the Bode diagrams of the impedance response of WE43/PPy after 24 h and 32 h shown in Figure 6.7. The phase angle curve recorded at 24 h shows the presence of three time constants corresponding to the capacitive loops at high and medium frequencies and the inductive loop at low frequencies observed in Figure 6.6, while the response after electrolyte renewal (32 h) shows only two time constants corresponding to the capacitive and inductive loops observed in Figure 6.6. This behaviour suggests a change in the corrosion mechanism after electrolyte renewal. It was also observed that the increase in the impedance response is similar in magnitude after every electrolyte renewal and that the impedance response decreases to its initial value 24 h after electrolyte renewal. These results suggest that the PPy/WE43 electrode reached quasi-

equilibrium after 24 h of immersion and that the system perturbation after electrolyte renewal is reversible, in agreement with the observed OCP behaviour (Figure 6.4).

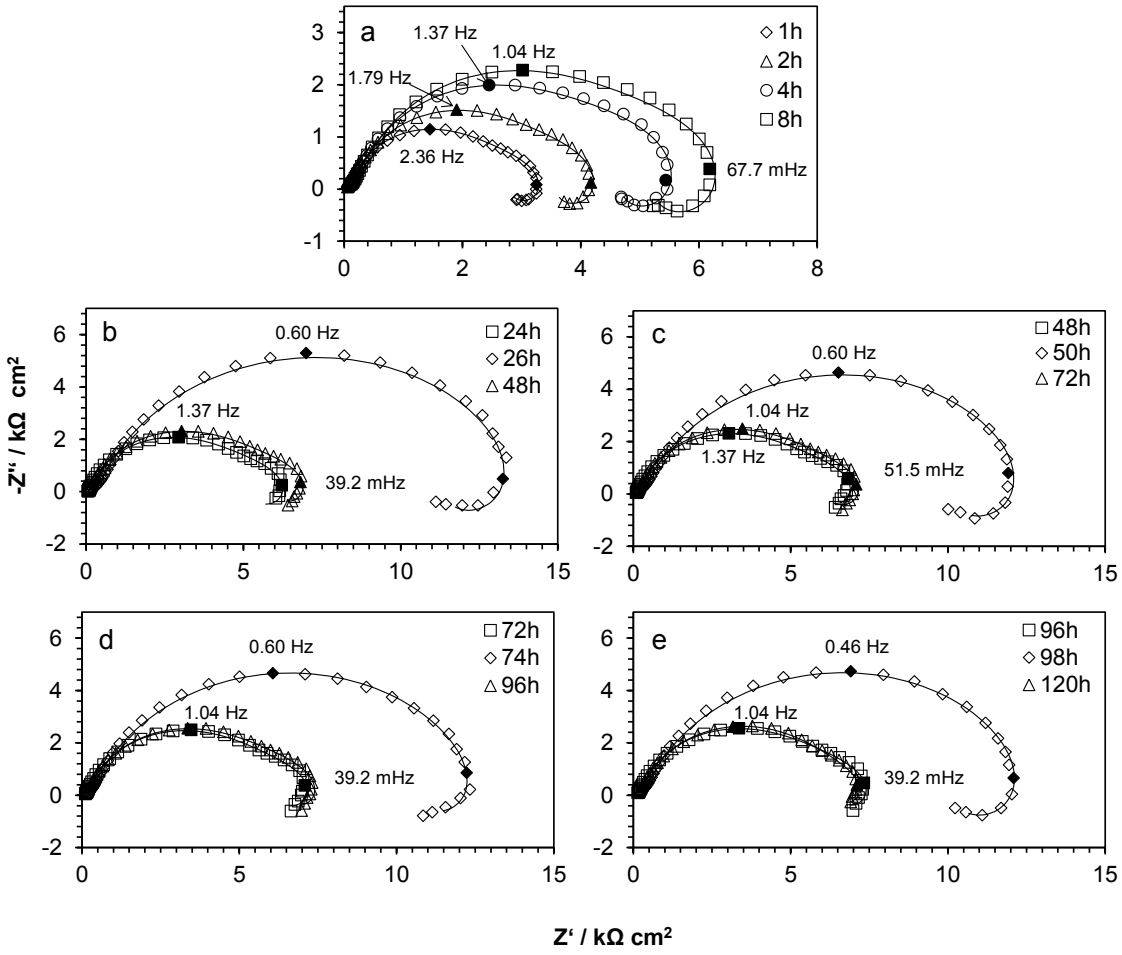

Figure 6.6: Electrochemical impedance response of PPy/WE43 Mg alloy in m-SBF with daily electrolyte renewal after different immersion times: (a) 1-8 h, (b) 24-48 h, (c) 48-72 h, (d) 72-96 h and (e) 96-120 h. Symbols represent experimental values, whereas continuous lines represent simulated spectra.

In order to identify the cause of the impedance perturbation observed after electrolyte renewal for PPy/WE43, the effect of the change in the electrolyte pH, concentration of Mg^{2+} ions and concentration of dissolved CO_2 was independently investigated. Table 6.3 describes the experiments performed and the corresponding

effect observed on the impedance response. It was concluded from these experiments that the decrease in pH (experiment 1) after electrolyte renewal is not the cause of the observed impedance increase. However, experiment 2 confirmed that the change in the concentration of one of the electrolyte components is responsible for the observed impedance perturbation. In experiment 3, the new electrolyte had about the same CO_2 concentration (both were 24 h old) and pH (7.65) as the old electrolyte (the one in which the alloy sample was kept for 24 h), but a lower Mg^{2+} concentration; this time, no variation in the impedance response was observed, indicating that a change in the concentration of Mg^{2+} is not the cause of the observed impedance increase. However, during the same experiment, 6 h after electrolyte renewal, CO_2 was introduced into the electrolyte until its pH reached the value of the fresh electrolyte, 7.4 (experiment 4); this time, the temporary increase in impedance response was observed, indicating that the variation in the concentration of dissolved CO_2 is a probable cause of the impedance perturbation observed in the experiments in Figure 6.6. These results were confirmed by duplicates. More specifically, Figure 6.8 shows the impedance response obtained in experiments 3 and 4. It can be observed that the same impedance response was obtained before (crosses) and 4 h after electrolyte renewal (triangles) during experiment 3. However, when CO_2 was introduced at 30 h during experiment 4 (note that the CO_2 bubbling was stopped when the pH of the solution decreased to 7.4, the value corresponding to that of the fresh electrolyte), an increase in the impedance response was recorded, reaching its largest value at 32 h (squares) and subsequently decreasing at longer immersion times; this confirms that the amount of CO_2 dissolved in the

electrolyte, not the corresponding pH, influences the impedance behaviour of the PPy/WE43 electrode.

Table 6.3: Experiments performed to investigate the impedance perturbation after electrolyte renewal and their effect on the impedance response.

Experiment	Parameter investigated	Experiment description	Outcome
1	pH	No electrolyte renewal. After 24 h, pH of electrolyte was decreased from 7.65 to 7.4 adding 1.3 ml of 2.5 wt.% H_2SO_4 solution	Impedance response decreased temporarily, reaching its smallest value 8h after electrolyte renewal and subsequently increasing again
2	Concentration of electrolyte components	Electrolyte was renewed after 24 h. Before electrolyte renewal, pH of new electrolyte was adjusted to pH of old electrolyte (7.65) adding 3 ml of 0.2 M NaOH solution	Impedance response increased temporarily, reaching its largest value 2h after electrolyte renewal and subsequently decreasing again
3	Concentration of dissolved Mg	Electrolyte was renewed after 24 h. Before electrolyte renewal, new electrolyte was kept at 37 ºC for 24 h allowing CO_2 release and reaching a pH value of 7.65	No variation in the impedance response was observed
4	Concentration of dissolved CO_2	Six hours after electrolyte renewal in (3), CO_2 was bubbled in the electrolyte for a few seconds until the pH decreased to a value of 7.4	Impedance response increased temporarily, reaching its largest value 4 h after CO_2 bubbling and subsequently decreasing again

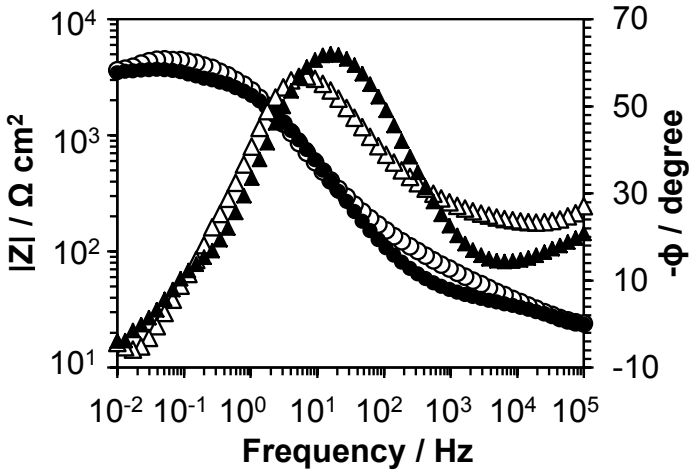

Figure 6.7: Bode plots of WE43/PPy Mg alloy in m-SBF recorded after 24 h (black triangles) and 32 h (white triangles).

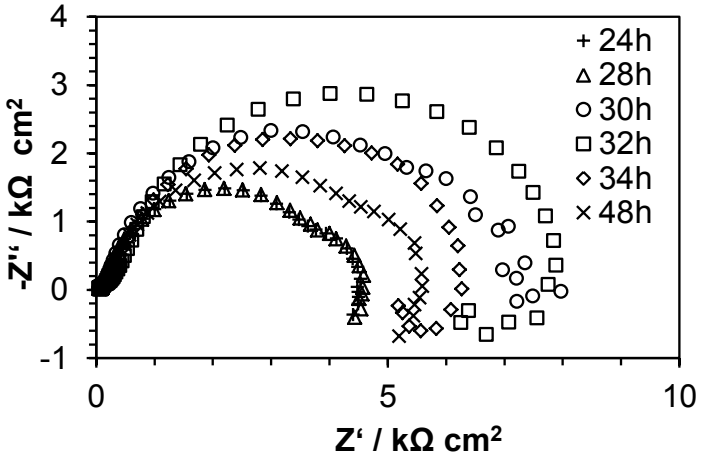

Figure 6.8: Electrochemical impedance response of PPy/WE43 in m-SBF obtained during experiments 3 and 4 described in Table 6.3. Electrolyte renewal during experiment 3 showed no variation in the impedance response (24-28 h). In experiment 4, CO_2 bubbling for a short time until the electrolyte pH was set to its initial value of 7.4 produced a transient increase in the impedance response (30-48 h).

The variation in the electrolyte CO_2 concentration after electrolyte renewal as the cause for the impedance perturbation observed for PPy/WE43 is supported by data reported in the literature [79-81]. It has been shown that exposure to CO_2 gas leads to a

decrease in the conductivity of PPy, which has motivated the investigation of PPy for CO_2 sensing applications [79]. It was proposed that CO_2 molecules form weak bonds with π-electrons of the PPy surface, which results in a decrease in the PPy conductivity. The adsorption of CO_2 is reversible and the change in the PPy conductivity depends on the CO_2 gas concentration. During the desorption process, the bonds formed with π-electrons of PPy break and PPy recovers its initial conductivity [80]. It was reported that a 570 nm thick PPy plasma-polymerised film showed quasi-constant adsorption-desorption cycles, with adsorption and desorption times of about 10 and 20 min, respectively [81]. In view of the previous data, the increase in the impedance response observed for PPy/WE43 after electrolyte renewal (Figure 6.6), can be related to a decrease in the PPy coating conductivity due to the reversible adsorption of solution-dissolved CO_2 gas on PPy. As the CO_2 concentration in the electrolyte decreases with time (due to its release into the atmosphere according to equation 6.7), so does the impedance response, reaching its initial value 24 h after electrolyte renewal.

In order to gain a better insight into the corrosion mechanisms and to more accurately assess the protective properties of the PPy coating, the impedance response was modelled using an equivalent electrical circuit (EEC) and the obtained fitting parameters were analysed as a function of time. Figure 6.9 shows the EECs used to model the impedance response of bare WE43 and PPy/WE43 Mg alloys. A three-time-constant circuit (Figure 6.9a) was used to model the impedance response of both bare WE43 and WE43/PPy electrodes. In the case of WE43/PPy, a two-time-constant circuit (Figure 6.9b) was used to model the impedance response after electrolyte renewal showing only one capacitive loop and one inductive loop. By using these EECs a good

fit was obtained (Figures 6.5-6.6, continuous lines) with average values of $\chi^2=3.33x10^{-4} \pm 1.07x10^{-4}$ and $\chi^2=1.55x10^{-4} \pm 1.36x10^{-4}$ for the bare and coated samples, respectively. A constant phase element (CPE) was used to model the electrode capacitive behaviour. CPEs are used to describe a non-ideal capacitive behaviour due to factors such as distributed surface reactivity, surface roughness and heterogeneities, electrode porosity and non-uniform potential and current distribution [82].

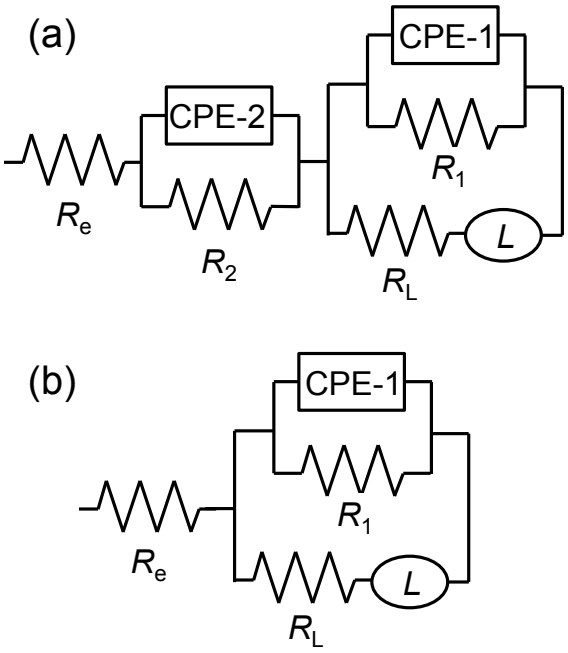

Figure 6.9: (a) Three time constant equivalent electrical circuit (EEC) used to model EIS data of bare WE43 and PPy/WE43 Mg alloys in m-SBF. (b) Two time constant EEC used to model EIS data of WE43/PPy at 2h, 4h and 8h after every electrolyte renewal.

In agreement with the corrosion models proposed by Song and Atrens [18] and Baril et al. [75], the EEC fitting parameters for bare WE43 (Figure 6.9a) can be interpreted as follows: R_1 and CPE-1 describe respectively the charge transfer

resistance and the combined electrochemical double layer/MgO barrier film capacitance at the substrate/electrolyte interface; R_2 and CPE-2 describe the diffusion of Mg^{2+} species through the outer $Mg(OH)_2$ corrosion layer; L and R_L describe respectively the inductance and inductance resistance due to the adsorption of intermediate Mg^+ species at the corrosion layer free surface; and R_e describes the electrolyte resistance. The EEC fitting parameters for PPy/WE43 (Figure 6.9a) can be interpreted as follows: R_1 and CPE-1 describe respectively the charge transfer resistance and the combined electrochemical double layer/Mg-oxide barrier film capacitance at the substrate/coating interface; R_2 and CPE-2 describe the response of the PPy coating; L and R_L describe respectively the inductance and inductance resistance due to the adsorption of intermediate Mg^+ species; and R_e describes the electrolyte resistance. After electrolyte renewal, adsorption of solution-dissolved CO_2 gas leads to a decrease in the PPy coating conductivity and to substrate/coating decoupling (as will be explained later in the text) and thus, the impedance contribution of the PPy coating can be eliminated from the EEC, as shown in Figure 6.9b.

Tables 6.4-6.5 show the EIS fitting parameters obtained after different immersion times for bare WE43 and PPy/WE43 Mg alloys, respectively. Figure 6.10a-b shows the time dependent behaviour of R_1 and R_2 for bare WE43 and PPy/WE43 Mg alloys. Bare WE43 Mg alloy shows a gradual increase in R_1 (Figure 6.10a, triangles), reaching a plateau at about 48 h, which can be related to the formation of a corrosion layer with increasing protective properties until quasi-equilibrium is reached after 48 h. This quasi-equilibrium state implies a dynamic equilibrium between the $MgO/Mg(OH)_2$ precipitation and dissolution reactions, leading to quasi-constant barrier film coverage. A small

decrease in R_1 can be observed after every electrolyte renewal, corresponding to partial dissolution of the corrosion layer and decrease in the barrier film properties, in agreement with the observed OCP behaviour (Figure 6.4). The decrease in the electrolyte pH and concentration of Mg^{2+} ions after electrolyte renewal leads to a shift in the corrosion layer solubility equilibrium towards $MgO/Mg(OH)_2$ dissolution – hence the drop in R_1, as shown in [66]. R_2 values (Figure 6.10b, triangles) show a gradual increase during the first 24 h, corresponding to an increase in the diffusion resistance, probably related to the formation of a more compact corrosion layer at a higher pH. After 24 h, R_2 values level off, showing only a temporary decrease after every electrolyte renewal, in agreement with the behaviour observed for R_1.

Table 6.4: EIS fitting parameters obtained for bare WE43 Mg alloy in m-SBF after different immersion times.

Time/ h	R_e/ $\Omega\,cm^2$	$Q_1\times10^5$/ $\Omega^{-1}cm^{-2}s^n$	n_1	C_{dl}/ $\mu F cm^{-2}$	R_1/ $\Omega\,cm^2$	$Q_2\times10^5$/ $\Omega^{-1}cm^{-2}s^n$	n_2	R_2/ $\Omega\,cm^2$
1	41.5	4.05	0.88	17.19	227.5	459.03	0.34	83.4
8	60.0	3.43	0.93	22.08	880.0	27.32	0.58	1459.3
24	128.6	2.42	0.89	12.22	2247.0	32.20	0.58	3646.7
28	123.8	3.08	0.90	16.26	1890.0	25.65	0.58	3127.0
32	133.7	2.79	0.90	14.75	2076.0	26.01	0.58	3436.7
48	192.3	2.21	0.90	11.77	2694.3	35.88	0.55	5160.0
52	186.9	2.54	0.89	13.24	2546.0	28.51	0.58	3843.3
56	192.4	2.49	0.89	12.85	2613.0	29.61	0.58	4140.0
72	228.2	2.19	0.89	11.63	2887.0	37.30	0.55	5700.0
76	214.3	2.36	0.90	12.76	2719.7	31.37	0.57	4256.7
80	214.9	2.37	0.90	13.21	2683.7	29.90	0.56	4370.0
96	237.3	2.21	0.89	11.72	2945.3	39.65	0.54	6180.0
100	216.7	2.35	0.89	12.47	2753.7	33.93	0.58	3946.7
104	211.4	2.39	0.90	12.99	2653.0	30.58	0.58	3830.0
120	223.9	2.23	0.89	11.80	2903.0	39.59	0.55	5573.3

Table 6.5: EIS fitting parameters obtained for PPy/WE43 Mg alloy in m-SBF after different immersion times.

Time/ h	R_e/ Ω cm^2	$Q_1\times10^5$/ Ω^{-1}cm^{-2}s^n	n_1	C_{dl}/ μFcm^{-2}	R_1/ Ω cm^2	$Q_2\times10^5$/ Ω^{-1}cm^{-2}s^n	n_2	R_2/ Ω cm^2
1	45.1	27.68	0.59	13.08	1776.3	4.00	0.96	1558.0
8	81.4	15.16	0.60	8.17	5263.3	4.65	0.98	2926.7
24	63.3	21.02	0.61	13.42	3796.7	3.11	0.90	3773.3
26	279.4	2.88	0.78	7.66	12653.3	-	-	-
32	169.4	3.67	0.78	8.97	8580	-	-	-
48	83.5	24.41	0.61	20.36	4120.0	3.00	0.88	4516.7
50	305.7	2.73	0.80	8.21	14163.3	-	-	-
56	179.1	3.72	0.78	9.23	8543.3	-	-	-
72	101.5	30.04	0.56	17.21	5216.7	3.19	0.90	4873.3
74	252.7	3.03	0.80	9.15	12950	-	-	-
80	196.2	3.77	0.78	9.83	9003.3	-	-	-
96	111.3	28.45	0.56	17.31	5926.7	3.41	0.91	4743.3
98	326.4	3.11	0.80	10.12	14216.7	-	-	-
104	213.6	3.89	0.79	10.64	9713.3	-	-	-
120	121.6	27.07	0.55	15.76	4710.0	3.63	0.91	4913.3

In the case of PPy/WE43 Mg alloy, significantly larger R_1 values with respect to those of the bare alloy can be observed (Figure 6.10a, circles), evidencing the protective properties of the PPy coating. R_1 values increase relatively steeply during the first 8 h, followed by a decrease between the 8th and the 24th h. However, a sudden increase in R_1 can be observed after every electrolyte renewal, followed by a rather fast decrease to a R_1 value close to that recorded just before the electrolyte renewal. The sudden increase in R_1 can be related to adsorption of CO_2 and the corresponding drop in the PPy layer conductivity, while its subsequent decrease can be related to the progressively diminishing concentration of dissolved CO_2 and to recovering of the PPy layer conductivity, as already explained. Assuming that CO_2 adsorption during the first 24 h of immersion led to a decrease in the coating conductivity, which is justified by the

above-explained behaviour in the R_1 trend after electrolyte renewal, the increase in R_1 during the first 8 h can then be related to the formation of a corrosion layer with increasing protective properties, while its decrease after 8 h can be related to recovery of the PPy coating conductivity by the diminishing concentration of dissolved CO_2. The R_1 increase/decrease cycles after each electrolyte renewal are similar in size, supporting the reversible adsorption of CO_2. Furthermore, the similar R_1 values observed right before electrolyte renewal (at 24 h, 48 h, etc.), show that after 24 h there is a small variation in the protective properties of the PPy/corrosion layer (disregarding the CO_2 adsorption effect), with a mean R_1 value of 4.75 ±0.76 $k\Omega\,cm^{-2}$. The previous results indicate that: (1) formation and growth of a corrosion layer reached quasi-equilibrium during the first 24 h, leading to quasi-constant corrosion layer coverage at longer immersion times and, (2) the increase/decrease in R_1 observed after each electrolyte renewal corresponds to the effect of reversible CO_2 adsorption on the PPy coating, the surface coverage of which depends on the concentration of dissolved CO_2, which varies with time. This is in agreement with the observed OCP behaviour (Figure 6.4), where the initially increasing OCP values levelled off after 24 h, showing an increase/decrease behaviour only as a result of electrolyte renewal. R_2 values show an initial gradual increase, leveling off after 48 h (Figure 6.10b). This behaviour can be related to an increase in the PPy coating resistance due to corrosion products accumulation and to corrosion-induced partial reduction of the PPy layer with the corresponding decrease in its conductivity, until quasi-equilibrium is reached after 48 h. It should be noted that the previous R_2 data describes the behaviour of the PPy coating

only when coupled to the substrate, while coating decoupling observed up to 8 h after electrolyte renewal yielded no R_2 values.

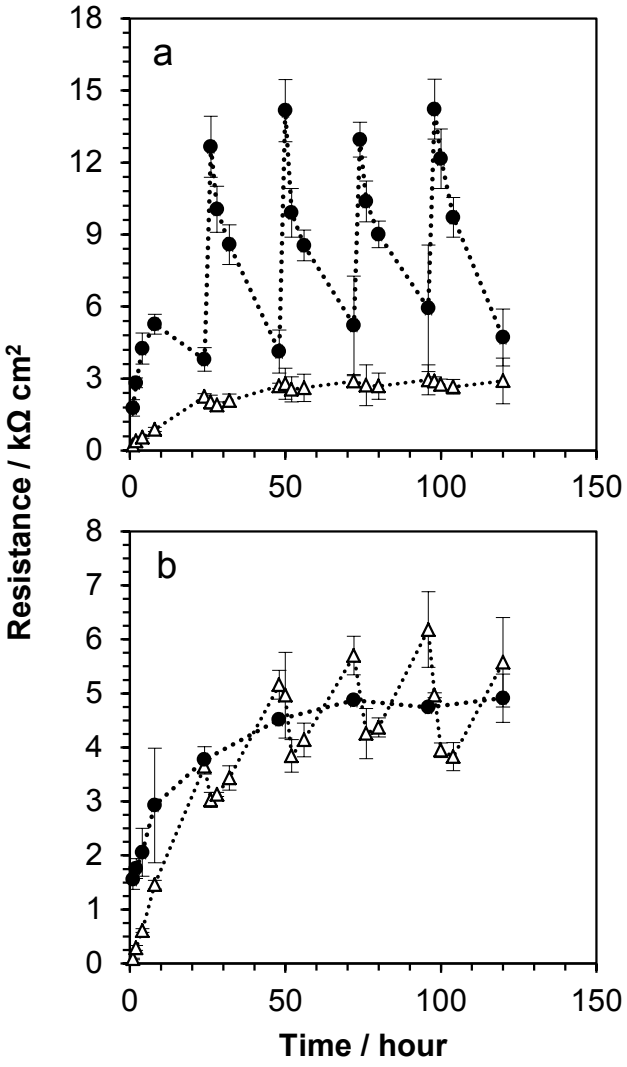

Figure 6.10: Time-dependent behaviour of (a) R_1 and (b) R_2 for bare WE43 (triangles) and WE43/PPy (circles) Mg alloys in m-SBF. R_1 corresponds to the electrode charge transfer resistance, while R_2 can be related to the corrosion layer diffusion resistance, for bare WE43, and to the PPy coating impedance response, for WE43/PPy.

The increased corrosion resistance and the observed change in the corrosion mechanism after electrolyte renewal can be explained by relating the decrease in the

PPy coating conductivity to: 1) an increase in the PPy barrier film properties and, 2) substrate/coating decoupling by a corrosion-induced Fermi level misalignment. Charge transfer through ICP coatings is a complex process that involves electronic and ionic transport. Charge carriers, such as electrons and holes, are able to move in solid phase along polymer chains, while solvated ionic species work as charge carriers in the coating pores [83]. The distribution of charge carriers inside the PPy coating must comply with the electroneutrality condition and the self-consistent electric field and thus, charge transport cannot be considered as pure diffusion [84]. Under these conditions, a decrease in the PPy conductivity would increase the coating barrier properties by hindering electron transport through the coating layer and limiting ionic mobility, i.e., decreasing ionic permeability and water penetration. On the other hand, hindered electron transport and coating positive charging due to uncompensated Mg^{2+} cations uptake might cause a Fermi-level misalignment between the substrate and the PPy coating, as explained by Rohwerder et al. [73], leading to substrate/coating decoupling and inhibiting the flow of Mg^{2+} ions by the established electric field. The substrate/coating decoupling after electrolyte renewal is evidenced by the shift in OCP to more positive values, reaching similar values to those observed for the corroded bare sample (Figure 6.4) Recovering of the PPy coating conductivity reactivates the substrate/coating coupling and the flow of electrons, with the corresponding decrease in R_1 and OCP.

6.4.4 Electrolyte analysis and hydrogen evolution

In order to further investigate the corrosion behaviour of bare WE43 and PPy/WE43 Mg alloys and to verify the corrosion protection properties of the PPy coating, the

production of hydrogen gas and the concentration of dissolved Mg-ions were monitored. Figure 6.11a-b shows daily cumulative volume of produced H_2 gas (normalized with respect to 1 cm^2 of the sample surface) and electrolyte Mg^{2+} concentration after different immersion times, up to 120 h (it should be noted that the electrolyte was replaced every 24 h, as in the electrochemical measurements discussed previously in the paper). Cumulative concentration values of Mg^{2+} were calculated by subtracting the average Mg^{2+} concentration of the fresh electrolyte, taken as control, corresponding to 33.8±0.5 ppm. The higher cumulative H_2 volume and electrolyte Mg^{2+} concentration values obtained for bare WE43 confirm the protective properties of the PPy coating, observed by electrochemical measurements previously discussed in the paper. A similar trend for both bare WE43 and PPy/WE43 Mg alloys can be observed, showing a faster rate of H_2 gas production and Mg dissolution during the first 24h, followed by a quasi-linear increase at longer immersion times.

Since both the amount of produced H_2 gas and the electrolyte Mg^{2+} concentration are proportional to the corrosion rate, coating protection efficiency values were calculated after different immersion times according to the following equation:

$$\eta(\%) = \frac{P_{uncoated} - P_{coated}}{P_{uncoated}} \times 100 \quad (6.12)$$

where η(%) is the coating protection efficiency and P is the cumulative volume of produced H_2 gas (cm^3cm^{-2}) or the cumulative concentration of corrosion-dissolved Mg^{2+} (ppm). Table 6.6 shows calculated PPy coating protection efficiency values. Two observations can be made: (i) lower protection efficiency values are obtained from the concentration values of dissolved Mg^{2+} and, (ii) while the protection efficiency calculated

on the basis of produced H_2 remains constant with time, the protection efficiency calculated on the basis of dissolved Mg decreases linearly with time. It is not currently clear to the authors the cause of the difference in the observed trend. These results, however, support that both water and oxygen species are reduced during the corrosion process of PPy/WE43 Mg alloy. This is attractive from a biomedical perspective, since a decrease in the production of hydrogen gas during the implant degradation process is desired.

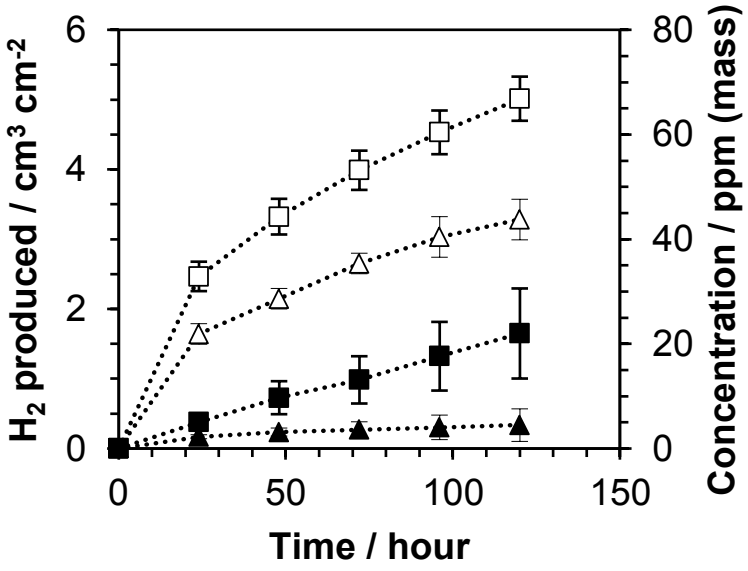

Figure 6.11: Time-dependent behaviour of cumulative produced hydrogen (triangles) and cumulative solution-dissolved Mg^{2+} concentration (squares) produced by corrosion of bare WE43 (white symbols) and PPy/WE43 (black symbols) Mg alloys in m-SBF.

Table 6.6: Corrosion protection efficiency calculated from cumulative values of produced H_2 and solution-dissolved Mg^{2+} concentration for PPy/WE43 in m-SBF after different immersion times.

Time / hour	η(%)	
	H_2	Mg^{2+}
24	89.8	84.7
48	89.0	78.1
72	89.9	75.3
96	90.0	70.8
120	89.7	67.1

6.4.5 Corrosion products characterization

Figure 6.12 shows SEM images of bare WE43 and PPy/WE43 electrodes after 120 h of immersion in m-SBF. The bare WE43 electrode displays a relatively uniform corroded surface with some globular aggregates of different size scattered on the surface (compare Figure 6.12a to the morphology of the freshly-polished bare WE43 electrode surface in Figure 6.2a). The presence of a cracked-mud surface morphology can be related to dehydration of the corrosion layer by the vacuum atmosphere during the SEM analysis. The PPy/WE43 electrode shows a uniform surface without visible precipitates and with no sign of delamination of the PPy coating (Figure 6.12d).

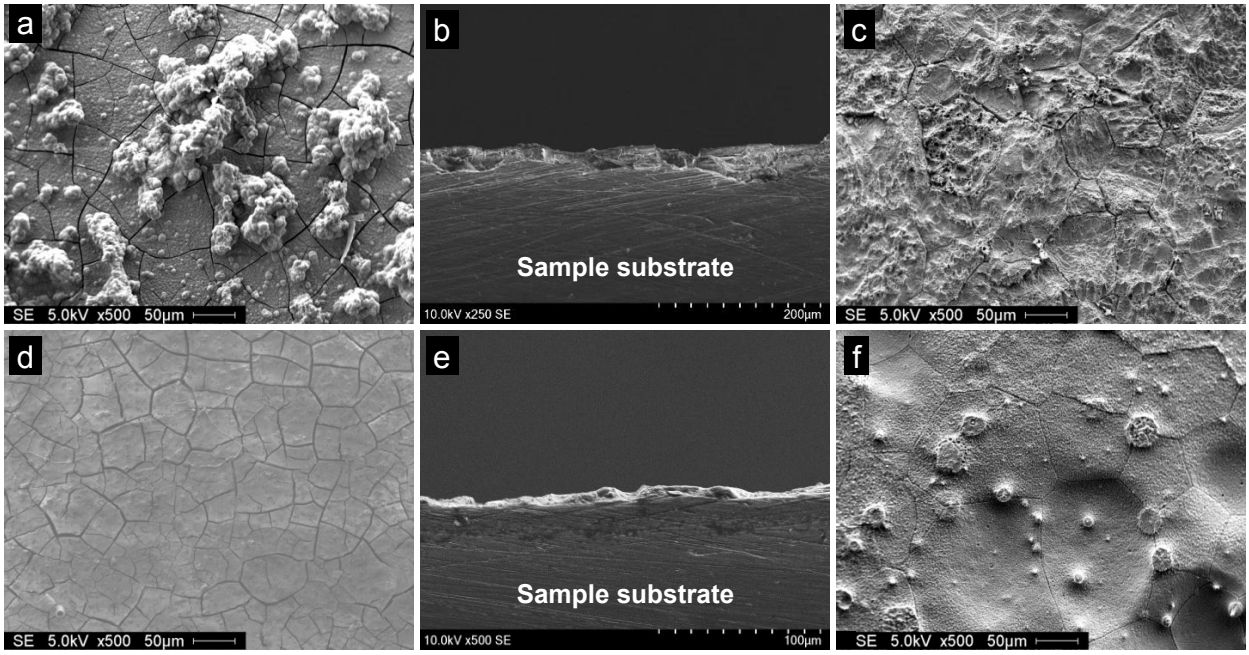

Figure 6.12: SEM images of bare WE43 and PPy/WE43 Mg alloys after 120h in m-SBF: (a) and (d) corroded surface, (b) and (e) cross-sectional view and, (c) and (f) substrate surface after removing the corrosion products of bare WE43 and PPy/WE43, respectively.

The presence of globular aggregates on bare WE43 can be related to precipitation of amorphous calcium phosphates (ACP), in agreement with the results obtained by ATR-FTIR (Figure 6.13). ACP have been identified as a precursor phase in the synthesis of hydroxyapatite in neutral to basic solutions [85]. It has been found that m-SBF is optimal for biomimetic production of bone-like apatite, probably due to its super-saturation and saturation with respect to apatite and calcite, respectively [57]. The formation of substituted apatite species has been reported by several groups during *in-vitro* investigations of the corrosion behaviour of Mg alloys in SBFs [86-89]. Lee [90] reported the presence of globular agglomerates corresponding to Mg-substituted amorphous calcium phosphates. The absence of such globular precipitates on

PPy/WE43 suggests that PPy is not a suitable surface for the deposition of apatite-like species. However, Jiang et al. [91] reported the synthesis of apatite coatings on a PPy substrate by immersion in a SBF. They observed that apatite could hardly be formed on undoped PPy, even after 21 days of immersion in SBF, while apatite coatings were successfully formed in the presence of dopants containing carboxyl and sulfonic groups.

Cross-sectional analysis of the bare WE43 electrode reveals an irregular corrosion layer with a thickness in the range of 20-50 μm (Figure 6.12b), while the cross-sectional image of the PPy/WE43 electrode displays a thinner corrosion layer with a thickness in the range of 2-10 μm (Figure 6.12e). The thinner corrosion layer observed for PPy/WE43 can be related to the barrier properties of the PPy coating, which hinder water penetration and ionic transport. Analysis of the substrate morphology after dissolution of the corrosion products and PPy coating showed that the WE43 substrate under the PPy coating has a smoother surface (Figure 6.12f) with respect to the bare electrode (Figure 6.12c), indicating that the presence of the PPy coating leads to a more uniform corrosion process. Some circular structures of different sizes can be observed on the PPy/WE43 substrate surface, which might be related to less corroded substrate cathodic regions; however, this hypothesis still needs to be demonstrated. Table 6.7 shows the elemental composition obtained by EDS of bare WE43 and PPy/WE43 samples before and after 120 h of immersion in m-SBF. The presence of N and the increase in the C content of PPy/WE43 with respect to the bare alloy can be related to formation of the PPy coating. After 120 h of immersion, the presence of P and Ca on the surface of bare WE43 is in agreement with the formation of Mg-substituted calcium phosphate precipitates, whereas the presence of P in

PPy/WE43 can be related to the precipitation of Mg-phosphates. It was determined that the composition of the corrosion layer and globular agglomerates (deposits) seen in Figure 6.12a is similar, with the latter showing a slight increase in the content of P and Ca.

Table 6.7: Elemental composition of bare WE43 and PPy/WE43 Mg alloys before and after 120 h of immersion in m-SBF.

Sample	Elemental composition at.%								
	Mg	C	O	Y	Nd	Na	N	P	Ca
Bare WE43	89.1	7.8	1.5	1.2	0.5	-	-	-	-
Ppy/WE43	4.0	78.1	13.2	0.4	-	0.2	4.0	-	-
Bare WE43 after 120 h	2.3	18.6	68.8	-	-	-	-	8.9	1.4
Bare WE43 after 120 h (deposit)	2.1	12.8	68.6	-	-	-	-	14.4	2.1
Ppy/WE43 after 120 h	1.1	64.8	30.7	-	-	-	2.1	1.3	-

Figure 6.13 shows ATR-FTIR microscopy spectra obtained for bare WE43 and PPy/WE43 Mg samples before and after 120 h of immersion in m-SBF. The analysis of a clean bare WE43 electrode showed no absorption peaks. After 120 h of immersion, the presence of phosphate and carbonate species was identified. The peaks at 1495 cm^{-1}, 1405 cm^{-1} and 850 cm^{-1} can be attributed to stretching and bending vibrations of CO_3^{2-} groups, while the peak at 1015 cm^{-1} corresponds to stretching of PO_4^{3-}. The peak around 1635 cm^{-1} can be attributed to a bending vibration of water molecules in the corrosion layer. Analysis of a freshly prepared PPy/WE43 sample confirmed the presence of PPy and salicylate species. Characteristic PPy peaks were detected around 1550 cm^{-1}, 1200 cm^{-1} and 1030 cm^{-1}, corresponding to C=C/C-C stretching, C-N stretching and C-H in-plane bending vibrations, respectively [53, 92, 93]. The peaks around 1590 cm^{-1} and 1370 cm^{-1} correspond to the presence of salicylate species and

can be attributed respectively to asymmetric and symmetric COO^- stretching, while the peak at 1470 cm^{-1} can be related to the aromatic ring stretching vibration [53, 55, 94]. The peaks around 935 cm^{-1} and 755 cm^{-1} can be attributed to the C-H out-of-plane bending [55, 92]. After 120 h of immersion of the PPy/WE43 sample, the salicylate peak at 1470 cm^{-1} can no longer be observed, probably due to the release of salicylate ions from the PPy coating. The intensity of the PPy peaks has also decreased after 120 hours, which might be related to precipitation of corrosion products on top of the PPy coating (Figure 6.12d). The broader peak around 1030 cm^{-1} can be related to overlapping of PPy and phosphate absorption peaks, corresponding to the deposition of phosphate species during the corrosion process.

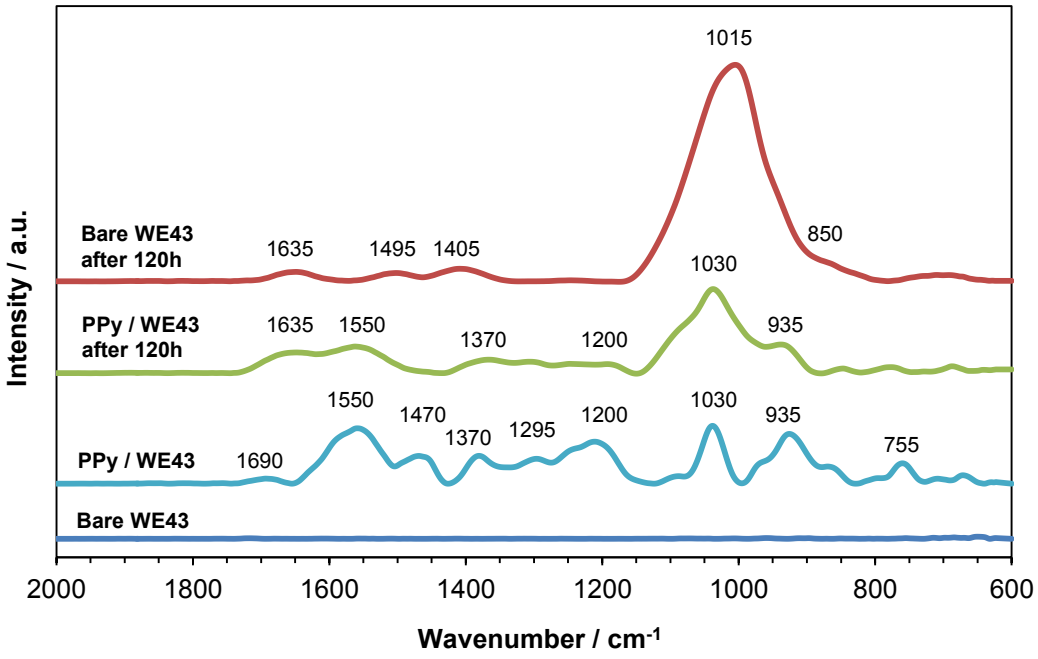

Figure 6.13: ATR-FTIR spectra of bare WE43 and PPy/WE43 before and after 120 h of immersion in m-SBF.

6.4.6 Corrosion mechanism

On the basis of the experimental results presented in this work and the available literature, the following corrosion mechanism is proposed for PPy/WE43 Mg alloy (Figure 6.14):

Stage 1 (1-8 h), Figure 6.14a. Initial Mg alloy substrate corrosion occurs through two simultaneous processes: 1) water penetration through the coating pores, leading to electrochemical and chemical corrosion, according to reactions 6.1-6.3 and, 2) electrochemical reduction of PPy, according to reaction 6.9. Adsorption of dissolved CO_2 species on the PPy coating leads to a decrease in the PPy conductivity, hindering charge transfer through the coating layer. The corrosion-induced increase in the local pH leads to formation of a $MgO/Mg(OH)_2$ corrosion layer (reaction 6.5) with increasing protective properties, as evidenced by the increase in R_1 (Figure 6.10a, circles) and OCP (Figure 6.4). The release of salicylate ions during PPy reduction may contribute to the stability of the formed corrosion layer. Transport of Mg^{2+} and OH^- ions through the coating layer and its diffusion to the bulk electrolyte lead to an increase in the electrolyte Mg^{2+} concentration (Figure 6.11, black squares) and pH (Figure 6.4), promoting the deposition of phosphate-containing corrosion products.

Stage 2 (8-24 h), Figure 6.14b. The corrosion layer reached quasi-constant barrier properties, as evidenced by the relative stabilization of the OCP values (Figure 6.4). The release of CO_2 into the atmosphere (reaction 6.7) and the resulting decrease in the concentration of dissolved CO_2, lead to recovery of the PPy coating conductivity, allowing for increased charge transport through the coating layer. Under these

conditions, formation of a substrate/coating galvanic couple occurs, as evidenced by the more negative OCP observed for PPy/WE43 with respect to the bare electrode. Formation of a galvanic element leads to increased substrate corrosion, as evidenced by the decrease in R_1, observed at 24 h. Substrate corrosion through reaction 6.9 is accompanied by oxygen reduction at the coating/electrolyte interface, leading to re-oxidation of PPy (reaction 10) and thereby, establishing a flow of electrons from the substrate to the coating/electrolyte interface.

Stage 3 (24-32 h), Figure 6.14c. After electrolyte renewal, the increase in the concentration of dissolved CO_2 leads to an increase in the surface coverage of adsorbed CO_2, decreasing the coating conductivity and hindering electron transport through the coating layer. Hence, coating positive charging occurs due to uncompensated Mg^{2+} ions uptake. As a result, a misalignment of the substrate and coating Fermi levels occurs, leading to substrate/coating decoupling, as evidenced by the increase in OCP, at 26 h, to potential values similar to those observed for the corroded bare sample (Figure 6.4). Substrate/coating decoupling leads to an increase in the corrosion resistance, as evidenced by the increase in R_1 (Figure 6.10a). Inhibition of the flow of Mg^{2+} ions by the established electric field might also contribute to the observed corrosion resistance increase. Recovering of the coating conductivity due to the decreasing CO_2 electrolyte concentration reactivates the flow of electrons through the PPy coating, leading to a decrease in OCP and R_1.

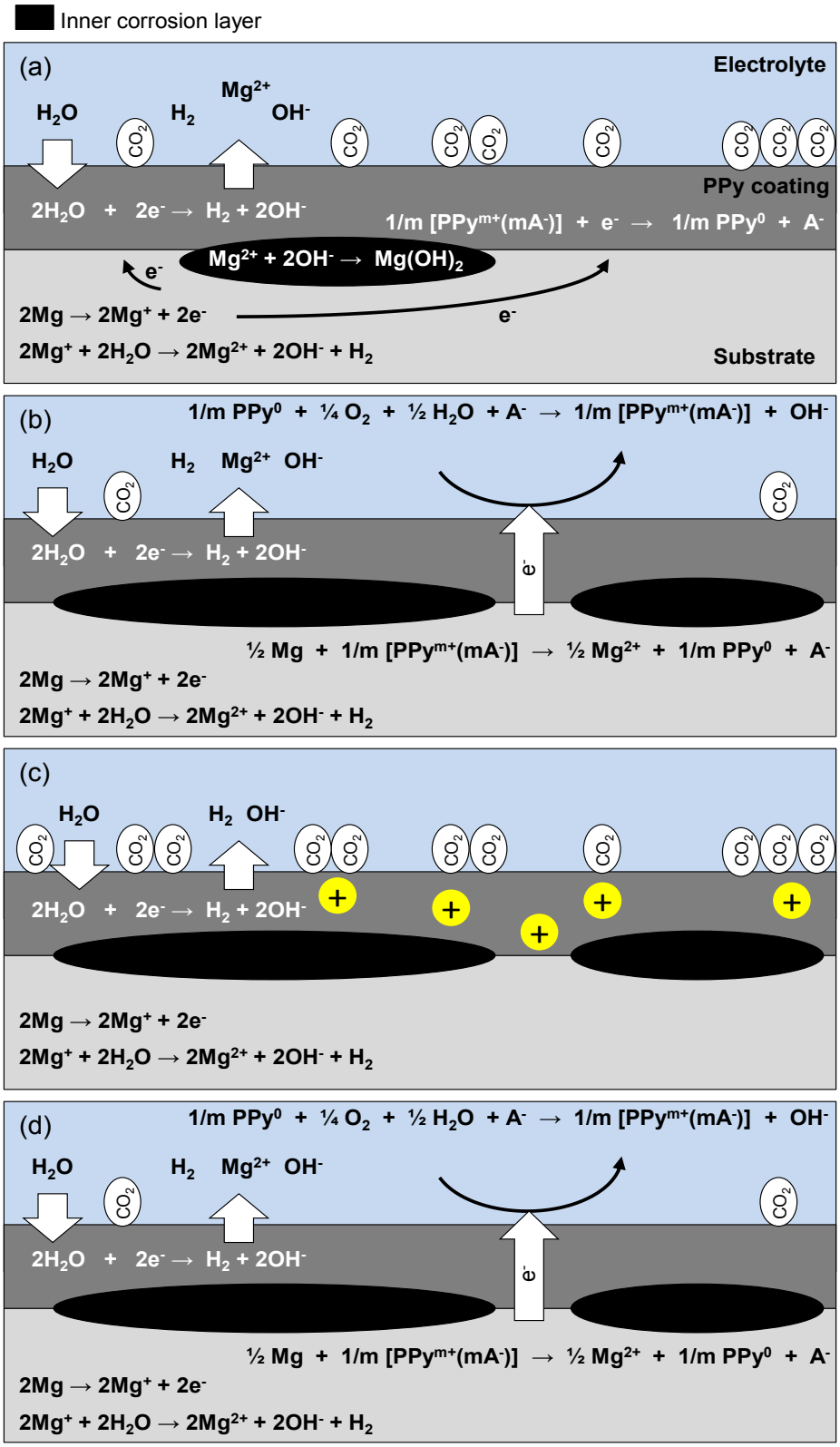
Inner corrosion layer
(a)
Electrolyte
H2O
H2
Mg2+
OH-
CO2
2H2O + 2e- → H2 + 2OH-
1/m [PPym+(mA-)] + e- → 1/m PPy0 + A-
PPy coating
Mg2+ + 2OH- → Mg(OH)2
e-
2Mg → 2Mg+ + 2e-
2Mg+ + 2H2O → 2Mg2+ + 2OH- + H2
Substrate
(b)
1/m PPy0 + ¼ O2 + ½ H2O + A- → 1/m [PPym+(mA-)] + OH-
½ Mg + 1/m [PPym+(mA-)] → ½ Mg2+ + 1/m PPy0 + A-
(c)
(d)

Figure 6.14: Corrosion mechanism of PPy/WE43 in m-SBF with daily electrolyte renewal. (a) Right after immersion, CO_2 adsorption leads to decreased coating conductivity. Substrate corrosion occurs through: 1) electrochemical and chemical reaction with water and, 2) PPy coating partial reduction, leading to formation of an insulating corrosion layer with increasing coverage; (b) At 24 h, the corrosion layer has reached quasi-constant coverage. Before electrolyte renewal, decreased electrolyte CO_2 concentration leads to recovery of the coating conductivity allowing for increased charge transport and formation of a substrate/coating galvanic couple. Oxygen reduction at the coating/electrolyte interface drives PPy re-oxidation; (c) After electrolyte renewal, decreased coating conductivity by CO_2 adsorption leads to decreased electronic transport, misalignment of the substrate/coating Fermi levels and substrate/coating decoupling, decreasing the substrate corrosion and hindering the flow of Mg^{2+} cations by the established electric field; and (d) At 48 h, before electrolyte renewal, decreased electrolyte CO_2 concentration leads to recovery of the coating conductivity, restoring the system conditions in (b). The corrosion behaviour observed at longer immersion times, up to 120 h, corresponds to a repetition of stages (3) and (4), with the corrosion rate ultimately controlled by the conductivity of the PPy coating and thus, by the CO_2 electrolyte concentration.

Stage 4 (32-48 h), Figure 6.14d. At 48 h, just before electrolyte renewal, recovery of the PPy coating conductivity and the corresponding increase in charge transport, restore the system semi-equilibrium conditions described in (2). Substrate corrosion is thus enhanced by the established substrate/coating galvanic couple; with the corrosion process involving the transport of electrons from the substrate to the coating/electrolyte interface, where reduction of dissolved oxygen takes place. The corrosion behaviour observed at longer immersion times, up to 120 h, corresponds to a repetition of stages (3) and (4), with the corrosion rate ultimately controlled by the conductivity of the PPy coating and thus, by the CO_2 electrolyte concentration.

6.5 CONCLUSIONS

PPy coatings were successfully synthesized on WE43 Mg alloys by cyclic voltammetry in a sodium salicylate containing aqueous solution. Among the potential regions investigated, electropolymerization between 0-1.25 V produced the most suitable coatings in terms of protective properties and coating adhesion. Investigation of the corrosion mechanisms and kinetics of PPy/WE43 in m-SBF by electrochemical, hydrogen evolution and Mg electrolyte concentration techniques showed that the PPy coating effectively contributes to a decrease in the corrosion rate of WE43 Mg alloy and production of H_2 gas. Coating efficiency values calculated from the volume of produced H_2 gas are higher than those obtained from the concentration of dissolved Mg^{2+} species, supporting the participation of dissolved O_2 in the PPy re-oxidation process. An increase in the coating protective properties observed after electrolyte renewal can be attributed to: 1) a decrease in the coating conductivity by the adsorption of CO_2 species, and to 2) substrate/coating decoupling due to uncompensated coating positive charging and misalignment of the substrate and coating Fermi levels. Formation of a protective corrosion layer reached quasi-equilibrium at about 24 h, with the variation in the corrosion resistance at longer immersion times being mainly related to the change in the concentration of dissolved CO_2 after electrolyte renewal. In this regard, electrolyte renewal allows for better control of the concentration of corrosion products and relevant electrolyte components, resembling physiological homeostasis. In addition, electrolyte renewal provides information on the effect of sensitive electrolyte parameters such as pH and carbonates concentration on the alloy corrosion process. Finally, PPy coatings show attractive properties for tailoring the corrosion degradation of Mg alloys for

biomedical applications, from its combination of corrosion protection mechanisms to its ability for controlled dopant and drug release; however, optimization of coating properties such as adhesion and coating thickness are still required, as well as the investigation of the coating corrosion behaviour at longer immersion times.

6.6 REFERENCES

[1] N.E.L. Saris, E. Mervaala, H. Karppanen, J.A. Khawaja, A. Lewenstam, Magnesium: An update on physiological, clinical and analytical aspects, Clinica Chimica Acta, 294 (2000) 1-26.

[2] M.P. Staiger, A.M. Pietak, J. Huadmai, G. Dias, Magnesium and its alloys as orthopedic biomaterials: A review, Biomaterials, 27 (2006) 1728-1734.

[3] C. Fox, D. Ramsoomair, C. Carter, Magnesium: its proven and potential clinical significance, Southern medical journal, 94 (2001) 1195-1201.

[4] B. Heublein, R. Rohde, V. Kaese, M. Niemeyer, W. Hartung, A. Haverich, Biocorrosion of magnesium alloys: A new principle in cardiovascular implant technology?, Heart, 89 (2003) 651-656.

[5] N. Erdmann, N. Angrisani, J. Reifenrath, A. Lucas, F. Thorey, D. Bormann, A. Meyer-Lindenberg, Biomechanical testing and degradation analysis of MgCa0.8 alloy screws: A comparative in vivo study in rabbits, Acta Biomaterialia, 7 (2011) 1421-1428.

[6] N. Erdmann, A. Bondarenko, M. Hewicker-Trautwein, N. Angrisani, J. Reifenrath, A. Lucas, A. Meyer-Lindenberg, Evaluation of the soft tissue biocompatibility of MgCa0.8 and surgical steel 316L in vivo: A comparative study in rabbits, BioMedical Engineering OnLine, (2010) 63.

[7] M. Maeng, L.O. Jensen, E. Falk, H.R. Andersen, L. Thuesen, Negative vascular remodelling after implantation of bioabsorbable magnesium alloy stents in porcine coronary arteries: a randomised comparison with bare-metal and sirolimus-eluting stents, Heart, 95 (2009) 241-246.

[8] Y. Ren, J. Huang, B. Zhang, K. Yang, Preliminary study of biodegradation of AZ31B magnesium alloy, Frontiers of Materials Science in China, 1 (2007) 401-404.

[9] R. Waksman, R. Pakala, P.K. Kuchulakanti, R. Baffour, D. Hellinga, R. Seabron, F.O. Tio, E. Wittchow, S. Hartwig, C. Harder, R. Rohde, B. Heublein, A. Andreae, K.H. Waldmann, A. Haverich, Safety and efficacy of bioabsorbable magnesium alloy stents in porcine coronary arteries, Catheterization and Cardiovascular Interventions, 68 (2006) 607-617.

[10] R. Waksman, R. Pakala, T. Okabe, D. Hellinga, R. Chan, M.O. Tio, E. Wittchow, S. Hartwig, K.H. Waldmann, C. Harder, Efficacy and safety of absorbable metallic stents with adjunct intracoronary beta radiation in porcine coronary arteries, Journal of Interventional Cardiology, 20 (2007) 367-372.

[11] F. Witte, J. Fischer, J. Nellesen, H.A. Crostack, V. Kaese, A. Pisch, F. Beckmann, H. Windhagen, In vitro and in vivo corrosion measurements of magnesium alloys, Biomaterials, 27 (2006) 1013-1018.

[12] F. Witte, J. Fischer, J. Nellesen, C. Vogt, J. Vogt, T. Donath, F. Beckmann, In vivo corrosion and corrosion protection of magnesium alloy LAE442, Acta Biomaterialia, (2009).

[13] R. Erbel, C. Di Mario, J. Bartunek, J. Bonnier, B. de Bruyne, F.R. Eberli, P. Erne, M. Haude, B. Heublein, M. Horrigan, C. Ilsley, D. Böse, J. Koolen, T.F. Lüscher, N. Weissman, R. Waksman, Temporary scaffolding of coronary arteries with bioabsorbable magnesium stents: a prospective, non-randomised multicentre trial, Lancet, 369 (2007) 1869-1875.

[14] P. Peeters, M. Bosiers, J. Verbist, K. Deloose, B. Heublein, Preliminary results after application of absorbable metal stents in patients with critical limb ischemia, Journal of Endovascular Therapy, 12 (2005) 1-5.

[15] R. Waksman, R. Erbel, C. Di Mario, J. Bartunek, B. de Bruyne, F.R. Eberli, P. Erne, M. Haude, M. Horrigan, C. Ilsley, D. Bose, H. Bonnier, J. Koolen, T.F. Luscher, N.J. Weissman, P.-A. Investigators, Early- and long-term intravascular ultrasound and angiographic findings after bioabsorbable magnesium stent implantation in human coronary arteries, Jacc: Cardiovascular Interventions, 2 (2009) 312-320.

[16] M. Haude, R. Erbel, P. Erne, S. Verheye, H. Degen, D. Böse, P. Vermeersch, I. Wijnbergen, N. Weissman, F. Prati, R. Waksman, J. Koolen, Safety and performance of the drug-eluting absorbable metal scaffold (DREAMS) in patients with de-novo coronary lesions: 12 month results of the prospective, multicentre, first-in-man BIOSOLVE-I trial, The Lancet, 381 836-844.

[17] G.L. Song, A. Atrens, Corrosion mechanisms of magnesium alloys, Advanced Engineering Materials, 1 (1999) 11-33.

[18] G. Song, A. Atrens, Understanding magnesium corrosion. A framework for improved alloy performance, Advanced Engineering Materials, 5 (2003) 837-858.

[19] G. Song, A. Atrens, D.S. John, X. Wu, J. Nairn, The anodic dissolution of magnesium in chloride and sulphate solutions, Corrosion Science, 39 (1997) 1981-2004.

[20] G. Song, A. Atrens, D. Stjohn, J. Nairn, Y. Li, The electrochemical corrosion of pure magnesium in 1 N NaCl, Corrosion Science, 39 (1997) 855-875.

[21] Y. Zhang, C. Yan, F. Wang, W. Li, Electrochemical behavior of anodized Mg alloy AZ91D in chloride containing aqueous solution, Corrosion Science, 47 (2005) 2816-2831.

[22] X.B. Chen, N. Birbilis, T.B. Abbott, Review of Corrosion-Resistant Conversion Coatings for Magnesium and Its Alloys, Corrosion, 67 (2011) 035005-035001-035005-035016.

[23] C. Zhong, F. Liu, Y. Wu, J. Le, L. Liu, M. He, J. Zhu, W. Hu, Protective diffusion coatings on magnesium alloys: A review of recent developments, Journal of Alloys and Compounds, 520 (2012) 11-21.

[24] J.E. Gray, B. Luan, Protective coatings on magnesium and its alloys — a critical review, Journal of Alloys and Compounds, 336 (2002) 88-113.

[25] S. Pommiers, J. Frayret, A. Castetbon, M. Potin-Gautier, Alternative conversion coatings to chromate for the protection of magnesium alloys, Corrosion Science, 84 (2014) 135-146.

[26] H. Hornberger, S. Virtanen, A.R. Boccaccini, Biomedical coatings on magnesium alloys – A review, Acta Biomaterialia, 8 (2012) 2442-2455.

[27] S. Feliu Jr, A. Samaniego, V. Barranco, A.A. El-Hadad, I. Llorente, P. Adeva, The effect of low temperature heat treatment on surface chemistry and corrosion resistance of commercial magnesium alloys AZ31 and AZ61 in 0.6 M NaCl solution, Corrosion Science, 80 (2014) 461-472.

[28] M.-J. Wang, C.-F. Li, S.-K. Yen, Electrolytic MgO/ZrO2 duplex-layer coating on AZ91D magnesium alloy for corrosion resistance, Corrosion Science, 76 (2013) 142-153.

[29] X.B. Chen, N. Birbilis, T.B. Abbott, A simple route towards a hydroxyapatite–Mg(OH)2 conversion coating for magnesium, Corrosion Science, 53 (2011) 2263-2268.

[30] L. Chang, L. Tian, W. Liu, X. Duan, Formation of dicalcium phosphate dihydrate on magnesium alloy by micro-arc oxidation coupled with hydrothermal treatment, Corrosion Science, 72 (2013) 118-124.

[31] G. Liu, S. Tang, D. Li, J. Hu, Self-adjustment of calcium phosphate coating on micro-arc oxidized magnesium and its influence on the corrosion behaviour in simulated body fluids, Corrosion Science, 79 (2014) 206-214.

[32] R.-C. Zeng, F. Zhang, Z.-D. Lan, H.-Z. Cui, E.-H. Han, Corrosion resistance of calcium-modified zinc phosphate conversion coatings on magnesium–aluminium alloys, Corrosion Science, 88 (2014) 452-459.

[33] T.F. da Conceição, N. Scharnagl, W. Dietzel, K.U. Kainer, Controlled degradation of a magnesium alloy in simulated body fluid using hydrofluoric acid treatment followed by polyacrylonitrile coating, Corrosion Science, 62 (2012) 83-89.

[34] M. Carboneras, M.C. García-Alonso, M.L. Escudero, Biodegradation kinetics of modified magnesium-based materials in cell culture medium, Corrosion Science, 53 (2011) 1433-1439.

[35] K.Y. Chiu, M.H. Wong, F.T. Cheng, H.C. Man, Characterization and corrosion studies of fluoride conversion coating on degradable Mg implants, Surface and Coatings Technology, 202 (2007) 590-598.

[36] A. Alabbasi, S. Liyanaarachchi, M.B. Kannan, Polylactic acid coating on a biodegradable magnesium alloy: An in vitro degradation study by electrochemical impedance spectroscopy, Thin Solid Films, 520 (2012) 6841-6844.

[37] L. Xu, A. Yamamoto, In vitro degradation of biodegradable polymer-coated magnesium under cell culture condition, Applied Surface Science, 258 (2012) 6353-6358.

[38] L. Xu, A. Yamamoto, Characteristics and cytocompatibility of biodegradable polymer film on magnesium by spin coating, Colloids and Surfaces B: Biointerfaces, 93 (2012) 67-74.

[39] M. Park, J. Lee, C. Park, S. Lee, H. Seok, Y. Choy, Polycaprolactone coating with varying thicknesses for controlled corrosion of magnesium, J Coat Technol Res, 10 (2013) 695-706.

[40] J. Degner, F. Singer, L. Cordero, A.R. Boccaccini, S. Virtanen, Electrochemical investigations of magnesium in DMEM with biodegradable polycaprolactone coating as corrosion barrier, Applied Surface Science, 282 (2013) 264-270.

[41] J. Zhang, C.-S. Dai, J. Wei, Z.-H. Wen, Study on the bonding strength between calcium phosphate/chitosan composite coatings and a Mg alloy substrate, Applied Surface Science, 261 (2012) 276-286.

[42] B.-D. Hahn, D.-S. Park, J.-J. Choi, J. Ryu, W.-H. Yoon, J.-H. Choi, H.-E. Kim, S.-G. Kim, Aerosol deposition of hydroxyapatite–chitosan composite coatings on

biodegradable magnesium alloy, Surface and Coatings Technology, 205 (2011) 3112-3118.

[43] S. Geetha, C.R.K. Rao, M. Vijayan, D.C. Trivedi, Biosensing and drug delivery by polypyrrole, Analytica Chimica Acta, 568 (2006) 119-125.

[44] L. Valero, J. Arias-Pardilla, J. Cauich-Rodríguez, M.A. Smit, T.F. Otero, Characterization of the movement of polypyrrole–dodecylbenzenesulfonate–perchlorate/tape artificial muscles. Faradaic control of reactive artificial molecular motors and muscles, Electrochimica Acta, 56 (2011) 3721-3726.

[45] X. Cui, V.A. Lee, Y. Raphael, J.A. Wiler, J.F. Hetke, D.J. Anderson, D.C. Martin, Surface modification of neural recording electrodes with conducting polymer/biomolecule blends, Journal of Biomedical Materials Research, 56 (2001) 261-272.

[46] M. Brett Runge, M. Dadsetan, J. Baltrusaitis, A.M. Knight, T. Ruesink, E.A. Lazcano, L. Lu, A.J. Windebank, M.J. Yaszemski, The development of electrically conductive polycaprolactone fumarate–polypyrrole composite materials for nerve regeneration, Biomaterials, 31 (2010) 5916-5926.

[47] A. Ramanavičius, A. Ramanavičienė, A. Malinauskas, Electrochemical sensors based on conducting polymer—polypyrrole, Electrochimica Acta, 51 (2006) 6025-6037.

[48] K. Kontturi, P. Pentti, G. Sundholm, Polypyrrole as a model membrane for drug delivery, Journal of Electroanalytical Chemistry, 453 (1998) 231-238.

[49] P. Deshpande, N. Jadhav, V. Gelling, D. Sazou, Conducting polymers for corrosion protection: a review, J Coat Technol Res, 11 (2014) 473-494.

[50] D. Tallman, G. Spinks, A. Dominis, G. Wallace, Electroactive conducting polymers for corrosion control, Journal of Solid State Electrochemistry, 6 (2002) 73-84.

[51] M. Rohwerder, Conducting polymers for corrosion protection: a review, International Journal of Materials Research, 100 (2009) 1331-1342.

[52] M. Rohwerder, A. Michalik, Conducting polymers for corrosion protection: What makes the difference between failure and success?, Electrochimica Acta, 53 (2007) 1300-1313.

[53] M.C. Turhan, M. Weiser, M.S. Killian, B. Leitner, S. Virtanen, Electrochemical polymerization and characterization of polypyrrole on Mg–Al alloy (AZ91D), Synthetic Metals, 161 (2011) 360-364.

[54] M.C. Turhan, M. Weiser, H. Jha, S. Virtanen, Optimization of electrochemical polymerization parameters of polypyrrole on Mg–Al alloy (AZ91D) electrodes and corrosion performance, Electrochimica Acta, 56 (2011) 5347-5354.

[55] A. Srinivasan, P. Ranjani, N. Rajendran, Electrochemical polymerization of pyrrole over AZ31 Mg alloy for biomedical applications, Electrochim Acta, 88 (2013) 310-321.

[56] M.C. Turhan, D. Rückle, M.S. Killian, H. Jha, S. Virtanen, Corrosion Behavior of Polypyrrole/AZ91D in Simulated Body Fluid Solutions and Its Functionalization with Albumin Monolayers, Corrosion, 68 (2012) 536-547.

[57] A. Oyane, H.M. Kim, T. Furuya, T. Kokubo, T. Miyazaki, T. Nakamura, Preparation and assessment of revised simulated body fluids, Journal of Biomedical Materials Research - Part A, 65 (2003) 188-195.

[58] Y.F. Jiang, X.W. Guo, Y.H. Wei, C.Q. Zhai, W.J. Ding, Corrosion protection of polypyrrole electrodeposited on AZ91 magnesium alloys in alkaline solutions, Synthetic Metals, 139 (2003) 335-339.

[59] A.C. Cascalheira, S. Aeiyach, J. Aubard, P.C. Lacaze, L.M. Abrantes, Electropolymerization of Pyrrole on Oxidizable Metals: Role of Salicylate Ions in the Anodic Behavior of Copper, Russian Journal of Electrochemistry, 40 (2004) 294-298.

[60] J. Petitjean, S. Aeiyach, J.C. Lacroix, P.C. Lacaze, Ultra-fast electropolymerization of pyrrole in aqueous media on oxidizable metals in a one-step process, Journal of Electroanalytical Chemistry, 478 (1999) 92-100.

[61] J. Colucci, V. Montalvo, R. Hernandez, C. Poullet, Electrochemical oxidation potential of photocatalyst reducing agents, Electrochimica Acta, 44 (1999) 2507-2514.

[62] K. Kratochvilová, I. Hoskovcová, J. Jirkovský, J. Klíma, J. Ludvík, A spectroelectrochemical study of chemisorption, anodic polymerization and degradation of salicylic acid on conductor and TiO2 surfaces, Electrochimica Acta, 40 (1995) 2603-2609.

[63] S. Asavapiriyanont, G.K. Chandler, G.A. Gunawardena, D. Pletcher, The electrodeposition of polypyrrole films from aqueous solutions, Journal of Electroanalytical Chemistry and Interfacial Electrochemistry, 177 (1984) 229-244.

[64] T.F. Otero, C. Santamaría, Dependence of polypyrrole production on potential, Synthetic Metals, 51 (1992) 313-319.

[65] D.A. Kaplin, S. Qutubuddin, Electrochemically synthesized polypyrrole films: effects of polymerization potential and electrolyte type, Polymer, 36 (1995) 1275-1286.

[66] M. Ascencio, M. Pekguleryuz, S. Omanovic, An investigation of the corrosion mechanisms of WE43 Mg alloy in a modified simulated body fluid solution: The effect of electrolyte renewal, Corrosion Science, 91 (2015) 297-310.

[67] A. Yamamoto, S. Hiromoto, Effect of inorganic salts, amino acids and proteins on the degradation of pure magnesium in vitro, Materials Science and Engineering C, 29 (2009) 1559-1568.

[68] J. Reut, A. Öpik, K. Idla, Corrosion behavior of polypyrrole coated mild steel, Synthetic Metals, 102 (1999) 1392-1393.

[69] T. Schauer, A. Joos, L. Dulog, C.D. Eisenbach, Protection of iron against corrosion with polyaniline primers, Progress in Organic Coatings, 33 (1998) 20-27.

[70] L. Zhong, S. Xiao, J. Hu, H. Zhu, F. Gan, Application of polyaniline to galvanic anodic protection on stainless steel in H2SO4 solutions, Corrosion Science, 48 (2006) 3960-3968.

[71] V.T. Truong, P.K. Lai, B.T. Moore, R.F. Muscat, M.S. Russo, Corrosion protection of magnesium by electroactive polypyrrole/paint coatings, Synthetic Metals, 110 (2000) 7-15.

[72] G. Williams, H.N. McMurray, Factors Affecting Acid-Base Stability of the Interface Between Polyaniline Emeraldine Salt and Oxide Covered Metal, Electrochemical and Solid-State Letters, 8 (2005) B42-B45.

[73] M. Rohwerder, L.M. Duc, A. Michalik, In situ investigation of corrosion localised at the buried interface between metal and conducting polymer based composite coatings, Electrochimica Acta, 54 (2009) 6075-6081.

[74] G. Baril, N. Pébère, Corrosion of pure magnesium in aerated and deaerated sodium sulphate solutions, Corrosion Science, 43 (2001) 471-484.

[75] G. Baril, G. Galicia, C. Deslouis, N. Pebere, B. Tribollet, V. Vivier, An Impedance Investigation of the Mechanism of Pure Magnesium Corrosion in Sodium Sulfate Solutions, Journal of the Electrochemical Society, 154 (2007) C108-C113.

[76] N. Pebere, C. Riera, F. Dabosi, Investigation of magnesium corrosion in aerated sodium sulfate solution by electrochemical impedance spectroscopy, Electrochimica Acta, 35 (1990) 555-561.

[77] R. Rettig, S. Virtanen, Time-dependent electrochemical characterization of the corrosion of a magnesium rare-earth alloy in simulated body fluids, Journal of Biomedical Materials Research - Part A, 85 (2008) 167-175.

[78] F. Zucchi, V. Grassi, A. Frignani, C. Monticelli, G. Trabanelli, Electrochemical behaviour of a magnesium alloy containing rare earth elements, Journal of Applied Electrochemistry, 36 (2006) 195-204.

[79] J.J. Miasik, A. Hooper, B.C. Tofield, Conducting polymer gas sensors, Journal of the Chemical Society, Faraday Transactions 1: Physical Chemistry in Condensed Phases, 82 (1986) 1117-1126.

[80] S.A. Waghuley, S.M. Yenorkar, S.S. Yawale, S.P. Yawale, Application of chemically synthesized conducting polymer-polypyrrole as a carbon dioxide gas sensor, Sensors and Actuators B: Chemical, 128 (2008) 366-373.

[81] J.L. Yagüe, S. Borrós, Conducting Plasma Polymerized Polypyrrole Thin Films as Carbon Dioxide Gas Sensors, Plasma Processes and Polymers, 9 (2012) 485-490.

[82] J.B. Jorcin, M.E. Orazem, N. Pébère, B. Tribollet, CPE analysis by local electrochemical impedance spectroscopy, Electrochimica Acta, 51 (2006) 1473-1479.

[83] N. Onnela, V. Savolainen, M. Hiltunen, M. Kellomaki, J. Hyttinen, Impedance spectra of polypyrrole coated platinum electrodes, in: Engineering in Medicine and Biology Society (EMBC), 2013 35th Annual International Conference of the IEEE, 2013, pp. 539-542.

[84] M.A. Vorotyntsev, L.I. Daikhin, M.D. Levi, Modelling the impedance properties of electrodes coated with electroactive polymer films, Journal of Electroanalytical Chemistry, 364 (1994) 37-49.

[85] L. Wang, G.H. Nancollas, Calcium orthophosphates: crystallization and dissolution, Chemical Reviews, (2008) 4628-4669.

[86] M. Ascencio, M. Pekguleryuz, S. Omanovic, An investigation of the corrosion mechanisms of WE43 Mg alloy in a modified simulated body fluid solution: The influence of immersion time, Corrosion Science, 87 (2014) 489-503.

[87] M. Bornapour, N. Muja, D. Shum-Tim, M. Cerruti, M. Pekguleryuz, Biocompatibility and biodegradability of Mg–Sr alloys: The formation of Sr-substituted hydroxyapatite, Acta Biomaterialia, 9 (2013) 5319-5330.

[88] R. Rettig, S. Virtanen, Composition of corrosion layers on a magnesium rare-earth alloy in simulated body fluids, Journal of Biomedical Materials Research - Part A, 88 (2009) 359-369.

[89] M.I. Jamesh, G. Wu, Y. Zhao, D.R. McKenzie, M.M.M. Bilek, P.K. Chu, Electrochemical corrosion behavior of biodegradable Mg–Y–RE and Mg–Zn–Zr alloys in Ringer's solution and simulated body fluid, Corrosion Science, 91 (2015) 160-184.

[90] D. Lee, P.N. Kumta, Chemical synthesis and characterization of magnesium substituted amorphous calcium phosphate (MG-ACP), Materials Science and Engineering: C, 30 (2010) 1313-1317.

[91] Z. Jiang, D. Ge, W. Shi, Q. Zhang, Apatite/polypyrrole composite prepared by a biomimetic process, Synthetic Metals, 151 (2005) 152-155.

[92] R.G. Davidson, T.G. Turner, An IR spectroscopic study of the electrochemical reduction of polypyrrole doped with dodecylsulfate anion, Synthetic Metals, 72 (1995) 121-128.

[93] X. Cui, X. Huang, Y. He, L. Dai, S. Wang, Y. Sun, W. Shi, D. Ge, Cathodic protection: A new strategy to enable the formation of nanostructured polypyrrole on magnesium, Synthetic Metals, 195 (2014) 97-101.

[94] L.M. Martins dos Santos, J.C. Lacroix, K.I. Chane-Ching, A. Adenier, L.M. Abrantes, P.C. Lacaze, Electrochemical synthesis of polypyrrole films on copper electrodes in acidic and neutral aqueous media, Journal of Electroanalytical Chemistry, 587 (2006) 67-78.

Chapter 7

Conclusions

The objective of this PhD study was to investigate the time-dependent corrosion behaviour of bare and polypyrrole-coated WE43 Mg alloy at *in vitro* experimental conditions partially resembling the physiological environment. It also aimed to investigate the effect of electrolyte renewal, as a method to better simulate physiological homeostasis, on the corrosion behaviour of bare and polypyrrole-coated WE43 Mg alloys. WE43 Mg alloy was selected as a model alloy due to its good corrosion resistance, which led to its use in clinical applications for the development of cardiovascular stents. WE43 Mg alloy is thus an important reference often used as a control in the investigation of the corrosion behaviour of Mg-based biodegradable materials. Immersion experiments were performed for a time period up to five days in a modified simulated body fluid (m-SBF) solution with an ionic composition similar to that of blood plasma. The m-SBF had a temperature of 37 ºC and an initial pH of 7.4, corresponding to the physiological values. Daily electrolyte renewal was performed in an attempt to better control the accumulation of corrosion products and the increase in electrolyte pH as a result of the corrosion process. The corrosion kinetics and mechanisms were investigated by electrochemical, hydrogen evolution and analytical techniques. The composition, morphology and thickness of the corrosion products layer were investigated by a variety of surface characterization techniques. Polypyrrole was selected as a coating material due to its well-known biocompatibility, its interesting

corrosion protection mechanisms and its drug-loading and surface-functionalization capabilities.

The following main conclusions can be drawn from the present study:

7.1 Corrosion kinetics and mechanisms of WE43 Mg alloy in a modified simulated body fluid (m-SBF) solution

i. Normalized corrosion rate values calculated from EIS, hydrogen evolution and ICP-OES data showed a relatively good agreement. An initial decrease in the corrosion rate of WE43 was attributed to formation of a corrosion layer with increasing protective properties, while an increase in the corrosion rate observed after 48 h was related to rupture of the corrosion layer and onset of a localized corrosion process.

ii. Despite the use of the buffering reagent HEPES, the electrolyte pH increased from an initial value of 7.4 to a final value of 8.2, after five days of immersion. The observed pH increase was attributed to the combined effect of the production of OH^- species (i.e. removal of H^+ as H_2 and the corresponding relative increase in OH^-) by the corrosion process and the decrease in the concentration of carbonates by the release of CO_2 gas to the atmosphere.

iii. Electrolyte analysis by ICP-OES after five days of immersion revealed an increase in the electrolyte concentration of Mg species from ca. 34 ppm to ca. 198 ppm, as a result of the corrosion process, and a decrease in the concentration of Ca and P species from ca. 103 ppm to ca. 54 ppm and from

ca. 27 ppm to ca. 11 ppm, respectively. The latter can be attributed to formation of insoluble Ca and P compounds forming part of the corrosion layer and to formation of precipitates in the bulk solution.

iv. A gradual decrease in the production of hydrogen gas observed during the first 48 h was attributed to formation of a corrosion layer with increasing protective properties, while the increase in hydrogen production at longer times was related to an increase in the substrate exposed area by the formation and growth of pits.

v. Analysis of the corrosion layer composition by EDS, XRD, ATR-FTIR and XPS revealed the presence of an amorphous carbonated apatite/$MgOH_2$ mixed corrosion layer.

vi. Analysis of the corrosion layer by SEM after different immersion times revealed a 'cracked-mud' surface morphology and the presence of rounded 'volcano-like' precipitates, which correspond to underlying cathodic regions. After five days of immersion, large pits with a length of about 2-4 μm, partially filled with corrosion products, were observed. Cross-sectional observation of the corroded sample revealed a non-uniform corrosion layer with a thickness in the range of 15-40 μm.

vii. The observed changes in the shape of the EIS response on the complex plane (Nyquist plot) after different immersion times were related to the presence of four corrosion stages with a changing corrosion mechanism.

viii. Four corrosion stages were proposed: a) (1-8 h) Substrate oxidation with formation of adsorbed Mg^+ intermediates and production of hydrogen gas.

This is accompanied by the formation of a carbonated apatite/$Mg(OH)_2$ corrosion layer with a growing thickness; b) (8-32 h) The increase in the corrosion layer protective ability leads to decreased water access to the substrate. Dehydration of the $Mg(OH)_2$ inner layer leads to formation of a MgO protective film with increasing coverage; c) (32-72 h) The increase in the MgO barrier film coverage leads to quasi-equilibrium conditions. The presence of aggressive Cl^- ions leads to local dissolution of the corrosion layer and onset of a localized corrosion process, i.e., formation of pits; and d) (72- 120 h) Increased corrosion rate and hydrogen production due to growth of pits.

7.2 Effect of electrolyte renewal on the corrosion kinetics and mechanisms of WE43 Mg alloy in a modified simulated body fluid (m-SBF) solution

i. Normalized corrosion rate values calculated from EIS, hydrogen evolution and ICP-OES data showed a relatively good agreement. An initial decrease in the corrosion rate was attributed to formation of a corrosion layer with increasing protective properties, while the increase in the corrosion rate observed after 72 h by ICP-OES was attributed to onset of a localized corrosion process.

ii. The increase in the corrosion layer protective properties with time is proposed to occur through the formation of an inner MgO barrier film with increasing coverage, underneath the $Mg(OH)_2$ corrosion layer.

iii. It was found that electrolyte renewal leads to a temporary decrease in the protective properties of the corrosion layer, as evidenced by the decrease in

OCP, charge transfer resistance (R_1) and diffusion resistance (R_2), and by the increase in the production rate of hydrogen gas observed after electrolyte renewal.

iv. SEM analysis revealed the dissolution/rupture of volcano-like precipitates after electrolyte renewal, which was attributed to local dissolution of calcium phosphate deposits as a result of the decrease in the electrolyte pH and concentration of Mg^{2+} species.

v. It was shown that electrolyte renewal affects the corrosion mechanism by promoting partial dissolution of the corrosion layer and by increasing mass transport through the corrosion layer, thereby delaying the increase in the MgO barrier film coverage and the occurrence of localized corrosion.

vi. The decreasing effect of electrolyte renewal with time on the protective properties of the corrosion layer was attributed to the corrosion layer thickening and increased MgO barrier film coverage at longer immersion times.

vii. It was demonstrated that variations in the electrolyte pH and in the concentration of relevant electrolyte components, such as calcium, phosphate and carbonate species, can be better controlled by performing electrolyte renewal, thereby better simulating physiological homeostasis with respect to stagnant immersion experiments (Chapter 4).

viii. Analysis of the corrosion layer by ATR-FTIR, XRD, SEM and EDS showed no significant variation in the corrosion layer morphology and composition with respect to the results obtained without electrolyte renewal (Chapter 4).

Cross-sectional analysis of the corroded sample revealed a corrosion layer with a thickness varying in the range of 25-140 μm. The observed thicker corrosion layer, with respect to the results obtained without electrolyte renewal (15-40 μm), can be attributed to increased mass transport as a result of the corrosion layer partial dissolution after electrolyte renewal.

ix. Corrosion rate values obtained with electrolyte renewal follow a similar trend to those obtained without electrolyte renewal (Chapter 4); however, the latter showed an earlier increase in the corrosion rate due to onset of localized corrosion.

x. The effect of electrolyte renewal on the overall corrosion behaviour of WE43 Mg alloy in m-SBF is small, compared to stagnant immersion conditions; however, this effect is expected to be larger in the presence of a continuous electrolyte flow with constant electrolyte renewal. This is demonstrated in the appendix of this thesis, where results on the corrosion behaviour of WE43 Mg alloy under continuous flow conditions are presented.

7.3 Corrosion behaviour of polypyrrole-coated WE43 Mg alloy in a modified simulated body fluid (m-SBF) solution with daily electrolyte renewal

i. PPy coatings were successfully synthesized on WE43 Mg alloy by cyclic voltammetry in a sodium salicylate containing solution. Among the potential regions investigated, electropolymerization in the region from 0 to 1.25 V vs. SCE produced the most suitable coatings in terms of coating adhesion and protective properties.

ii. Analyses by SEM and ATR-FTIR showed the presence of a PPy coating with a globular morphology and a thickness of 1.7 ± 0.2 μm.

iii. EIS, hydrogen evolution and ICP-OES results demonstrated that PPy coating effectively contributes to a decrease in the corrosion rate of WE43 Mg alloy in m-SBF and in the production of hydrogen gas during the time period investigated.

iv. It is proposed that substrate oxidation is accompanied by the reduction of PPy at the substrate/coating interface, and that PPy re-oxidation is driven by the reduction of oxygen at the coating/electrolyte interface, thereby establishing a flow of electrons from the substrate to the coating/electrolyte interface. The participation of oxygen in this process is supported by the higher coating corrosion protection efficiency values calculated from the volume of hydrogen produced, compared to the coating efficiency values calculated from the concentration of dissolved Mg^{2+} species.

v. It was demonstrated that a temporary increase in the EIS response and in the charge transfer resistance observed after every electrolyte renewal is related to the increase in the concentration of dissolved CO_2 in the m-SBF.

vi. An initial decrease in the corrosion rate was attributed to formation of a corrosion layer with increasing protective properties, reaching quasi-equilibrium at about 24 h. At longer immersion times, the variation in the corrosion resistance was related to the change in the concentration of dissolved CO_2 due to electrolyte renewal and the release of CO_2 gas to the atmosphere.

vii. The corrosion protection mechanisms of the PPy coating can be attributed to: i) the PPy coating barrier properties, and ii) the adsorption of dissolved CO_2 species on the PPy coating. It is proposed that reversible adsorption of CO_2 leads to a decrease in the PPy coating conductivity and to substrate/coating decoupling due to uncompensated coating positive charging and misalignment of the substrate and coating Fermi levels.

viii. SEM analysis of the corroded surface (that was not protected by PPy) after 5 days of immersion revealed a “cracked-mud” morphology with some globular precipitates on the surface, which were attributed to formation of amorphous calcium phosphates. On the other hand, the PPy/WE43 alloy showed a “cracked-mud” morphology without visible precipitates and with no sign of coating delamination.

ix. SEM analysis of the substrate morphology after dissolution of the corrosion products evidenced that the presence of the PPy coating leads to a more uniform corrosion process. Cross-sectional analysis of corroded samples revealed that the bare (uncoated) alloy had a corrosion layer with a thickness in the range of 20-50 μm, while the PPy/WE43 Mg alloy had a corrosion layer with a thickness in the range of 2-10 μm. The thinner corrosion layer observed for PPy/WE43 was related to the barrier properties of the PPy coating, which hinder water penetration and ionic transport.

x. It was shown that, in addition to allowing for better control of the electrolyte pH and variation in the concentration of electrolyte components, electrolyte renewal provides information on the effect of relevant electrolyte

parameters, such as variations in pH and the concentration of carbonate species, on the corrosion mechanisms.

Chapter 8

Original contributions and future work

8.1 Original contributions to knowledge

The following are the major contributions of this work:

i. A systematic investigation of the time dependence of the corrosion behaviour of WE43 Mg alloy in a m-SBF was performed for the first time.

ii. A four-stage corrosion mechanism was proposed taking into account the time dependence of the EIS fitting parameters, the corrosion kinetics and the surface characterization of the substrate and corrosion products. The proposed mechanism is in agreement with the formation of a protective dehydrated inner MgO film and the presence of adsorbed Mg intermediates at the film-free regions.

iii. A systematic investigation of the influence of electrolyte renewal on the corrosion kinetics and mechanisms of WE43 Mg alloy in m-SBF was performed for the first time.

iv. It was demonstrated that electrolyte renewal allows for better control of the electrolyte pH, accumulation of corrosion products and depletion of Ca and P species, thereby better simulating physiological homeostasis compared to traditional stagnant immersion experiments.

v. It was shown that electrolyte renewal affects the corrosion mechanism by promoting partial dissolution of the corrosion layer and by increasing mass

transport, thereby delaying the increase in the corrosion layer protective ability and the occurrence of localized corrosion.

vi. An investigation of the corrosion behaviour of polypyrrole-coated WE43 Mg alloy in m-SBF with daily electrolyte renewal was performed for the first time.

vii. It was shown that variations in the concentration of dissolved CO_2 species affect the corrosion mechanisms and kinetics of WE43 Mg alloy in m-SBF.

viii. It was proposed that reversible adsorption of CO_2 leads to a decrease in the PPy coating conductivity and to substrate/coating decoupling due to uncompensated coating positive charging and misalignment of the substrate and coating Fermi levels.

8.2 Suggestions for future work

The following aspects of research on the corrosion of WE43 Mg alloy for biodegradable applications are suggested:

i. It was shown that electrolyte renewal affects the corrosion mechanism of WE43 Mg alloy by promoting partial dissolution of the corrosion layer, thereby delaying the increase in the corrosion layer protective ability and the occurrence of localized corrosion. Consequently, it is recommended that the investigation of the corrosion behaviour of Mg alloys in a flow set-up that allows for continuous electrolyte renewal and thus, for a better control of the electrolyte pH and concentration of electrolyte components, be performed.

ii. It was shown that the release of CO_2 to the atmosphere leads to a decrease in the electrolyte concentration of carbonate species, which is accompanied by the

increase in the electrolyte pH. It is recommended that the customization of the experimental set-up is done in order to keep a constant concentration of dissolved CO_2, e.g., by the use of a CO_2 bubbler coupled to a pH controller, thereby better simulating physiological control of pH and avoiding the decrease in the concentration of CO_2.

iii. It was shown that the corrosion kinetics of Mg alloys can be monitored by EIS, ICP-OES and hydrogen evolution, with each technique having a limited accuracy. It is recommended that the customization of the experimental set-up be done in order to simultaneously measure the corrosion kinetics by the three previous techniques; in this way, more accurate and reliable corrosion rate values can be obtained. In addition, the relationship between the obtained values can provide information on the corrosion mechanisms, e.g., dominance of chemical or electrochemical reactions.

iv. It is proposed to gradually increase the complexity of the corrosive media to more closely emulate the physiological environment; first through the addition of biomolecules such as proteins, lipids and carbohydrates, and eventually through the addition of living cells.

v. Electrodeposited PPy coatings on WE43 Mg alloys showed a weaker adhesion at the sample upper edge (the sample was placed vertically during the electrodeposition) probably due to a non-uniform potential and current distribution. It is recommended to optimize the electrodeposition set-up to obtain a more uniform coating adhesion.

vi. It was proposed that adsorption of CO_2 onto the PPy coating leads to a decrease in the PPy conductivity, thereby increasing the Mg alloy corrosion resistance. It is recommended to further investigate the influence of CO_2 adsorption on PPy by using a non-corroding substrate, e.g. gold.

vii. The participation of oxygen in the corrosion process of PPy-coated WE43 Mg alloy is supported by the higher coating efficiency values obtained from hydrogen evolution measurements, compared to the efficiency values obtained from the concentration of dissolved Mg^{2+}. It is recommended to further investigate the influence of oxygen in the corrosion process by performing immersion experiments with a varying oxygen concentration, e.g., decreasing the concentration of oxygen by purging the electrolyte solution with argon gas.

viii. It is recommended to investigate the corrosion behaviour of PPy-coated WE43 Mg alloy in corroding medium with constant CO_2 concentration and for longer immersion times.

ix. It is recommended to investigate the effect of substrate pretreatments, e.g., etching and zinc plating, and coating functionalization, e.g., protein binding, on the corrosion behaviour of PPy-coated WE43 Mg alloy.

Appendix A

Corrosion behaviour of WE43 Mg alloy in a modified simulated body fluid solution under continuous flow conditions

M. Ascencio[1], M. Pekguleryuz[2] and S. Omanovic[1]

(1) Department of Chemical Engineering, (2) Department of Mining and Materials Engineering
McGill University, Montreal, Quebec, H3A 0C5, Canada

PREFACE

This chapter is comprised of a set of experimental results on the investigation of the corrosion behaviour of WE43 Mg alloy in a modified simulated body fluid (m-SBF) solution under continuous flow conditions. Representative results are presented and briefly discussed. The focus of this part of the study was to develop an immersion test platform with a continuous electrolyte flow that allowed for electrochemical measurements, investigate the corrosion behaviour of WE43 Mg alloy under continuous electrolyte flow conditions and compare the results with the corrosion behaviour obtained from static immersion experiments presented in Chapters 4-5. Immersion experiments under continuous flow conditions were performed for a time period up to 5 days at room temperature. Interfacial processes such as charge transfer, adsorption of Mg intermediates and diffusion of Mg^{2+} ions were investigated and monitored after different immersion times by electrochemical impedance spectroscopy (EIS). Concentration of Mg, Ca and P species in the electrolyte was determined after different

immersion times by ICP-OES. The corrosion products layer composition and morphology were investigated by SEM, EDS and ATR-FTIR.

The co-authors of the manuscript presented in this chapter are listed above. The contributions of each author were the following: Mario Ascencio designed the experiments, prepared samples, performed the experimental work, analyzed results and wrote the manuscript. Prof. Mihriban Pekguleryuz provided samples and contributed in the interpretation and discussion of results. Prof. Sasha Omanovic provided guidance, contributed in the interpretation and discussion of results and corrected the manuscript.

The authors gratefully acknowledge the financial support from the Natural Science and Engineering Research Council of Canada (NSERC) and the National Council of Science and Technology of Mexico (CONACyT). The contribution of Pierre Vermette in the casting of the Mg alloy samples is also acknowledged.

A.1 INTRODUCTION

The development of biodegradable Mg alloys is hampered by the lack of a complete understanding of the Mg alloy biodegradation mechanisms *in vivo* and by difficulties at emulating the physiological environment *in vitro*. As was shown in Chapters 4 and 5, traditional static immersion tests are often accompanied by an increase in the electrolyte pH above the physiological value, the accumulation of corrosion products such as Mg^{2+} ions and the depletion of relevant electrolyte components such as Ca and P, possibly affecting the Mg alloy corrosion mechanisms and leading to degradation behaviour results not closely representing those under real conditions, i.e. those

experienced by an implanted Mg alloy material. Test platforms to simulate the physiological shear stress to which stents are exposed after implantation in the coronary arteries have been developed [1, 2]. It was shown that the corrosion rate and corrosion mechanisms of AM60B-F Mg alloy in modified Hank's solution varied with the applied shear stress [2] and that the presence of circulating m-SBF increased the corrosion rate of a MgZn alloy, compared to results obtained from static immersion experiments [1]; however, little information has been provided regarding the Mg alloy corrosion mechanisms and the corresponding interfacial phenomena, such as charge transfer, under continuous flow conditions. Therefore, the objective of this work was to investigate the short-term corrosion behaviour and corrosion mechanisms of WE43 Mg alloy under continuous electrolyte flow conditions and compare the outcome with previous results obtained from traditional static immersion experiments and static immersion experiments with daily electrolyte renewal.

A.2 EXPERIMENTAL SECTION

Test samples with a final exposed area of 0.67 cm^2 were prepared from cast WE43 Mg alloy as indicated in section 4.3.1. Modified simulated body fluid (m-SBF) prepared as indicated in section 4.3.1 was used as electrolyte. The m-SBF was left in contact with air for 24 h to reach equilibrium prior to adjusting the electrolyte final pH to the physiological value of 7.4. A home-made test platform was designed (Figure A.1) to have an electrochemical cell (EC) with continuous inward and outward electrolyte flow, with a flow rate of 745 ml day^{-1}. A peristaltic pump (Cole-Parmer, Masterflex, USA) was used to induce the flow of "new" electrolyte from the reservoir to the EC and the "old" electrolyte coming out of the EC was collected in a separate container. A magnetic

stirrer was used at a low speed to increase the electrolyte concentration uniformity in the EC. The electrolyte-volume to surface-area ratio in the EC was 50 ml cm^{-2}. Immersion experiments were performed in triplicate, at room temperature (22 ºC) and for a period time up to 5 days.

Electrochemical measurements were carried out using a potentiostat/galvanostat (Autolab PGSTAT30, Netherlands) equipped with a frequency response analyser. WE43 Mg alloy samples were used as working electrode, a graphite rod as counter electrode and a commercial saturated calomel electrode (SCE, Fisher Scientific Accumet, USA) as reference electrode. All potentials in this chapter are referred to the SCE. Open circuit potential measurements were performed over a time period of 5 days. Electrochemical impedance spectroscopy (EIS) was used to investigate the kinetics and mechanisms of the alloy corrosion. EIS measurements were carried out at open circuit potential with AC amplitude of ±10 mV over the frequency range of 10 mHz to 100 kHz.

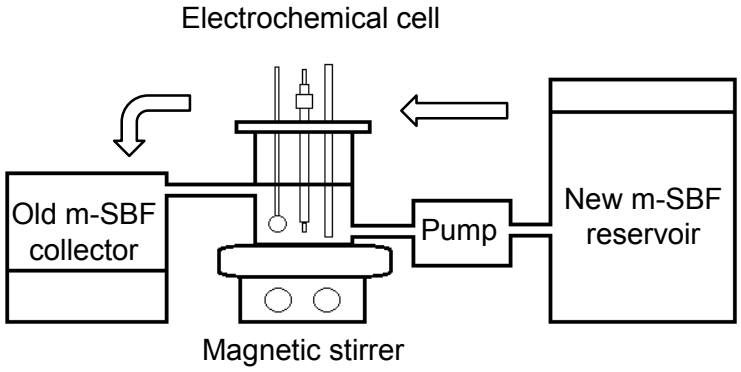

Figure A.1: Diagram of home-made test platform for corrosion experiments under continuous electrolyte flow conditions.

Inductively coupled plasma optical emission spectroscopy (ICP-OES, Thermo Jarrell Ash Trace Scan, USA) was used to measure the electrolyte concentration of magnesium, calcium and phosphate species at wavelengths of 285.2, 422 and 178.2 nm, respectively. The morphology and composition of the sample surface were characterised by scanning electron microscopy (FE-SEM, Philips XL-30, Netherlands) equipped with an energy-disperse spectrometer (EDS). The corrosion layer thickness was measured by cross-sectional SEM analysis of the sample. Attenuated total reflectance Fourier transform infrared spectroscopy (ATR-FTIR, Bruker Hyperion, USA) analysis was performed to investigate the presence of chemical groups in the corrosion product layers.

A.3 RESULTS AND DISCUSSION

Figure A.2 shows the open circuit potential (OCP) and pH time-dependent behaviour of the Mg alloy for a time period up to 5 days under continuous electrolyte flow conditions. A fast increase in the OCP during the first 24 h can be observed, followed by a slow increase at longer immersion times around a value of ca. -1.7 V vs. SCE. The observed increase in OCP can be related to formation of a protective $MgO/Mg(OH)_2$ layer with increasing protective properties over time. This process was accompanied by a slight increase in the electrolyte pH during the first 4 h (Figure A.2), from pH 7.4 to 7.5, followed by the attainment of the latter value at longer immersion times. The slight initial pH increase can be related to fast corrosion of the Mg alloy sample right after immersion, while the quasi-constant pH at longer immersion times can be related to attainment of a steady state, the sample corrosion contributing to the pH increase, and

the buffer and continuous electrolyte renewal counterbalancing such increase. The pH increase in the flow experiment in Figure A.2 is significantly lower than that recorded under stagnant electrolyte conditions (Figure 4.4b), which was to be expected due to the constant electrolyte refreshment (renewal) in the electrochemical cell.

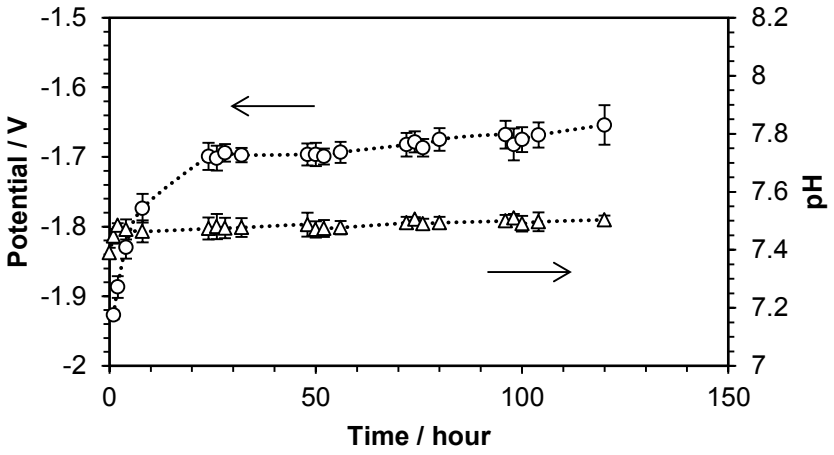

Figure A.2: Time-dependent open circuit potential (circles) and pH (triangles) behaviour of WE43 Mg alloy in m-SBF under continuous electrolyte flow conditions.

Figure A.3a shows the impedance response obtained after different immersion times up to 120 h. A progressive increase in the impedance response can be observed, which can be related to formation of a corrosion layer with increasing protective properties. Two capacitive loops at high and medium frequencies and one inductive loop at low frequencies can be observed at all immersion times, with only small changes in their relative size, suggesting no variations in the corrosion mechanism over time. The relationship between the shape of the impedance response and the corrosion mechanism was discussed in section 4.4.2. The shape of the impedance response after different immersion times was compared by normalizing the obtained spectra (Figure A.3b). Impedance normalization was done by subtracting the electrolyte resistance (R_e)

to the real part of the impedance and dividing the real and the imaginary parts of the impedance response by the maximum imaginary and real components, respectively, for each diagram. It can be seen that the overlaid spectra have a similar shape with an apparent decrease in the size of the inductive loop at longer immersion times.

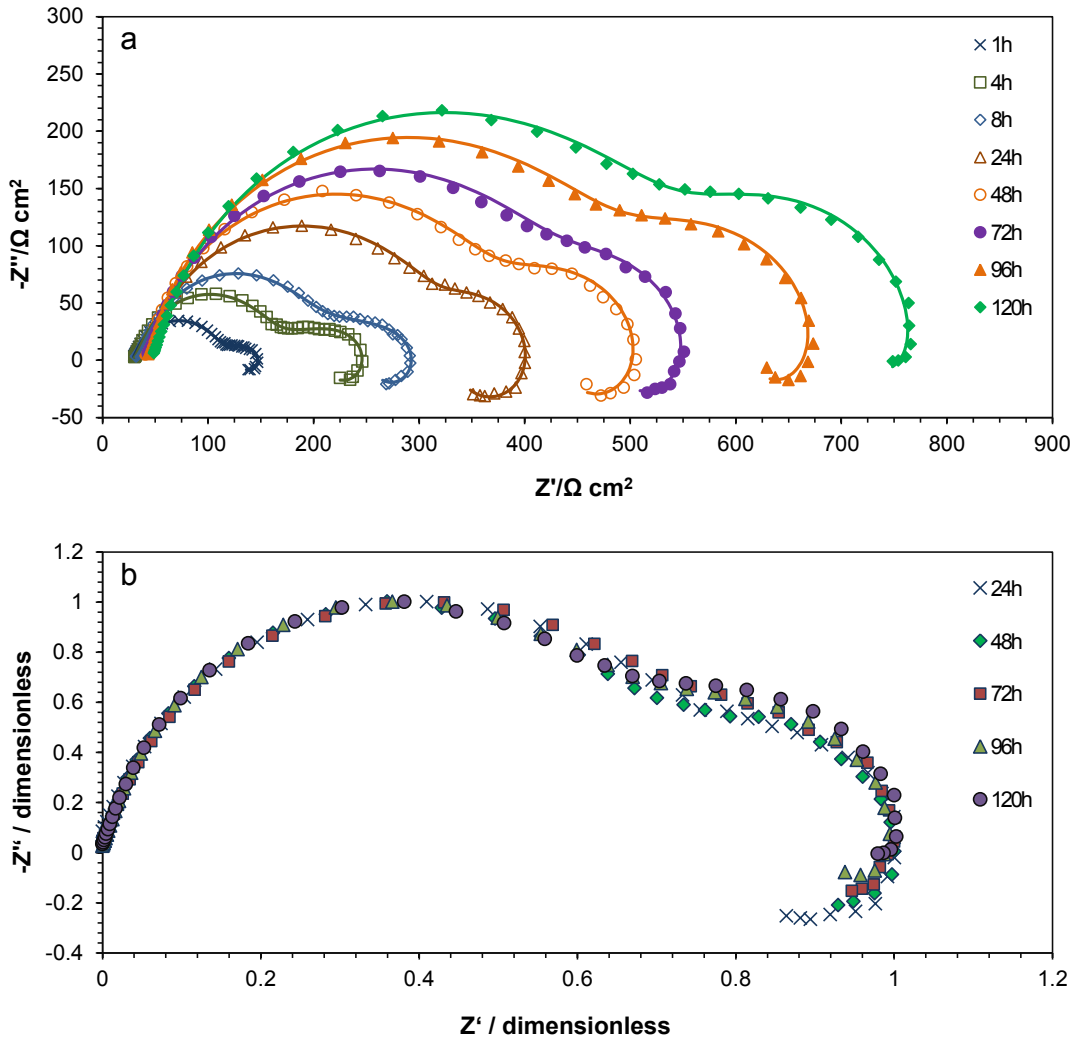

Figure A.3: EIS response of WE43 Mg alloy in m-SBF under continuous flow conditions (a) from 1-120 h, and (b) normalized values from 24-120 h. Symbols represent experimental values, whereas lines represent simulated spectra.

The observed increase in the impedance response can be related to formation of a barrier-type corrosion layer with increasing coverage over time. Based on the corrosion mechanisms proposed by Song et al. [3] and Baril et al. [4], the observed increase in the impedance response with time can be related to formation of an inner protective MgO passive film underneath a porous $Mg(OH)_2$ outer layer, with the corrosion reaction occurring at MgO-free areas. The gradual decrease in the size of the inductive loop with time can be related to a decrease in the MgO-free areas.

To better evaluate the time dependence of the Mg alloy charge transfer (R_1) and diffusion resistance (R_2) values, the impedance response obtained after different immersion times was fitted using an electrical equivalent circuit (EEC), as described in Chapter 4 (Figure 4.6). Continuous lines in Figure A.3a, corresponding to the modelled spectra, show a good agreement with the experimental data (symbols). Figure A.4 shows R_1 and R_2 time-dependent values. An increase in R_1 with time can be observed, faster during the first 4 h and slower at longer immersion times. R_1 values increase during the first 8 h and then fluctuate around a value of 140 Ω cm^2 at longer immersion times. The increase in R_1 over the complete immersion time indicates a continuous increase in the coverage of the MgO inner film, in contrast to the results obtained from immersion experiments with no electrolyte renewal (Chapters 4) and with daily electrolyte renewal (Chapter 5), where R_1 levelling off after 48 h and 72 h, respectively, was related to quasi-constant MgO coverage.

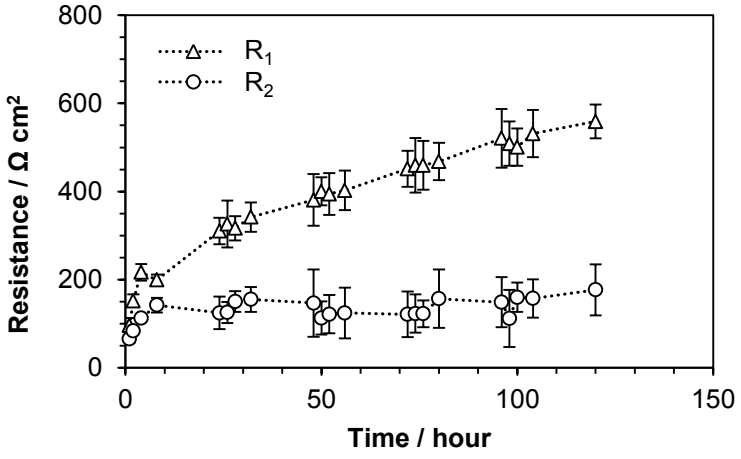

Figure A.4: Time dependent behaviour of the charge transfer resistance (R_1) and diffusion resistance (R_2) of WE43 Mg alloy in m-SBF under continuous flow conditions.

Figure A.5 shows the concentration of Mg, Ca and P in the electrochemical cell with continuous electrolyte flow as a function of time, measured by ICP-OES. A sharp increase in the Mg concentration right after immersion (the value at zero time refers to the amount of Mg species already present in the electrolyte before the sample immersion) can be related to the sample's fast initial corrosion rate, while its levelling off at longer immersion times can be related to attainment of the system steady state, in agreement with the pH behaviour (Figure A.2). No significant variation in the Ca and P concentration after different immersion times was observed, with values fluctuating around the initial electrolyte concentration (electrolyte concentration values without corroding sample). The stabilization of the pH and concentration of Mg, Ca and P after 24 h of immersion demonstrate the efficacy of the test platform with continuous electrolyte flow in maintaining a constant electrolyte concentration with time, thereby closer simulating physiological homeostasis compared with traditional static immersion experiments. The previous results are in contrast to electrolyte concentration values

obtained from static immersion experiments with no electrolyte renewal and daily electrolyte renewal, the former showing a fivefold increase in the Mg electrolyte concentration and a decrease in the Ca and P electrolyte concentration to respectively 53% and 41% with respect to the control, after five days of immersion (Figure 4.10a); and the latter showing a daily increase in the Mg electrolyte concentration in the range of 70-200% and a daily decrease in the concentration of Ca and P by about 87% and 75%, respectively, with respect to the control values (Figure 5.7).

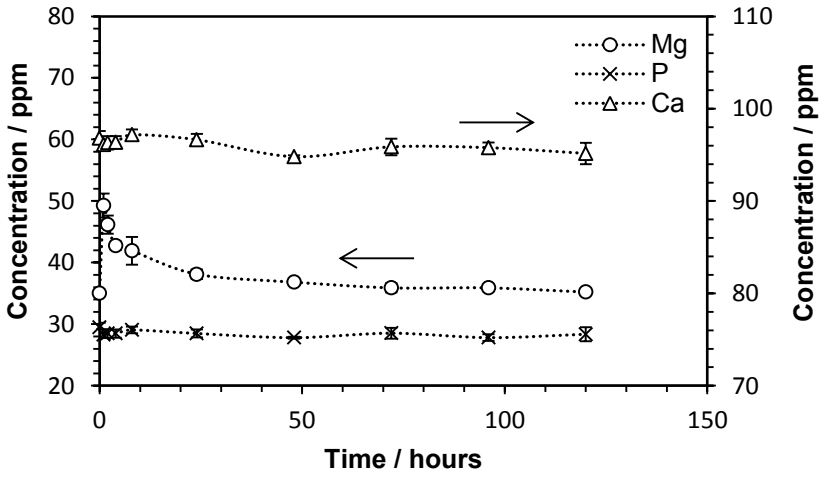

Figure A.5: Time dependent behaviour of daily Mg, P and Ca electrolyte concentration in the electrochemical cell with continuous electrolyte flow.

Characterization of a corroded WE43 Mg alloy sample by SEM after 5 days of dynamic degradation (Figure A.6a) revealed the presence of a cracked-mud surface morphology with no signs of corrosion layer break-down or localized corrosion. Cross-sectional observation of the corroded sample revealed a corrosion layer with a thickness in the range of 90-165 μm (Figure A.6b). Comparison of the measured corrosion layer thickness with values obtained from static immersion tests with no

electrolyte renewal (15-40 μm) in Chapter 4 (Figure 4.3), and static immersion tests with daily electrolyte renewal (25-140 μm) in Chapter 5 (Figure 5.11), indicate that the immersion experiment with continuous electrolyte flow leads to formation of a thicker corrosion layer.

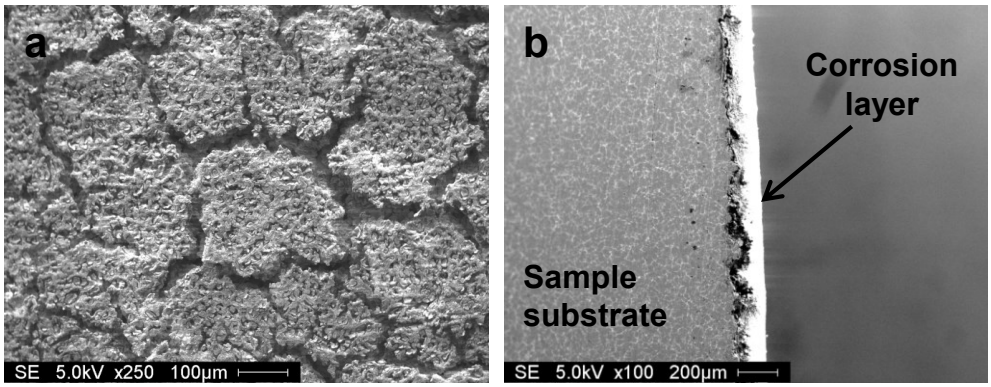

Figure A.6: SEM images of WE43 Mg alloy after 5 days of immersion in m-SBF under continuous flow conditions. (a) Corroded surface morphology and (b) sample cross-sectional view.

Analyses of the Mg alloy sample corroded surface by EDS and ATR-FTIR after 5 days of dynamic immersion revealed the presence of C, O, Na, Mg, P and Ca elements (Table A.1) and carbonate and phosphate functional groups (Figure A.7), respectively, suggesting the presence of a carbonated apatite $MgO/Mg(OH)_2$ mixed corrosion layer. These results are in agreement with the corrosion layer composition determined in static immersion experiments in Chapters 4-5 (Table A.1 and Figure A.7).

Figure A.8 shows the time-dependent charge transfer resistance (R_1) behaviour of WE43 Mg alloy from static immersion with no electrolyte renewal (Chapter 4), static immersion with daily electrolyte renewal (Chapter 5) and immersion with continuous electrolyte flow. Error bars were omitted for the sake of clarity. The behaviour of each

curve was previously described. Comparison of the time-dependent charge transfer behaviour from the different experimental set-ups investigated indicates that the immersion experiment with continuous electrolyte flow leads to a slower increase in the barrier-type corrosion layer surface coverage, compared to static immersion experiments, resulting in a higher corrosion rate. Regarding the corrosion mechanism, while static immersion experiments with daily electrolyte renewal led to a delay in the onset of localized corrosion, compared to experiments with no electrolyte renewal; no signs of localized corrosion were observed for the experiment with continuous electrolyte flow. The previous results indicate that the occurrence of localized corrosion is related to attainment of a “maximum” barrier-type corrosion layer surface coverage, above which pit formation takes place. In static immersion experiments with no electrolyte renewal, fast increase in the electrolyte pH and accumulation of dissolved Mg^{2+} ions lead to decreased mass transport, favouring the formation of a thinner corrosion layer with increased protective properties, which reaches the maximum barrier-type corrosion layer surface coverage at around 48 h of immersion. Daily electrolyte renewal promotes partial dissolution of the corrosion layer and increased mass transport, as a result of the lower electrolyte pH, leading to formation of a thicker corrosion layer and attaining the maximum barrier-type corrosion layer surface coverage at around 72 h. Finally, immersion experiments under continuous flow lead to more efficient control of the electrolyte pH and Mg^{2+} concentration, leading to increased mass transport, slower increase in the barrier-type corrosion layer surface coverage and formation of a thicker corrosion layer, with a barrier-type surface coverage below the “maximum” value after 5 days of immersion.

Table A.1: Elemental composition of the WE43 Mg alloy corrosion layer obtained by EDS from static immersion with no electrolyte renewal (SNER), static immersion with daily electrolyte renewal (SDER) and immersion with continuous electrolyte flow (CEF).

Experimental set-up	Elemental composition at. %							Ca/P
	C	O	Na	Mg	P	Ca	Cl	
SNER, after 8 h	32.31	53.13	0.91	5.52	6.51	1.62	-	0.25
SDER, after 24 h	19.64	56.19	1.05	5.93	10.73	6.46	-	0.60
CEF, after 5 days	21.52	54.78	0.82	2.31	12.34	8.22	-	0.67

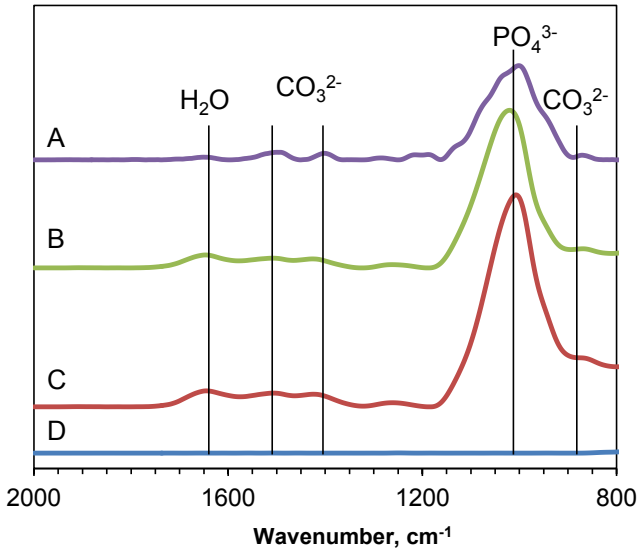

Figure A.7: ATR-FTIR spectra of WE43 Mg alloy after 5 days of immersion in m-SBF from (A) immersion with continuous electrolyte flow, (B) static immersion with daily electrolyte renewal and (C) static immersion with no electrolyte renewal tests. (D) Clean polished WE43 Mg alloy sample used as control.

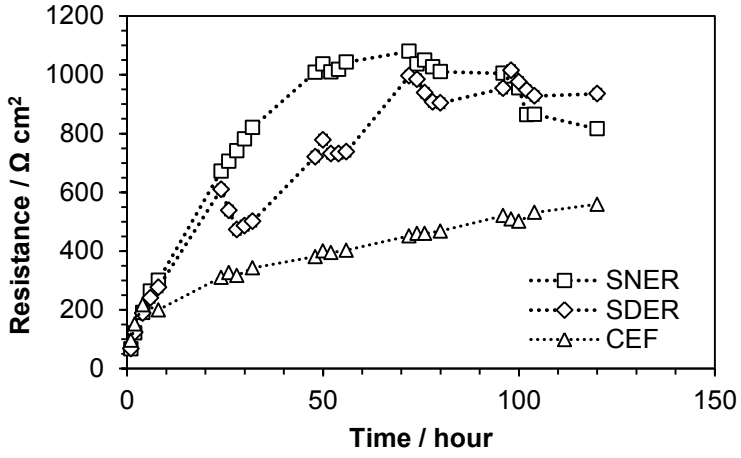

Figure A.8: Time-dependent charge transfer resistance (R_1) behaviour of WE43 Mg alloy in m-SBF from static tests with no electrolyte renewal (SNER) and daily electrolyte renewal (SDER) at 37 ºC, and immersion test with continuous electrolyte flow (CEF) at 22 ºC.

A.4 CONCLUSIONS

The corrosion behaviour of WE43 Mg alloy in m-SBF under continuous electrolyte flow conditions was investigated over a 5-day period time. The electrochemical cell reached steady state after 24 h, showing a quasi-constant pH and electrolyte concentration of Mg, Ca and P. EIS results showed a gradual increase in the charge transfer (R_1) with time, which were related to formation of a barrier-type corrosion layer with increasing coverage over time. Characterization of the corrosion layer after 5 days of immersion showed the presence of a carbonated apatite $MgO/Mg(OH)_2$ mixed corrosion layer with a thickness in the range of 90-165 μm and with no signs of fracture or localized corrosion. Comparison of the Mg alloy corrosion behaviour under continuous flow conditions, with results obtained from static immersion experiments showed that the presence of a continuous electrolyte flow leads to a slower increase in the barrier-type

corrosion layer surface coverage, i.e., faster corrosion rate, as a result of increased mass transport, thereby delaying the onset of localized corrosion, which occurs above a "maximum" barrier-type corrosion layer surface coverage.

The present results describe the corrosion behaviour of WE43 Mg alloy at conditions that better resemble physiological homeostasis (continuous flow), with respect to traditional static immersion tests, and demonstrate the importance of the experimental set-up for the accurate determination of the Mg alloy corrosion behaviour.

ACKNOWLEDGEMENTS

The authors gratefully acknowledge the financial support from the Natural Science and Engineering Research Council of Canada (NSERC) and the National Council of Science and Technology of Mexico (CONACyT). The contribution of Pierre Vermette in the casting of the Mg alloy samples is also acknowledged.

A.5 REFERENCES

[1] Y. Chen, S. Zhang, J. Li, Y. Song, C. Zhao, X. Zhang, Dynamic degradation behavior of MgZn alloy in circulating m-SBF, Materials Letters, 64 (2010) 1996-1999.

[2] J. Levesque, H. Hermawan, D. Dube, D. Mantovani, Design of a pseudo-physiological test bench specific to the development of biodegradable metallic biomaterials, Acta Biomaterialia, 4 (2008) 284-295.

[3] G. Song, A. Atrens, Understanding magnesium corrosion. A framework for improved alloy performance, Advanced Engineering Materials, 5 (2003) 837-858.

[4] G. Baril, G. Galicia, C. Deslouis, N. Pebere, B. Tribollet, V. Vivier, An Impedance Investigation of the Mechanism of Pure Magnesium Corrosion in Sodium Sulfate Solutions, Journal of the Electrochemical Society, 154 (2007) C108-C113.